National Library of Canada

Acquisitions and Bibliographic Services Branch

395 Wellington Street
Ottawa, Ontario
K1A 0N4

Bibliothèque nationale du Canada

Direction des acquisitions et des services bibliographiques

395, rue Wellington
Ottawa (Ontario)
K1A 0N4

Your file Votre référence

Our file Notre référence

NOTICE

The quality of this microform is heavily dependent upon the quality of the original thesis submitted for microfilming. Every effort has been made to ensure the highest quality of reproduction possible.

If pages are missing, contact the university which granted the degree.

Some pages may have indistinct print especially if the original pages were typed with a poor typewriter ribbon or if the university sent us an inferior photocopy.

AVIS

La qualité de cette microforme dépend grandement de la qualité de la thèse soumise au microfilmage. Nous avons tout fait pour assurer une qualité supérieure de reproduction.

S'il manque des pages, veuillez communiquer avec l'université qui a conféré le grade.

La qualité d'impression de certaines pages peut laisser à désirer, surtout si les pages originales ont été dactylographiées à l'aide d'un ruban usé ou si l'université nous a fait parvenir une photocopie de qualité inférieure.

Canada

The Magnetic Properties of Annite:

a SQUID Magnetometry and ^{57}Fe Mössbauer Spectroscopy Study.

by

Iain A. D. Christie

Thesis submitted to the School of Graduate Studies and Research, University of Ottawa, in partial fulfillment for the PhD. degree in the:

Ottawa-Carleton Institute of Physics
Ottawa, Ontario, Canada

June, 1994

ISBN 0-612-00581-X

UNIVERSITÉ D'OTTAWA
UNIVERSITY OF OTTAWA

UNIVERSITÉ D'OTTAWA
UNIVERSITY OF OTTAWA

For Pam

"If Patience is a Virtue,
Persistence is its part.
It's Better to Light a Candle,
Than Stand and Curse the Dark"

- James Keelaghan

Abstract

Annite is the Fe rich end-member of the phlogopite-biotite-annite series of micas. The ideal structural formula of annite is: $\{K^+\}[Fe_3^{2+}]\langle Al^{3+}Si_3^{4+}\rangle O_{10}^{2-}(OH^-)_2$. Two samples of annite have been studied, a synthetic, true end-member (in the form of a fine powder) and a natural, near end-member (in the form of single crystal). The samples have been studied using SQUID magnetometry and Mössbauer spectroscopy at temperatures ranging from 4.2 K to 295 K using a purpose-built Mössbauer cryostat and insert.

In disagreement with earlier predictions it has been determined that the magnetic ground state of annite consists of planes of predominantly ferromagnetic spins stacked antiferromagnetically along the c* axis. In further contrast to earlier predictions, it has been found that, for annite, the ordering temperature, T_N, is greater than 10 K, with the synthetic sample having $T_N = 58$ K. It is proposed that the planar antiferromagnetic structure is part of the intrinsic zero-field magnetic domain structure and that this structure is stabilized by inter-layer dipole-dipole forces.

Mössbauer spectroscopy measurements indicate some striking features of the temperature development of magnetic state of both annite samples. In particular, the results indicate that there is a persistent paramagnetic Fe^{2+} contribution at temperatures as low as 0.1 T_N; and that the Fe^{3+} moments disorder at temperatures significantly below T_N. Plausible causes for these features are discussed.

The first documented attempt to fit the low temperature spectrum of annite is reported. A method for stripping the Fe^{3+} contribution from the liquid helium spectrum of synthetic annite is discussed and a hierarchy of simple models is constructed and applied in attempt to fit the remaining Fe^{2+} subspectrum. An acceptable fit is not obtained. The consequences of the failure of the simple models are examined.

Acknowledgments

I would like to begin by thanking my supervisor, Dr. Denis Rancourt, for his patience, and perseverance in steering this project toward something resembling a conclusion. I would also like to thank him for the generosity of his support, the thoughtfulness of his advice, and the excellence of his instruction. I have learned to appreciate them all.

I would like to recognize NSERC and the University of Ottawa for generous financial support to me personally for the first two years of this program.

This thesis could not have been completed without the material contributions of Dr. J.-L. Robert, who synthesized one of the samples in this study; Dr. G. Lamarche who conducted the low field SQUID measurements, and Dr. S. Flandrois, who conducted the high field SQUID measurements. I would also like to thank Dr. R.C. Thiel for turning a cranky and leaking cryostat into an actual working Mössbauer experiment.

I would also like to state here, that the success of the Mössbauer experiments is directly related to the professionalism and expertise of the technical support staff at the physics department. In particular, I would like to thank Len (who practically built the probe), Bob, Charlie, Art and Mike.

Aside from the material contributors to this thesis, I feel it is important to recognize the many contributors to both my physical and mental well being over the last four and half years.

First of all, to the students who have passed through the doors of the Mössbauer lab: Pam, Paula, Mike, Dang, and Myriam: thanks for your camaraderie, conversation and company.

Secondly, I must mention my remarkable and special friends who have added their support in a myriad of diverse ways. I would like to thank Dave LeBlanc and Rob Parent for sharing the "joys" of working in the physics department; Jake Wedge for being crazy, Laura Jayne for occasionally being on time; Steve and Genevieve Janveau-Brennan for being great "new" friends; Aspa Tzaras for being her inimitable self and for having a fantastic family; Jill Jensen for her company and always stimulating conversation; Mario Moniz de

Sa for his extraordinary common sense and for his remarkable wife Claudia; and finally the incomparable Paul Newman with whom I obtained my graduate degrees in Non-Linear Thinking, Kite Flying, Rocketry, and Funny Accents. I will miss you all.

I would also like to extend my gratitude to that most wonderful of Canadian institutions, CBC radio. To the local morning folks: John, Fraser, Bert, and now Marguerite (and of course Bob Johnson, Phil Tilney and the guys at the weather office); to Peter Gzowski and the Morningside crew; and to Vicky Gabereau, Bill Richardson and the Gabereau gang: you have been a constant source of entertainment, information, conversation, and companionship (and occasionally distraction) through many hours spent staring into a computer screen waiting for this thesis to write itself (which it steadfastly refused to do). Thank you all, keep it up, and God Bless the CBC!

Finally and most importantly, I would like to say to my wife, Pam: *thank you for going through this with me*. It was awful nice to have the company, I couldn't have done it any other way.

Table of Contents

List of Figures

List of Tables

List of Appendices

List of Symbols and Abbreviations

[ ]	Denotes a cation in the octahedral sheet of a layer silicate.
⟨ ⟩	Denotes a cation in the tetrahedral sheet of a layer silicate.
//	parallel to the c* axis.
⊥	Perpendicular to the c* axis (*i.e.* lying in the **ab** plane).
γ	Line half width of a Lorentzian.
Γ	Fitting Lorentzian HWHM.
δ	Centre shift.
Δ	Quadrupole splitting.
ΔE_{hf}	Shift in energy due to the hyperfine field.
Δ_0	Central value of the Δ distribution.
ε	Line shift induced by a non-zero EFG in a situation where $\frac{1}{2}e^2qQ \ll g^* \mu_N H$.
η	EFG asymmetry parameter.
θ	Polar angle between H and EFG.
θ_{cw}	Curie- Weiss Temperature.
θ_D	Debye temperature.
μ_B	Bohr Magneton.
μ_N	Nuclear Magneton.
μ_i	local magnetic moment of ion i.
ν	Energy in mm/s.
ν_c	Centre line Position.
χ	Magnetic susceptibility.
χ_p	Magnetic Susceptibility of a powder.
χ^2	Chi-Squared statistical figure of merit function.
$\overline{\chi}^2$	Reduced Chi-Squared.
ρ	Density.
σ_Δ	Gaussian width of the Δ distribution.
σ_H	Gaussian width of the H distribution.
$\psi_s(0)_A$	s-electron Schrödinger wavefunction of the absorber at r = 0.
$\psi_s(0)_S$	s-electron Schrödinger wavefunction of the source at r = 0.
ϕ	Azimuthal angle between H and EFG.
A	Spectral area.
ab plane	Plane of the octahedral layer.

b	Unit cell length of octahedral unit cell.
BG	background.
C	Curie Constant.
c	Speed of light.
c*	The axis perpendicular to the plane of the octahedral sheet in a layer silicate.
C(i)	The number of counts in channel i.
CS	Centre Shift.
d-d	dipole dipole.
DD	Dependent distribution broadening model.
d	Fitting bin width.
d_k	Width fitting bin k
d_t	Tetrahedral bond length.
e	Electron charge.
eq	Maximum value of the EFG tensor.
$\frac{1}{2}e^2qQ$	Splitting due to EFG in the absence of a hyperfine field.
f	Ration of octahedral iron to total octahedral sites.
EFG	Electric Field Gradient.
FC	Field Cooling.
FW	Field Warming.
g	average ionic g factor (chapter 4 and 5); or ground state nuclear g-factor (chapter 6 and 7).
g*	ground state nuclear g-factor.
$g^*\mu_N H$	Splitting due to the presence of a hyperfine field in the absence of an EFG.
H	Applied Magnetic Field Strength (chapter 4 and 5); or Hyperfine magnetic field strength (chapter 6 and 7).
H	Hyperfine magnetic field.
H_A	Applied magnetic field (chapter 6).
H_D	Dipole magnetic field.
H_L	Electron current magnetic field.
H_{local}	Local hyperfine field.
H_S	Fermi contact magnetic field.
H_{THF}	Transferred hyperfine field.
H_{STHF}	Supertransferred hyperfine field.
H_{sf}	Spin flop field.
ID	Independent distribution model.
IS	Isomer Shift.

J	Average near neighbour magnetic exchange constant.
J_{22}	Exchange between a pair of neighbouring Fe^{2+} ions.
J_{33}	Exchange between a pair of neighbouring Fe^{3+} ions.
J_{23}	Exchange between Fe^{2+} and Fe^{3+}.
k_B	Boltzman Constant.
LHT	Liquid He temperature.
LHe	Liquid He.
LN_2	Liquid N_2.
LNT	Liquid nitrogen temperature.
LRO	Long range order.
LW	Line width broadening model.
M	Magnetization.
MCS	Multi-channel scaler.
MES	Mössbauer effect Spectroscopy.
MPA	Microprobe analysis.
N	Number of atoms.
N_b	Number of bins in the fitting model.
nn	Near neighbour.
nnn	Next near neighbour.
p_2	Ration of ferrous iron to total iron.
p^{2+}	Effective magneton number for Fe^{2+}.
p^{3+}	Effective magneton number for Fe^{3+}.
p_{eff}	Effective magneton number.
$P(\mu)$	Probability distribution of magnetic moments
$P(\Delta)$	Probability distribution of quadrupole splitting.
$P(H_{hf})$	Probability distribution of hyperfine field.
P(k)	Probability distribution of Mössbauer "sites".
P_k	Probability of fitting bin k.
Q	Nuclear quadrupole moment.
RT	Room Temperature
S	Spin
SEM	Scanning Electron Microscope.
SOD	Second Order Doppler Shift.
SQUID	Superconducting Quantum Interference Device.
T	Temperature.
T_N	Ordering temperature

TM	Transition Metal.
T(i)	The theoretical number of counts assigned to channel i by the fitting model.
V	Volume (chapter 4 and 5); or Electrostatic potential (chapter 6).
v	Molecular volume
V_{ZZ}	First principal component of the EFG tensor.
V_{XX}	Second principal component of the EFG tensor.
V_{YY}	Third principal component of the EFG tensor.
XRD	X-ray Diffraction.
z	average number of magnetic near neighbours.
ZFQ	Zero-field quench.

Chapter 1

Introduction

Layer silicates in general, and micas in particular, are large classes of materials which have long been important to geologists as probes of rock formation conditions. For instance, the Fe^{3+} to Fe^{2+} ratio in mica is the basis of an oxygen fugacity scale in the study of igneous and metamorphic rocks (Wones and Eugster, 1965). Reviews of the properties and geological importance of mica are provided by Deer *et al* (1966), Zoltai and Stout (1984) and Bailey (1984).

For physicists, mica also offers a convenient laboratory for the study of two-dimensional (2D) magnetism. The crystal structure of mica results in truly exchange-wise isolated 2D magnetic layers that are separated by several planes of diamagnetic ions and distance on the order of 10Å (Rancourt *et al.*, 1990). Although the magnetic properties of over 60 samples of various types of layer silicates have been reported, there has been little attempt to exploit layer silicates for a systematic exploration of 2D magnetism (see chapter 4 and references therein). This may, in large measure, be due to the fact that the reported samples have been ill-characterized natural samples with complicated compositions involving many different magnetic and non-magnetic ionic species.

This thesis is the first part of a larger project in which the 2D magnetism of layer silicates will be comprehensively examined. As a starting point for this larger project, two samples of the Fe-rich mica, annite have been chosen. The magnetic properties of these samples (a synthetic, true end member, powder, and a natural, single crystal, near end-member) are reported in this thesis.

The choice of annite as a starting point for an investigation of 2D magnetism is natural because it corresponds to the end-member composition of three different solid solution series. The composition[1] of true annite is:

$$\{K^+\}[Fe_3^{2+}]\langle Al^{3+}Si_3^{4+}\rangle O_{10}^{2-}(OH^-)_2 \quad . \tag{1.1}$$

It forms solid solutions with phologopite :

$$\{K^+\}[Mg_3^{2+}]\langle Al^{3+}Si_3^{4+}\rangle O_{10}^{2-}(OH^-)_2, \tag{1.2}$$

flourannite:

$$\{K^+\}[Fe_3^{2+}]\langle Al^{3+}Si_3^{4+}\rangle O_{10}^{2-}(F^-)_2, \tag{1.3}$$

and oxyannite:

$$\{K^+\}[Fe^{2+}Fe_2^{3+}]\langle Al^{3+}Si_3^{4+}\rangle O_{12}^{2-} . \tag{1.4}$$

The phlogopite-annite solid solution is formed by progressively replacing diamagnetic Mg^{2+} ions with magnetic Fe^{2+}, producing variation in magnetic site disorder. Note that intermediate compositions are traditionally known as biotites so that the series is often known as the phlogopite-biotite-annite series. The flourannite-annite series is formed by progressively replacing F^- anions with OH^- anion groups. This substitution produces variation in magnetic bond disorder since it has a strong effect on the superexchange interaction between neighbouring Fe^{2+} ions. The oxyannite-annite series is formed by the replacement of Fe^{3+} ions with Fe^{2+} by nondestructive reduction techniques (Hogg and Meads, 1975; Tripathi, *et al.*, 1978; Rancourt *et al.*, 1993a;)[2]. Since the Fe^{2+}-Fe^{2+}, Fe^{2+}-Fe^{3+}, and Fe^{3+}-Fe^{3+} exchange interactions have different magnitudes and signs (Rancourt, 1990 and references therein) this series allows adjustment of both site and bond disorder.

The selection of annite provides a base experimental system for studying the effects of bond, site and combined bond and site disorder in a 2D Heisenberg ferromagnet with easy plane anisotropy[3]. The state of theoretical models is more problematic. There has been extensive theoretical research into the problem of low dimensional magnetic systems (see for instance Kramers and Wannier, 1941; Onsager, 1944; Bonner and Fisher, 1964; Stanley and Kaplan 1966 and Mermin and Wagner, 1966; Beresinskii and Blank, 1973). However, although work has been done to show that it is possible for an ordered state to exist for a 2D Heisenberg system under the effects of dipole-dipole forces or easy

---

[1]The meanings of {}, [ ], and ⟨ ⟩ are discussed in chapter 2.

[2]The reverse reaction (Fe^{2+} to Fe^{3+}) is also accessible through oxidation.

[3]This magnetic state is discussed in chapter 4 and 5.

plane anisotropy (see for instance Beresinkii, 1973; Villain, 1974; Pokrovsky, 1979), no theoretical model of such a system exists.

In short, the current situation is one in which the simple theoretical models do not provide information which is applicable to the complicated experimental systems and the experimental systems cannot be analyzed with the existing theoretical models. Given this lack of a coherent theoretical framework, the approach of this work has been to describe certain aspects of the magnetism of annite in the hopes that this will motivate the needed theoretical studies which treat realistic experimental features. These features include: the presence of paramagnetic Fe^{2+} at temperatures which are 50 K below the ordering temperature (T_N), and the disappearance of Fe^{3+} moments at temperatures 20 K below T_N.

This is not to imply that the results of this study cannot be directly compared to the current literature. In particular, the annite data directly addresses the contention that $T_N <$ 10 K for all biotites. This conclusion has been based on work by Coey and Ghose (1988), Ballet, *et al* (1982) and Beausoleil *et al* (1983) and has apparently become the accepted view, having been published in a Mössbauer spectroscopy text (Mitra, 1992). The data from annite shows conclusively that the contention is false, as the annite samples have T_N > 40 K. Also, the SQUID measurements point out the strong shape dependence of the susceptibility which has not been previously remarked upon. This shape dependence is proof of the critical (but largely unmentioned) role played by dipole-dipole forces in the ordering of layer silicates.

For the purposes of this thesis the discussion of the magnetic properties of annite is divided into three principal sections dealing with: annite, magnetism, and Mössbauer spectroscopy respectively. Each section consists of a background chapter followed by a chapter of results and discussion. Chapter 2 is a brief overview of the structure of layer silicates in general, and of annite in particular. Chapter 3 is devoted to describing and characterizing the two samples of annite studied in this work. Chapter 4 is a review of the literature that has dealt with the magnetism of layer silicates. This is followed, in chapter 5, by the presentation and discussion of the SQUID magnetization measurements on the annite. In chapter 6 the principles of Mössbauer spectroscopy are briefly reviewed. In chapter 7 the design and operation of a purpose built Mössbauer spectrometer is described, and results of Mössbauer studies using this equipment are presented. Chapter 7 also provides an in depth qualitative description of the low temperature synthetic annite spectrum and the details of the failure of attempts to extract the distribution of Fe^{2+} hyperfine fields using a hierarchy of simple fitting models.

Chapter 2

Structure and Crystal Chemistry of Annite

2.1 Layer Silicates

Layer silicates are a large class of minerals. Their crystallographic structure consists of layers of transition metal (TM) oxide sheets which are either separated by large cations (*e.g.* K^+, Na^+ etc.) or separated by water molecules or weakly bonded by Van der Waals forces. Within the TM oxide layers there are two different types of sheets with octahedral and tetrahedral cation coordination. The materials are classified according to the layer structure as either 1:1, 2:1, or 2:1:1. The first category of materials have layers which consist of a single tetrahedral sheet and a single octahedral sheet. The 2:1 materials have layers made up of single octahedral sheets sandwiched between two tetrahedral sheets. The final structure (2:1:1) consists of 2:1 layers which are separated by isolated octahedral sheets (known as hydroxide layers).

2.1.1 The Octahedral Sheet

An octahedral sheet consists of TM ions at the center of edge shared octahedra. Cations in these sites are denoted by []. The 6 corners of each octahedron are occupied by either O^{2-} ions or OH^- groups[1]. The position and nature of the coordinating anions is determined by the layer structure. In isolated layers all the corners are occupied by OH^- groups. In 1:1 materials two of the sites are shared with the tetrahedral sheet and are occupied by O^{2-}. In the 2:1 structure there are four shared, O^{2-} corners. The TM species which typically occupy the octahedral sites include Fe^{2+}, Fe^{3+}, Mg^{2+}, Mn^{2+}, Al^{3+},

[1] The OH^- groups are occasionally replaced by F^- and Cl^-, this can have a dramatic effect on the magnetic properties of the silicate but these samples should be considered as a special class of materials and are beyond the scope of this thesis.

Cu^{2+}, Co^{2+} and Cr^{2+}. If the sheet is fully occupied (trioctahedral), the TM sites form a triangular lattice. In sheets which are only 2/3 full (dioctahedral), the TM sites form a honeycomb lattice.

2.1.2 The Tetrahedral Sheet

A tetrahedral sheet consists of smaller tri- or quadravalent TM cations at the centers of corner shared tetrahedra. Ions in these sites are denoted by ⟨⟩. The corners of tetrahedra are occupied by O^{2-}. While an octahedral sheet can exist alone (as in the chlorite structure), a tetrahedral sheet is always paired with an octahedral sheet in layer silicates. The apices of the tetrahedra point toward the octahedral layer and the apex O^{2-} are shared with the octahedral layer. The cations which typically occupy the tetrahedral layer are: Si^{4+}, Al^{3+}, Fe^{3+} and Ti^{4+}.

2.1.3 The Interlayer

In all cases, the interlayer chemistry is dictated by the requirements of overall charge balance. In materials such as mica, which have a relatively large negative layer charge, the interlayer consists of large singly or doubly valent cations. In materials which have neutral layers the interlayer may consist of neutral water molecules or there may be no interlayer species at all (as in talc) in which case layers are bonded by Van der Waals forces.

2.2 Structure and Crystal Chemistry of Annite

2.2.1 Ideal Structure of Annite

Annite is a mica. Micas are a large family of 2:1 layer silicates with relatively high layer charge. In particular, annite is the Fe-rich end-member of the phlogopite-biotite-annite family. The crystal structure of this family is treated in more detail by Hazen and Burnham (1973). The structural formula of this solid solution is:

$$K^{+}\left[\left(Fe_{x}^{2+}Mg_{1-x}^{2+}\right)_{3}\right]\left\langle Al^{3+}Si_{3}^{4+}\right\rangle O_{10}^{2-}\left(OH^{-}\right)_{2} \qquad (2.1)$$

And therefore, the ideal structural formula of annite is:

$$K^{+}\left[Fe_{3}^{2+}\right]\left\langle Al^{3+}Si_{3}^{4+}\right\rangle O_{10}^{2-}\left(OH^{-}\right)_{2} \qquad (2.2)$$

In short, the ideal annite structure consists of an octahedral sheet which is completely filled with Fe^{2+} and a tetrahedral sheet filled at random with Al^{3+} and Si^{4+} in a 1:3 ratio. As described above, the apex O^{2-} of both the top and bottom tetrahedral layers are shared with the octahedral layer. When viewed from above (or below) these apex oxygens form six fold rings (see figure 2.1). At the center of each of these rings is an anion site which is part of the octahedral layer but is not shared with the tetrahedral layer. These sites are occupied by OH^- groups.

Figure 2.2 shows a view of the resulting octahedral layer. The octahedral sites are classified into CIS and TRANS families based on the arrangement of the OH^- groups. In the ideal annite structure there are exactly two CIS sites for every TRANS site.

2.2.2 Structural Distortions and the Real Structure of Annite

Because the apex oxygens of the tetrahedral sheets are shared with the octahedral sheet the size matching of the two sheets is of critical importance in the formation of a stable 2:1 layer structure. The size of the tetrahedral sheet is characterized by the tetrahedral bond length, d_t. The size of the octahedral sheet is characterized by the dimension b as shown in figure 2.2. In an undistorted structure it follows from the layer geometry that:

$$b = 4\sqrt{2}d_t \tag{2.3}$$

However, in real materials this ratio is rarely obtained exactly and some structural distortion is required to match the sheets.

In a study of cation substitution in micas, Hazen and Wones (1972) describe four structural distortions which account for a size mismatch between an octahedral sheet which is too small for an accompanying tetrahedral sheet. Of these mechanisms, the two which predominate are: (1) the compression of octahedra along the c axis which stretches the octahedral sheet; and (2) the rotation of tetrahedra about their apex oxygens, which contracts the tetrahedral sheet. There are, however, no structural methods for expanding the tetrahedral sheet or contracting the octahedral sheet to account for an octahedral sheet which is too large. This means that equation 2.3 effectively places an upper limit on b in terms of d_t.

For the $AlSi_3$ tetrahedral sheet it has been shown that $d_t = 1.643$ Å (Hazen and Wones, 1972). This corresponds to a maximum value of b = 9.294 Å. Hazen and Wones have also shown that since b is directly proportional to the size of the octahedral cation, $AlSi_3$ tetrahedral sheets do not form stable compounds with octahedral sheets in which the

average cation radius is greater that a certain critical radius (0.76 Å). Since the radius of $[Fe^{2+}]$ is 0.78 Å (which corresponds to b = 9.35 Å), it is not possible to form the ideal annite structure.

It is however possible to form a structure with near-ideal annite stoichiometry by substituting some $[Fe^{3+}]$ for $[Fe^{2+}]$. When substituted directly for Fe^{2+} in the octahedral sheet, Fe^{3+} (which has a radius of 0.63 Å in octahedral coordination) reduces the average b. If the Fe^{3+} is also exchanged with Al^{3+} in the tetrahedral sheet the average value of d_t is increased (an $Fe^{3+}Si_3$ tetrahedral sheet has d_t = 1.68 Å) and b is further reduced (since the radius of $[Al^{3+}]$ is 0.55 Å). Thus, the structural formula of real annite will be of the form:

$$K^{+}\left[Fe^{2+}_{3-x-y}Fe^{2+}_{x}Al^{3+}_{y}\right]\left(Al^{3+}_{1-y}Fe^{3+}_{y}Si^{4+}_{3}\right)O^{2-}_{10+x+y}\left(OH^{-}\right)_{2-x-y} \qquad (2.4)$$

The values of x an y are dependent on the synthesis conditions, particularly the oxygen fugacity (Redhammer *et al.* 1993). Nonetheless, the matching of the tetrahedral and octahedral sheet places minimum values on x and y. These are linearly dependent on one another. The line defined by their relationship has been calculated by Rancourt (unpublished) and is:

$$y = -3.74x + 0.483 \qquad (2.5)$$

There are some important differences between the ideal annite structure and the real annite structure. The most obvious of these is the changing valence of some of the octahedral sites. This in turn results in changing anion stoichiometry as each octahedral site occupied by a triply valent ion has one of its coordinating hydroxide groups "dehydroxyalted" (to become O^{2-}) in order to maintain local charge balance. It must be noted that, although such anion sites are no longer occupied by OH^{-}, they are still crystallographically distinct from the sites occupied by the tetrahedral apex oxygens.

Another structural effect is the distortion of the octahedra and tetrahedra to accommodate ions of differing size and valences. For instance, consider the case of an octahedral TRANS site occupied by an Fe^{3+} ion (figure 2.3). The combined effect of the smaller ionic radius and larger valence of the Fe^{3+} ion cause the anions to contract around it, particularly the two unshared sites. This distortion in turn causes slight expansion of the neighbouring octahedral cages containing Fe^{2+}. It can easily be seen that the presence of a single Fe^{3+} ion has the effect of potentially distorting all of the neighbouring octahedra to some extent. Thus, even small amounts of Fe^{3+} can affect the local environments of a large proportion of the Fe^{2+} ions.

Similarly, there will be some distortion of the tetrahedral layer to accommodate the different sized cations. These distortion will be transmitted to the octahedral layer through

the shared apex oxygens. In fact, such distortions would occur even in the ideal structure since the Al^{3+} and Si^{4+} also are of different sizes and randomly distributed.

In summary, the net effect of the cation substitutions necessary to form the real annite structure is that there are variations in both the near-neighbour (anion) and second near-neighbour (cation) chemistry of the octahedral sites throughout the crystal structure. It is these variations which underlie much of the interesting physics which are the subject of the remainder of this work.

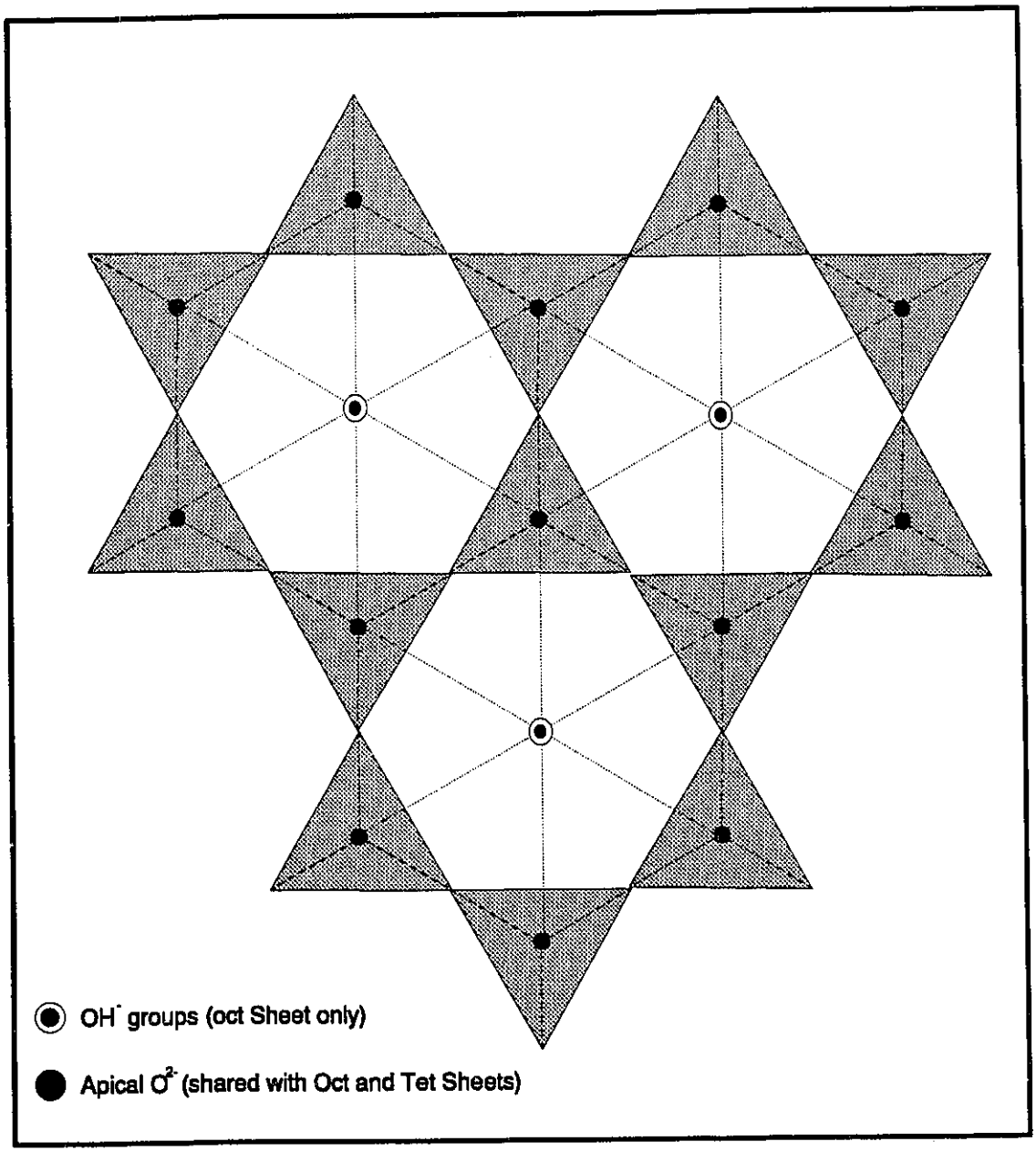

Figure 2.1 *Top view of the annite TOT layer showing the placement of tetrahedra above the octahedral sheet. For clarity the tetrahedral cations have been omitted.*

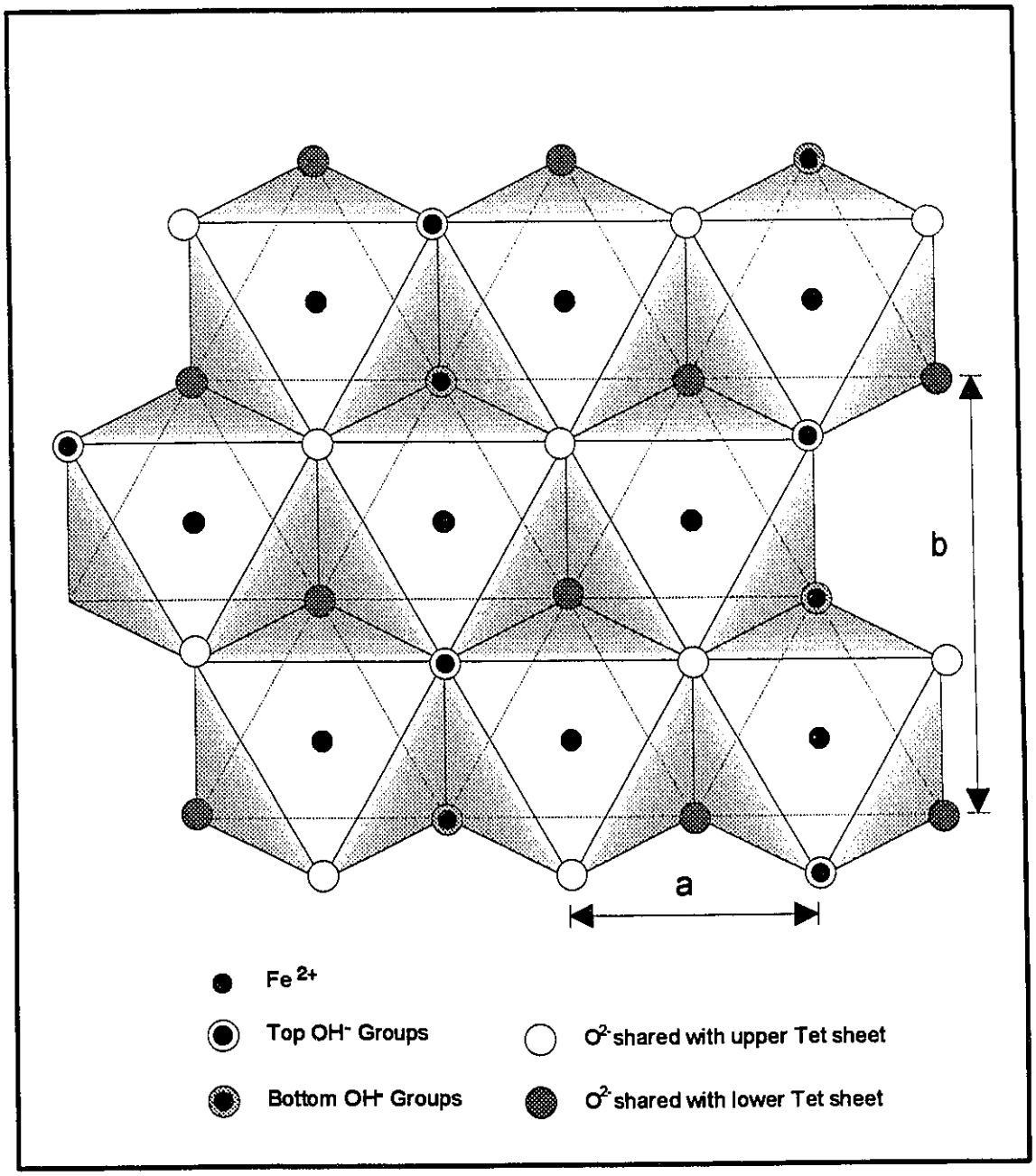

***Figure 2.2** The ideal annite octahedral sheet structure showing the placement of shared O^{2-} ions and unshared OH^- groups. The resulting arrangement of CIS and TRANS octahedral sites can also be seen.*

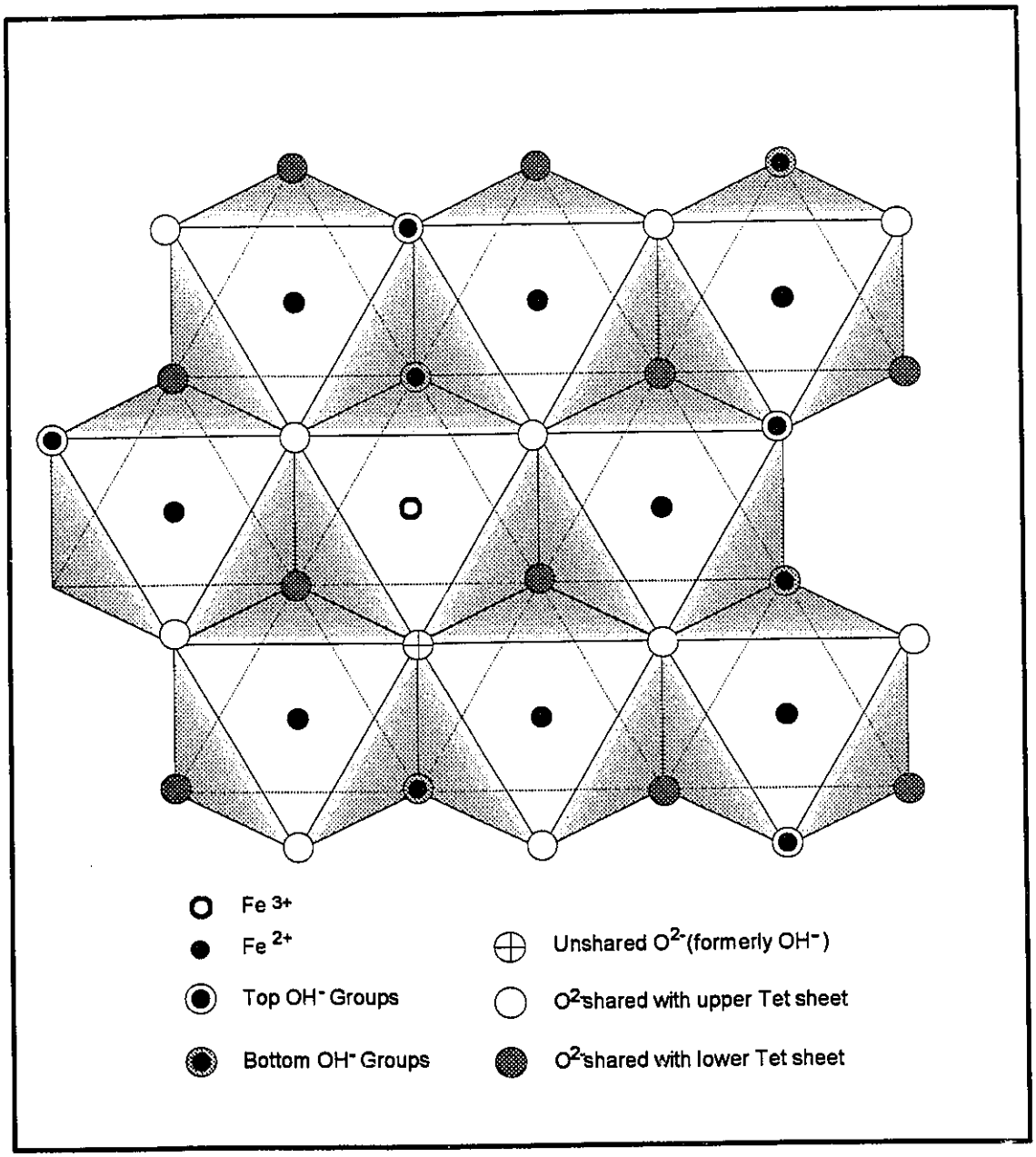

Figure 2.3 *Defect caused by the substitution of a single Fe^{3+} ion in an Fe^{2+} octahedral sheet. One of the OH^- groups coordinating the substitution site has been dehydroxylated to O^{2-} in order to maintain charge balance. This affects the symmetry of two neighbouring Fe^{2+} sites.*

Chapter 3

Characterization and Synthesis of Annite Samples

3.1 General Description

In this study measurements were performed on two different samples of annite: A synthetic sample and a natural sample. The synthetic sample was in the form of a fine powder (≤ 0.1 μm). The Natural sample is a near end-member of the phlogopite-biotite-annite series in the form of a series single crystal flakes. It was obtained from the Royal Ontario Museum collection (sample no. M42126) and was originally mined at Mont St. Hilaire, PQ.

3.2 Synthesis and Characterization of Synthetic Sample

The synthesis was performed by J.-L. Robert at Orléans by starting from a fine mechanical mixture of a specifically prepared silicate gel and a metallic iron powder. Full details of the synthesis process can be found elsewhere (Rancourt, *et al.*, 1994).

The result of the synthesis was pure annite to within the resolution of X-ray diffraction, XRD (Rancourt, *et al.*, 1994). No iron-bearing impurities were detected in subsequent Mössbauer spectra or any SQUID magnetometry measurements (Rancourt *et al.*, 1994, and see chapters 5 and chapter 7) or in scanning electron microscope (SEM) pictures (Rancourt, *et al.*, 1994). Thus, in the absence of cation substitution the structural formula of the synthesized annite would be that of the ideal annite (equation 2.2).

However, as discussed in chapter 2, the ideal stoichiometry is not obtainable so the extent of cation substitution was determined using Mössbauer spectroscopy. These results are part of a detailed study presented elsewhere (Rancourt *et al.*, 1994) and are summarized in table 3.1.

From these results, and assuming no octahedral vacancies the structural formula of the synthetic sample is:

$$K^{+}\left[Fe^{2+}_{2.67}Fe^{3+}_{0.21}Al^{3+}_{0.12}\right]\left\langle Al^{3+}_{0.88}Fe^{3+}_{0.12}Si^{4+}_{3}\right\rangle 0^{2-}_{10.33}OH^{-}_{1.67} \qquad (3.1)$$

Physically, the synthetic sample is in the form of a powder. SEM pictures shows it to have particles ranging in size from 2μm to 0.1μm. In mineralogical terms, the powder would be classified as a clay.

3.3 Characterization of Natural Sample

The chemical composition of the natural sample was determined by micro-probe analysis (MPA). The result of this analysis are presented in table 3.2. As in the synthetic case, the chemical composition is not sufficient to determine the structural formula because the site populations of the various species of Fe ([Fe^{2+}], [Fe^{3+}], and $\langle Fe^{3+}\rangle$ cannot be accurately determined by MPA.

Once again Mössbauer spectroscopy was used to determine the various site populations (Rancourt and Lalonde unpublished, see table 3.1). Based on these results the chemical formula of the natural sample is:

$$K^{+}_{0.937}Na^{+}_{0.075}\left\{\left[Fe^{2+}_{2.25}Fe^{3+}_{0.28}Mn^{2+}_{0.18}Mg^{2+}_{0.07}Ti^{4+}_{0.08}Al^{3+}_{0.001}\right]\left\langle Al^{3+}_{0.98}Fe^{3+}_{0.20}Si^{4+}_{2.8}\right\rangle 0^{2-}_{11}OH^{-}_{1.84}F^{-}_{0.15}Cl^{-}_{0.005}\right. \qquad (3.2)$$

Although the distribution of the octahedral cations in the octahedral sheet has not been explicitly determined, it is expected, based on the literature, that the various cations fill the sheet at random (Manceau *et al.*, 1990).

Table 3.1 Unit cell parameters, stacking polytype and site populations in two samples of annite. The unit cell parameters and stacking polytype have been determined by XRD. The site populations have been determined by Mössbauer spectroscopy (see Rancourt *et al.*, 1994 and Rancourt *et al*, 1992).

Sample	Unit Cell parameters			Polytype	Fe/[][a]	$[Fe^{3+}]/Fe$	$\langle Fe^{3+}\rangle/Fe$
	a (Å)	b (Å)	c (Å)				
Synthetic	5.393	9.342	10.332	1M	100 %	7.0 ± 0.2 %	4.00 ± 0.15 %
Natural	5.389	9.343	10.291	1M	91%	10.3± 1.0 %	7.2± 1.0 %

[a] Ratio of total Fe to total number Octahedral sites.

Table 3.2 Results of MPA analysis on natural sample of annite.

Microprobe Results		Composition	
SiO_2	33.82	$\langle Si^{4+}\rangle$	5.882
TiO_2	1.25	$\langle Al^{3+}\rangle$	1.959
Al_2O_2	9.95	$\langle Fe^{3+}\rangle$	0.388
Fe_2O_3	7.59	$\langle\ \rangle_{tot}$	8.000
FeO	32.18	$[Al^{3+}]$	0.002
MnO	2.47	$[Ti^{4+}]$	0.158
MgO	0.59	$[Fe^{3+}]$	0.567
CaO	0	$[Fe^{2+}]$	4.499
Na_2O	0.46	$[Mn^{2+}]$	0.350
K_2O	8.78	$[Mg^{2+}]$	0.147
F	0.56	$[\ ]_{tot}$	5.723
Cl	0.03	$\{Ca^{2+}\}$	0
O=F	-0.24	$\{Na^{+}\}$	0.150
O=Cl	-0.01	$\{K^{+}\}$	1.873
Total	100.73	$\{\}_{tot}$	2.022
		F^-	0.296
		Cl^-	0.010
		OH^-	3.694

Chapter 4

Magnetism of Layer Silicates

In this chapter the work which has been reported on the magnetism of layer silicates is reviewed, a magnetic classification system is proposed and a general description of the samples which have been studied is presented. Finally, the results of various types of measurements including magnetic susceptibility, Mössbauer effect spectroscopy (MES), and neutron diffraction measurements are discussed.

4.1 Magnetic Classification of Samples

In studying the magnetic properties of layer silicates it is necessary to re-examine the classification of these minerals. Although the system of classifying layer silicates according to layer structure (as described in chapter 2) is useful geologically, it is inadequate for describing their magnetic properties because the topology of magnetic exchange bonds in these minerals is largely independent of the layer structure.

Although several magnetic elements are found in the octahedral sites, (e.g. Co, Cu, Cr) the most common is Fe, which is some 40 times as common as the next most common. The Fe occurs in two valence states, Fe^{2+} and Fe^{3+}. Both forms occur predominantly in the octahedral sheet[1]. Each octahedral sheet is isolated from neighbouring sheets by either diamagnetic cations or a Van der Waals gap. The result is that most phyllosilicates, regardless of layer structure, have a magnetic structure which

[1] Fe^{3+} can also occupy tetrahedral sites. Relatively less common silicates such as ferriphlogopite have the majority of Fe in these sites. In most samples a relatively small proportion of the magnetic ions are in the tetrahedral sheet and thus, the magnetic properties are chiefly determined by the octahedral Fe ions.

consists of exchange-wise isolated sheets of octahedrally coordinated magnetic ions on a triangular (or honey comb) lattice.

For this reason, the magnetic properties of the system are more strongly dependent on the chemistry of the octahedral layer than on the structural class of the material. It is useful, therefore, to derive a classification system based on the total concentration of Fe in the octahedral layer and on the relative proportions of each valence state present. For the remainder of this discussion samples will be classified as concentrated ($f = [Fe]/[\ ] > 0.33$) or dilute ($f \leq 0.33$) and as ferrous ($p_2 = Fe^{2+}/Fe > 0.5$) or ferric ($p_2 = \leq 0.5$).

4.2 Samples

Measurements on 63 samples of layer silicates have been reported. Samples from all three structural classes and from every magnetic classification have been studied (Tables 4.1, 4.2 and 4.3). The bulk of the work has tended to focus on the concentrated samples with particular attention being paid to the concentrated ferrous samples. Fifteen concentrated ferrous samples have been studied including the 1:1 compounds Greenalite and Berthierine (Coey *et al.*, 1981), several biotite micas (Ballet and Coey, 1982; Beausoleil *et al.*, 1983; Longworth and Townsend, 1987), ferrous talc (Minnesotaite, Coey *et al.*, 1990), and several minerals in the chlorite family (Ballet *et al.*, 1985; Townsend *et al.*, 1987).

In addition, seven concentrated ferric samples have been studied including two that were obtained by oxidizing three ferrous chlorites and a ferrous biotite (Longworth and Townsend, 1985; Longworth *et al.*, 1987).

The remaining 14 dilute samples have been included in three separate studies (Ballet and Coey, 1982; Ballet *et al.*, 1985; Townsend *et al.*, 1987). However, less data are available for these samples.

4.3 Crystal Field at Fe Sites

Before discussing results reported in the literature, it is important to briefly consider the crystal field at the octahedral Fe sites in layer silicates. This crystal field is thought to be responsible for significant magneto-crystalline anisotropy for the ferrous ions.

As discussed in detail in chapter 2, Fe occupies a site at the center of an octahedron which is compressed along the crystalline c^* axis (the c^* axis is defined as the

axis normal to the plane of the layer). If the coordinating anion sites are identical, this leads to a site with trigonal symmetry about the c^* axis. Of course, the coordinating sites are not identical. The sites may be occupied by different anions and may also be crystallographically distinct when the octahedral sheet is paired with a tetrahedral sheet. Four of the sites (two above and two below the TM site) can be shared with tetrahedral layers. The other two sites are always shared only with adjacent octahedra. There is also the added complication of the distinction between CIS and TRANS arrangements of the unshared anion sites in the 2:1 structure. Nevertheless, a trigonal model has been used successfully to model the crystal field at the TM site (Aldridge, 1991; Coey *et al.*, 1981, Beausoleil *et al.*, 1983). The effect of the crystal field on the resident TM ion is dependent to a large degree on the electronic configuration of that ion. The two Fe species have very different crystal field couplings.

The Fe^{3+} ion has an outer 4s shell which is spherically symmetric and does not couple strongly to the crystal field. It is expected, therefore, that the [Fe^{3+}] ions will show a much smaller magneto-crystalline anisotropy induced by the crystal field. Ballet and Coey (1982) concluded that there was no magneto-crystalline anisotropy at all at the Fe^{3+} site.

In contrast, the Fe^{2+} site has an outer 3d shell that is anisotropic and couples strongly to the crystal field. Ballet and Coey (1982) and Beausoleil *et al.* (1983) have proposed a model whereby the trigonal distortion lifts the three-fold orbital degeneracy of the T_{2g} cubic crystal field ground state. The result is an orbital A_1 singlet ground state. These authors further postulate that the crystal field reduces the effective spin from 2 to 1.

One effect of this crystal field is a strong magneto-crystalline anisotropy with an easy plane perpendicular to the c^* axis. This implies that the spin structure of the ordered state in the ferrous samples should consist of spins confined to the **ab** plane (Beausoleil *et al.*,1983; Ballet *et al.*, 1985).

4.4 Experimental Results

4.4.1 Room Temperature Mössbauer Spectroscopy

Many of the samples have been characterized extensively by standard chemical techniques and by room temperature (RT) MES. In most cases the final chemical formula of the sample is reported without extensive discussion. Fitted RT Mössbauer spectra are usually presented without a detailed description of the fitting model and the final fitting parameters are often not reported. It is therefore difficult to assess the quality of the

reported site populations since there are some important considerations which affect the accuracy of Mössbauer-determined site populations (Rancourt, 1989; 1993a). The reported values of RT MES parameters are summarized in Table 4.4.

4.4.2 Low Field Magnetic Susceptibility

Low field susceptibility curves are also widely reported in the literature. Such measurements are typically used to characterize the magnetic behaviour of a sample by fitting inverse susceptibility versus temperature to the Curie-Weiss law:

$$\chi^{-1} = \frac{T}{C} - \frac{\theta_{cw}}{C} \quad . \tag{4.1}$$

This form results from a high temperature expansion of the susceptibility. The first term is the infinite temperature limit and is independent of the form of the magnetic Hamiltonian. The Curie constant, C, is (see for example Ashcroft and Mermin, 1976):

$$C = \frac{N}{V} g^2 \mu_B^2 \frac{S(S+1)}{3k_B}. \tag{4.2}$$

The first order correction term contains θ_{CW}, which is normally called the Curie-Weiss temperature. For an isotropic Heisenberg Hamiltonian this is found to be (see Aschroft and Mermin, 1976):

$$\theta_{cw} = 2zJ \frac{S(S+1)}{3k_B}. \tag{4.3}$$

In these two expressions N is the number of magnetic ions in the sample, V is the sample volume, g is the average ionic g factor, μ_B is the Bohr magneton, z is the average number of magnetic near neighbours, J is the average near neighbour magnetic exchange constant, S is the average ionic spin, and k_B is the Boltzman constant.

Note that because of the strong planar magneto-crystalline anisotropy it is necessary to distinguish between measurements taken with fields applied parallel to the c^* axis and those with fields applied in the ab plane (distinguished by // and $\perp$ respectively). Of course, such distinctions can only be made for measurements on oriented samples. For random powder samples it is not possible to determine the two contributions separately. However the susceptibility of a powder can be written as:

$$\chi_p = \frac{1}{3}\left(2\chi_\perp + \chi_{//}\right). \tag{4.4}$$

The above derivation of the Curie-Weiss law for the inverse susceptibility is not strictly valid for layer silicates, particularly in the powder form, because the derivation of θ_{cw} given by equation 4.3 assumes an isotropic magnetic Hamiltonian. Nevertheless, Curie-Weiss temperatures for samples reported in the literature can be considered as an empirical characterization of the high temperature behaviour of $\chi(T)$ in these samples.

High temperature susceptibility measurements are available for 15 samples (Table 4.5). Samples of various structures and compositions have been studied, but they are restricted mainly to samples in the concentrated ferrous group with only four dilute ferrous and one dilute ferric sample present. Plots of C and θ_{cw} versus f are shown in figure 4.1 and figure 4.2.

To compare the experimental values to the theoretical values of C it is useful to make the following substitutions in equation 4.2:

$$\frac{N}{V} = 6\frac{f}{\mathrm{v}} \tag{4.5}$$

and

$$g^2 S(S+1) = p_{eff}^2 \tag{4.6}$$

where v is the molecular volume and p_{eff} is the effective magneton number (Ashcroft and Mermin, 1976) which can be written in terms of p_2 as:

$$p_{eff} = p_2 p^{2+} + (1-p_2)p^{3+}. \tag{4.7}$$

Here p^{2+} and p^{3+} are the effective magneton numbers of Fe^{2+} and Fe^{3+} ions respectively. Typical values are: $p^{2+} = 5.4$, $p^{3+} = 5.9$ (Ashcroft and Mermin, 1976, p658).

Finally, equation 4.2 must be divided by the density, ρ, to obtain the Curie constant for the susceptibility per unit mass. C can then be written as:

$$C = \frac{6f\mu_B^2}{3k_B\rho v}\left[p_2 p^{2+} + (1-p_2)p^{3+}\right]^2 \tag{4.8}$$

This expression is linear in f. The line in figure 4.1 is generated from equation 4.8 using the following representative values: $\rho = 3.32$ g/cm^3, v = 512Å^3, and $p_2 = 0.8$[2]. The line is a good fit to the data in the literature. The slight scatter of the data points around the line arises because of variation in the actual values of ρ, v, and p_2.

The same kinds of substitutions can be made in the expression for θ_{cw} (equation 4.3). Here the linear dependence on f enters through the fact that z = 6f. The dependence on p_2 enters through S as in equations 4.6 and 4.7 and through J which can be written as:

[2]Here, the values of ρ and v are those determined for synthetic annite and the value of p_2 an approximate mean of the samples in figure 4.1.

$$J = \left[p_2^2\left(J_{22} - J_{23} - J_{33}\right) + p_2\left(J_{23} - 2J_{33}\right) + J_{33}\right] \quad (4.9)$$

where the J_{22} is the exchange between a pair of neighbouring Fe^{2+} ions, J_{33} is the exchange between a pair of neighbouring Fe^{3+} ions,, and J_{23} is the exchange between Fe^{2+} and Fe^{3+}. With these substitutions θ_{CW} can be written as:

$$\theta_{cw} = \frac{12f}{3k_B}\left[p_2 p^{2+} + \left(1 - p_2\right)p^{3+}\right]^2\left[p_2^2\left(J_{22} - J_{23} - J_{33}\right) + p_2\left(J_{23} - 2J_{33}\right) + J_{33}\right] \quad (4.10)$$

This expression is also linear in f. No attempt has been made to compare the predicted relationship in 4.10 to the data in figure 4.2 because the values of the J_{ij} are not known.[3]

Many of the samples have also been studied at low temperatures. Of these, the more concentrated are reported to have an antiferromagnetic ordered state at liquid He temperatures. The ordering temperature (T_N) is not reported for all samples (table 4.5). The limited compositional range of the data does not allow for determination of the effect of f or the relative populations of the two valence states of Fe (figure 4.3). It should be noted, however, that several authors (Coey and Ghose,1988; Ballet, *et al.*,1982; and Beausoleil *et al.*,1983) have concluded that there is an upper limit of ~10 K on the value of T_N in biotites.

4.4.3 High Field Magnetization

High Field magnetization measurements have been reported on samples Bi-2, Bi-3, Bi-4, Bi-5, Mn-1,Gr, Th, Ch-2, Ri-1, Am, and Cl-3. Results are reported in the form of plots of magnetization (M) versus applied field strength (H). Plots have been included for fields applied parallel and perpendicular to the c^* axis. Measurements are reported for field strengths of up to 150 kG.

The plots of $M_\perp(H)$ show a fairly rapid rise at low fields (H < 50 kG) followed by a slow approach to saturation. The initial slope and high field magnetization increase with Fe concentration. For three of the most concentrated samples (Greenalite, biotite Bi-4 and Minnesotaite) an inflection point in the $M_\perp(H)$ curve is reported at very low fields (<5 kG). This inflection point is identified as either a spin-flop or a metamagnetic

[3]Also, as noted above, equation 4.3 is not neccessarily the correct form for the Curie-Weiss temperature in these samples.

transition in which the ordered magnetic structure of the materials changes from planar antiferromagnetic[4] to ferromagnetic.

The slow approach to saturation of the $M_{\perp}(H)$ curves has led the authors of these studies to speculate that strong intra-plane antiferromagnetic interactions prevent the alignment of all of the spins in the plane of the layer (see for example Beausoleil *et al.*, 1983; Ballet *et al.*, 1985).

In general, the values of $M_{//}$ are an order of magnitude smaller than the values of $M_{\perp}$ at the same value of H. The $M_{//}(H)$ curves do not exhibit the steep rise at low fields and do not approach saturation values (the curve shown for Bi-4 in Beausoleil *et al.* is linear for all $H < 150$ kG). This behaviour is interpreted as confirmation that these materials have a magnetic easy plane perpendicular to the c^* axis.

Magnetic hysteresis measurements for Minnesotaite, Greenalite and biotite have also been presented (all three are found together in figure 3 of Coey (1987)). All three samples showed a significant amount of hysteresis and the samples of Minnesotaite and Greenalite show evidence of the spin-flop transition on the initial arm of the magnetization, but not on subsequent cycling.

The hysteresis curve of Minnesotaite has been studied in more detail by Coey *et al.* (1990) who conducted neutron diffraction studies at various points on the curve. They concluded that, on the initial arm of the curve the magnetic state changes from planar antiferromagnetic to ferromagnetic. Upon cycling of the field the planar antiferromagnetic state does not reappear, but rather the ordered ferromagnetic state persists. Thus, the initial arm of the hysteresis curve is not retraced unless the temperature is raised above T_N.

4.4.4 Low Temperature MES and Neutron Diffraction

The presence of a magnetically ordered state has been verified for many samples with low temperature MES measurements. The complexity of these low temperature spectra has prevented authors from reporting fitted parameters for many of the samples. Furthermore, since none of the fits in the literature are satisfactory (in that there are large regions of systematic differences between the model and the spectra) the quoted parameters should be considered only as characteristic of the spectra themselves and not as being physically meaningful.

---

[4]Planar antiferromagnetic is defined as antiferromagnetic stacking of ferromagnetically ordered planes of spins.

However, even without completely reliable quantitative results, the qualitative features of the spectra are useful. The ferrous samples have all shown extremely broad Fe^{2+} lines with hyperfine splittings of 130 kG to 170 kG. The width of the lines indicates that all the materials have an ordered state in which there is a wide distribution of hyperfine fields implying magnetic inhomogeneity. The spectra have also shown Fe^{3+} contributions which have had hyperfine splittings much larger than the Fe^{2+} (450 - 500 kG). Only the outermost lines of these patterns are visible as small peaks at the outside of the Fe^{2+} patterns.

The ferric samples showed a broadened six line pattern with hyperfine fields of ~ 450 kG and quadrupole splittings of ~0.5mm/s. The fits to the ferric spectra were of somewhat better quality than those to the ferrous samples owing to the smaller role played by angular quantities because of the higher symmetry of the ferric ion and because the quadrupole splittings were much smaller than the hyperfine field.

A final feature of the low temperature MES results which has been common to many of the samples reported in the literature is the presence of a paramagnetic Fe^{2+} contribution to the spectra. This was usually a small effect and has not often been remarked upon. In samples where such a contribution was obvious (see for instance Townsend *et al*, 1986) it was assumed to result from a range of ordering temperatures in the sample and from the measurements being carried out at temperatures not much lower than T_N.

Coey and co-workers have performed neutron diffraction measurements on several samples including Minnesotaite, Greenalite, a concentrated ferrous biotite (Bi-4) and thuringite (Coey *et al.*, 1988). In the first two samples the results showed a (00½) reflection, which arises from an ordered state consisting of ferromagnetic planes stacked anti-ferromagnetically. However, in the biotite and thuringite this reflection was absent. The authors claim, therefore, that long range order (LRO) is not present in biotite and thuringite. The authors note that the latter two samples also have values of p_2 that are lower than in the first two samples. The absence of LRO is explained by invoking a Kosterlitz-Thouless spin vortex model (Ballet, *et al.*, 1985; Coey *et al.*, 1988). According to this model the LRO is disrupted by the presence of Fe^{3+}-Fe^{3+} antiferromagnetic pairs in the largely ferromagnetic Fe^{2+} lattice. The authors postulate that this disorder leads to a reduction of correlation length and eventually to the formation of a spin vortex state.

The existence of this vortex state is disputed by Townsend, Longworth and co-workers on the basis of in-field low temperature MES measurements. These authors have concentrated on the Fe^{3+} site, both in ferric and ferrous materials (Townsend *et al.*, 1986, 1987; Longworth *et al.*, 1987). This last work consisted of measurements on two

concentrated biotites and their oxidation products. In the ferric (fully oxidized) sample the Fe^{3+} was found to order antiferromagnetically. This is taken as proof that the Fe^{3+}-Fe^{3+} exchange is antiferromagnetic. However, the Fe^{3+} moments in the ferrous biotites were found to be aligned ferromagnetically with the in-plane magnetization. From this the authors infer that the Fe^{3+}-Fe^{3+} antiferromagnetic exchange is not strong enough to overcome the predominant Fe^{2+}-Fe^{3+} exchange, which is ferromagnetic. This discounts the possibility of a spin vortex state since the vortex state proposed by Ballet & Coey has as its central postulate strong antiferromagnetic coupling of Fe^{3+} pairs which disrupt the long range ferromagnetic order of the layer.

4.5 Summary

There is general agreement in the literature that the empirical qualities of these minerals are determined much more strongly by the overall concentration of Fe and the relative abundances of Fe^{2+} and Fe^{3+} than by other structural properties. It is also well established that an ordered magnetic state exists at low temperatures for samples which are concentrated in Fe.

There is, however, disagreement over the nature of the ordered magnetic state. The ordering produces a zero (or very small) net magnetization which excludes bulk ferromagnetic ordering. In samples with relatively high T_N and high ferrous content, the state has been established as an antiferromagnetic stacking of ferromagnetic planes. In samples with lower relative ferrous populations the state does not appear to exhibit LRO. This has led Ballet *et al.*, (1985) to postulate a spin-glass or vortex ordered state. Townsend *et al.* (1985, 1986, 1987) have rejected this claim, invoking more conventional models which include the effects of structural disorder.

Table 4.1 Concentrated ferrous samples. The samples are characterized by the proportion (f) of octahedral sites occupied by Fe and the proportion (p_2) of Fe ions in the divalent state. f has been determined by wet chemical analysis or X-ray fluorescence analysis. All Fe has been assumed to be in octahedral coordination.

Sample	Name	Structure	f	P_2	Study
Mg-Chamosite	Ch-1	2:1:1	0.34[d] 0.17	0.96[a]	Townsend *et al*, 1986
Minnesotaite	Mn	2:1	0.75	0.92[b]	Ballet *et al*, 1985
Biotite	Bi-3	2:1	0.47	0.92[a]	Beausoleil *et al.*, 1983
Ripidolite	Ri-1	2:1:1	0.36[e]	0.92[b]	Ballet *et al.*, 1985
Biotite(1)	Bi-10	2:1	0.4	0.92[a]	Longworth *et al.*, 1987
Chamosite	Ch-2	1:1	0.46	0.86[a]	Ballet *et al.*, 1985
Glauconite	Gl-1	2:1 dioct	0.42	0.87[a]	Ballet & Coey, 1982
Biotite B-4	Bi-4	2:1	0.8	0.87[a]	Beausoleil *et al.*, 1983
Biotite (2)	Bi-12	2:1	0.6	0.86[a]	Longworth *et al.*, 1987
Greenalite	Gr	1:1	0.87	0.83[a]	Coey *et al.*, 1982
Biotite B-7	Bi-7	2:1	0.55	0.8[a]	Beausoleil *et al.*, 1983
Biotite B-9	Bi-9	2:1	0.42	0.8[a]	Beausoleil *et al.*, 1983
Biotite B-8	Bi-8	2:1	0.62	0.78[c]	Beausoleil *et al.*, 1983
Thuringite	Th	2:1:1	0.61[e]	0.75[b]	Ballet *et al.*, 1985
Berthierine	Be	1:1	0.49	0.74[a]	Coey *et al.*, 1982
Ferro-Brucite	FB	0:1	1	0.7[c]	Ballet *et al.*, 1985
Oxy-Biotite	Bi-11	2:1	0.4	0.61[a]	Longworth *et al.*, 1987

a. Determined by MES.

b. Method of determination unknown.

c. Assumed value from wet chemical analysis.

d. Samples with 2:1:1 structure for which [Fe] concentrations are given for both 2:1 layer (top number) and Hydroxide layer (bottom number).

e. Samples with 2:1:1 structure for which only overall [Fe] concentrations are provided.

Table 4.2 Concentrated ferric samples. The samples are characterized by the proportion (f) of octahedral sites occupied by Fe and the proportion (p_2) of Fe ions in the divalent state. f has been determined by wet chemical analysis or X-ray fluorescence analysis. All Fe has been assumed to be in octahedral coordination.

Sample	Name	Structure	f	P_2	Study
Oxy-Mg-	Ch-2	2:1:1	0.34[c]	0.2[a]	
Chamosite			0.17[c]		Townsend *et al.*, 1986
Glauconite	Gl-2	2:1 dioct	1[b]	0.04[a]	Townsend *et al.*, 1987
Nontronite	No-1	2:1	1[b]	0[a]	Townsend *et al.*, 1987
Oxy-Biotite(2)	Bi-13	2:1	0.6	0[a]	Longworth *et al.*, 1987
Nontronite	No-2	2:1 dioct	0.57	0[a]	Ballet & Coey, 1982

a. Determined by MES.

b. Method of determination unknown.

c. Samples with 2:1:1 structure for which [Fe] concentrations are given for both 2:1 layer (top number) and Hydroxide layer (bottom number).

Table 4.3 Dilute samples. The samples are characterized by the proportion (f) of octahedral sites occupied by Fe and the proportion (p_2) of Fe ions in the divalent state. f has been determined by wet chemical analysis or X-ray fluorescence analysis. All Fe has been assumed to be in octahedral coordination.

Sample	Name	Structure	f	P_2	Study
Mn-Mg-Chamosite	Ch-4	2:1:1	0.26[c]	0.93[a]	Townsend *et al.*, 1986
			0.24[c]		
Oxy-Mn-Mg-	Ch-5	2:1:1	0.26[c]	0.4[a]	
Chamosite			0.24		Townsend *et al.*, 1986
Biotite LEP	Bi-1	2:1	0.25	0.84b	Beausoleil *et al.*, 1983
Biotite B-6	Bi-6	2:1	0.24	0.59b	Beausoleil *et al.*, 1983
Biotite B-5	Bi-5	2:1	0.18	0.79[a]	Beausoleil *et al.*, 1983
Biotite B-2	Bi-2	2:1	0.12	0.66[a]	Beausoleil *et al.*, 1983
Vermiculite 2	Ve-2	2:1	0.12	0[a]	Ballet & Coey, 1982
Clinochlore	Cl-1	2:1	0.11[c]	1[d]	Townsend *et al.*, 1986
			0.03[c]		
Oxy-Clinochlore	Cl-2	2:1:1	0.11[c]	0.23[d]	Townsend *et al.*, 1986
			0.03		
Vermiculite 1	Ve-1	2:1	0.1	0.57[a]	Ballet & Coey, 1982
Clinochlore	Cl-3	2:1:1	0.1	0.77b	Ballet *et al.*, 1985
Montmorillonite	Mo	2:1	0.07	0.1[a]	Ballet & Coey, 1982
Muscovite	Mu	2:1 dioct	0.07	1[a]	Ballet & Coey, 1982
Amesite	Am	2:1:1	0.01	0.67[a]	Ballet *et al.*, 1985

a. Determined by MES.

b. Method of determination unknown.

c. Samples with 2:1:1 structure for which [Fe] concentrations are given for both 2:1 layer (top number) and Hydroxide layer (bottom number).

Table 4.4 Reported room temperature MES parameters. Because various methods were used to fit the spectra the values for some samples represent the weighted average of more than one pattern required to obtain a fit.

Sample	Species	n[a]	δ[b] (mm/s)	Δ[b] (mm/s)	Γ_{min}[c] (mm/s)	Γ_{max}[d] (mm/s)
Bi-10	Fe^{2+}	2	1.03	2.36	0.32	0.32
	Fe^{3+}	1	0.31	0.80	0.64	
Bi-12	Fe^{2+}	2	1.12	2.40	0.22	0.34
	Fe^{3+}	2	0.41	0.91	0.72	1.16
Bi-11	Fe^{2+}	2	1.14	2.29	0.32	0.50
	Fe^{3+}	2	0.31	0.66	0.28	0.30
Bi-13	Fe^{3+}	2	0.38	1.35	*	*
Gr	Fe^{2+}	1	1.16	2.75	0.34	
	Fe^{3+}	1	0.39	0.73	0.48	
Be	Fe^{2+}	1	1.13	2.57	0.40	
	Fe^{3+}	1	0.38	0.78	0.60	
Th	Fe^{2+}	1	1.13	2.62	0.36	
	Fe^{3+}	1	0.36	0.74	0.68	
Ch-2	Fe^{2+}	1	1.15	2.62	0.38	
	Fe^{3+}	1	0.45	0.76	0.60	
Ri-1	Fe^{2+}	1	1.13	2.26	0.32	
	Fe^{3+}	1	0.45	0.71	0.55	
Cl-3	Fe^{2+}	1	1.13	2.61	0.36	
	Fe^{3+}	1	0.40	0.61	0.48	
Am	Fe^{2+}	1	1.12	2.60	0.36	
	Fe^{3+}	1	0.32	0.49	0.48	
Mn	Fe^{2+}	1	1.15	2.75	0.36	
	Fe^{3+}	1	0.26	0.40	0.37	
Gl-1	Fe^{2+}	1	1.45	2.27	0.36	

a. Number of patterns used in fit.
b. Average of pattern parameters weighted by spectral areas.
c. Minimum "linewidth" obtained in fit. This is assumed to mean the FWHM, although it is not explicitly defined.
d. Maximum "linewidth" obtained in fit. Where this parameter is not reported a single linewidth (equal to Γ_{min}) was used in the fit.
* Value not reported.

Table 4.5 Magnetic parameters calculated for various samples.

Sample	f [a]	p_2 [b]	T_N [c]	$C_\perp$ [e]	$C_{//}$ [f]	θ_p [d]	$\theta_\perp$ [e]	$\theta_{//}$ [f]
Bi-4	0.8	0.87	7.2	19.2	16.8	-	44	-4
Bi-12	0.6	0.86	*	*	*	-	43	*
Mn	0.75	0.92	28	-	-	38	-	-
Bi-8	0.62	0.78	5	13.2	11.8	-	35	0.5
Bi-3	0.47	0.92	3	10.5	9.9	-	30	-10
Bi-7	0.55	0.80	*	13.0	11.3	-	29	-6
Bi-9	0.42	0.80	*	10.4	8.5	-	24	9
Gr	0.87	0.83	17	-	-	24	-	-
Bi-6	0.24	0.59	*	5.35	4.74	-	22	-10
Be	0.49	0.74	9	-	-	22	-	-
Bi-10	0.40	0.92	7	*	*	-	19	*
Ve-1	0.10	0.57	*	2.6	2.2	-	-2	-4
Bi-13	0.60	0.00	*	-	-	5	-	-
Mu	0.07	1.00	*	*	*	-	-21	*
Ve-2	0.12	0.00	*	2.7	2.7	-	-4	*

[a] Proportion of Octahedral sites occupied by Fe ions.

[b] Ratio of Fe^{2+} to total Fe as estimated by a variety of methods including MES.

[c] Reported value of critical temperature.

[d] Value of θ_{cw} reported for random powder samples. No values of C are reported for powder samples.

[e] Value of C and θ_{cw} determined from measurements on oriented samples with field applied perpendicular to the c^* axis.

[f] Value of C and θ_{cw} determined from measurements on crystalline samples with field applied parallel to the c^* axis.

* Value not reported.

- N/A.

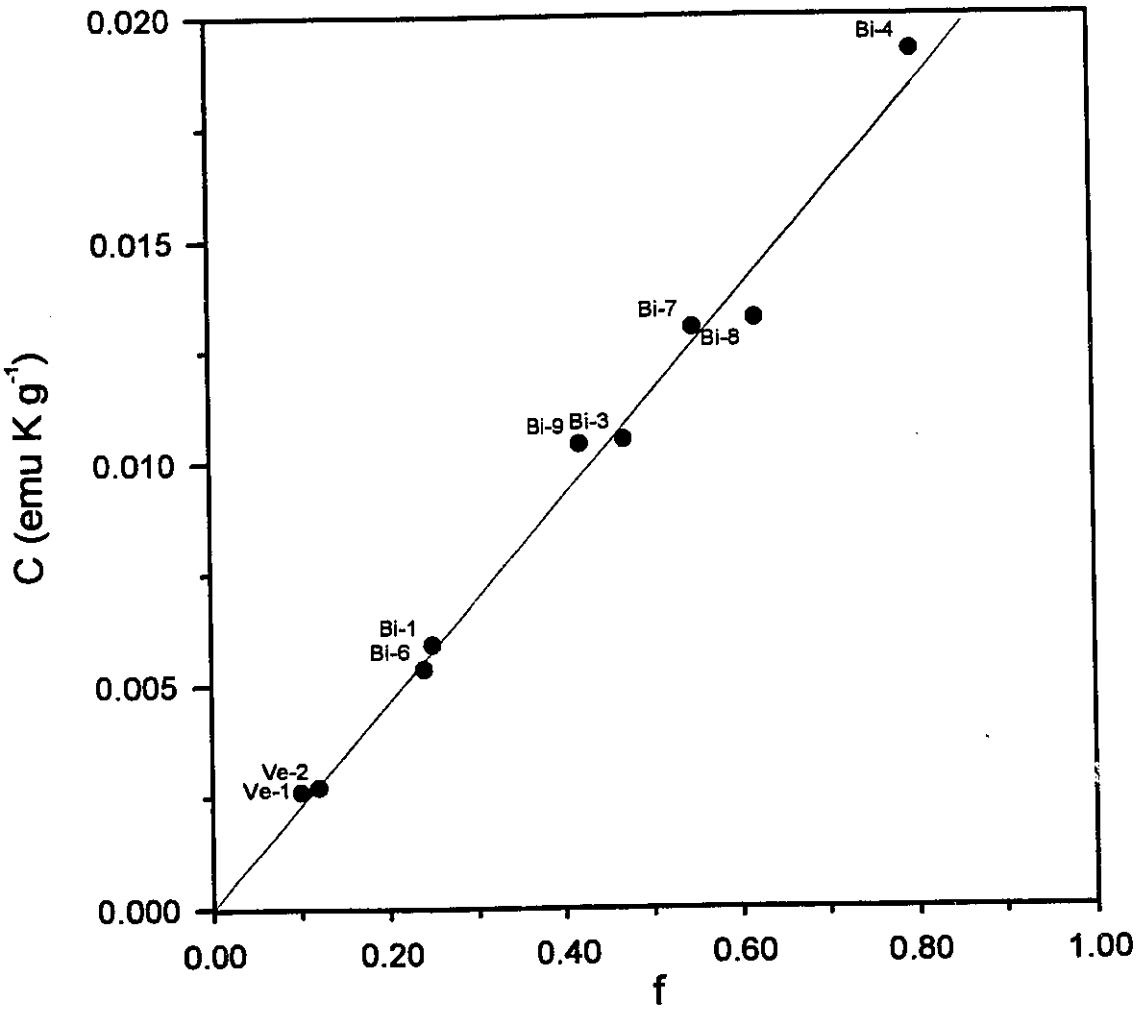

Figure 4.1 *Curie constants (C) reported in the literature for layer silicate samples as a function of the fraction (f) of octahedral sites occupied by Fe. The points are labeled with the sample names as listed in tables 4.1, 4.2, and 4.3. The solid line is the theoretical prediction based on equation 4.8 (see text for details).*

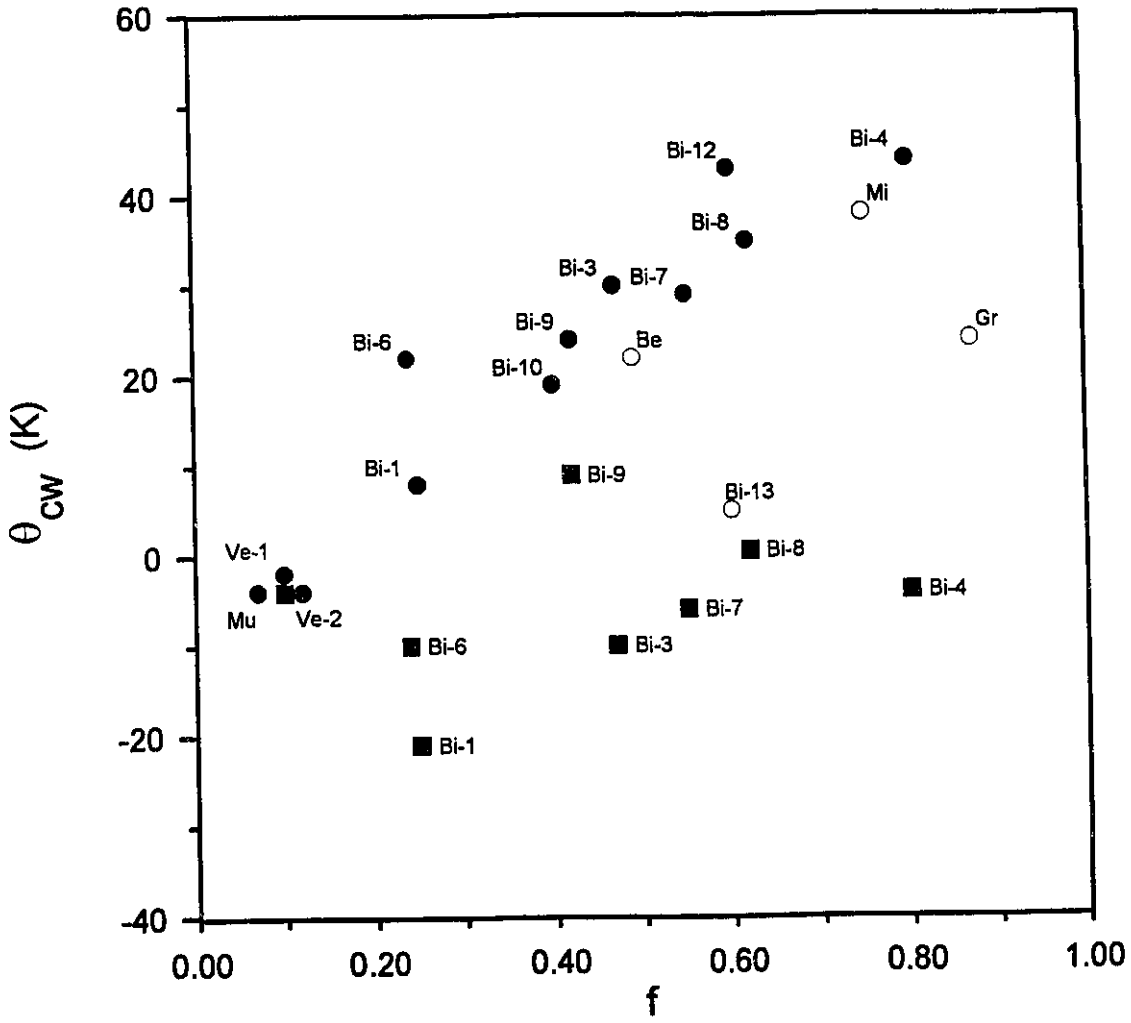

***Figure 4.2** Curie-Weiss temperatures (θ_{CW}) reported in the literature for layer silicate samples as a function of the fraction (f) of octahedral sites occupied by Fe. The points are labeled with the sample names as listed in tables 4.1, 4.2, and 4.3. Measurements were reported for both random powder (O) and oriented samples. For oriented samples values of θ_{CW} were obtained for fields applied along the crystalline c^* axis (■) and in the ab plane (●).*

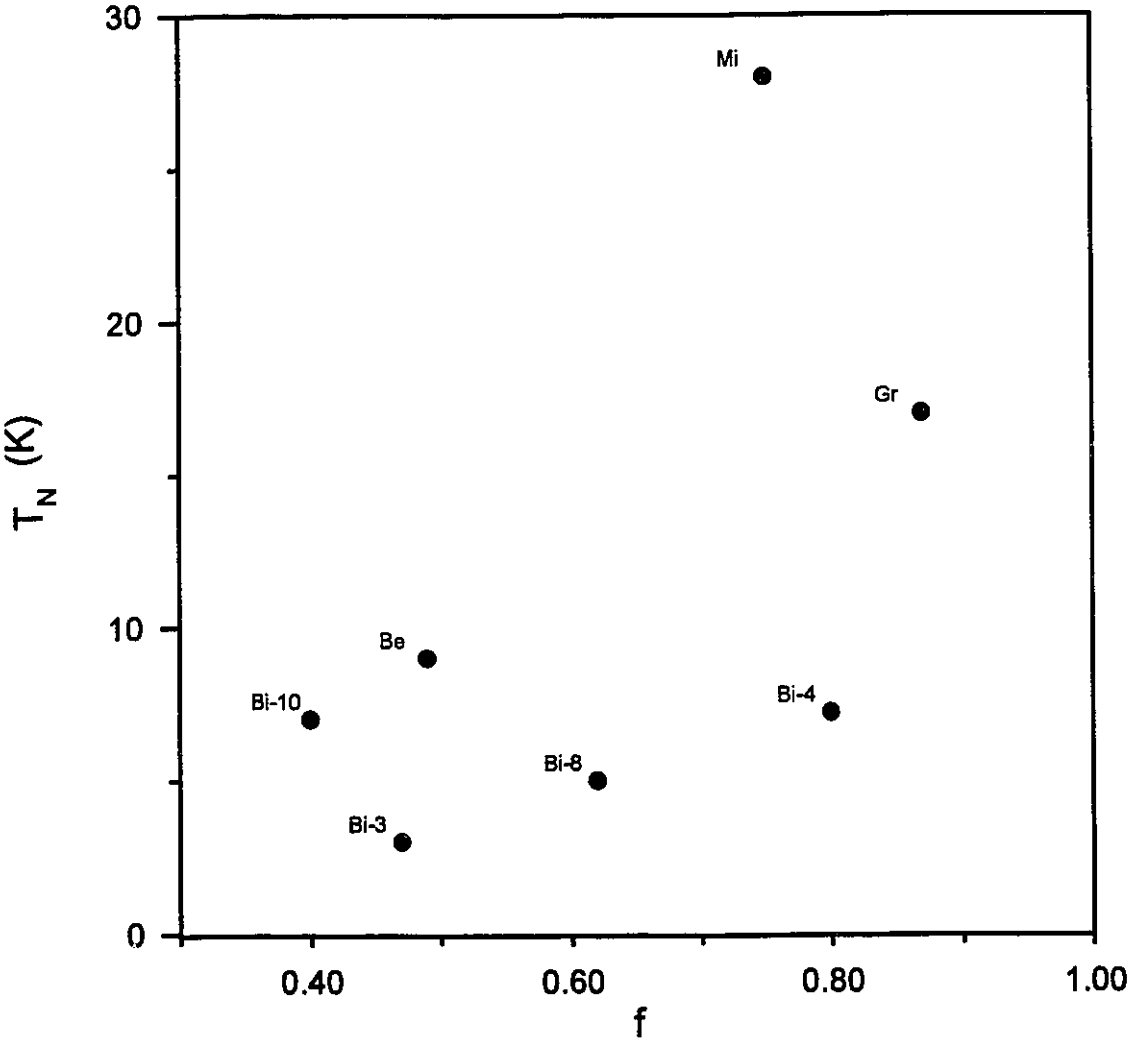

Figure 4.3 *Critical temperatures (T_N)reported in the literature for layer silicate samples as a function of the fraction (f) of octahedral sites occupied by Fe. The points are labeled with the sample names as listed in tables 4.1, 4.2, and 4.3.*

Chapter 5

Magnetization of Annite: Methods, Results and Discussion

5.1 Methods

Low field magnetization measurements were conducted using a magnetometer described by G. Lamarche (1989). From these measurements low field susceptibilities, χ, were determined as:

$$\chi = M/H \tag{5.1}$$

where M is the induced magnetization and H is the applied field.

High temperature measurements (i.e. $T > T_N$) were conducted on 5 mg of synthetic annite powder and on a 3 mg square flake of natural annite. Low temperature measurements were conducted on these two samples and on a 1 mg sliver of natural annite with a length to width ratio of 5:1. For these measurements the natural samples were oriented with the c^* axis perpendicular to the applied field. Additional measurements with H applied parallel to the c^* axis were conducted on a small (< 1mg) flake of natural annite. A three step procedure was used in the low temperature tests. First, the sample was quenched to 4.2K in near-zero (earth's) field (hereafter referred to as zero-field quench, ZFQ); then, with a small field applied, the sample was warmed to a temperature above T_N (field warming, FW). Finally, the sample was cooled in the same field to 4.2K once again (field cooling, FC). The temperature ranges and applied field strengths used in these measurements are shown in table 5.1.

High field magnetization measurements were conducted on a SQUID magnetometer at Centre de Recherche Paul Pascal. A single square flake (5mg) of the natural sample was used. Measurements to determine the saturation value of M(H) were conducted at 4.2 K with fields up to 60 kG applied perpendicular to the c^* axis. As well,

a hysteresis curve at 4.2 K was obtained from 60 kG to -60 kG, with particular attention paid to the region between 5 kG and -5 kG.

5.2 Results and Discussion

5.2.1 Low Field Susceptibility - Paramagnetic Region

Plots of the high temperature inverse susceptibility as a function of temperature are shown in figures 5.1 and 5.2. The straight lines in the figure represent linear regressions to data above T_N. The temperature ranges of the data used in the regressions and the results of the regressions are found in table 5.2. Using a Curie-Weiss law as discussed in chapter 4, the Curie constant and Curie-Weiss temperature can be derived from these relationships. The Curie constants and Curie-Weiss temperatures calculated from the regressions are reported in table 5.2.

As noted in chapter 4, the inverse susceptibility of random powders of materials with a large magnetic anisotropy should not necessarily follow the standard Curie-Weiss law. Nonetheless, the $\chi(T)$ curve for the synthetic sample is approximately linear in the temperature region $75K < T < 150K$ (see figure 5.2). This region has been fitted to a straight line to obtain the parameters shown in table 5.2. In interpreting these parameters it must be remembered that, while C is properly represented by equation 4.2 for a random powder, equation 4.3 is not the correct physical expression for θ_{cw} in this sample. Nonetheless, θ_{cw} serves as an empirical characterization of the high temperature susceptibility of the synthetic annite sample.

The validity of the regression is confirmed by comparisons of the Curie-Weiss temperatures with results from the literature (figure 5.3). The annite data are consistent with the linear trends discussed in chapter 4. As well, the regression can be tested by considering the value of the effective magneton number, p_{eff}, which is derived from the value of C (see equation 4.8). The values of p_{eff} can be compared to the expected values based on the composition of the samples. In both cases the values of p_{eff} are slightly less than the calculated values.

5.2.2 Low Field Susceptibility - Low Temperatures

Figure 5.4 shows the $\chi_p(T)$ curve for the synthetic sample whilst figures 5.5 and 5.6 show the $\chi_\perp(T)$ curves for the two different geometries of the natural sample. The FW and FC arms are shown separately in each figure.

The T_N for each sample can be deduced from the point of inflection of the FC $\chi(T)$ curves (table 5.4). The value of T_N for the natural sample is independent of sample shape. In figure 5.7 these values are compared to the values in the literature by plotting T_N versus f. The value of T_N for the two samples of annite is significantly higher than any yet reported. These values are also significantly higher than the 10 K upper limit for T_N of biotites proposed by Coey and Ghose (1988) and Ballet *et al.* (1985).

Ballet *et al.* (1985) found a correlation between the value of T_N and the probability (p_{33}) of finding nn Fe^{3+}-Fe^{3+} pairs in the octahedral sheets. According to these authors there is a further correlation between p_{33} and the type of magnetic ordered state with higher p_{33} ratios associated with the random ferromagnetic ordered state and lower values associated with the planar antiferromagnetic state (see chapter 4). The data from annite do not support the findings Ballet *et al.* (1985) (see table 5.4). The value of p_{33} for natural annite is five times the value for Minnesotaite yet the value of T_N is more than double and the magnetic state is planar antiferromagnetic.

Below T_N, the three $\chi(T)$ curves (figures 5.4 to 5.6) are similar. They are characterized by a soft cusp in the FW curve with significant hysteresis between the FC and FW arms at temperatures below the cusp. However, the details of the curves differ significantly, even between the flake and sliver of the natural annite. Such shape dependent behaviour has not been previously reported for layer silicates.

Shape dependence of the susceptibility implies that the configuration of the ordered magnetic state is determined by relatively long-range interactions. Such behaviour is typical of materials consisting of exchange-wise isolated layers of ferromagnetically coupled magnetic ions (Rancourt *et al.*,1990). Rancourt *et al.* reported on the role of long range dipole-dipole (d-d) forces in the magnetic ordering of layer silicates and layered graphite intercalation compounds (GIC's). They confirmed that, in materials consisting of exchange-isolated layers, the presence of 3D magnetic order is the result of dipole-dipole coupling between layers. The dipole-dipole forces, which are normally considered to be negligible in comparison to the short range exchange interactions, become important in layered materials when there are significant intra-layer ferromagnetic correlations.

This leads to a certain dichotomy in the magnetic properties of such materials. The onset of magnetic ordering is related to the growth of intra-layer correlations determined by short-range exchange interactions and is independent of the macroscopic properties of the sample. The critical temperature is thus determined by the microscopic composition of the layers and is an intrinsic property of a given material. In contrast, the 3D magnetic configuration obtained below T_N is determined by long-range dipole-dipole forces between layers. The effect of these forces is dependent on the macroscopic properties of

the sample. Since the magnetic susceptibility is determined by this magnetic configuration it is shape-dependent. For these reasons both geometries of the natural sample have the same critical temperature but different $\chi_{\perp}(T)$ curves.

The strong magnetic anisotropy in layer silicates is confirmed by comparing the $\chi_{//}(T)$ curve shown in figure 5.8 to the $\chi_{\perp}(T)$ curves in figures 5.5 and 5.6. The values of $\chi_{//}$ are ~20 times smaller than the values of $\chi_{\perp}$ at the same temperatures, indicating that the c^* is a hard magnetic direction.

5.2.3 High Field Magnetization

High field SQUID measurements were conducted on the natural sample to determine the M(H) hysteresis curve in the plane of the layer (figure 5.9). The initial arm of the M(H) curve is relatively flat up to H = 0.5 kG. This is followed by a rapid rise which is suggestive of a spin-flop transition. This feature has been reported in other samples (see for instance Ballet *et al.*, 1985). At H = 2.0 kG the M(H) curve begins a slow approach to saturation. When the applied field is cycled between 60 kG and -60 kG the magnetization traces a hysteresis loop but does not retrace the initial curve unless the sample is heated above T_N. This pattern bears strong resemblance to the behaviour of a sample of Minnesotaite under similar conditions (Ballet *et al.*, 1985).

As postulated by Ballet *et al.* (1985) and Coey (1987) the magnetization curve can be understood in terms of the following phenomenological model. The ZFQ sample consists of layers which order ferromagnetically with moments in the plane of the layer. The layers are, in turn, stacked antiferromagnetically. This antiferromagnetic stacking of ferromagnetic layers has been confirmed in the synthetic sample by neutron diffraction measurements (Rancourt *et al.*, unpublished).

Below the spin flop field (H_{sf}) the bulk magnetization is small and virtually independent of the applied field. This implies that the dominant magnetic structure is antiferromagnetic and that it is not significantly disturbed by the applied field.

Far above H_{sf}, M is large and approaches saturation. This implies that the magnetic structure has changed to a bulk ferromagnetic state. Therefore, in the spin-flop region a transition takes place in which the ferromagnetic planes within domains rotate to lie parallel to each other and to the applied field. When the applied field is reduced and then reversed the original domain structure is not re-established because there is no mechanism for nucleating the domains (Coey *et al.*, 1990).

It must be noted that the magnitude of H_{sf} is largely dependent on the strength of the dipole-dipole forces between layers within a given domain. As noted in the low-field SQUID measurements, these forces are strongly dependent on sample shape. Thus, it is not correct to assume that the value of H_{sf} is intrinsic to a particular structure or material.

The slow approach to saturation in layer silicates has been previously remarked upon (Beausoleil *et al.*, 1983; Ballet and Coey, 1982; Coey and Ghose, 1988). The difficulty in achieving saturation is probably caused by the presence of Fe^{3+} in the octahedral sheets. The antiferromagnetic exchange between Fe^{3+}-Fe^{3+} pairs acts against the ferromagnetic ordering. The energy of the exchange bonds is much larger than the energy of the d-d forces which force the planes to align antiferromagnetically. Thus, it requires much higher field strengths to overcome these forces than to cause the spin flop, and the approach to saturation is slow.

Various attempts have been made to determine the field required for saturation and the moment per ion at saturation. The difficulty in determining these quantities can be demonstrated by plotting M versus H^{-1} (figure 5.10). Extrapolation to infinite field is ambiguous and thus it is not possible to determine the saturation magnetization. The value of H required for saturation cannot be determined from this figure but it is much greater than the 60 kG applied in these tests.

5.5 Summary and Conclusions

The results presented in this chapter confirm that the bulk magnetic properties of annite are similar to those reported for other layer silicates. In particular, the bulk magnetic ordered state is anti-ferromagnetic. Low-field susceptibility measurements confirmed that there is strong magneto-crystalline anisotropy which confines the spins in the plane of the layers. In addition, the large positive value of θ_{cw} measured in the plane of the layer indicates that the intra-plane interactions are predominantly ferromagnetic in nature. The nature of the inter-plane interactions is more difficult to determine because these interactions are probably the result of dipole-dipole interactions between groups of spins. The long range nature of these forces introduces shape-dependence in measurements of quantities related to the strength of the inter-layer forces. Thus, quantities such as H_{sf} are not intrinsic to annite, but are sample shape dependent.

The high field hysteresis curve is interpreted in terms of a zero-field antiferromagnetic stacking of ferromagnetic planes that is stabilized by inter-plane d-d forces. This interpretation agrees with the findings of Ballet *et al.* (1985) for samples

Minnesotaite and Greenalite. However, the results for annite do not support the contention that the appearance of the planar antiferromagnetic state is strongly dependent on the relative proportion of nn of Fe^{3+}-Fe^{3+} pairs in the octahedral sheet. Rather, the results for the annite samples indicate that T_N is most strongly dependent on the concentration of Fe in the octahedral sheet. In addition, the T_N for both annite samples is found to be significantly higher than the accepted biotite T_N upper limit of 10K.

Table 5.1 Experimental parameters used in low field susceptibility measurements. For the high temperature tests the sample was quenched to T_{min} in zero field and then field warmed (with $H = H_a$) to T_{max}. For the low temperature tests the sample was quenched to T_{min} in zero field, field warmed to T_{max}, and then field cooled to T_{min}.

Sample	Test	T_{min} (K)	T_{max} (K)	H_a (Gauss)
Synthetic	High Temp	56	200	62.0
Natural Flake	High Temp	4.2	164	9.0
Synthetic	Low Temp	4.2	70	12.3
Natural Flake	Low Temp	4.2	58	5.0
Natural Sliver	Low Temp	4.2	61	5.0
Natural small Flake	Low Temp	4.2	63	18.0

Table 5.2 Parameters derived from low-field susceptibility measurements. Values of the Curie constant (C) and Curie-Weiss temperature (θ_{cw}) for two samples of annite. For the natural samples the magnetic field was applied perpendicular to the c^* axis.

Sample	f[a]	p_2[b]	T_{min}[c] (K)	T_{max}[c] (K)	m[d]	b[e]	C (emu K g^{-1})	θ_{cw} (K)
Synthetic	0.96	0.89	75	150	47.3	-2793	.021±.002	59.0±0.5
Natural	0.84	0.83	55	164	53.6	-3265	.019±.001	60.9±0.5

[a] Proportion of octahedral sites containing Fe.

[b] Ratio of Fe^{2+} to total Fe

[c] Temperature limits used in computing linear regression to $\chi^{-1}(T)$ curve.

[d] Slope of linear regression to $\chi^{-1}(T)$ curve in (g emu^{-1} K^{-1}).

[e] Intercept of linear regression to $\chi^{-1}(T)$ curve in (g emu^{-1}).

Table 5.3 Measured and calculated values of the effective magneton number for two samples of annite. Here p_{eff} is the value of the effective magneton number calculated from the Curie constants. p_{calc} is the magneton number which results from applying equation 4.7 with p^{2+}=5.40 and p^{3+}=5.90 (See Ashcroft and Mermin, 1976).

Sample	Z[a]	p_{eff}	p_2[b]	p_3[c]	p_{calc}
Synthetic	6.00	5.35±0.05	0.89	0.11	5.46
Natural	5.46	5.40±0.05	0.83	0.17	5.49

[a] Number of Fe ions per unit cell.

[b] Ratio of Fe^{2+} to total Fe.

[c] Ratio of Fe^{3+} to total Fe.

Table 5.4 Critical temperatures of ferrous layer silicates. After the suggestion of Ballet *et al.* (1985) the critical temperature T_N is compared to the relative probability of the occurrence of nn Fe^{3+}-Fe^{3+} pairs (p_{33}) for six samples from the literature and for two samples of annite. For the literature samples the type of magnetic ordering (as reported by Ballet *et al.* 1985) is also reported. The samples from the literature are identified by the code used in chapter 4 (see table 4.1 for more details).

Sample	T_N	f	p_3	p_{33}[a]	Magnetic Order[b]
FB	34	1	0	0	af
Gr	24	0.87	0.12	0.032	af
Ch-2	12	0.5	0.12	0.011	
Mn-1	19	0.75	0.08	0.011	af
Bi-4	7	0.87*	0.13	0.039	rf
Th	5	0.61	0.25	0.079	rf
Synthetic	58	0.96	0.07	0.014	af
Natural	45	0.84	0.17	0.061	af

[a] p_{33} is calculated according to the method of Ballet *et al.* (1985) as $p_{33} = \frac{1}{12}(6fp_3)^2$.

[b] **af** indicates a planar antiferromagnet, **rf** indicates a random antiferromagnet as determined by Ballet *et al.* (1985).

* In the original study in which this sample is reported (Ballet and Coey, 1982) this sample has f=0.8. In table 3 of Ballet *et al.* (1985) the value of Z is reported as 5.3 which corresponds to f = 0.87. Use of f = 0.8 for this sample yields p_{33} = 0.324.

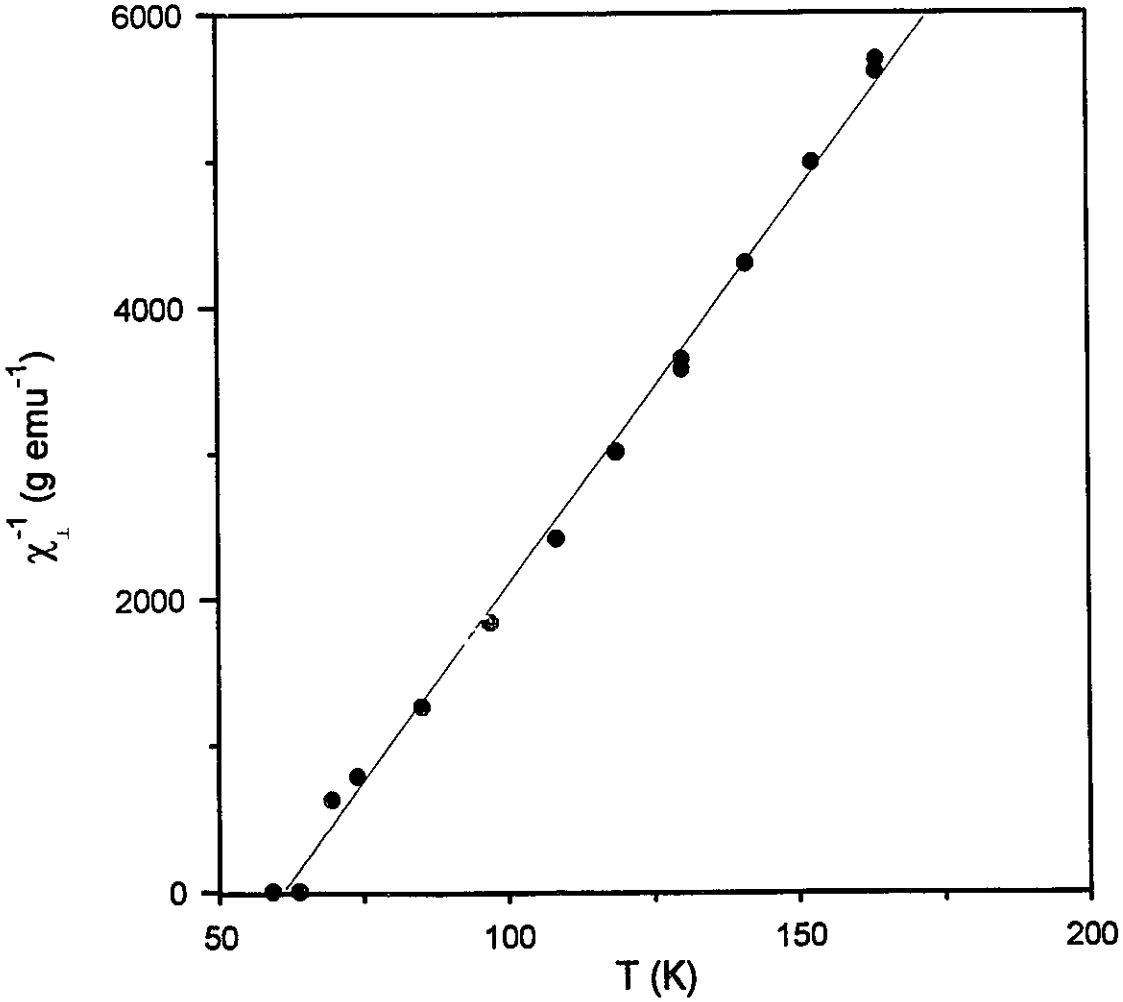

Figure 5.1 *Inverse susceptibility of the natural sample as a function of temperature. The line is a linear regression which is used to derive the Curie-Weiss parameters reported in table 5.2.*

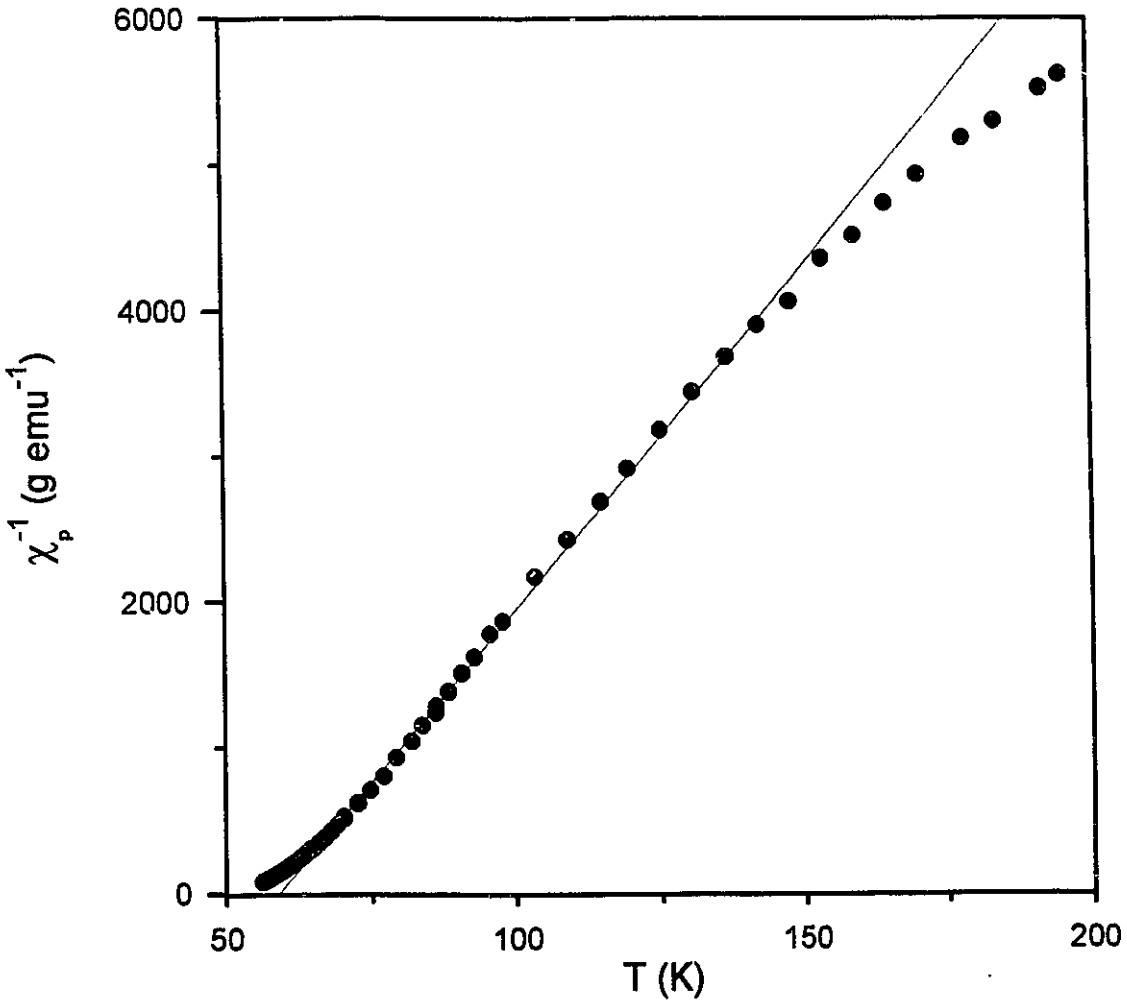

Figure 5.2 *Inverse susceptibility of the synthetic sample of annite as a function of temperature. The line is a linear regression to the region between 75K and 150K which is used to derive the Curie-Weiss parameters reported in table 5.2.*

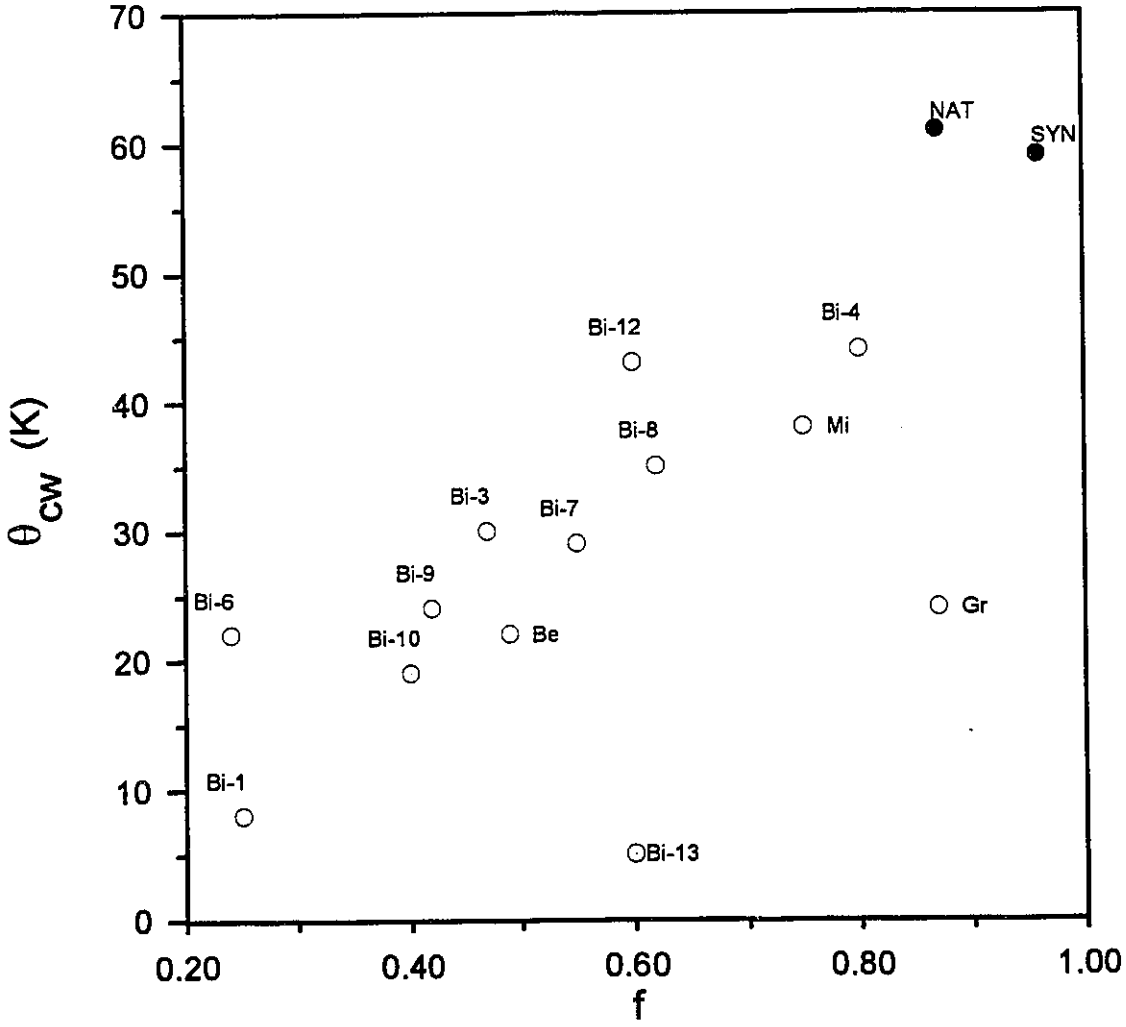

Figure 5.3 *Curie-Weiss Temperature (θ_{CW}) as a function of proportion (f) of Fe in the octahedral layer in two samples of annite (●) and for samples in the literature (O). The codes for the literature samples are identical to those in chapter 4, NAT labels the point for the natural annite and SYN labels the point for the synthetic annite.*

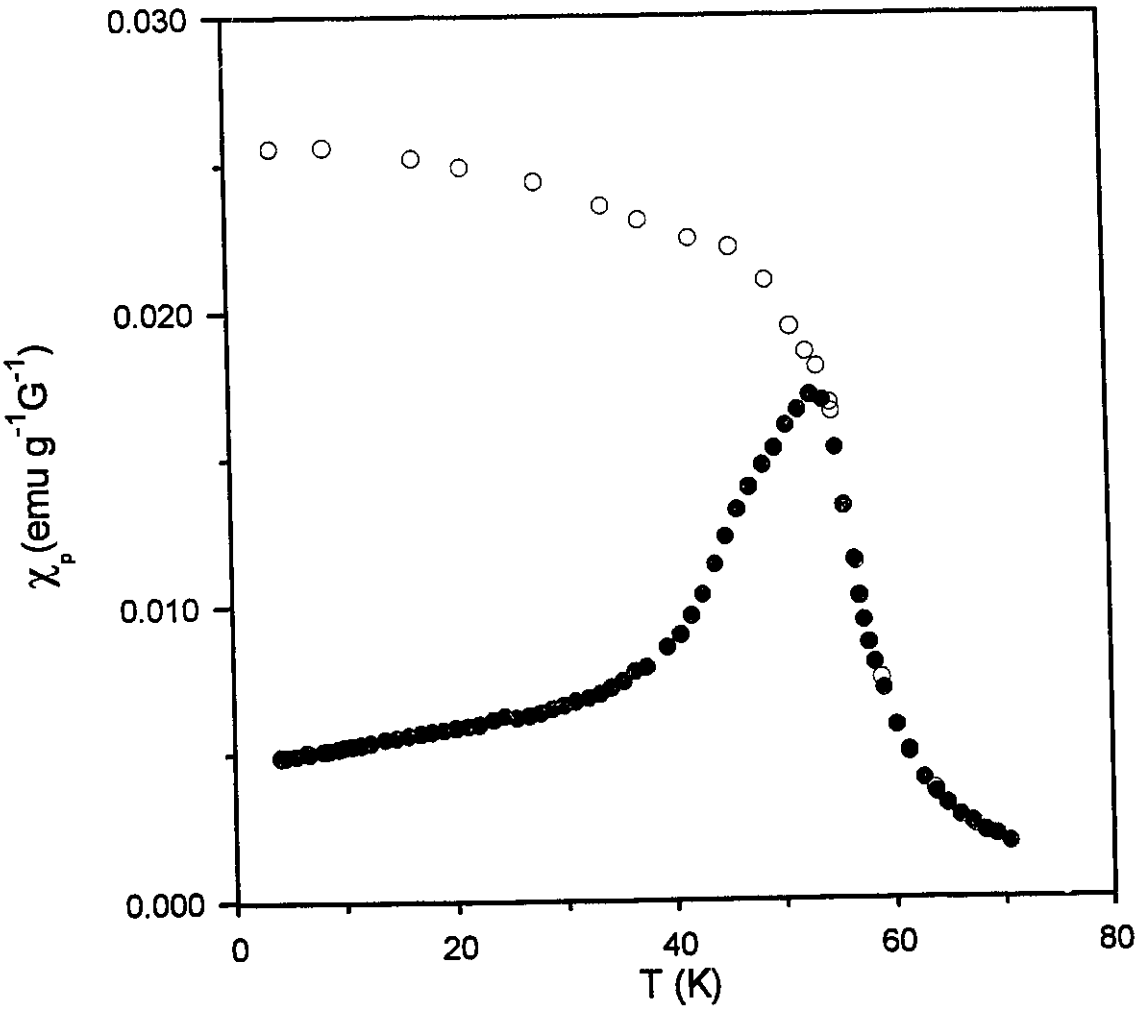

Figure 5.4 *Magnetic susceptibility of synthetic annite as a function of temperature. Results are shown for the field warming (●) and field cooling (O) measurements.*

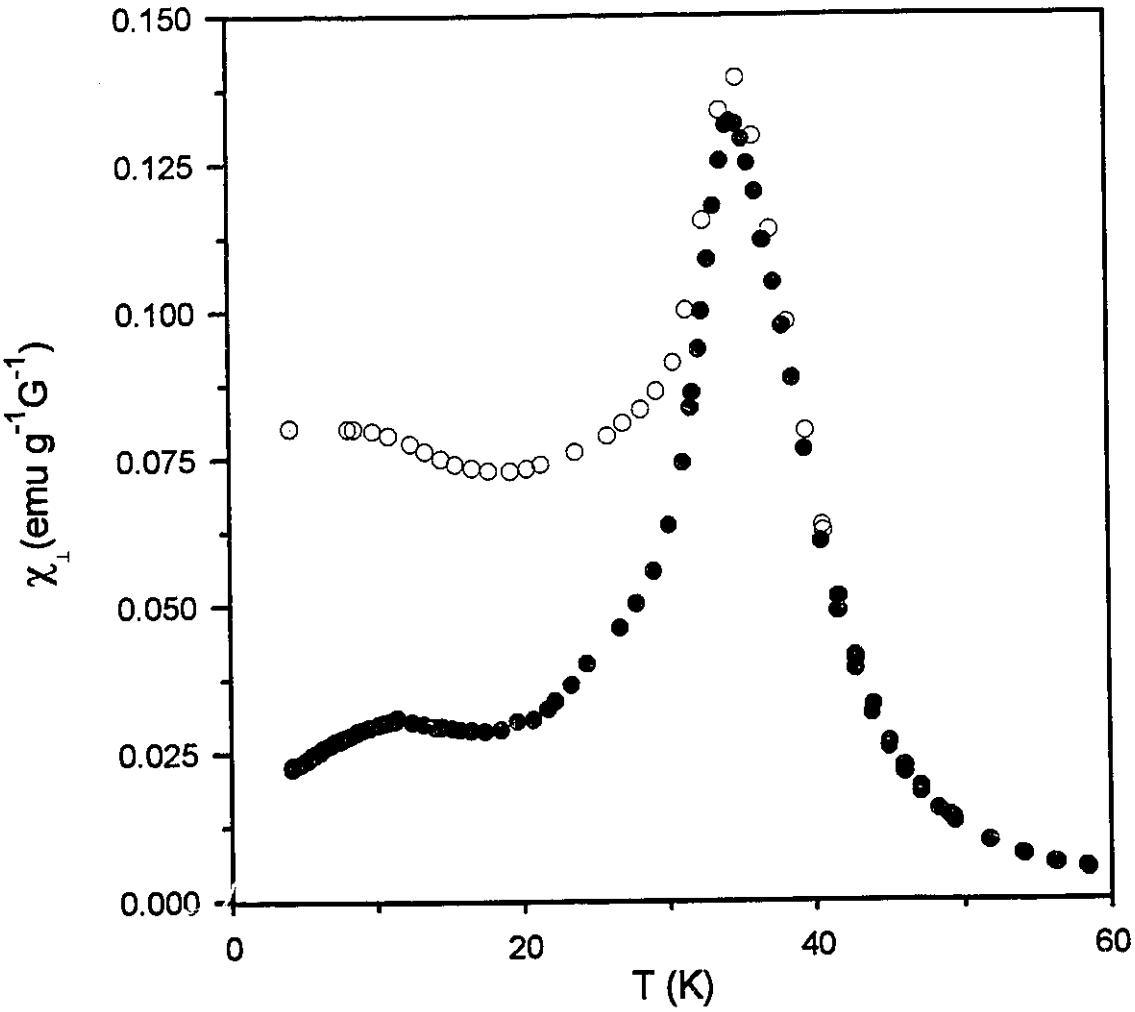

***Figure 5.5** In-plane magnetic susceptibility of a square flake of the natural annite as a function of temperature. Results are shown for the field warming (●) and field cooling (O) measurements.*

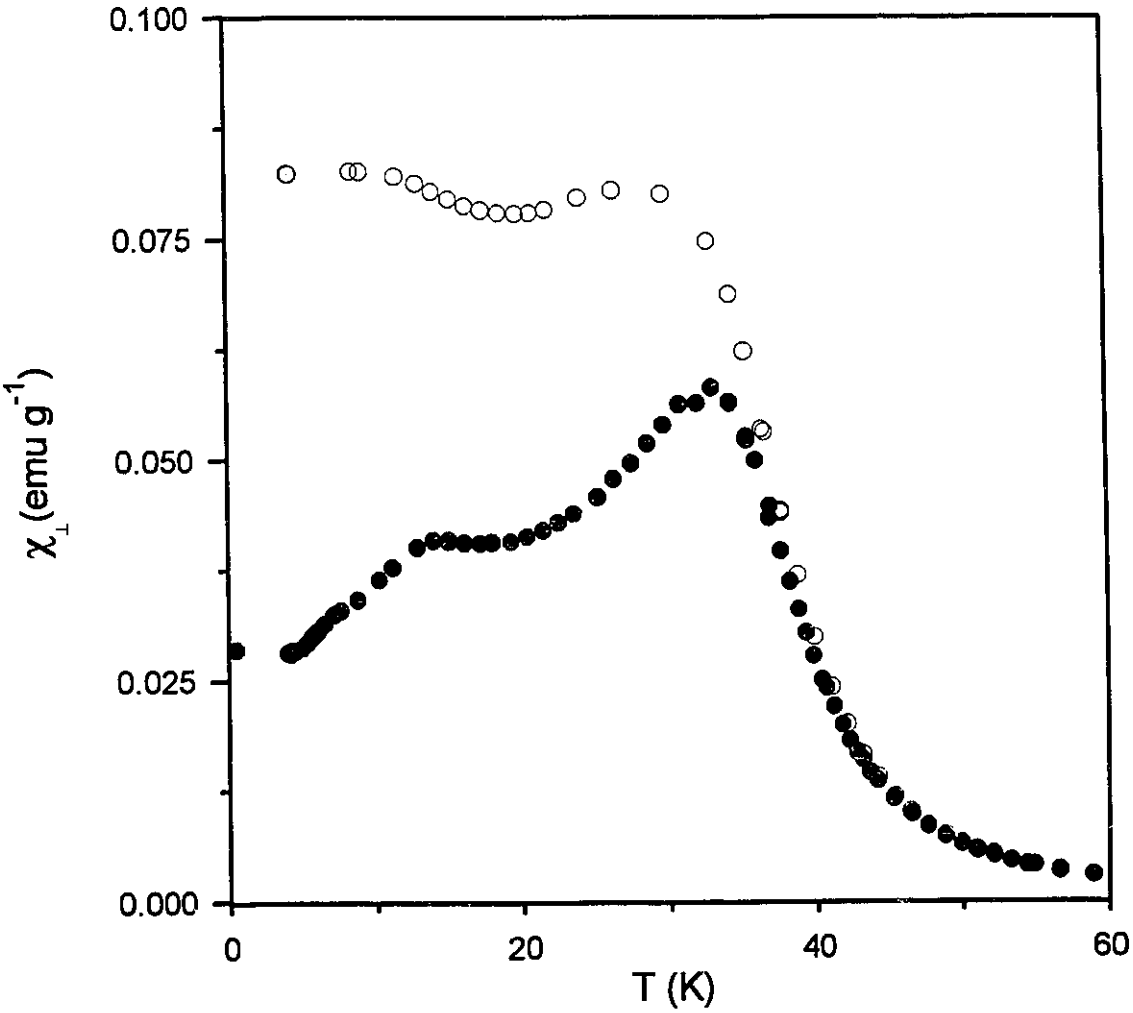

***Figure 5.6** In-plane magnetic susceptibility of a needle shaped sample of natural annite as a function of temperature. Results are shown for the field warming (●) and field cooling (○) measurements.*

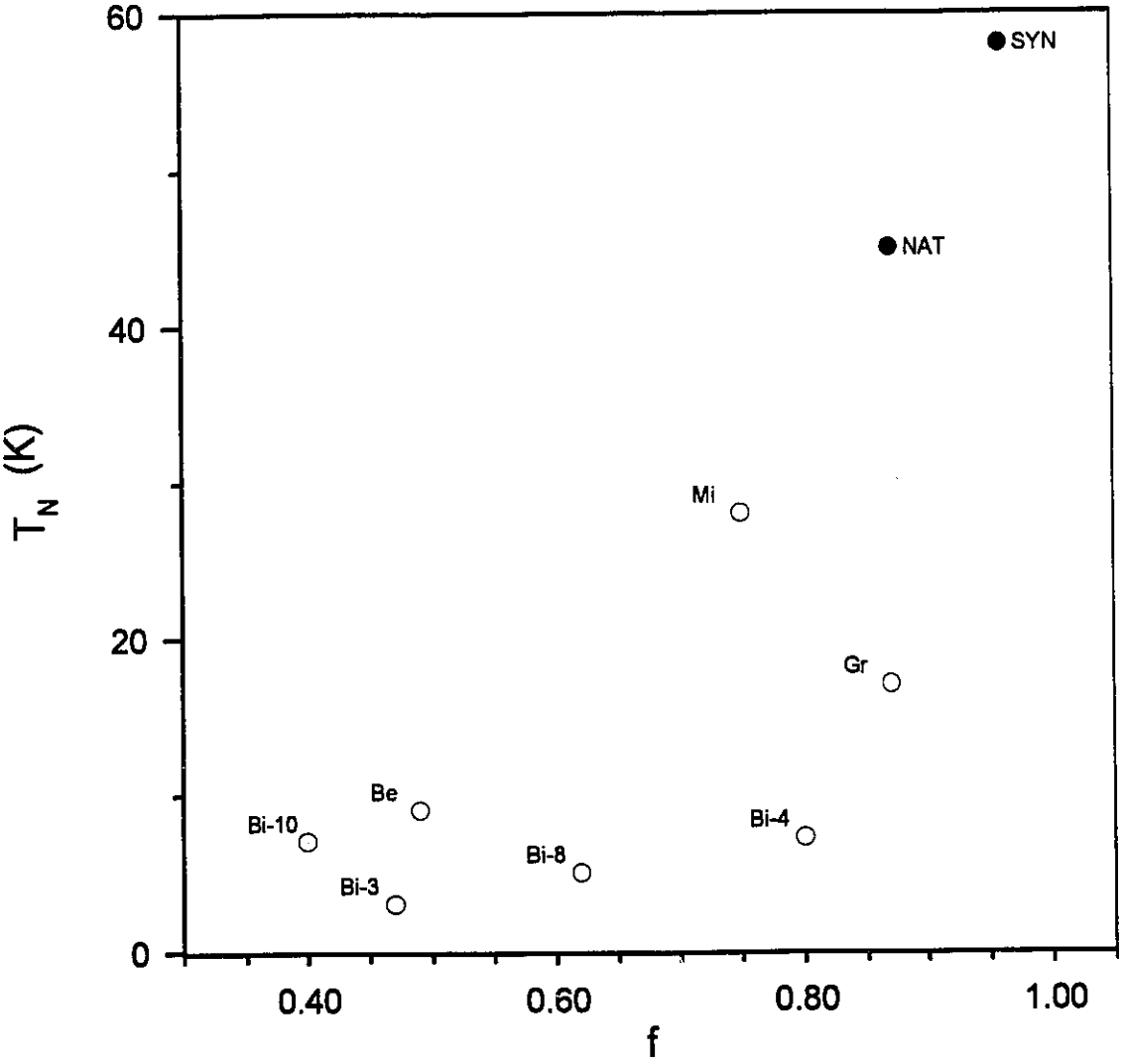

Figure 5.7 *Critical temperatures (T_N) for two samples of annite (●) and for other layer silicates (O). The codes for the literature samples are identical to those in chapter 4, NAT labels the result for the natural annite and SYN labels the point for the synthetic annite.*

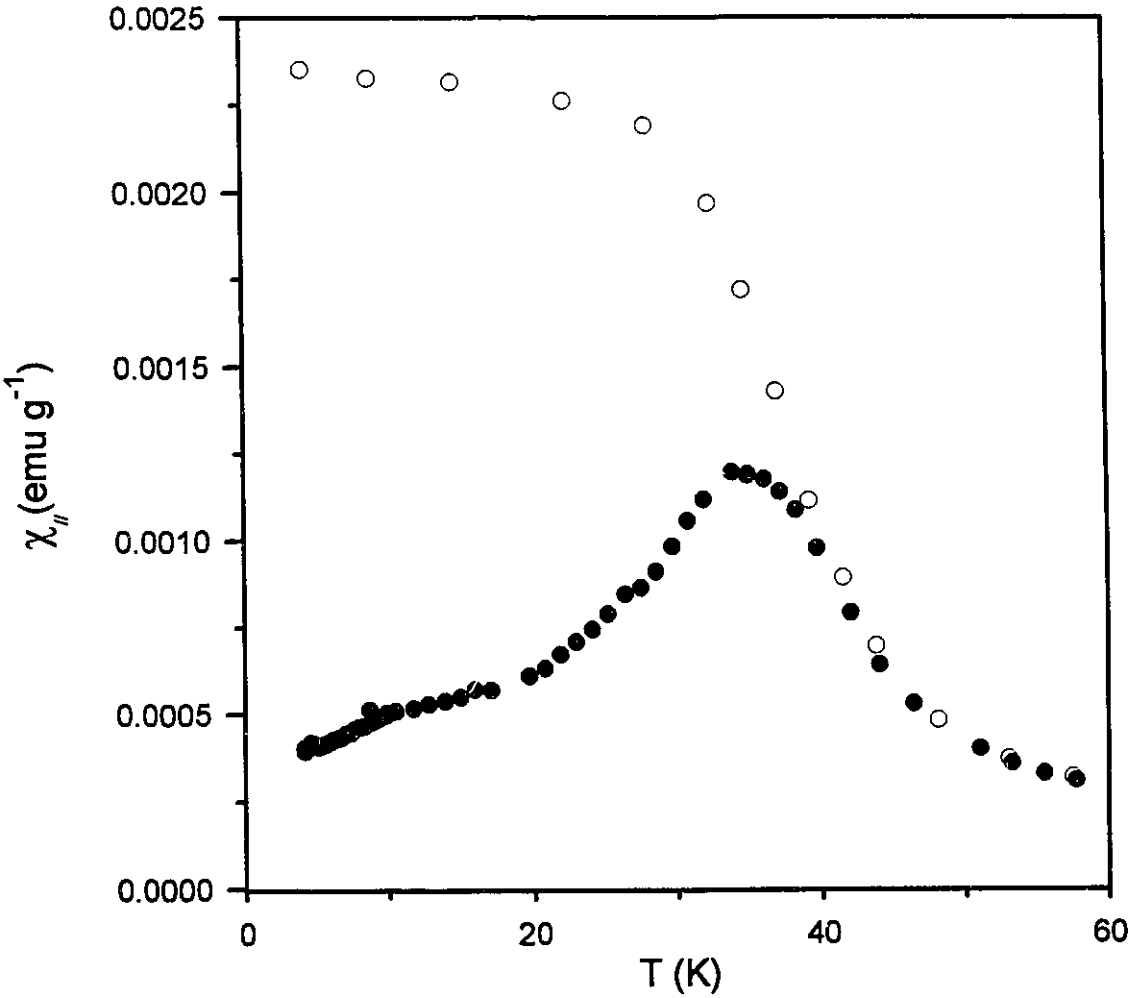

Figure 5.8 *Magnetic susceptibility along the c* axis as a function of temperature for a square flake of natural annite . Results are shown for the field warming (●) and field cooling (○) measurements.*

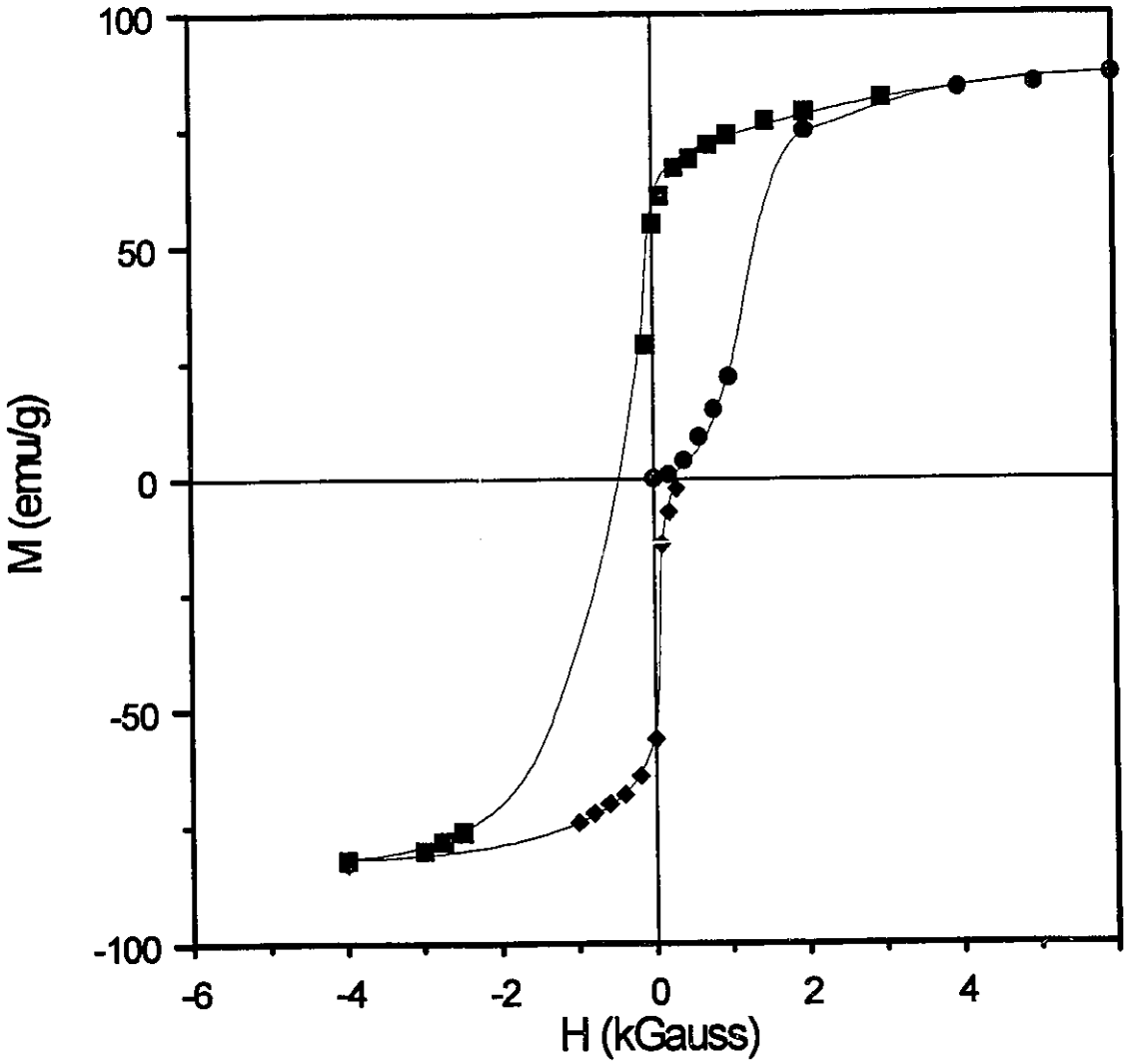

Figure 5.9 *Magnetic hysteresis curve for natural annite; (●) H= 0 kGauss to 6 kGauss, (■) H= 5 kGauss to -4 kGauss, (◆) H =-4 kGauss to 1 kGauss. The measurements were taken with the field applied in the ab plane.*

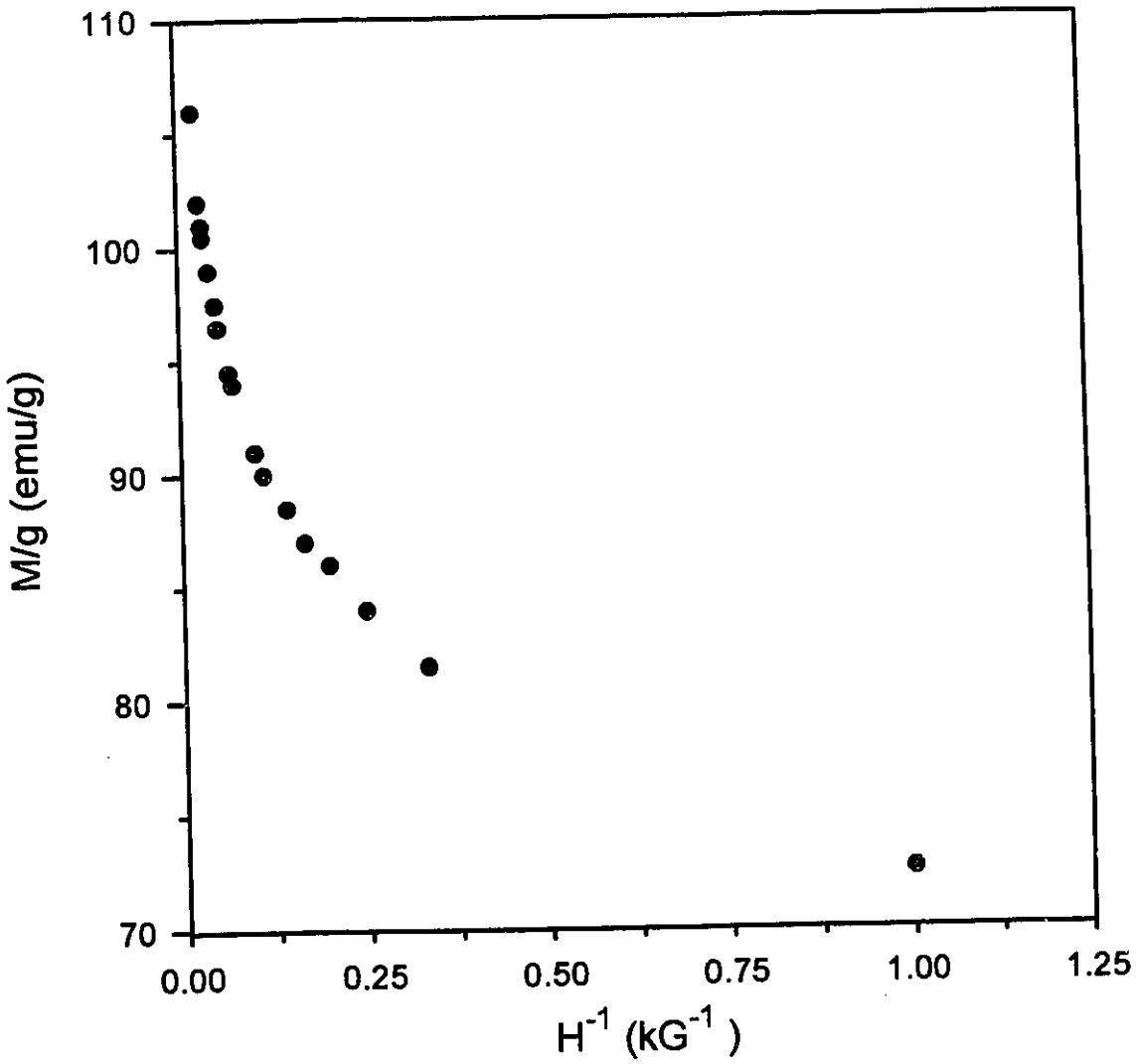

Figure 5.10 *High field, in plane magnetization of natural annite as a function of inverse applied field. The plot demonstrates that extrapolation to infinite field is ambiguous, and hence it is not possible to accurately determine the in-plane saturation magnetization.*

Chapter 6

The Mössbauer Effect and the Hyperfine Field

6.1 The Mössbauer Effect

Mössbauer effect spectroscopy is a nuclear spectroscopy. It relies on the recoilless emission and subsequent recoilless resonant absorption of a gamma ray. In the absence of recoil the width of the γ-ray distribution is restricted to the Heisenberg natural linewidth which is on the order of the 10^{-9}eV to 10^{-6}eV for nuclear γ-rays. Typically, nuclear γ-ray energies are on the order of 10^{4}eV to 10^{5}eV. Thus, the potential resolving power of MES is on the order of one part in 10^{10} to 10^{14}. This resolving power and the short range nature of the hyperfine interactions make MES sensitive to subtle variations in the local electronic and magnetic environment of the probe nuclei.

This sensitivity has been particularly useful in the study of site populations of the two species of Fe in layer silicates (Häggstrom *et al.*, 1969; Dyar and Burns, 1986; Ferrow, 1987; Hawthorne, 1989, Rancourt 1989; Hargraves *et al.*, 1990; Christie *et al.*, 1993; Rancourt *et al.*, 1994). These investigations have concentrated on the local electronic environments that distinguish the [Fe^{2+}], [Fe^{3+}], and $\langle Fe^{3+} \rangle$ sites. The technique has also been used successfully in the study of magnetism of layered compounds (see for instance Ohashi and Tsujikawa, 1974) In the current study MES has also been applied to the study of the synthetic and natural samples of annite at temperatures from RT to 4.2 K. The results of the Mössbauer spectroscopy are presented in chapter 7. The remainder of this chapter provides a brief review of the relationship between hyperfine interactions, Mössbauer spectroscopy and annite.

6.2 Hyperfine Interactions in ^{57}Fe

The transition that produces the ^{57}Fe Mössbauer γ–ray is the decay of an I = ½ nuclear excited state to the I = ½ ground state. In an isolated bare nucleus the excited state is four fold degenerate and the ground state is doubly degenerate. The result is a single transition (figure 6.1a). There are three relevant hyperfine interactions that can partially or totally lift the degeneracy of this transition:

1. The center shift,
2. The electric quadrupole interaction, and
3. The magnetic hyperfine interaction.

The centre shift (δ) is the combination of two terms, the isomer shift (IS) and the second order Doppler shift (SOD). The first effect is a result of the electrostatic interaction between the nucleus and the surrounding electrons. Only those electrons that have non-zero density within the nuclear volume participate in the effect. The effect of the interaction is to shift the energy of the levels with respect to those of the bare nucleus without lifting the degeneracy of either state. This leads to a single transition that is shifted in energy from the bare nuclear case (figure 6.1b). The difference in energy is the isomer shift. In a Mössbauer experiment, the IS that is measured is the difference in IS between the source and the absorber. Thus the measured IS is written as (Greenwood and Gibb, 1971):

$$IS = const\left\{\left|\psi_s(0)_A\right|^2 - \left|\psi_s(0)_S\right|^2\right\} \tag{6.1}$$

where $\psi_S(0)$ is the s-electron Schrödinger wavefunction at r = 0, and A and S are the absorber and source nuclei respectively. In order to provide a calibration standard for the IS the total centre shift of the absorber is normally given with respect to α-Fe at RT.

The SOD is a relativistic temperature dependent contribution to the centre shift (Pound and Rebka, 1960; Josephson, 1960). The SOD arises from the vibration of the emitting and absorbing atoms on their lattice sites. The contribution appears as a Doppler shift in the energy of the emitted photon. It is called the *second* order Doppler shift because it is dependent on the square of the velocity of the atom. Calculation of the SOD requires the choice of a particular phonon model for the solid. In the case of the Debye model, the SOD is given by:

$$SOD = \frac{\langle v^2 \rangle}{2c} = -\frac{3k_B\theta_D}{2mc}\left[\frac{3}{8} + 3\left(\frac{T}{\theta_D}\right)^2 \int_0^{\theta_D/T} \frac{x^3}{\left(e^x - 1\right)}\,dx\right] \tag{6.2}$$

where v is the nuclear vibration velocity, c is the speed of light, k_B is the Boltzman constant, θ_D is the Debye temperature and T is the temperature.

The second relevant hyperfine interaction arises from the interaction of the nuclear quadrupole moment with the surrounding electric field gradient (EFG). In a non-zero EFG this interaction partially lifts the degeneracy of the excited state (figure 6.1c), by an amount (Greenwood and Gibb, 1971):

$$\Delta = \tfrac{1}{2} e^2 qQ\left(1+\tfrac{\eta^2}{3}\right)^{\frac{1}{2}}, \tag{6.3}$$

where e is the electronic charge, Q is the nuclear quadrupole moment, eq is the maximum value of the EFG, and η is the asymmetry parameter.

The EFG is a tensor whose elements are defined by the second derivatives of the electrostatic potential V:

$$V_{ij} = \frac{\partial^2 V}{\partial x_i \partial x_j}; \quad \left\{x_i, x_j = x, y, z\right\}. \tag{6.4}$$

The asymmetry parameter is defined in terms of the diagonal elements of the diagonalized EFG tensor as:

$$\eta = \frac{\left|V_{xx} - V_{yy}\right|}{V_{zz}}. \tag{6.5}$$

The value of η is constrained to lie between 0 and 1 by requiring that $|V_{ZZ}| \geq |V_{XX}| \geq |V_{YY}|$.

The Mössbauer effect spectrum resulting from a nucleus in a non-zero EFG would thus consist of a doublet whose peaks are separated by Δ which is called the quadrupole splitting.

The magnetic hyperfine interaction is the interaction between the nuclear magnetic dipole moment and the hyperfine field. This interaction lifts the degeneracy of both excited and ground states (figure 6.2b). The shift in energy, in the absence of an electric quadrupole interaction is given by:

$$\Delta E_{hf}^{I} = -g^{I} \mu_N m_I H \tag{6.6}$$

where g^I is the level specific nuclear g-factor, μ_N is the nuclear magneton, and H is the magnetic hyperfine field experienced by the nucleus over the Mössbauer effect measurement time (*i.e.* the lifetime of the excited state ~10^{-9} s)[1].

[1] *This distinction is important because in many cases (such as with paramagnetic materials) there is a non-zero hyperfine field but its direction varies rapidly enough that the net H_{hf} seen by the nucleus averages to zero over the measurement time.*

The hyperfine field lifts the degeneracy of both states completely. However, because the emitted γ-ray is electric dipole radiation, only transitions with $|\Delta m_I| \leq 1$ are allowed. This restriction reduces the number of possible transitions from eight to six.

Equations 6.1, 6.3 and 6.6 refer only to situations where a single hyperfine interaction exists. The effect of a combination of a non-zero EFG and a non-zero H can also be determined analytically for the case of $\frac{1}{2}e^2qQ \ll g^*\mu_N H$ (figure 6.2c). In this regime the energy levels are shifted from the $e^2qQ = 0$ positions by an amount (Greenwood and Gibb, 1971):

$$\varepsilon = \frac{e^2qQ}{4}\left[1 - \tfrac{1}{2}\left(3 - \eta\cos 2\phi\right)\sin^2\theta\right] \qquad (6.7)$$

Where θ and φ are the polar and azimuthal angles of H in the coordinate system defined by the principal axes of the EFG.

In cases where $\frac{1}{2}e^2qQ \simeq g^*\mu_N H$, perturbation theory is not applicable and analytic solutions are not available. In these cases the energy levels must be determined by the solution of the full hyperfine Hamiltonian (see Matthias, 1962; Greenwood and Gibb, 1971). Note that because the resulting energy levels will be mixtures of the various m_I states, all eight transitions are possible.

Also, analysis is further complicated by a possible relationship between the asymmetry parameter and the average hyperfine field. It has been shown (Rancourt *et al*, 1985) that the onset of magnetic ordering can affect the value of η. The magnitude of this effect is dependent on many factors including the valence state of the probe ion and the relative orientations of the EFG and **H**.

6.3 The Mössbauer Lineshape

The Mössbauer lineshape is the expression that describes the Mössbauer spectrum. When all probe nuclei occupy equivalent sites with identical sets of hyperfine parameters (δ, Δ, η, **H**) and in the absence of dynamic effects, the lineshape is defined by a sum of up to 8 Lorentzians:

$$I(\nu) = \sum_{i=1}^{8} L(\nu_c^i, \gamma, h^i; \nu) \qquad (6.8)$$

where

$$L(\nu_c, \gamma, h; \nu) = \frac{h\gamma^2}{(\nu_c - \nu)^2 + \gamma^2}\,. \qquad (6.9)$$

Each Lorentzian has a line width, 2γ, determined by the excited state lifetime, a line position, ν_c, and intensity, h, determined by the hyperfine Hamiltonian which contains the hyperfine parameters described above.

In many materials probe nuclei occupy a variety of inequivalent sites. Each site has its own set of hyperfine parameters. In this case the resulting spectrum is a superposition of contributions from all sites. In order to calculate a lineshape, the hyperfine parameters (δ^k, Δ^k, η^k, H^k) and relative probability (P(k)) of the occurrence of each site, k, must be known. The line positions and intensities of each site's contribution are then calculated from the site-specific hyperfine Hamiltonian. The final lineshape is the weighted sum:

$$I(\nu) = \sum_{k=1}^{N} \sum_{i=1}^{8} P(k) L(\nu_c^{ki}, \gamma, h^{ki}; \nu) \qquad (6.10)$$

In this study two different approaches were used to model the P(k). The first is the Voigt-based method of Rancourt and Ping (1989). The Voigt line shape is the convolution of a Gaussian and a Lorentzian. Use of Voigt lines is equivalent to using a Gaussian distribution of hyperfine parameters. By using more than one set of Voigt lines an arbitrary distribution that is the sum of Gaussians can be modeled. The Voigt based method is restricted to cases where there is no hyperfine field or to cases where $\frac{1}{2} e^2qQ \ll g^*\mu_N H$. In cases where these conditions are not met, a numerical approach, in which the distribution of hyperfine parameters is modeled with a series of discrete contributions, can be used. The numerical method used in this study is described in more detail in chapter 7.

6.4 The Hyperfine Field

The hyperfine field may be written as the following sum of terms:

$$H = H_A + \tfrac{4}{3}\pi M - DM + H_L + H_D + H_S \qquad (6.11)$$

The first term, H_A, is the applied field and is zero in the absence of an external field. The second and third terms are the Lorentz field and the demagnetizing field respectively. Both of these terms are proportional to the bulk magnetization. In layer silicates, the bulk magnetic state is antiferromagnetic, and these terms will be zero in the absence of an applied field.

The third term in the equation 6.11 is the contribution from the orbital electron current. This current is given by:

$$H_L = 2\mu_B \langle r^{-3} \rangle \langle L \rangle \qquad (6.12)$$

where $\langle L \rangle$ is the expectation value of the net electronic angular momentum. It has been shown (Beausoleil *et al.*, 1983; see chapter 4) that octahedral Fe^{2+} in layer silicates

occupies a ground state which is an orbital singlet, which implies that ⟨L⟩ is quenched and therefore $H_L = 0$.

The term H_D in equation 6.11 is the contribution to H from the interaction of the nuclear and electronic dipole moments, given explicitly by:

$$H_D = -2\mu_B\left\langle 3\mathbf{r}(\mathbf{s}\cdot\mathbf{r})\mathbf{r}^{-5} - s\mathbf{r}^{-3}\right\rangle \tag{6.13}$$

where s, is the spin moment of the ion, and r is the radius of the ion. For axial symmetry this reduces to (Greenwood & Gibb, 1971):

$$H_D = -2\mu_B\langle S\rangle\left\langle r^{-3}\right\rangle\left\langle 3\cos^2\theta - 1\right\rangle. \tag{6.14}$$

This quantity can be related to the EFG tensor by noting that:

$$e^2qQ = 2e^2Q\left\langle r^{-3}\right\rangle\left\langle 3\cos^2\theta - 1\right\rangle\langle S\rangle, \tag{6.15}$$

so that H_D can be expressed in terms of the principal axis value of the EFG tensor q as:

$$H_D = \mu_B q. \tag{6.16}$$

The final, and often largest, term in H is the Fermi contact term. This is the field that is caused by a net spin polarization of s electrons at the nucleus. It can be written as:

$$H_S = \left(\tfrac{16\pi}{3}\right)\mu_B\left\langle\sum_{i=1}^{N} S_i^2\,\delta(r_i)\right\rangle \tag{6.17}$$

Where the quantity in angular brackets is the expectation value of the spin density, with S_i and r_i being the spin and radial coordinate of the i^{th} electron. A net spin density arises from the interaction between s electrons and unpaired p and d electrons both on the probe ion and on neighbouring ions. There are three principle contributions to H_S:

$$H_S = H_{local} + H_{THF} + H_{STHF}. \tag{6.18}$$

Here, H_{local} is the field arising from the polarization of core s electrons by the local spin moments in p and d orbitals of the probe ion. The net polarization of these electrons tends to pull the s electrons of similar polarization outwards leaving a net s electron polarization in the opposite direction at the probe nucleus. Because the net polarization of the p and d orbitals is just the ionic magnetic moment (μ_i) H_{local} can be written as (Ebert, *et al.*, 1988, 1990):

$$H_{local} = -a_i\mu_i \tag{6.19}$$

The constant a_i is specific to each ion and contains all the information about the interaction between the s electrons and the unpaired p and d electrons. The minus sign indicates the H_{local} is in the opposite direction to the ionic moment.

H_{THF} is the field due to the polarization of s electrons by conduction band electrons that overlap the s orbitals. This effect is prevalent in metals and alloys (Ebert, *et al.*, 1988, 1990) but does not contribute in layer silicates and other insulating oxides.

H_{STHF} is the supertransferred hyperfine field. It is the result of the transfer of spin polarization to the s orbitals of one metal ion from the p and d valence orbitals of another via covalent bonds with a mutual neighbour anion such as oxygen. This process is analogous to magnetic superexchange, except that it must be stressed that only spin polarization transferred directly to s orbitals contributes to H_{STHF}. The process is illustrated phenomenologically in figure 6.3. Here the B ion is the site on which H is to be measured, A is a neighbouring metal ion and O is an intervening anion. There are two dominant mechanisms of transfer of polarization. The first (shown in figure 6.3) is the transfer of actual spin and charge density from a d orbital on ion B to an ion A s orbital through mutual overlap with the O ion orbitals (Grandjean, 1987). The second is the polarization of core s electrons on ion B through overlap with ligand p and s orbitals which are themselves polarized by overlap with the d orbitals of A (Evans & Swartzendruber, 1972).

The supertransferred field at ion A arising from the presence of ion B can be written as (Huang *et al.*, 1967):

$$H_{STHF}^{AB} = \tfrac{8\pi}{3} g\mu_B \mu_2 \left[-\sum_{n=1}^{n-m=1} \mu_{ns}\phi_{ns} + a\phi_{ms} \right]^2 \qquad (6.20)$$

where μ_2 is the ionic moment of ion B, ϕ_{ns} are the core s orbital wavefunctions of ion A, ϕ_{ms} is the lowest unoccupied s orbital wavefunction of ion A, μ_{ns} are the coefficients of the molecular orbital resulting from the mixing of the s orbitals and the ligand orbitals and a is the transfer parameter giving the amount of charge transferred to the ms orbital. The size of H_{STHF} is sensitive to the species of both magnetic ions and the ligand ion, and to the bond angle A-O-B (Grandjean, 1987). Equation 6.20 can be simplified by writing all of this dependence in a single term b_{12}.

$$H_{STHF}^{AB} = b_{12}\mu_2 \qquad (6.21)$$

Thus, the total contribution at any ion i can be written as a sum over the near magnetic neighbours (j) as:

$$H_{STHF} = \sum_{j=1}^{N} b_{ij}\mu_j . \qquad (6.22)$$

Collecting all the non-zero terms, H in a typical layer silicate in zero applied field may now be written as:

$$H = \mu_B q + a_i\mu_i + \sum_{j=1}^{N} b_{ij}\mu_j . \qquad (6.23)$$

With this form of H, it is possible to extract microscopic information directly from the distribution of hyperfine fields, P(H). The complexity of the analysis and the degree of

a priori knowledge of spin structure that is required to extract this information depends on the relative sizes of the various contributions to H.

For instance, if $e^2qQ \simeq 0$ and $H_{STHF} \ll H_{local}$, the extracted P(H) is directly related to the distribution $P(\mu)$ of local magnetic moments. This information can then be compared to the $P(\mu)$ predicted by various microscopic models. It is important to note that in this case the extraction of $P(\mu)$ is not dependent on an *a priori* knowledge of the local spin configuration.

In the case where $e^2qQ \neq 0$, $\eta \simeq 0$ (axial symmetry) and the supertransferred field is small, it is possible to extract the local moment distribution only if a model relating the moment to the EFG tensor at each site is known. This may not be a severe restriction since these distributions may be independent and $P(\Delta)$ is often available from high temperature measurements in which $H = 0$. Nevertheless, there is still no requirement for a model of the local spin configuration in order to extract $P(\mu)$.

If, however, $H_{STHF} \sim H_{local}$ then $P(\mu)$ cannot be extracted without a detailed knowledge of the local spin configuration since H at any site is a function of the neighbouring moments as well as the local moment.

6.5 Hyperfine Interactions in Annite

In order to apply the above discussion to the problem of magnetic ordering in annite it is necessary to briefly discuss the nature of the hyperfine interactions in annite. This discussion is linked to the structure of annite which was covered in chapter 2.

6.5.1 EFG Tensor in "Ideal" Annite

To begin the discussion of the EFG tensor in annite, it is useful to restrict consideration to the ideal annite structure referred to in chapter 2. Although this structure is not realizable, it provides a useful point of departure. Since the bulk of the Fe ions occupy the octahedral cation site, this site is of principal interest in the annite structure. In the ideal structure each of these sites is occupied by an Fe^{2+} ion and each ion is coordinated by 4 O^{2-} ions and 2 OH^- groups in either a CIS or TRANS arrangement (see figure 2.2). To a first approximation, the local electronic structure of the $[Fe^{2+}]$ site is determined entirely by these nn anions.

The EFG tensor is described by equations 6.4 and 6.5 above. The components of the EFG tensor can also be expressed as (Ingalls, 1964):

$$\frac{V_{zz}}{e} = q = (1-R)q_{val} + (1-\gamma_\infty)q_{lat} \tag{6.24}$$

and

$$\frac{(V_{xx} - V_{yy})}{e} = (1-R)\eta_{val}q_{val} + (1-\gamma_\infty)\eta_{lat}q_{lat}\,. \tag{6.25}$$

Here the subscript **val** refers to the contribution from the charge distribution of the ferrous ion's 3d valence electrons. The subscript **lat** refers the contribution from the charge distribution of the neighbouring ions in the crystalline lattice. The Sternheimer factors (1- R) and ($1-\gamma_\infty$) are added to correct for the polarization of the ferric-like (^6S, $3d^5$) core by the EFG of the valence and lattice charge distributions (Ingalls, 1964).

In the ferrous ion the valence contributions are dominant because the outer d^5 orbital is quite asymmetric. However, the form of q_{val} is dependent on the local crystal field which, in turn, is primarily due to the first coordination shell anions. Thus, to calculate the elements of the EFG tensor at the Fe^{2+} site in annite, it is necessary to estimate the crystal field of the octahedral site.

As discussed in chapter 4, crystal field calculations are often performed on a simplified annite structure that neglects the difference between the OH^- and O^{2-} anions. In this model, the [Fe^{2+}] ion is at the center of a trigonally symmetric octahedral cage which is compressed along the c* axis. According to Ballet and Coey (1982), this crystal field lifts the five-fold degeneracy of the $3d^5$ orbital and results in a $^5A_{1g}$ singlet ground state for the valence electron. The resulting EFG is axially symmetric with V_{ZZ} lying along the c* axis.

The more complicated calculation that considers the difference between the OH^- and O^{2-} groups explicitly has not been completed. However, Ballet and Coey consider that the effect of these considerations should be small. This claim is supported by the results of Aldridge *et al.* (1986) whose quantitative calculations of Δ in biotite are based on an oxygen only coordination model, but which agree closely with experimental values. Even in the absence of the explicit calculation it is possible to make some arguments concerning the effect of placing the OH^- groups by geometric considerations alone.

Specifically, regardless of the size of the effect of the OH groups the TRANS site must still have an EFG that is axially symmetric. Therefore it is to be expected that η=0 and V_{ZZ} is along the c* axis of the octahedron. However, in the CIS site, the axial symmetry is destroyed so that at the very least a non-zero η is expected. If the effect of the OH^- groups is sufficiently large the V_{ZZ} axis may lie in the XY plane (probably along the b axis) and the c* axis may become either the V_{XX} or even V_{YY}. There is some support for this model (Hargraves *et al.*,1990) but since separating CIS and TRANS sites in mica

Mössbauer spectra is notoriously difficult (Rancourt *et al.* unpublished), this evidence should not be considered to be conclusive.

6.5.2 Effects of Substitutions and Defects

The differences between the ideal and real annite structures were discussed in detail in chapter 2. Two main differences are: modification of the valence of the octahedral cation and an associated replacement of an OH^- group by O^{2-}, and structural distortion of the octahedral and tetrahedral sheets to accommodate cations of differing sizes. Both of these modifications have some effect on the EFG tensor at the octahedral cation site.

Fe^{3+} in the octahedral site has a dramatically different EFG tensor than that of $[Fe^{2+}]$. The valence electron in Fe^{3+} is $4s^2$ which is a highly symmetric state. For this reason the valence contribution to the components of the EFG tensor is much smaller and the lattice contributions in equations 6.24 and 6.25 dominate. Thus, the EFG at the $[Fe^{3+}]$ site is smaller than at $[Fe^{2+}]$ sites. Because the contributions from $[Fe^{3+}]$ to the Mössbauer spectrum of annite are distinct from those of Fe^{2+}, Mössbauer spectroscopy can be used as a characterization tool in layer silicates (Rancourt *et al.*, 1994; Hawthorne, 1989). Similarly, the $\langle Fe^{3+} \rangle$ also makes a distinct contribution to the spectrum since both the EFG and the IS of the tetrahedral site differ from those at the octahedral site. As well, it must be remembered that for every $\langle Fe^{3+} \rangle$ ion there is a corresponding $[Al^{3+}]$ ion which does not contribute to the Mössbauer spectrum but does affect the structure of the octahedral layer.

The presence of small amounts of $[Fe^{3+}]$ and $[Al^{3+}]$ can modify the environments of a large proportion of the Fe^{2+} environments. The EFG at the $[Fe^{2+}]$ site will be affected by both the chemical replacement and structural distortion stemming from cation substitutions. The relative magnitude of each of these effects is not known. However, it is expected that in the real annite structure the complete characterization of an octahedral site depends not only on the arrangement of nn anions, but also on the nnn cation chemistry, and the local chemistry of the tetrahedral layers above and below the site. Taking all of these factors into consideration, it is not possible to adequately catalog all of the possible local environments in the real annite structure. Instead, it is assumed that the number of different environments is large enough and the variations between environments are subtle enough, that the EFG parameters of all sites form approximately continuous distributions. For this reason the Mössbauer spectrum of annite must be modeled using a distribution of Mössbauer parameters as described above (section 6.3).

It must also be noted that, although the form of the structural distortion of a particular site is undoubtedly linked to its classification as either CIS or TRANS, the relative importance of the distortion effects of the CIS/TRANS arrangement of unshared ions is not known. Therefore, it is quite possible that the width of the distribution of parameters due to structural distortions is larger that the separation between CIS and TRANS site parameters for a given local distortion. If this is the case the separation of the contributions into CIS and TRANS sites cannot be resolved. This accounts for the uncertainty involved in attempting to separate [Fe^{2+}] ME spectra of micas into CIS and TRANS contributions (Rancourt *et al.* unpublished).

6.5.3 Hyperfine Field in Annite

The hyperfine field in annite is only observed in the Mössbauer spectrum at temperatures below T_N. While the EFG is determined by the local electronic structure, and is chiefly dependent on the first coordination shell, the hyperfine field is a function of the local magnetic environment which is determined by the six neighbouring octahedral cations.

In the ideal annite structure, this magnetic environment is quite simple. Each [Fe^{2+}] is bordered by six other [Fe^{2+}]. The interaction between the Fe^{2+} ions is superexchange mediated by the O^{2-} ions and OH^- groups. This exchange is ferromagnetic. Thus, the ideal structure would be expected to form a collinear ferromagnetic state below T_N.

The local magnetic environment in the real annite structure is complicated by the presence of [Fe^{3+}], and [Al^{3+}]. As discussed in chapters 4 and 5, there is good evidence that the Fe^{3+}-Fe^{3+} superexchange interactions are antiferromagnetic. This causes frustration on a hexagonal lattice and the resulting magnetic state has significant inhomogeneity. This inhomogeneity will be expressed as a distribution of hyperfine parameters in the low temperature Mössbauer spectra.

In attempting to extract the distributions of hyperfine field from Mössbauer spectra the considerations discussed in section 6.4 must be borne in mind. In particular the relative magnitudes of the three terms in equation 6.23 are of critical importance for the reasons outlined above. The size of the first term can be calculated explicitly once the size of q is determined from measurements conducted above T_N. It can be shown that this term is quite small compared to the size of $H^{(2)}$. The size of the third (supertransferred) term is more difficult to determine. However, measurements on other materials

---

[2] *Proof of this fact is deferred until chapter 7.*

(particularly spinels) have demonstrated that Fe-O-Fe STHF is relatively small compared to the size of the local contribution (Grandjean, 1987). Thus, it is expected that, to a first approximation it should be possible to determine P(μ) without the aid of a model of the local magnetic structure provided the P(H) can be determined from the Mössbauer spectrum.

However, determining P(H) is complicated by combined effects of the H and the EFG. In particular, knowledge of the angle between the principal axis of the EFG tensor and the **H** for each site is required in order to fit the spectrum. It will therefore be necessary to assume particular models of the EFG tensor and **H** in order to attempt to fit the Mössbauer spectra. These models will be based on the various classes of sites in the octahedral sheet. This process is inherently difficult because it is not clear that classification according to discrete classes is applicable to the annite structure. Further discussion of these models is postponed until the Mössbauer spectroscopy results have been presented in detail.

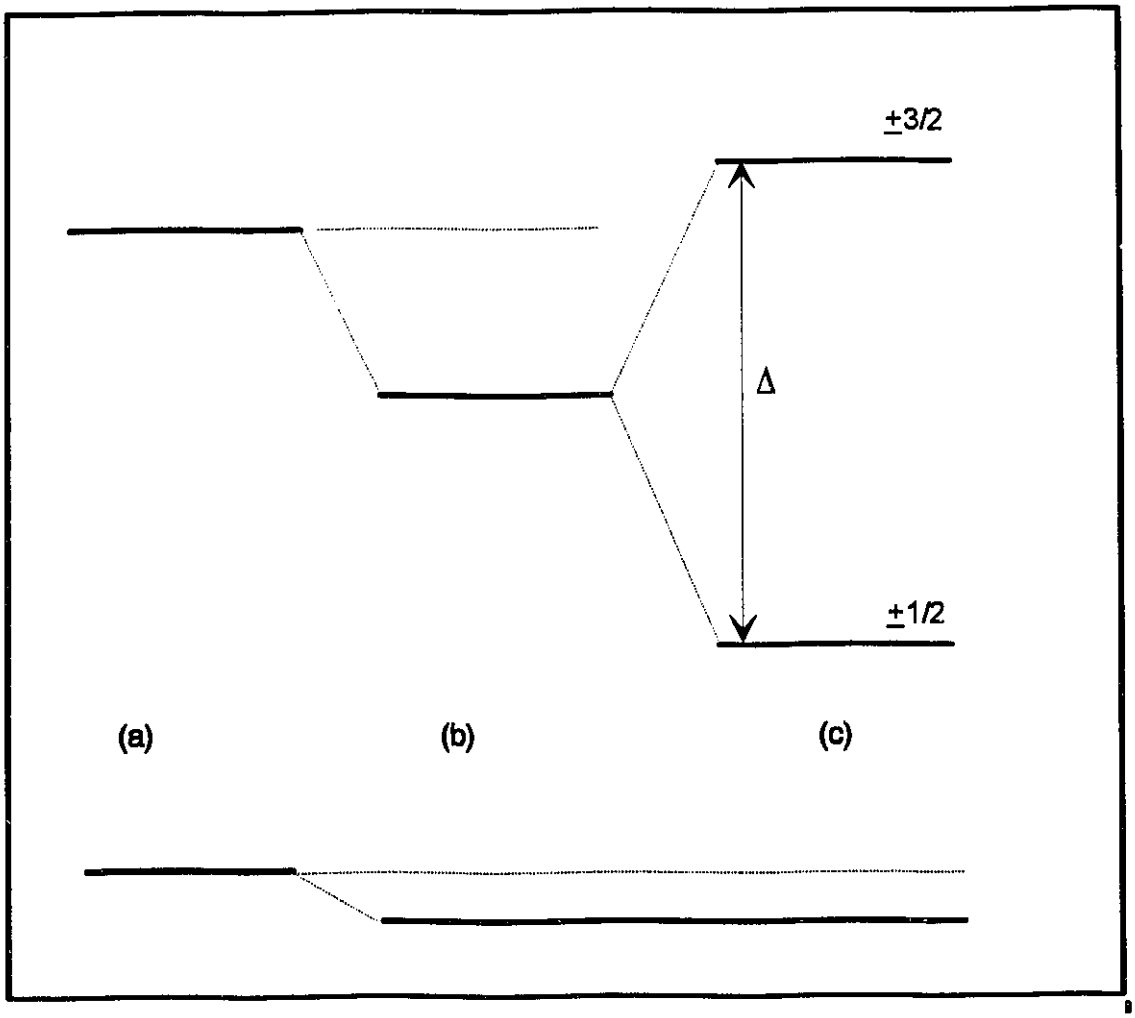

Figure 6.1 *Energy Level Diagram of ^{57}Fe showing (a) the bare isolated nucleus, (b) the effects of the isomer shift which shifts both states. (c) the electronic quadrupole interaction which splits the excited state into a doublet separated by* $\Delta = \frac{1}{2}e^2qQ\left(1+\frac{\eta^2}{3}\right)^{\frac{1}{2}}$

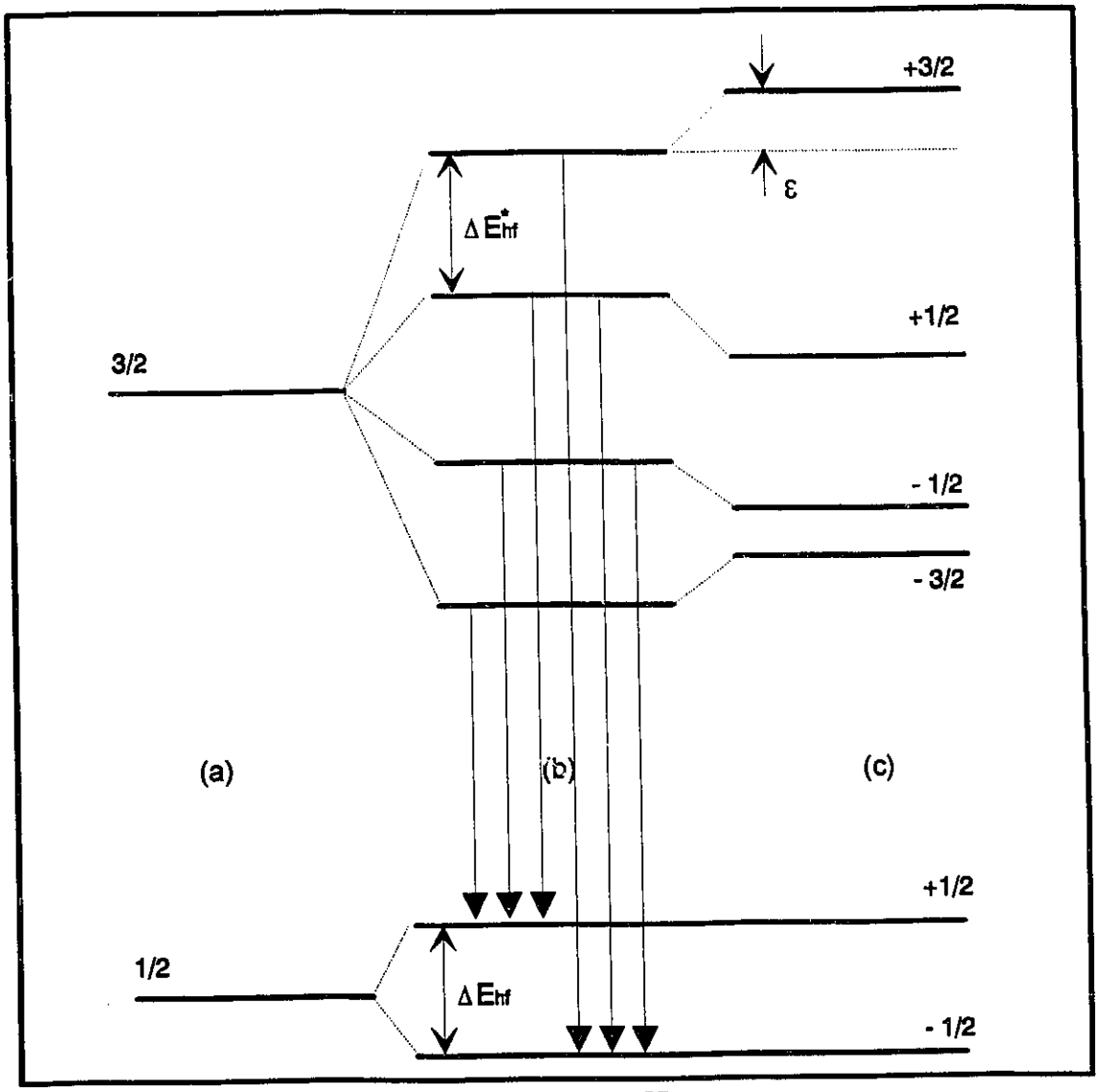

***Figure 6.2** Energy level diagram of ^{57}Fe in a magnetic field. (a) $H = 0$ (b) No quadrupole interaction; the level splitting is given by $\Delta E^{I}_{hf} = g^{I}\mu_N m_I H$, the arrows indicate the six allowed transitions ;and (c) $\frac{1}{2}e^2qQ << g^{*}\mu_N H$ in which case the excited state energy levels are shifted by:*

$$\varepsilon = \frac{e^2qQ}{4}\left[1 - \tfrac{1}{2}\left(3 - \eta Cos2\phi\right)Sin^2\theta\right].$$

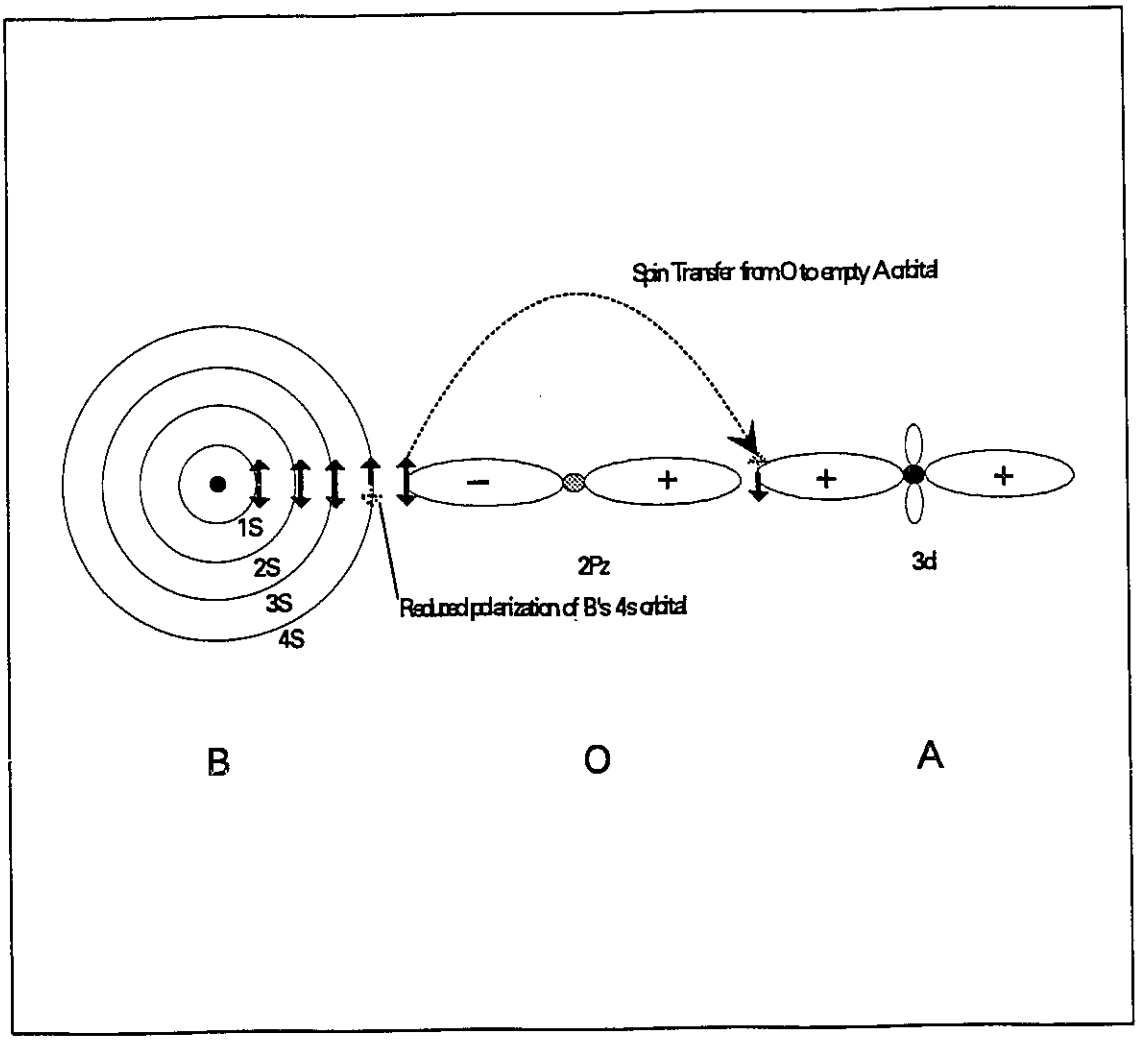

***Figure 6.3** Mechanism for supertransferred hyperfine field (from Grandjean, 1987). The cations A and B both bond with anion O. Spin density is transferred from the 2p orbital of O into the empty 3d orbital of A. There is a resulting decrease of the spin density on the 4s orbital on B. This in turn reduces the hyperfine field at the nucleus of B.*

Chapter 7

Mössbauer Effect Spectroscopy of Annite: Methods, Results, and Discussion

7.1 Apparatus and Experimental Methods for Mössbauer Measurements

7.1.1 Cryostat and Cryostat Stand

The LHT Mössbauer measurements were performed on a Wissel Mössbauer spectrometer mounted on a JANIS model 10DT-VT cryostat. The cryostat consisted of two concentric cryogen cans separated by vacuum spaces and an inner tube to accommodate the spectrometer. The outer cryogen can had a liquid capacity of 11 l and was typically filled with liquid nitrogen (LN_2). The LN_2 level was continuously monitored by means of a 75 cm capacitance sensor and a Cryomagnetics model 50 LN_2 controller. This instrument was also used to automate the control of the LN_2 level in the standard way. The inner cryogen can had a capacity of 9 l and was typically filled with liquid helium (LHe) for low temperature experiments. The LHe level was monitored by a 40 cm superconducting wire sensor connected to a Cryomagnetics model 12 display. This sensor was calibrated in inches with 16" being the full scale reading. The sample space consisted of a 75 cm long, 7.5 cm diameter tube. The lower 50 cm of the sample space was surrounded by the inner cryogen can (figure 7.1a).

The entire cryostat assembly was supported by a specially designed vibration isolation stand (figure 7.1b). The stand consisted of a bottom plate supported by four 45 cm Al legs which were affixed to the floor, a 10 cm thick polyurethane foam pad for vibration isolation and a top plate which rested on the foam. The cryostat support was hung from the top plate and consisted of a 30 cm square bottom plate suspended on 45 cm legs. When assembled, the cryostat support hung down through a 30 cm square hole cut

in the foam and the bottom plate. The cryostat was inserted through a circular hole in the top plate to rest on the cryostat support plate. This arrangement provided a stable and vibration free platform for the cryostat since the cryostat was rigidly connected only to the top plate which was isolated from ambient vibrations by the foam pad. The arrangement also obviated the need of excessive squeezing or constricting the sides of the cryostat since its weight was supported by the cryostat support plate.

7.1.2 Mössbauer Spectrometer

The spectrometer consisted of a Wissel DFG 1200 Mössbauer function generator operating in linear mode and a Wissel MDU 1200 Mössbauer drive unit connected to a Wissel MVT 1000 transducer. The MVT unit was mounted vertically on the cryostat by means of a specially designed mounting flange which also contained the electrical feed-throughs for the temperature monitoring and control connections. The source and sample stages were hung from this flange by three 30 cm long, 0.001" thin walled stainless steel tubes (see figure 7.2). The source was connected to the transducer via another 30 cm thin-walled stainless steel rod. A brass leaf spring attached to the source stage was used to centre the source and constrain its motion to the vertical direction.

The brass sample stage was mounted 1 cm below the source stage (see figure 7.2). Samples were mounted on a copper annulus which was affixed to the stage by means of two screws, with thermal contact ensured by a layer of Apiezon N vacuum grease. This copper mounting ring had an outer diameter of 2.67 cm and an inner diameter of 1.4 cm. Two absorbers were used in the experiments. The synthetic sample absorber consisted of 85.1 mg of powder placed in the hole of the ring and sandwiched between an layer of pure Al foil and a layer of 3M pure Al tape. The natural sample absorber consisted of three single crystal flakes laid flat in the centre of the copper annulus and sandwiched between layers of pure Al foil. This arrangement ensured that the **ab** planes of the flakes would be perpendicular to the γ-ray direction. The average thickness of the flakes was 250 μm.

The γ-rays from the source passing through the sample passed out of the cryostat through mylar windows in the bottom of the cryostat cans and through a 2 cm hole in the center of the cryostat support platform. A gas proportional counter was mounted in a bracket under the platform with the detector aperture aligned with the windows (figure 7.1b).

The output of the preamplifier was passed to a spectroscopy amplifier, then to a single channel analyzer which discriminated the Mössbauer pulses by means of an upper and lower gate voltage. Finally, the discriminated output was sent to an ORTEC multi-channel scaling (MCS) card installed in an IBM PC/XT-clone computer. The MCS

was synchronized to the transducer motion by means of the SYNC and CHannel ADVance signals from the DFG.

7.1.3 Temperature Measurement and Control

Sample temperature was measured using a Lakeshore model DT-470-SD-11 diode connected to a model 805 temperature controller. The diode was mounted on a flat stage milled on a Teflon cylinder. This cylinder was inserted into a hole drilled vertically in the sample stage so that the diode rested at the level of the sample ring. Thermal contact was ensured with a layer of vacuum grease (see figure 7.2). The four wire electrical connections from the diode consisted of 32 gauge copper wires which were wound around the sample stage for thermal grounding and then passed up inside one of the stainless steel tubes, out through the feed-throughs and finally to the temperature controller via shielded cable. This system of measuring temperature had a precision of 0.01K, and an accuracy rating of 0.25K at 4.2 K and 0.5K at RT.

Temperature control was achieved using a 25Ω heater formed from resistance wire which was counter wound around the sample stage at the level of the sample mounting ring. The connections for the heater were also passed up the stainless steel tubes, out through a feed-though and to the controller via a shielded cable separate from the sensor cable.

7.1.4 Typical Experimental Conditions

In a typical experimental run the entire apparatus was pre-cooled to 77K by filling the outer cryogen can with LN_2. For pre-cooling, the inner cryogen can was filled with He gas to a pressure of 1 atm and the sample chamber was filled with He gas to $\sim 10^{-2}$ mbar. After pre-cooling, the temperature was further reduced to the experimental temperature by filling the inner cryogen can with LHe. During the cooling phase, the sample chamber pressure was typically held at between 10^{-1} and 10^{-2} mbar.

Once the sample temperature was stable at the desired experimental temperature, the spectrometer was started and data collection began. Sample chamber gas pressure was adjusted based on experimental temperatures and LHe boil off rates. For experiments at 4.2K, sample chamber pressures of $\sim 10^{0}$ mbar resulted in boil off rates of ~100 ml per hour. For higher temperatures, significantly lower pressures were needed in order to obtain similar boil off rates. For instance, at 55K, a sample chamber pressure of 10^{-3} mbar resulted in a boil-off rate of ~500 ml per hour.

These higher boil off rates placed a practical constraint on collection times at higher temperatures, so that while spectra at 4.2K were collected for between 48 and 60 hours, spectra at higher temperatures were usually collected for only 12 to 24 hours in order to conserve LHe.

Although the temperature controller was capable of measuring temperature to 0.01 K, the experimental configuration typically resulted in temperature stability of ±0.2K for temperatures between 4.2K and 25K and of ± 0.5K for temperatures between 25K and 77K. For temperatures above 77K, stability of ±0.2K could once again be obtained. The differences in temperature stability were likely due to a combination of the thermal properties of the sample stage and the tuning of the differential and integral temperature control settings.

7.1.5 Fitting Programs

All fitting of Mössbauer spectra was carried out on an IBM 80486 PC-clone. The RT and liquid nitrogen temperature (LNT) spectra were fit using the Voigt-based quadrupole distribution fitting programs which are described elsewhere (Rancourt and Ping, 1989). The Fe^{3+} patterns in the LHT spectrum were fit using similar Voigt based methods for modeling hyperfine field distributions, this program is also described elsewhere (Rancourt and Ping, 1989). For fitting the Fe^{2+} contributions to the LHT spectrum, two new programs were used. Both of these programs obtain line positions and intensities by diagonalization of the full hyperfine Hamiltonian of the form proposed used by Brand (1987). The actual fitting was accomplished using the minimization program MINUIT developed at CERN (James and Ross, 1975). The function to be minimized was the standard chi squared (χ^2) function calculated as:

$$\chi^2 = \sum_{i=1}^{512} \frac{(C(i) - T(i))^2}{C(i)} \qquad (7.1)$$

where C(i) is the number of counts in channel i, and T(i) is the theoretical number of counts assigned to channel i, by the fitting model.

The first of these programs, called BRFIT, was used in the line-width broadening and dependent distribution fitting (these fitting models are described in detail in section 7.4.2). The second program, LTFIT, was used in the independent distribution broadening fitting (which is also described in section 7.4.2). See appendix A for listings of the subroutines which were used to interface with MINUIT.

Both programs are capable of fitting several different distinct contributions to the spectrum (each contribution is referred to as a site). Both programs are similar to the Voigt-based methods in that they represent the distribution of parameters by a sum of

Gaussians. However, unlike the Voigt-based methods, these programs derive the lineshape by splitting each Gaussian into a number of bins and summing the spectral contributions from the parameters assigned to each bin to obtain the full distribution broadened pattern.

The two new programs differ primarily in the method which is used to break the distributions into bins, and the method of assigning parameters to each bin. In BRFIT, the number of bins (N_b) is specified in the parameter file, based on this number and the value of the Gaussian width (σ_Δ) of the Δ-distribution a value of Δ is assigned to each bin, k, as:

$$\Delta^k = (\Delta_0 - 3\sigma_\Delta) + \left(\frac{k}{N_b - 1}\right) 6\sigma_\Delta \tag{7.2}$$

here, Δ_0 is the central value of the Δ distribution, which is also specified in the parameter file.

The value of $g^*\mu_N H$ for each bin is determined from the value of Δ and the value of $g^*\mu_N H_0$ (from the parameter file) as:

$$g^*\mu_N H^k = g^*\mu_N H_0^k + 0.2\Delta^k \tag{7.3}$$

This formula assumes that the only site to site differences in H stem from the dipolar contribution to the hyperfine field (see section 6.2). Effectively, this means that the distribution of $g^*\mu_N H$ has a width which is 0.2 times that of the distribution of Δ[1].

The intensities of the lines in each bin's contribution is determined by applying a normalized Gaussian profile. The normalization condition is determined by analogy to the normalization condition for a continuous Gaussian which is:

$$\int_0^\infty G(\Delta_o, \sigma_\Delta; \Delta) d\Delta = 1. \tag{7.4}$$

For a discrete distribution where the probabilities (P_k) of the bins are distributed on a Gaussian profile and the width of each bin is d_k, the resulting normalization condition is:

$$\sum_{k=1}^{N_b} P_k d_k = 1. \tag{7.5}$$

In this case the bins are uniformly spaced, and the width of each bin is:

$$d_k = d = \frac{6\sigma_\Delta}{N_b - 1} \tag{7.6}$$

So, the normalization condition becomes:

$$\sum_{k=1}^{N_b} P_k = \frac{N_b - 1}{6\sigma_\Delta} \tag{7.7}$$

Therefore, the normalized probability of each bin is calculated as:

[1] Appendix B contains an explicit calculation of the factor 0.2.

$$P_k = \left(\frac{1}{A_{N_b}}\right)\frac{6\sigma_\Delta}{N_b - 1}\, e^{\frac{(\Delta_k - \Delta_o)^2}{2\sigma_\Delta^2}} \tag{7.8}$$

where

$$A_{N_b} = \sum_{k=1}^{N_b} e^{\frac{(\Delta_k - \Delta_o)^2}{2\sigma_\Delta^2}} \tag{7.9}$$

is the un-normalized intensity of N_b bins distributed on a Gaussian profile.

In a case where there is no distribution of parameters (i.e. line-width broadening only), the number of bins is set to 1 and Δ and $g^*\mu_N H$ are treated as independent rather than being related by equation 7.3.

The second program, LTFIT, uses a "look-up table" method to model independent distributions of Δ and $g^*\mu_N H$. The look-up table is generated with another program, LTGEN. It is an array whose rows are indexed by values of Δ and whose columns are indexed by values of $g^*\mu_N H$. Each entry in the array consists of the eight line positions and intensities derived from diagonalizing the hyperfine Hamiltonian formed using values of the Δ and $g^*\mu_N H$ for that entry[2]. The maximum and minimum values of Δ and $g^*\mu_N H$ and the number of values of each to calculate must be specified when running LTGEN. The following values were used throughout the fitting process.

	Max	Min	Steps
Δ	-2.0 mm/s	-3.8 mm/s	19
$g^*\mu_N H$	0 mm/s	2.4 mm/s	25

Once the look-up table has been generated, the fitting program proceeds by moving through the array of Δ and $g^*\mu_N H$ values and assigning a probability to each entry based on the Gaussians parameters defined in the parameter file. This means that the probability of each entry in the array is determined as the product of a Δ-probability and a H-probability:

$$P_{kl}^T = P_k^\Delta \bullet P_l^H \tag{7.10}$$

Once again the bin probabilities are normalized so that:

$$\sum_{k=1}^{N_q} P_k^\Delta d_k = 1 \tag{7.11a}$$

$$\sum_{l=1}^{N_H} P_l^H d_l = 1 \tag{7.11b}$$

where, the bin widths are given by:

[2]The remaining hyperfine parameters are specified by a parameter file and are fixed for the entire look-up table.

$$d_k = d_\Delta = \frac{Max_\Delta - Min_\Delta}{(Steps_\Delta - 1)} \quad (7.12a)$$

$$d_l = d_H = \frac{Max_H - Min_H}{(Steps_H - 1)} \quad (7.13b)$$

The program then selects those entries which have an $P_{kl}^T > 0.01$ and calculates the spectral contribution from Lorentzian lines with the positions and intensities specified in the look-up table entry. These elemental spectral contributions are then summed to obtained the broadened pattern. This method was chosen for modeling independent distributions over the simple bins method of BRFIT because it allowed for denser sampling of the Δ and g^* $_N$H spaces at a large computational saving. However, the drawback of the method is that it does not allow fitting of the hyperfine parameters θ, ϕ, and η which are frozen at the time of the generation of the look-up table. It does however allow fitting of δ.

7.2 Mössbauer Results

Mössbauer Spectra were collected for the synthetic sample at eight temperatures (RT (295K), LNT (83K), 50K, 45K, 35K, 25K, 15K, 7K) and for the natural sample at RT, LNT and LHT. The synthetic sample temperature series is shown in order of increasing temperature in figure 7.3. The natural sample temperature series is shown in figure 7.4.

The spectra are described qualitatively below. In addition, the synthetic sample spectra taken above T_N (that is at RT and at LNT, collectively referred to as high temperature) are examined in some detail in section 7.3 in order to derive constraints on the magnitude of the Δ and δ parameters. These constraints are used in section 7.4 in fitting the synthetic sample LHT.

Spectra were also collected for two samples of oxidized synthetic annite, but these samples were not analyzed in sufficient detail to warrant formal inclusion in the study. For interest, these spectra are presented in appendix D.

7.2.1 Synthetic Sample Spectra

The spectra can be divided into two groups based on the presence or absence of hyperfine field splitting (HFS). At temperatures above T_N (T = 295 K and 83 K, figure 7.3g and h), there is no evidence of HFS, the spectra consist of quadrupole split doublets only. At temperatures below T_N (figure 7.3a to f) the dominant contribution to the spectra is from HFS [Fe^{2+}]. In addition to this contribution, it is possible to identify subspectral contributions from HFS $\langle Fe^{3+} \rangle$, [Fe^{3+}] (in figures 7.3a to d) and from

paramagnetic [Fe^{2+}] (in all spectra for T £ 50 K). In some of the spectra it is expected that there is a contribution from paramagnetic Fe^{3+}, but this contribution is too weak to be resolved clearly[3].

The main features of the dominant HFS [Fe^{2+}] subspectrum are denoted by A, B and C in figure 7.3a. These lines are extremely broad, much broader than the lines in the high temperature doublets (compare figure 7.3 g & h to a). This implies that the pattern results from a distribution of hyperfine parameters including the hyperfine field. The exact shape of the parameter distributions can only be determined by fitting the spectrum with a physically correct model.

The ordered [Fe^{2+}] contribution develops with increasing temperature by contracting around the center of the distribution, implying that the mean hyperfine field at the ordered [Fe^{2+}] sites decreases with increasing temperature. As the pattern contracts, the principal lines (A, B, C) become less distinct and the proportion of the spectral area contained in the peaks decreases. The greatest development in the [Fe^{2+}] subspectrum appears to occur between 25 K and 50 K. There is relatively less development from 7 K to 25 K.

Lines from the ordered $\langle Fe^{3+} \rangle$ and [Fe^{3+}] subspectra are found at the outer edges of the spectra (marked T and O respectively in figure 7.3a). These are the outer lines (i.e. lines 1 and 6) of two six line patterns with approximate HFS of 17.5 mm/s and 14.5 mm/s respectively. Line 2 of the O pattern is also visible on the shoulder of peak A at -4 mm/s. The contributions are ascribed to $\langle Fe^{3+} \rangle$ and [Fe^{3+}] based on a spectral area analysis (appendix C, Rancourt *et al.*, 1994). This analysis indicates that all the Fe^{3+} in the sample is ordered at 7 K.

In contrast to the HFS [Fe^{2+}], the Fe^{3+} contributions have HFSs which are relatively insensitive to temperature. However, the spectral areas of the HFS Fe^{3+} patterns vary markedly with temperature below T_N The variation in spectral area of the hyperfine split Fe^{3+} contribution can be plotted against temperature (figure 7.5) to show an abrupt "turning on" at a temperature between 45 K and 35 K. In addition the figure also shows that the two Fe^{3+} populations ($\langle Fe^{3+} \rangle$ and [Fe^{3+}]) have different temperature dependencies, with the $\langle Fe^{3+} \rangle$ having disappeared at 35 K, while the [Fe^{3+}] lines persist. This behaviour is indicative of the relatively weak coupling of the Fe^{3+} ions to the dominant ferromagnetic [Fe^{2+}] backbone. In particular, the $\langle Fe^{3+} \rangle$ are dangling moments connected to the octahedral sheet by single superexchange bonds. The [Fe^{3+}] is more strongly connected to the [Fe^{2+}] background, having up to six [Fe^{2+}] neighbours.

[3]However, in a sample with higher Fe^{3+} concentration a paramagnetic contribution is evident at temperatures above 4.2 K (see appendix D).

However, the [Fe^{3+}] is weakly bonded enough that a significant fraction has no HFS even at temperatures down to 0.5 T_N.

The paramagnetic [Fe^{2+}] peaks are denoted by P in figure 7.3a. These peaks are ascribed to a paramagnetic contribution based on three facts. Firstly, the peaks are extremely narrow compared to the other [Fe^{2+}] features with widths on the order of those found in the high temperature doublets. Secondly, the peaks occur at precisely the same locations as the [Fe^{2+}] doublet positions in the high temperature series (compare figure 7.3a to figures 7.3 g & h). Finally, if the entire temperature series is considered, there is a continuous development of these two peaks. From the 7K spectrum through to the LNT spectrum the relative intensity of the doublet peaks increases with increasing temperature.

It should be noted that simulations have shown (see sections 7.4.3 and appendix E) that it is possible to generate similar peaks at these locations from HFS patterns. However, while this may explain some or all of the intensity in the P peaks at 7 K, it cannot account for temperature dependence of the peaks because the intensity of the main HFS pattern decreases with increasing temperature while the intensity of the P peaks increases with increasing temperature.

The development of the paramagnetic fraction has been quantified in figure 7.5 by plotting the ratio of paramagnetic [Fe^{2+}] to total [Fe^{2+}]. This fraction is obtained from spectral area contributions using the method described in appendix C. The principal source of error in these measurements is the estimation of the background [Fe^{2+}] contribution which must be subtracted in order to obtain the area of the doublet peak. Figure 7.5 also indicates an apparent connection between the decrease of the paramagnetic [Fe^{2+}] and the appearance of the HFS Fe^{3+} lines. Discussion of the implications of this connection is postponed until section 7.2.3.

7.2.2 Natural Sample Spectra

Mössbauer spectra of the natural annite were obtained at three temperatures 4.2 K, 83K and 295 K (figures 7.4). The 4.2 K spectrum of the natural sample consists of extremely wide lines with many of the same features found in the synthetic sample spectrum. For instance, the same four subspectral contributions found in the synthetic sample spectrum can be identified in the natural sample spectrum (compare 7.4a to 7.3a).

There is a high degree of correspondence between the line positions of the prominent features in the natural sample LHT spectrum an those in figure 7.3a. However, the relative intensities of the lines are quite different. For instance, in figure 7.3a line B is much deeper than line A, while in the natural sample spectrum the reverse is true. Also, the two Fe^{3+} contributions are more intense in the natural sample spectrum than in the synthetic sample spectrum. Finally, note that within the [Fe^{3+}] subspectrum, the second

and fifth lines of the pattern (at -4 mm/s and 5 mm/s respectively) are relatively more prominent than in figure 7.3a.

The differences between the Mössbauer spectra of the natural sample and the synthetic sample there are due to two effects: composition and texture. The effect of composition is primarily seen in the change in the relative intensities of the various subspectral contributions. The effect of texture is seen in the change in the relative intensities of lines within a given subspectrum. In other words, the increase in the intensity of the [Fe^{3+}] lines with respect to the [Fe^{2+}] lines is a result of the higher [Fe^{3+}] site population in the natural sample (see table 3.1); but the increase in the intensity of the second and fifth line within the [Fe^{3+}] subspectrum is a result of texture.

Texture effects enter because the intensity of each line in a Mössbauer spectrum is determined by the relative orientations of the EFG tensor principal axes, the hyperfine field, and the γ-ray direction. The natural sample absorber consists of a number of plates oriented with their **ab** planes perpendicular to the γ-ray direction, while the synthetic sample consists of a fine random powder. Thus, the relative line intensities in the synthetic spectra are an average over all γ-ray directions while the line intensities in the natural sample spectrum stem from a single γ-ray direction (along the c* axis).

The effect of texture can also be seen in a comparison of the LNT spectra for both samples (figure 7.3g and 7.4b). In the synthetic sample spectrum, the two dominant lines are approximately equal in intensity while in the natural sample spectrum the high energy line is significantly less intense.

Despite these differences, the 4.2 K natural sample spectrum has all of the important features which have been identified in the synthetic sample: a HFS [Fe^{2+}] component with extremely broad lines; clear and distinguishable HFS $\langle Fe^{3+} \rangle$ and [Fe^{3+}] contributions with splittings of 17.0 mm/s and 14.5 mm/s respectively; and distinct narrow lines at positions which exactly correspond to the doublet line positions in the high temperature spectra.

7.2.3 Summary

Both the natural and synthetic samples appear to have a significant contribution from paramagnetic [Fe^{2+}] ions in their LHT spectra. The presence of such a paramagnetic fraction at temperatures which are on the order of 0.1 T_N is surprising. Although this behavior has been recognized in layer silicates before (Longworth *et al.*, 1986), no mechanism explaining the presence of the paramagnetic contribution to the low temperature Mössbauer spectrum has been provided. Instead, the phenomenon has been attributed to experimental temperatures that are very near T_N. This argument clearly does

not apply to the current samples since the measurements are taken at temperatures well below T_N.

The appearance of a paramagnetic contribution in both samples and the variation in the paramagnetic fraction over a wide temperature range in the synthetic sample indicates that this paramagnetic contribution is not the result of compositional inhomogeneities, the presence of an impurity phase, or a distribution of ordering temperatures. In order to explain the behaviour, a mechanism which is intrinsic to the magnetic state of annite must be found. The search for such a mechanism is hampered by the lack of detailed theoretical models of the annite-like magnetic state (2D Heisenberg ferromagnet with easy plane anisotropy). The construction of such a detailed model is beyond the scope of this work. However, the following two phenomenological models are proposed as possible mechanisms.

In the first model, the paramagnetic fraction appears because the distribution of the $[Fe^{2+}]$ moments is wide enough to contain a significant fraction of sites which have zero or near zero moments and which therefore produce doublet contributions in the Mössbauer spectra. This broad distribution is the result of the distortions caused by octahedral vacancies, cation substitutions, and anion substitutions with their attendant effect on the superexchange bonds. There are precedents for such coupling between local moments and local environments in 3D disordered alloys (D.G. Rancourt *et al.*, 1993b). In the annite case, it is expected that $[Fe^{2+}]$ sites with the smallest moments are likely in close proximity to the Fe^{3+} sites given that: (a) especially in the synthetic annite, the $[Fe^{3+}]$ substitution sites are the principle source of distortion of the octahedral sheet, (b) the relative lack of magneto-crystalline anisotropy of the Fe^{3+} ions, (c) the relatively weak coupling of the Fe^{3+} ions to the $[Fe^{2+}]$ backbone, and (d) the antiferromagnetism of the Fe^{3+}-Fe^{3+} exchange.

The Fe^{3+} ions are therefore at the centres of regions of relatively weak magnetism. These regions grow as temperature increases, generating a larger paramagnetic $[Fe^{2+}]$ contribution to the Mössbauer spectra. Since the moment on a give site is a function of both the moments surrounding site and the coupling of the ion at the site to these moments, this is a plausible explanation for rapid disappearance of the Fe^{3+} HFS contributions. In addition since the $\langle Fe^{3+} \rangle$ ions are generally less strongly coupled to the magnetic backbone this may also explain why the $\langle Fe^{3+} \rangle$ contribution decreases more rapidly than $[Fe^{3+}]$.

The second explanation involves the vibrations of intra-layer domain walls which separate regions of oppositely oriented spins. These vibrations cause a certain region of spins to undergo spin reversals. If the vibrations are rapid on the scale of the Mössbauer measurement time (see chapter 6) then the affected spins will appear to have a net zero

magnetic moment. As temperature increases, the amplitude of the domain wall fluctuation also increases and the fraction of paramagnetic [Fe^{2+}] grows. Now, it can be imagined that the defects caused by cation substitutions constitute sites to which the domain walls are pinned. If this is the case, the regions of paramagnetic spins would again be centred on Fe^{3+} sites and the connection between the growth of the paramagnetic [Fe^{2+}] fraction and the disappearance of the Fe^{3+} sites could once again be established.

Having analyzed the temperature series of both the natural and synthetic samples in a semi-quantitative it is desirable to attempt to understand the low temperature spectrum in more detailed way. The following sections are the first documented attempt to comprehensively examine low temperature layer silicate Mössbauer spectrum.

This analysis is restricted to the synthetic sample because the treatment of the Mössbauer spectra is significantly simplified when considering random powders instead of poly-crystalline samples (such as the natural sample). The analysis proceeds in three steps. Firstly fitting constraints for the low temperature spectra are derived by examining the high temperature spectra. Secondly, the Fe^{3+} contribution is stripped from the spectrum. Finally, various fitting techniques are applied to the stripped spectrum.

The fitting results do not provide a conclusive description of the hyperfine field, primarily because the fitting models are overly simple. However, the simple models provide some quantitative basis for the description of the low temperature spectrum. Furthermore the inadequacies of the simple fitting models provide information which is useful in the formulation of possible future fitting models.

7.3 Constraints Derived from High Temperature Results.

7.3.1 Qualitative Description of High Temperature Results

The RT and LNT spectra are shown separately on an expanded scale in figure 7.6. The RT spectrum consists of a broadened asymmetric doublet. A comparison with an elemental doublet (Figure 7.7) reveals the extent of the broadening. A careful examination of the spectra also reveals that there is some definite structure between the two main doublet lines in the region 0.4 mm/s to 1.2 mm/s. These spectra have been analyzed in detail by Rancourt *et al.* (1994). They report that fitting the spectra to series of Voigt doublets reveals that there are three distinct contributions due to $[Fe^{2+}]$, $[Fe^{3+}]$ and $\langle Fe^{3+} \rangle$. Each of these contributions has a distribution of Δ's. The parameters of a typical fit to the RT spectrum using this model are shown in Table 7.1a. The resulting fit including the separate site contributions, is shown in Figure 7.8a. Note that the contribution of the $[Fe^{2+}]$ site requires three separate Voigt lines. This means that it requires three Gaussian components to adequately model the distribution of Δ and δ for this site.

A qualitative inspection of the LNT spectrum in figure 7.6b reveals that it is similar to the RT spectrum. Note that the main doublet has a wider splitting and there is consequently more distinct structure around 0.5 mm/s. This spectrum has also been analyzed using a model similar to that used for the RT spectrum. Once again the spectrum has been fit to a three site model. Typical fitting parameters are shown in Table 7.1b. The resulting fit including the separate site contributions, is shown in Figure 7.8b.

7.3.2 Effects of Temperature on δ

From such detailed analyses of these high temperature results, it is possible to derive a number of constraints on the δ and Δ which can be of use in fitting the low temperature spectra. However, in order to apply these constraints correctly it is necessary to account for the temperature dependence of δ and Δ.

As explained in chapter 6, δ contains two terms, the isomer shift (IS) which is relatively insensitive to temperature and the second order Doppler shift (SOD) which is temperature dependent and is given by equation 6.2 for the Debye model. The SOD is negative and increases in magnitude with temperature (see table 7.2).

It must also be remembered that δ is a relative measurement and that the SOD affects both source and sample. Thus, the temperature of both source and sample must be accounted for in comparing spectra which have been calibrated under different conditions. In the case of these experiments, all calibrations have been performed by comparison to an enriched ^{57}Fe foil at RT. This ensures that all spectra are calibrated to a consistent energy

scale because the energies of the lines in the calibration foil do not change. However, in order to achieve consistency the source should have been at the experimental temperature when conducting the calibration. In the course of these experiments, it was not always possible to calibrate with the source at the experimental temperature. For example, the 7K spectrum of the synthetic sample was calibrated with the source at RT. The effect of this procedure is that the entire spectrum is shifted left from its true position because at RT the source SOD is larger (i.e. more negative) than at the experimental temperature, T_{exp}. In any given channel, then, the γ– ray energy is lower at RT than at T_{exp} and thus during calibration each channel is assigned an erroneously low energy value. The size of this shift is the difference in source SOD between RT and T_{exp}. This difference is $\simeq 0.12$ mm/s (see Table 7.2 and assume $\theta_D \simeq 450$K).

7.3.3 Effects of Temperature on Δ

Since Δ is not a relative measurement it is not subject to the sort of calibration problems described above. However, the temperature dependence of Δ is more complicated and is not easily described theoretically. In general, the temperature dependence of the Δ should depend on the species of ion and the local chemical environment. The subject of the temperature dependence of the Δ of Fe^{2+} has been analyzed in some detail by Ingalls (1964). The results of this analysis indicate the temperature dependence is greatest at high temperatures, and that the Δ(T) curve is relatively flat in the region between 77K and 4K. This would imply that the value of Δ for Fe^{2+} at LHT should be well approximated by the value at LNT. Further, the analysis indicates that the principle temperature dependence in Δ is a result of the valence contribution to Δ. This contribution is much larger in Fe^{2+} than in Fe^{3+}. It is expected, therefore, that the Fe^{3+} Δ should be much less sensitive to temperature than that of Fe^{2+}.

The process of determining the value of Δ below T_N is further complicated by the fact that the size of the asymmetry parameter, η, can be quite different above and below T_N. Rancourt *et al.* (1985) have shown that the onset of magnetic ordering can induce an asymmetry in the EFG in systems which have zero η above the magnetic ordering temperature. The effect of changing η is seen directly as an increase in the value of Δ (see equation 6.3).

7.3.4 Fitting Constraints on Fe^{3+} Contributions

Having determined the effect of temperature on the δ and Δ parameters, it is possible to determine how the high temperature results can be used to constrain these parameters when fitting the low temperature spectra. However, some explanation of the

application of constraints on Δ is required. The parameter which is used in the fitting process it not Δ, rather it is the line shift (ε) induced by the presence of a non-zero EFG which is given (in the perturbation limit) by equation 6.7. In order to constrain ε, it is necessary to know the sign of e^2qQ, the asymmetry parameter η, and the angles θ and ϕ. In general, these parameters are not known because they cannot be derived from high temperature measurements on powder samples. It is therefore necessary to make some assumptions in order to apply the high temperature constraints to the Fe^{3+} patterns.

In the case of the $[Fe^{3+}]$ it is assumed that $\theta \simeq 0$ and that η is small (≤ 0.5). With this information it is possible to determine that the sign of e^2qQ is negative from the position of line two in the six line pattern in figure 7.3a.

In the case of $\langle Fe^{3+} \rangle$ it is assumed that $\theta \simeq 0$, η is small, and the sign of e^2qQ is opposite to that of $[Fe^{3+}]$ (i.e. positive). This information is the result of a RT study in which spectra of a single crystals of biotite were taken at many different angles (Rancourt *et al.* unpublished). Neither model specifies the angle ϕ.

To use the above information in conjunction with the constraint information derived from the high temperature spectra, it is necessary to relate the value of ε for each type of site to the value of Δ (through equations 6.3 and 6.7). Table 7.3 lists values of ε in terms of Δ for two values of η, for both Fe^{3+} sites. In the case of $[Fe^{3+}]$ values for two different ϕ's are given. For $\langle Fe^{3+} \rangle$ the value of ϕ has no effect since $\theta = 0$.

Now, consider the constraints on the $\langle Fe^{3+} \rangle$ parameters derived from high temperature results. Rancourt *et al.* (1992), in a study of many samples in the literature, have concluded that in true trioctahedral micas at RT these parameters are:

$$\delta^{\langle 3+ \rangle} = 0.17 \pm 0.01 \text{ mm/s} \quad (7.14a)$$

(with respect to the α-Fe CS)

$$\Delta^{\langle 3+ \rangle} = 0.50 \pm 0.10 \text{ mm/s} \quad (7.14b)$$

Applying the difference in sample SOD's in going from RT to 7K (0.14 mm/s) and the calibration anomaly shift (-0.12 mm/s) the constraint on $\delta^{\langle 3+ \rangle}$ in the LHT spectrum is:

$$\delta^{\langle 3+ \rangle} = 0.19 \pm 0.01 \text{ mm/s} \quad (7.15a)$$

(with respect to the 0 velocity position in the folded 7K spectrum)

It is expected that the temperature dependence of $\Delta^{\langle 3+ \rangle}$ is small so that the values can be used directly as constraints at low temperatures. Using the values from table 7.3 the constraint on ε is:

$$\varepsilon^{\langle 3+ \rangle} = 0.25 \pm 0.06 \text{ mm/s} \quad (7.15b)$$

For [Fe^{3+}] the constraints are less well defined. Because the [Fe^{3+}] is a relatively small fraction of the high temperature spectra, and because the contribution is not well resolved, there is some uncertainty in the final fitting parameters derived from the high temperature spectra. Chiefly this is the result of trade off errors amongst $\delta^{[3+]}$ and $\Delta^{[3+]}$ and between these parameters and the other fitting parameters. The range of possible values $\delta^{[3+]}$ and $\Delta^{[3+]}$ can be demonstrated graphically by plotting the value of $\delta^{[3+]}$ versus $\Delta^{[3+]}$ for a number of fits to the high temperature spectra (see figure 7.9). The points in the figure represent fits which are physically equivalent. That is, all of these points represent fits which have equivalent values of χ^2. Also, in all cases the subspectral area ratios are consistent with the site populations in the sample. The constraints derived from this graph are:

$$\delta^{[3+]} = 0.35 \pm 0.10 \text{ mm/s} \quad (7.16a)$$

(with respect to the α-Fe CS)

$$\Delta^{[3+]} = 1.05 \pm 0.15 \text{ mm/s} \quad (7.16b)$$

Applying the correction for SOD and the calibration anomaly shift yields:

$$\delta^{[3+]} = 0.37 \pm 0.10 \text{ mm/s} \quad (7.17a)$$

(with respect to the 0 velocity position in the folded 7K spectrum)

Using table 7.3 and assuming $\eta < 0.5$, the constraint on ε is:

$$\varepsilon^{[3+]} = 0.11 \pm 0.12 \text{ mm/s} \quad (7.17b)$$

7.3.5 Fitting Constraints of Fe^{2+} Contributions

Trade-off errors also affect the value of $\delta^{[2+]}$ and $\Delta^{[2+]}$ derived from the high temperature fits. From the fitting of the high temperature spectra the limits on $\delta^{[2+]}$ are determined to be:

$$\delta^{[2+]} = 1.28 \pm 0.08 \text{ mm/s} \quad (7.18)$$

(relative to the 0 velocity position in the folded 7K spectrum)

Of greater concern in the case of Fe^{2+} is the width of the distribution and strong temperature dependence of $\Delta^{[2+]}$. The most useful method of imposing constraint on $\Delta^{[2+]}$ is to consider the parameter distribution, $P(\Delta)$ (see figure 7.10) rather than a single value of Δ. This is a particularly useful method of imposing constraint since it can be shown (Rancourt, unpublished) that the overall shape of $P(\Delta)$ is relatively insensitive to trade-off errors. Because the temperature dependence of $\Delta^{[2+]}$ is relatively weak between 77K and 4.2K, the $P(\Delta)$ derived from the LNT spectrum can be used as the basis for the constraint on $\Delta^{[2+]}$. The full $P(\Delta)_{LNT}$ is shown in figure 7.10.

This distribution is used as a constraint in fitting in the following ways. Whenever a P(Δ) is required in fitting, the shape of P(Δ) is constrained to be that of a single Gaussian with a width (σ_Δ) of 0.2. This roughly approximates $P(\Delta)_{LNT}$ and is shown for comparison in figure 7.10. The central value of this distribution is constrained by $2.8 \leq \Delta_0 \leq 3.05$. When a single value of Δ is required that single value is constrained by $2.8 \leq \Delta \leq 3.05$. These boundaries are chosen as they lie approximately one Gaussians half-width[4] on either side of the mean value of the LNT distribution, the limits are illustrated in figure 7.10 by dashed lines.

7.4 Fitting The LHT Spectrum

The LHT spectrum of the synthetic sample has been selected for a more detailed quantitative analysis. The aim of this analysis is not to determine definitively the magnetic ground state of annite, but rather to attempt to describe more fully the Mössbauer spectrum itself. Such an understanding is an important first step in the eventual construction of a model of the magnetic state.

The fitting process proceeds as follows. First, the LHT spectrum is further simplified by stripping the Fe^{3+} contributions. Next, a hierarchy of increasingly complex fitting models is constructed; and finally the models are applied to the Fe^{2+}- only spectrum and the results of the fitting are discussed.

7.4.1 Stripping the Fe^{3+} Contribution from LHT spectrum

The presence of the well resolved outside lines of the HFS Fe^{3+} patterns provides the opportunity of simplifying the fitting process. By fitting those channels which contain only background or contributions which are solely due to Fe^{3+}, the shape of the entire Fe^{3+} contribution (including that part which is hidden in the Fe^{2+} lines) can be obtained. When this pattern is subtracted channel by channel from the spectrum the result will be the subspectrum which is due only to Fe^{2+}.

The fitting of the Fe^{3+} contribution is simplified by the fact that, unlike Fe^{2+}, $\frac{1}{2}e^2qQ^{[3+]} \ll g^*\mu_N H$ so that the Voigt-based method of Rancourt and Ping (1989) can be used. Because the two Fe^{3+} contributions overlap somewhat, the $[Fe^{3+}]$ and $\langle Fe^{3+}\rangle$ patterns must be fitted at the same time as separate sites. Also, great care must be taken in this process because only two lines are usable for each pattern; and two lines of a six line

[4] Of course, since the distribution is a composite of three separate Gaussians, the concept of a single gaussian half-width is not strictly applicable. However, it provides a useful guide for constraining the central value of QS for future fits.

pattern do not provide sufficient information to define all of the hyperfine parameters (δ, ε, $g^*\mu_N H$) uniquely. Extra constraints must, therefore, be used to ensure that the fit is correct. There are four sources of constraint available:

1. The constraints from the high temperature measurements which restrict δ and Δ to certain values;
2. The area ratios of the [Fe^{3+}] and $\langle Fe^{3+}\rangle$ sites which are well known and can be confirmed by spectral area calculations (see appendix C).
3. The presence of a distinguishable line belonging to the [Fe^{3+}] pattern at ~ -4 mm/s. This is the second line in the six line pattern. Although its line position is not known exactly, it serves to further constrain the values that δ and Δ.
4. The spectrum which remains after the stripping process. This stripped spectrum must look physically reasonable. This is a qualitative criterion, but it can be used to separate models which are equivalent in all other ways.

In using the Voigt-based approach to fitting a spectrum, it is assumed that the distribution of $g^*\mu_N H$ can be represented as a sum of Gaussians. Since the number of Gaussians required to adequately model a given distribution varies, the standard technique is to begin with the fewest possible Gaussians for each site and to increase this number only until an acceptable fit is reached (Rancourt and Ping, 1989). In fitting the Fe^{3+} patterns, different models were examined. These models are classified by the number of Gaussians used for the [] and $\langle\rangle$ sites respectively (i.e. a 1-2 model is one in which one Gaussian is used for the [] site and two Gaussians are used for the $\langle\ \rangle$ site).

An acceptable fit was obtained with a 2-2 model (see Table 7.4). A 1-1 model was unacceptable because it could not fit the data in the outer channels, principally because of the asymmetry of the outer lines which cannot be modeled with a single Gaussian distribution of hyperfine field. The 2-1 model was unacceptable because it required area ratios well outside the constraints in order to obtain a satisfactory fit. The 1-2 model provided an acceptable fit within the first three constraints. However, the resulting stripped spectrum had an anomalous line at 5 mm/s for all otherwise acceptable fits within this model (see figure 7.11). The 2-2 model fits the outer lines and also leaves a stripped spectrum which does not have this anomalous feature (see figure 7.12). Therefore, the spectrum resulting from the stripping of the 2-2 model (figure 7.12b) has been selected as the Fe^{2+}-only spectrum.

It will be noted that the value of $\delta^{[3+]}$ for the 2-2 fit is slightly outside the constraints derived from the high temperature results. This is a consequence of the manner in which these constraints were applied. The fitting was conducted in two steps: a first fit in which all fitting constraints were imposed and a second refined fit in which the constraints were relaxed in order to find the best "local" fit. The improvement in the fit

which resulted from refining the value of $\delta^{[3+]}$ was significant enough to warrant relaxing the constraint.

7.4.2 Fitting Models

Once the Fe^{3+} contribution has been stripped the remaining spectrum consists entirely of contributions due to $[Fe^{2+}]$. This pattern is substantially more complicated than the Fe^{3+} patterns because $\frac{1}{2}e^2qQ \sim g^*\mu_N H$, requiring that the line positions and intensities be determined only by solution of the full hyperfine Hamiltonian. To solve such a problem all the hyperfine parameters including Δ, δ, η, θ, and ϕ must be specified. Additionally, some method of accounting for the broadening of the line must be proposed.

At the present time no there is no definitive model from which all of the hyperfine parameters can be derived. The high temperature Mössbauer data on powder samples are sufficient to define the magnitude of Δ only. They do not contain information to address the question of the size of η or the orientation of the EFG principal axes. Also, the local electronic environment of $[Fe^{2+}]$ in the real annite structure varies considerably (see chapters 2 and 6) and the effects of these variations is not known.

In the absence of an established model the approach to the problem in this work has been to construct and test a hierarchy of increasingly complex models. These models are related to the known crystal structures and allow for the effects of structural and electronic distortions on the hyperfine parameters. These models are classified in two ways:

1. according to the number of distinct sites provided for in the model (sites in this context means a complete set of parameters including Γ, η, θ, ϕ, δ ,Δ, and $g^*\mu_N H$). Table 7.5 lists the various classes of site models.
2. According to the method of accounting for line broadening. This broadening can either be modeled by allowing Γ to take on a value greater than the theoretical elemental value, or by allowing distributions of various fitting parameters (see Table 7.6).

7.4.1.1 Single Site Models

Table 7.5 divides the models into single site models (A-models) and two-site models (B-models). The single site models are further divided into a symmetric site (A1) model and an asymmetric site (A2) model. The symmetric single site model represents an octahedral site in the ideal annite structure where all coordinating cations are identical (or at least the differences between the anions have no practical effect on the Mössbauer spectrum). In this model, it is assumed that there is a slight compression of the octahedron along the c^* axis (which is the axis perpendicular to the **ab** plane). The result

is a model of the EFG tensor in which V_{zz} // $\mathbf{c}^*$, $\eta = 0$ and V_{xx} and V_{yy} are in the **ab** plane (the specific directions do not matter since $\eta = 0$). It is also assumed that **H** is in the **ab** plane so that $\theta = 90^o$ (and once again the azimuthal angle, ϕ, is unimportant since $\eta = 0$).

The asymmetric single site is similar to the symmetric single site, but allows more fitting freedom because $\eta > 0$ and therefore the directions of V_{xx}, V_{yy} and **H** must be fully specified. It should be noted that this model does not represent a physical situation, it implies that the difference between coordinating anions gives rise to an asymmetry in the EFG tensor, but ignores the difference between CIS and TRANS arrangements of the OH^- groups. As in the symmetric site V_{zz} // $\mathbf{c}^*$ and now V_{xx} and V_{yy} are specified (V_{xx} // **a**, and V_{yy} // **b**).

Determining the direction of **H** in this model is less straightforward. The process can be simplified by assuming that **H** lies in the plane (Coey *et al.*, 1990). In the plane, the symmetry of the magnetic near neighbours defines twelve possible magnetic easy directions (*i.e.* assuming the **H** is directed either directly at a nn cation or directly between nn cations). The symmetry of the octahedral sheet reduces the number of crystallographically equivalent directions to four (see figure 7.13). The various relevant Mössbauer angles arising from each of the four possible magnetic directions in this model are listed in table 7.8.

7.4.1.2 Two Site Models

In the two-site models (B-models, table 7.5) the sites are labeled as TRANS and CIS. This terminology is used somewhat loosely since the TRANS/CIS 1:2 area ratio is not enforced in the fitting process. Rather, the TRANS parameters represent a site similar to the single site model (usually with η small), and the CIS parameters represent a site which is quite different than the single site (and possibly with η large). The models are sub-divided into five classes by pairing one of five different CIS site models (See figure 7.14 and table 7.7a to e) with the TRANS site specified in table 7.7a. In the B1 model, the CIS site is essentially an asymmetric TRANS site. In the remainder of the models the principal axis of the CIS site EFG lies in the **ab** plane. The models also specify the sign of the Δ (i.e. e^2qQ) for the CIS site. The high temperature fitting of the powder absorber provides information on the magnitude of Δ, but not the sign. The B2 and B3 models are equivalent except for the sign of Δ of the CIS site, as are the B4 and B5 models.

7.4.1.3 Line Broadening Models

Each of the above site models can be combined with one of the line broadening models to obtain a complete fitting model for the spectrum. Of the broadening models, the line width (LW) method is the least computationally demanding. It is also a method

which has been used by many authors to attempt to fit such spectra (such as Ballet and Coey, 1982; Ballet *et al*, 1985; Coey *et al*, 1981; Longworth *et al.*, 1987).

The other two broadening models are parameter distribution models. The physical basis for dependent distribution (DD) models is the dipolar contribution to the hyperfine field (see equation 6.16). This model assumes that the distribution of H is solely due to the distribution of Δ. The method of implementing this form of distribution model is described in section 7.1.5. Note that in using this form of distribution there is an underlying assumption that $\eta = 0$, since this is the condition which gives rise to equation 6.16. Thus, it is only strictly correct to combine this broadening model with the single symmetric site model.

The independent distribution (ID) model assumes that the distribution of $g^*\mu_N H$ is not related to the distribution of Δ. This is essentially equivalent to assuming that the magnetic and electronic environments are independent. If the dipolar contribution to H is small this is a good first approximation since the electronic environment is mainly due to the near neighbour anions whereas the magnetic environment is predominantly determined by the next near neighbour cations.

From these site and broadening models a hierarchy of increasingly complex models can be formed. The results of fitting attempts with these models are discussed in the following sections.

7.4.3 Fitting Results - Single Site Models

7.4.3.1 Symmetric Site - LW Model

The method of applying constraints to the fitting process naturally depends on the fitting model in use. For the first model (single symmetric site - line width broadening, A1-LW) the values of H, Γ, δ, and Δ were fitted. δ and the magnitude of Δ were constrained within the limits determined from the LNT spectrum. However, the LNT spectrum does not provide any information regarding the sign of e^2qQ. Therefore two separate fits were performed, one for each sign of Δ, these fits are shown in figure 7.15 and figure 7.16. The fitting parameters are shown in table 7.8.

In this table and all succeeding tables the figure of merit $\overline{\chi}^2$ is the reduced chi squared which is calculated as

$$\overline{\chi}^2 = \frac{\chi^2}{(N-\nu)} \tag{7.19}$$

Where N is the number of fitted data points, and ν is the number of free parameters in the fit. With a correct model , the ideal value is $\overline{\chi}^2 \sim 1$.

The $\Delta < 0$ fit (figure 7.15) is significantly better that the $\Delta > 0$ fit (figure 7.16). This is obvious from table 7.8 since the value of $\overline{\chi}^2$ for the former is over 5 times smaller that of the latter. It is also obvious from the figures. In the $e^2qQ < 0$ case the lines of the theoretical lineshape occur at approximately the correct positions and there are no lines in the model lineshape which do not also occur in the experimental spectrum. In the $e^2qQ > 0$ case the theoretical lineshape bears no qualitative resemblance to the actual spectrum. For this reason further single site models will be fitted only with $e^2qQ < 0$.

Although the $e^2qQ < 0$ fit is qualitatively similar to the experimental spectrum, it is obviously not good fit. It is useful to examine the nature of the failings of this fit. There are two types of misfit:

1. Misfit resulting from discrepancies in the shape of the lines between the experimental and theoretical patterns.
2. Misfit resulting from discrepancies between the positions and intensities in the lines in the experimental and theoretical patterns.

As a particular example of the first type of misfit, note that while there is a variation of the line-width with line height in the experimental data (i.e. lines A and D in figure 7.15 are wider and less deep that line B), this variation is not reproduced in the theoretical lineshape (all the lines have the same width). Also, note that there is some trade-off in the fit between the shoulders of the lines and the tails or BG. This is particularly obvious on the high velocity shoulder of line D where the BG is overestimated while the shoulder of the line is underestimated.

As an example of the second kind of misfit, note that there is a large area on the low velocity shoulder of peak A for which there is no corresponding intensity in the theoretical pattern. Also note that the small peak on the low velocity shoulder of peak B is missing entirely in the model pattern.

7.4.3.2 Asymmetric Site - LW Model

The effect of using an asymmetric site with line width broadening (A2-LW) is demonstrated by considering fits with each of the four angle cases for two values of η. (see figure 7.17 and figure 7.18). The values of $\overline{\chi}^2$ from table 7.8 demonstrate that the overall quality of the fit is not improved by using the asymmetric site. A close examination of the fits in figures 7.17 and 7.18 reveals that although the fits evolve significantly with increasing η, improvement in one area of the spectrum is always offset by misfit in another area. In addition, none of the fits significantly improve the relative intensity ratios over the symmetric site fit, nor is the small line on the low velocity shoulder of peak B present in any of these theoretical lineshapes. Finally, note that the discrepancies in the shape of the theoretical lines in figure 7.15 persist in the asymmetric site fits.

7.4.3.3 Dependent Distribution Broadening

Within the single site models, it remains to consider the effect of distribution broadening. The dependent distribution method is illustrated by a simple simulation using the symmetric site model. In this simulation the parameters of the best A1-LW fit are used (table 7.8) except that a Gaussian distribution of Δ's (with $\sigma_\Delta = 0.2$) is applied. The distribution of $g^*\mu_N H$ is derived from this distribution as described in equation 7.3. The result of this simulation is compared to the actual spectrum in figure 7.19.

The lines generated by the DD simulation are on the order of one tenth as wide as the lines in the spectrum. Since the width of the distribution of H values is, effectively, $0.2\sigma_\Delta$ (see equation 7.3), the only mechanism for increasing the line-widths generated by this model is to increase the width of the Δ distribution. However, to obtain line-widths of the appropriate size it would be necessary to increase σ_Δ to over 2.0 mm/s (*i.e.* ten times the σ_Δ used in figure 7.19). Such a distribution width is extremely unlikely given the RT and LNT P(Δ) distributions. Thus, it is doubtful that this method of broadening can yield the linewidths necessary to fit the spectrum. For this reason the DD broadening model will not be considered further in the fitting process.

7.4.3.4 Independent Distribution Broadening

In considering the effects of the ID model it is instructive of compare the results of this model to the results of the LW model. This comparison is done by simulating ID broadened Mössbauer patterns for comparison to LW broadened patterns generated from similar parameter sets. In all simulations a value $\sigma_\Delta = 0.2$ mm/s is used. Simulations using three different values σ_H of are illustrated in figure 7.20 (ii to iv). These three patterns are compared to the single symmetric site best fit from figure 7.15 (figure 7.20(i)). For consistency, the central values of Δ and $g^*\mu_N H$ were constrained to the values obtained in the line-width broadened fit; also the values of δ and total spectral area in the simulated patterns were set to the values from this fit (table 7.9).

Notice that in the distribution broadened patterns there is a variation in the width of the lines across the spectrum that is not present in the linewidth broadened pattern. This effect is due to the fact that the width of any given line in the distribution broadened pattern is approximately proportional to its displacement from its $g^*\mu_N H = 0$ position.

In order to visualize this it is useful to think of the low temperature spectrum as having evolved from a symmetric doublet[5]. With the application of a non-zero hyperfine field each of the doublet lines is split into separate lines which are displaced by different

[5]Appendix E shows examples of the development of elemental patterns as a function of increasing H.

amounts from the doublet position because each line's position has a different dependence on the applied field.

Now, if a distribution of fields is applied to a number of Mössbauer nuclei, the pattern due to each nuclei will have lines displaced by different amounts. The resulting spectrum will consist of six broadened lines. However, because each line has a different dependence on the applied field the lines will be broadened by different amounts. Since lines which are closer to their original (H=0) positions have a smaller dependence on H, it follows that these lines will be narrower under the effect of a distribution of hyperfine fields.

The variation in the width of lines in proportion to their displacement from their H=0 positions is known as differential broadening. It is further demonstrated in figure 7.21. This figure shows an asymmetric site fit and three distribution broadened simulations for different values of σ_H. Once again the central values of Δ and $g^*\mu_N H$, and the values of δ and spectral area are fixed to the corresponding parameters in the line width broadened fit. The particular feature of note in this series is the narrow line at ~0 mm/s. This line arises only in patterns with $\eta > 0$[6]. The position of this line is only slightly dependent on $g^*\mu_N H$ and it therefore remains quite narrow, even for large values of σ_H. Although the line is also present in the LW fits, it is not preferentially narrow and is therefore not resolved. It is only the differential broadening mechanism which produces the sharp and well defined line.

From this comparison of the two methods of spectral broadening, it might be expected that the ID model would provide a significant improvement over the LW model in fitting the spectrum. It does not. In fact the best fit using distribution broadening (see figure 7.22 and table 7.11) produces a value of $\overline{\chi}^2$ which is higher than the line-width broadened fit for a single symmetric site ($\overline{\chi}^2 = 37.4$ compared to 24.8). Qualitatively, however, the distribution broadened fit reproduces the general line width and height ratios more faithfully that the linewidth broadened fit. Note also that the tails of the distribution broadened lines are much less pronounced so that there is no pronounced underestimation of the BG.

In considering this fit, it must be stressed that it is based on a very simple distribution of $g^*\mu_N H$ using only a single Gaussian component. It would be possible to obtain a better fit with a more generalized distribution using more Gaussians. However an analysis of the single component fit indicates that there is little to be gained from using a more generalized distribution. For example, notice that in order for a more general

[6] It arises because for $\eta > 0$, there is some mixing of the nuclear excited states which allows the possibility of all eight transitions (see chapter 6) .

distribution to improve the fit it must add intensity in the region from -4 mm/s to -2 mm/s while reducing the intensity in the region from 6 mm/s to 8 mm/s. Now, with the single site model a single constrained value of δ is used for the pattern regardless of the shapes of the distributions of D and $g^*\mu_N H$. This means that the addition of more Gaussian components to the distribution can preferentially add intensity at the center or at the edges of the pattern, but not preferentially to one side of the distribution. Thus, it would not be possible to simultaneously improve the fit either the low velocity or high velocity region without worsening it in another. To solve this problem, it is necessary to use a second component which has different values of δ, η, θ, and ϕ. Such a pattern constitutes a second site.

7.4.4 Fitting Results - Two Site Models

There are five different two-site models (B1 through B5), each of which is divided into 4 separate angle cases ((a) to (d) figure 7.13). Of these, there are two sets of doubly degenerate cases (B2(d) & B4(d) and B3(d) & B5(d)) so that there are 18 different fits which must ultimately be considered.

7.4.4.1 Fitted Area Ratios

For computational simplicity we return to the LW broadening model. The fits vary considerably both in the quality of fit as represented by the value of $\overline{\chi}^2$ (Table 7.11) and in the shape of the final fitted spectrum (see figures 7.23 to 7.27). However, all of the fits are consistent in that the TRANS site is the dominant contribution, comprising between 67% and 92% of the fitted area of all trials. In most cases (14 out of 18), this TRANS site is also highly symmetric (i.e. $\eta \sim 0$). Effectively this means that the dominant contribution to all fits is essentially the single symmetric site pattern shown in figure 7.15 (but reduced in intensity by up to $\frac{1}{3}$). Given this fairly consistent TRANS contribution, the variation in the fits stems from the ability of the CIS site model to account for the discrepancies between the symmetric site pattern and the experimental data. This variation is marked. In examining the fits further, it is useful to divide the models into three groups based on the value of $\overline{\chi}^2$. The first group has $\overline{\chi}^2 \geq 19.2$ and represent negligible and small improvements over the single site models. The fits in this group are referred to as the "bad" fits. The second group is the "moderate" group of fits which have $15.6 \leq \overline{\chi}^2 \leq 17.2$. And finally, the "good" fits are those with $\overline{\chi}^2 \leq 13$.

There are five fits in the bad group (B2 (c) & (d), B3(a) & (b), and B4(b)). There fits are characterized by TRANS sites which account for between 86% and 92% of the spectral area. Not surprisingly, these fits strongly resemble the single symmetric site patterns, with the possible exception of B2(d).

The moderate sites have a wider range of TRANS site areas. In these fits, the TRANS site accounts for between 67% and 88% of the spectral area. These fits bear fairly strong resemblance to figure 7.15 as well. In all cases, there is significant improvement in some regions of the spectrum but not in others. For instance, in the B5(b) fit, the agreement between the fit and the experimental data is improved on the shoulders of the patterns, but the intensity ratios in the center of the pattern are not particularly better than the symmetric site fit.

The good group of fits consists of the remaining eight fits (B1(d), B2(a) & (b), B3(c) & (d), B4(a), and B5(c) & (d)). However, two of these (B3(c) and B5(c)) are actually degenerate because the CIS site has $\eta = 0$. Thus, there are actually seven distinct fits in the group. All of these represent significant improvement over the single site fits. Qualitatively, this improvement can be seen in all regions of the fit, although the shape of the fitted spectrum varies considerably from model to model. Despite this variation, and despite the fact that at least one fit from each CIS site model is in the "good" group, all the fits in this group are have equivalent values of $\overline{\chi}^2$.

Comparison of the parameters in table 7.11 reveals a number of important differences between the fits. The most obvious difference is the sign of the CIS site Δ which is enforced by the fitting models. Good fits are obtained with both signs of Δ. There are some interesting distinctions between the fits based in the sign of Δ. The three fits with $\Delta > 0$ have symmetric CIS sites with $g^*\mu_N H \sim 0.75$ mm/s. The four fits with $\Delta < 0$ have generally asymmetric CIS sites with a range of $g^*\mu_N H$ values from 0.8 mm/s to 1.5 mm/s and values of $\frac{\Gamma}{2}$ ranging from 0.28 mm/s to 0.37 mm/s.

7.4.4.1 Fixed Area Ratios

The area ratios in table 7.11 demonstrate that the best fits with each model are obtained for CIS/TRANS ratios which are quite different than the 2:1 ratio which occurs in the annite structure. Freezing this ratio results in fits which are significantly worse than the single site fits for some of the models (see table 7.12). The increase in $\overline{\chi}^2$ is largest for the two models with $\Delta > 0$, the best fits are obtained for models in which the CIS site has $\theta = 90^o$ and $\eta = 0$, which means that the fitted CIS site has a "TRANS-like" character.

For comparison some of the fixed area fits are shown in figure 7.28. In many cases the fixed area fits do not appear to be significantly worse than the best fits. This is often because the misfit is systematic across the entire spectrum. Because the dominant contribution is forced to come from a pattern which does not fit the spectrum well, it has an extremely large Γ and results in a theoretical lineshape which consistently smears out the lines in comparison to the experimental data.

Because of the computational complexity required, it was not possible to complete a comprehensive survey of the two site fitting models with the ID line broadening model.

7.4.5 Summary of Fitting Results and Discussion

Although none of these fitting models produces a theoretical lineshape that reproduces the experimental data, the results indicate a number of important features of the spectrum.

Firstly, even given the admitted over-simplicity of the site models the fits in hand do provide two quantitative results. For instance, the average value of $g^*\mu_N H$ is remarkably consistent across all site and broadening models, this value is 1.15 ± 0.05 mm/s, which corresponds to a hyperfine field of 170 kG ± 7 kG. Also, the average linewidth in the LW fits consistently found to be $\frac{\Gamma}{2} \sim 0.45$ mm/s. Now, it is not possible to draw a direct correspondence between $\frac{\Gamma}{2}$ in the LW model and σ_H in the ID model, but the A2-ID model fit has $\sigma_H = 0.489$ mm/s which corresponds to a half-width in the distribution of local magnetic moment of over 30% of the central value of the distribution.

Furthermore, it is obvious from the failure of the DD broadening model that the distribution of hyperfine fields is not due solely to the dipolar hyperfine field term which is the result of the distribution of EFG magnitudes. In other words, the distribution of hyperfine fields is a result of the distribution of magnetic environments (*i.e.* variation in nn cation species, nn magnetic moments, exchange bond topology etc.), and not merely an artifact of the distribution of electronic environments.

The failure of the fitting models to produce good agreement between the theoretical fits and the experimental data is of note; although it is not surprising considering the fairly simplistic nature of the fitting models which were employed. In particular, the most comprehensive fitting was done using a line width broadening model which is not a truly physical method for accounting for broadening. Comparison of line-width broadening model fits to simulations using the independent distribution model demonstrate that the latter method produces lines whose general shape more closely resembles the experimental data's line-width to intensity ratios. Furthermore, there is less trade off between the shoulders and the tails of the patterns generated by the ID method than in the equivalent LW broadened patterns. However, computational complexity limited consideration of the ID broadening models to simple Gaussian distributions of parameters. These distributions were not general enough to approach the value of $\overline{\chi}^2$ for the best line-width broadening fits.

The results of both the single site and two site models indicate that the dominant contribution to the spectrum is from a site which has $e^2qQ < 0$ and a polar angle between V_{ZZ} and **H** of near 90°. There are also strong indications that this site is quite symmetric. Evidence for the site symmetry is found in the single symmetric site fit and in the two-site fits. The single-site fit pattern reproduces most of the spectral features without having any

lines which do not appear in the experimental data. In two-site fits where relative areas and values of η are left free, the fits consistently converge on solutions which have a dominant symmetric TRANS site regardless of the accompanying CIS site.

Finally, the results demonstrate that the TRANS/CIS division of sites is clearly incorrect. In the annite octahedral sheet structure, the CIS to TRANS site ratio is 2:1, but in the best fitting models the intensity ratios are on the order of 1:3 or 1:4. When the actual CIS to TRANS ratio is enforced there is a significant worsening of the quality of the fits. This reinforces the contention that the local electronic and magnetic environment of a given octahedral ion is strongly influenced by local structural and electronic distortions making it impossible to simply divide sites based the CIS or TRANS classification of the idealized sites. In fact, the distortions caused by cation substitution and replacement of O^{2-} by OH^{-} have a stronger effect on the local environment than the arrangement of the unshared anion sites. As discussed previously in chapter 2 and chapter 6, even small amounts of cation substitutions can result in the distortion of a relatively large fraction of the [Fe^{2+}] sites. This large number of subtle variations in the nature of these distortions make it impossible to simply divide the [Fe^{2+}] sites into a finite number of classes. Rather, as with the high temperature fitting, the structural distortion can probably only be accounted for with a continuous distribution of fitting parameters.

While the form of the correct parameter distributions could not be derived from the fitting models presented in this work, there are three important features which are revealed by these models. Firstly, the LW broadening model is inadequate, pointing to a parameter distribution model as the agency of line-broadening. Further, the failure of the single Gaussian distribution models indicate that a more complex distribution is required if a single site is used. Secondly, the dominant symmetric site contribution indicates that between 65% and 80% of the sites have EFG parameters which are relatively close to an ideal undisturbed site.

Table 7.1a Room temperature Mössbauer fitting parameters for synthetic annite.

Site		δ_0 (mm/s)	δ_1	Δ_0 (mm/s)	σ_Δ (mm/s)	A
$[Fe^{2+}]$	1	1.244	-0.050	2.589	0.071	0.442
	2			2.310	0.183	0.380
	3			1.596	0.546	0.062
$[Fe^{3+}]$	1	0.428	0	0.949	0.475	0.083
$<Fe^{3+}>$	1	0.173	0	0.531	0.0001	0.031

The spectrum was fit using the Voigt-based method of Rancourt and Ping (1989). δ_0 and Δ_0 are the center values of δ and Δ, σ_Δ is the width of the Gaussians distribution of Δ, the linear coupling δ-Δ coupling parameter is δ_1, and A is the relative are of each pattern in the total spectrum. For all patterns the Lorentzian full width (Γ) was 0.2858 mm/s (reproduced from Rancourt *et al.*, 1994).

Table 7.1b Liquid nitrogen temperature Mössbauer fitting parameters for synthetic annite.

Site		δ_0 (mm/s)	δ_1	Δ_0 (mm/s)	σ_Δ (mm/s)	A
$[Fe^{2+}]$	1	1.208	+0.016	3.010	0.138	0.477
	2			2.783	0.223	0.347
	3			2.390	1.625	0.065
$[Fe^{3+}]$	1	0.629	0	0.657	0.364	0.072
$<Fe^{3+}>$	1	0.374	0	0.466	0.0001	0.038

The spectrum was fit using the Voigt-based method of Rancourt and Ping (1989). δ_0 and Δ_0 are the center values of δ and Δ, σ_Δ is the width of the Gaussians distribution of Δ, the linear coupling δ-Δ coupling parameter is δ_1, and A is the relative are of each pattern in the total spectrum. For all patterns the Lorentzian full width (Γ) was 0.2104.

Table 7.2 Values of SOD at RT, LNT, and LHT for four values of θ_D.

Experimental Temp (K)	**θ_D = 250K (mm/s)**	**θ_D = 300K (mm/s)**	**θ_D = 350K (mm/s)**	**θ_D = 450K (mm/s)**
RT	-0.22	-0.22	-0.23	-0.24
LNT	-0.08	-0.09	-0.10	-0.13
LHT	-0.07	-0.08	-0.09	-0.12

Table 7.3 Constraint on ε in terms of Δ for LHT Fe^{3+} sites.

	θ	ϕ	$\varepsilon_{0.2}$	$\varepsilon_{0.5}$
$[Fe^{3+}]$	90	0	-0.060 Δ	-0.0005 Δ
	90	90	-0.139 Δ	–0.199 Δ
$<Fe^{3+}>$	0	0	0.497 Δ	0.480 Δ

The constraint on ε is determined by the constraints on the quadrupole splitting (Δ) and equation 6.7. The two columns of values of ε are determined from this equation assuming values of η =0.2, and η =0.5 respectively. Since the value of ϕ is not known, the two values are shown for $[Fe^{3+}]$ to give the minimum and maximum limits of equation 6.7.

Table 7.4 Fitting parameters for fits to Fe^{3+} contributionsto the 7K Mössbauer spectrum of synthetic annite.

Fit	Site		$g^*\mu_N H$ (mm/s)	σ_H (mm/s)	ε_Q (mm/s)	δ_Q (mm/s)	A/A_{tot} (%)
1-2	$[Fe^{3+}]$	1	3.070	0.095	0.119	0.25	7.0
	$\langle Fe^{3+} \rangle$	1	3.50	0.176	0.233	0.20	3.3
		2	3.68	0.027	0.233	0.20	1.1
2-2	$[Fe^{3+}]$	1	3.07	0.049	0.171	0.24	3.5
		2	3.30	0.269	0.171	0.24	4.0
	$\langle Fe^{3+} \rangle$	1	3.40	0.379	0.312	0.17	2.5
		2	3.68	0.021	0.312	0.17	1.0

The spectral contributions were fit using the Voigt based methods of Rancourt and Ping (1989). σ_H is the Gaussians width of the distribution of $g^*\mu_N H$. ε_Q is the shift introduced by the quadrupole splitting (Δ) as determined by equation 6.4. δ_Q is the center shift. A/A_{tot} is the spectral area of each pattern as a fraction of the total spectral area. Throughout the fitting process the line width, Γ was fixed at 0.2 mm/s and the line intensity ratios were fixed at 3:2:1.

Table 7.5 Descriptions of site models used in fitting 7K Mössbauer spectrum of synthetic annite.

Model	Description	Remarks
A1	Single Symmetric Site	η=0, Represents idealized compressed octahedral site. No distinctions between CIS and TRANS arrangements of OH^- groups. Use TRANS model of EFG axes.
A2	Single Asymmetric Site	Same as A1 model but allow η>0.
B1	Two Sites	TRANS and CIS^1 site models
B2	Two Sites	TRANS and CIS^2 site models
B3	Two Sites	TRANS and CIS^3 site models
B4	Two Sites	TRANS and CIS^4 site models
B5	Two Sites	TRANS and CIS^5 site models

One of these site models is combined with a line broadening model (table 7.7) to specify a complete fitting model. The complete specifications of the TRANS and CIS^i sites are found in table 7.7.

Table 7.6 Line broadening models used in fitting 7K Mössbauer spectrum of synthetic annite.

Model	Description	Remarks
LW	Line-Width Broadening	No Distributions. Single value of all parameters for each site. Line Broadening through the value of the Lorentzian line-width Γ only.
DD	Dependent Distribution Broadening	Line Broadening accomplished with distributions of Δ and $g^*\mu_N H$. Distribution of $g^*\mu_N H$ is dependent of Δ according to equation 7.3.
ID	Independent Distribution Broadening	Line Broadening accomplished with independent distributions of Δ and $g^*\mu_N H$.

One of these models is combined with one of the site models in table 7.5 to specify a complete fitting model.

Table 7.7a Relation of hyperfine field (**H**) and EFG principal axes (V_{xx}, V_{yy}, and V_{zz}) to crystalline axes (**a**, **b**, and **c**); resulting angles of hyperfine field in EFG tensor coordinate system, and sign of e^2qQ for TRANS site and for CIS[1] sites. "Case" refers to the angle case as shown in figure 7.13. H is the direction of the hyperfine field in the ab plane, with reference to either the **a** or **b** axes. V_{xx}, V_{yy} and V_{zz} are the orientations of the EFG axes in terms of the crystalline axes. θ and ϕ are the resulting polar and azimuthal angles in the EFG coordinate system.

Case	H	V_{xx}	V_{yy}	V_{zz}	θ	ϕ	e^2qQ
a.	**b**	**a**	**b**	$\mathbf{c}^*$	90	90	<0
b.	**a**+60	**a**	**b**	$\mathbf{c}^*$	90	60	<0
	a+120	**a**	**b**	$\mathbf{c}^*$	90	120	<0
c.	**a**+30	**a**	**b**	$\mathbf{c}^*$	90	30	<0
	a+150	**a**	**b**	$\mathbf{c}^*$	90	150	<0
d.	**a**	**a**	**b**	$\mathbf{c}^*$	90	0	<0

Note that for cases (b) and (c) there are two lines because there are two directions which are equivalent crystallographically but distinct in terms of Mössbauer parameters.

Table 7.7b Relation of hyperfine field (**H**) and EFG principal axes (V_{xx}, V_{yy}, and V_{zz}) to crystalline axes (**a**, **b**, and **c**); resulting angles of hyperfine field in EFG tensor coordinate system, and sign of e^2qQ for CIS^2 site.

Case	H	V_{xx}	V_{yy}	V_{zz}	θ	ϕ	e^2qQ
a.	**b**	**-c***	**b**	**a**	90	90	<0
b.	**a**+60	**-c***	**b**	**a**	90	60	<0
	a+120	**-c***	**b**	**a**	90	120	<0
c.	**a**+30	**-c***	**b**	**a**	90	30	<0
	a+150	**-c***	**b**	**a**	90	150	<0
d.	**a**	**-c***	**b**	**a**	90	0	<0

Table 7.7c Relation of hyperfine field (**H**) and EFG principal axes (V_{xx}, V_{yy}, and V_{zz}) to crystalline axes (**a**, **b**, and **c**); resulting angles of hyperfine field in EFG tensor coordinate system, and sign of e^2qQ for CIS^3 site.

Case	H	V_{xx}	V_{yy}	V_{zz}	θ	ϕ	e^2qQ
a.	**b**	**-c***	**b**	**a**	90	90	>0
b.	**a**+60	**-c***	**b**	**a**	90	60	>0
	a+120	**-c***	**b**	**a**	90	120	>0
c.	**a**+30	**-c***	**b**	**a**	90	30	>0
	a+150	**-c***	**b**	**a**	90	150	>0
d.	**a**	**-c***	**b**	**a**	90	0	>0

Table 7.7d Relation of hyperfine field (**H**) and EFG principal axes (V_{xx}, V_{yy}, and V_{zz}) to crystalline axes (**a**, **b**, and **c**); resulting angles of hyperfine field in EFG tensor coordinate system, and sign of e^2qQ for CIS^4 site.

Case	H	V_{xx}	V_{yy}	V_{zz}	θ	ϕ	e^2qQ
a.	**b**	**b**	**c***	**a**	90	0	<0
b.	**a**+60	**b**	**c***	**a**	60	0	<0
	a+120	**b**	**c***	**a**	120	0	<0
c.	**a**+30	**b**	**c***	**a**	30	0	<0
	a+150	**b**	**c***	**a**	150	0	<0
d.	**a**	**b**	**c***	**a**	0	0	<0

Note that CIS^2 case-d is degenerate with CIS^4 case-d

Table 7.7e Relation of hyperfine field (**H**) and EFG principal axes (V_{xx}, V_{yy}, and V_{zz}) to crystalline axes (**a**, **b**, and **c**); resulting angles of hyperfine field in EFG tensor coordinate system, and sign of e^2qQ for CIS^5 site.

Case	H	V_{xx}	V_{yy}	V_{zz}	θ	ϕ	e^2qQ
a.	**b**	**b**	**c***	**a**	90	0	>0
b.	**a**+60	**b**	**c***	**a**	60	0	>0
	a+120	**b**	**c***	**a**	120	0	>0
c.	**a**+30	**b**	**c***	**a**	30	0	>0
	a+150	**b**	**c***	**a**	150	0	>0
d.	**a**	**b**	**c***	**a**	0	0	>0

Note that CIS^3 case-d is degenerate with CIS^5 case-d.

Table 7.8 Fitting parameters for single site models. All fits used the line-width distribution broadening model. η is the EFG asymmetry parameter, θ and ϕ are the polar and azimuthal angles between the EFG principal axis and the hyperfine field direction. δ is the center shift, Γ is the Lorentzian full width, Δ is the quadrupole splitting, $g^*\mu_N H$ is the hyperfine splitting parameter and $\overline{\chi}^2$ is the reduced chi squared.

Model	η	θ	ϕ	δ (mm/s)	$\frac{1}{2}\Gamma$ (mm/s)	Δ (mm/s)	$g^*\mu_N H$ (mm/s)	$\overline{\chi}^2$
A1-LW $\Delta<0$	0.000	90	0	1.250	0.667	-2.800	1.114	24.8
A1-LW $\Delta>0$	0.000	90	0	1.350	0.750	3.050	1.349	132.4
A2(a) -LW	0.200	90	90	1.249	0.694	-2.800	1.079	28.0
A2(b)-LW	0.200	90	60	1.254	0.685	-2.800	1.112	28.1
A2(c)-LW	0.200	90	30	1.237	0.663	-2.800	1.102	27.3
A2(d)-LW	0.200	90	0	1.246	0.633	-2.800	1.127	24.2
A2(a)-LW	0.500	90	90	1.227	0.694	-3.050	1.011	33.8
A2(b)-LW	0.500	90	60	1.234	0.625	-3.050	1.040	25.7
A2(c)-LW	0.500	90	30	1.350	0.700	-2.800	1.042	54.6
A2(d)-LW	0.500	90	0	1.237	0.610	-2.800	1.147	31.5

Table 7.9 Parameters used in single site independent distribution broadening simulations. All parameters have the same meaning as table 7.8 and σ_H and σ_Δ are the Gaussian half-widths of the distributions of $g^*\mu_N H$ and Δ respectively.

Figure	η	θ	ϕ	$\frac{1}{2}\Gamma$ (mm/s)	$g^*\mu_N H$ (mm/s)	σ_H (mm/s)	Δ (mm/s)	σ_Δ (mm/s)
7.18(ii)	0	90	0	0.1	1.114	0.30	-2.8	0.2
(iii)	0	90	0	0.1	1.114	0.45	-2.8	0.2
(iv)	0	90	0	0.1	1.114	0.60	-2.8	0.2
7.19(ii)	0.2	90	90	0.1	1.114	0.30	-2.8	0.2
(iii)	0.2	90	90	0.1	1.114	0.45	-2.8	0.2
(iv)	0.2	90	90	0.1	1.114	0.60	-2.8	0.2

Table 7.10 Parameters of best possible fit using the single asymmetric site with independent distribution broadening. All parameters have the same meanings as tables 7.9 and 7.10.

Model	η	θ	ϕ	δ (mm/s)	$\frac{1}{2}\Gamma$ (mm/s)	Δ (mm/s)	σ_Δ (mm/s)	$g^*\mu_N H$ (mm/s)	σ_H (mm/s)	χ^2
A2-DD (d)	0.5	90	0	1.29	0.1	–2.80	0.2	1.2	0.489	37.4

Table 7.11 Fitting parameters for two-site line width broadening models. Model refers to the site model used in the fit including the angle case. For descriptions of the models refer to table 7.5. In each fit site 1 is the TRANS site and site 2 is CIS site. The remaining parameters are as in table 7.8 except Δ_{avg} and $g^*\mu_N H_{avg}$ which are the mean values of Δ and $g^*\mu_N H$ respectively and A_{rel} which is the relative area of each site.

Fit	Site	η	θ	ϕ	½Γ (mm/s)	δ (mm/s)	Δ (mm/s)	Δ avg	$g^*\mu_N H$ (mm/s)	$g^*\mu_N H$ Avg	A_{rel}	$\overline{\chi}^2$
B1 (a)	1	1.000	90	90	0.262	1.200	-3.050		0.779		0.26	
	2	0.000	90	90	0.677	1.260	-2.800	-2.864	1.257	1.135	0.74	16.4
B1 (b)	1	0.000	90	60	0.650	1.200	-3.050		1.195		0.74	
	2	0.886	90	60	0.266	1.200	-2.800	-2.984	0.850	1.104	0.26	17.6
B1 (c)	1	0.950	90	30	0.450	1.200	-3.050		1.455		0.33	
	2	0.408	90	30	0.457	1.200	-2.800	-2.882	1.037	1.173	0.67	17.6
B1 (d)	1	0.650	90	0	0.367	1.200	-3.050		1.555		0.28	
	2	0.000	90	0	0.520	1.230	-2.800	-2.870	1.025	1.173	0.72	13.0
B2 (a)	1	0.330	90	90	0.608	1.250	-2.800		1.291		0.70	
	2	1.000	90	90	0.279	1.200	-3.050	-2.874	0.787	1.142	0.30	12.4
B2 (b)	1	0.400	90	60	0.626	1.250	-2.800		1.217		0.75	
	2	1.000	60	90	0.313	1.260	-2.800	-2.800	0.811	1.116	0.25	11.8
B2 (c)	1	0.579	90	30	0.518	1.261	-3.024		1.063		0.85	
	2	1.000	30	90	0.299	1.200	-3.050	-3.028	1.001	1.053	0.15	19.2
B2 (d)	1	0.000	90	0	0.635	1.270	-2.810		1.126		0.92	
	2	0.000	0	90	0.155	1.320	-2.800	-2.809	1.223	1.133	0.08	19.2
B3 (a)	1	0.060	90	90	0.611	1.275	-2.800		1.135		0.92	
	2	1.000	90	90	0.421	1.350	2.800	-2.367	1.455	1.160	0.08	23.2
B3 (b)	1	0.000	90	60	0.586	1.250	-2.950		1.105		0.86	
	2	0.000	60	90	0.626	1.250	2.950	-2.106	1.276	1.129	0.14	24.0
B3 (c)	1	0.000	90	30	0.669	1.205	-2.800		1.236		0.75	
	2	0.000	30	90	0.289	1.327	2.900	-1.384	0.761	1.118	0.25	11.0
B3 (d)	1	0.198	90	0	0.657	1.230	-2.800		1.208		0.83	
	2	0.000	0	90	0.463	1.350	2.800	-1.830	0.699	1.119	0.17	11.2
B4 (a)	1	0.000	90	90	0.521	1.230	-2.800		1.026		0.72	
	2	0.650	90	0	0.361	1.200	-3.050	-2.869	1.560	1.173	0.28	13.2
B4 (b)	1	0.000	90	60	0.606	1.310	-2.800		1.146		0.84	
	2	0.000	60	0	0.272	1.200	-2.800	-2.800	0.982	1.119	0.16	20.8
B4 (c)	1	0.000	90	30	0.608	1.270	-2.800		1.130		0.91	
	2	0.650	30	0	0.224	1.200	-3.020	-2.820	1.084	1.126	0.09	21.4
B4 (d)	1	0.000	90	0	0.635	1.270	-2.810		1.126		0.92	
	2	0.000	0	0	0.155	1.320	-2.800	-2.809	1.223	1.133	0.08	19.2
B5 (a)	1	0.020	90	90	0.556	1.210	-2.800		1.059		0.76	
	2	1.000	90	0	0.272	1.200	3.050	-1.413	1.601	1.188	0.24	15.6
B5 (b)	1	0.000	90	60	0.645	1.250	-2.950		1.105		0.88	
	2	1.000	60	0	0.286	1.250	2.950	-2.261	1.047	1.098	0.12	17.2
B5 (c)	1	0.000	90	30	0.665	1.210	-2.800		1.237		0.75	
	2	0.000	30	0	0.283	1.330	2.800	-1.416	0.771	1.122	0.25	11.0
B5 (d)	1	0.000	90	0	0.657	1.230	-2.800		1.208		0.83	
	2	0.000	0	0	0.463	1.350	2.800	-1.830	0.699	1.119	0.17	11.2

Table 7.12 Fitting parameters for two-site line width broadening models with TRANS:CIS ratio fixed at 1:2. All parameters have the same meanings as in Table 7.11

Fit	Site	η	θ	ϕ	$\frac{1}{2}\Gamma$ (mm/s)	δ (mm/s)	Δ (mm/s)	Δ_{Avg}	$g^*\mu_N H$ (mm/s)	$g^*\mu_N H_{Avg}$	A_{rel}	$\overline{\chi}^2$
B1 (a)	1	0	90	90	0.477	1.32	-2.80		1.404		0.33	
	2	0.47	90	90	0.511	1.23	-3.05	-2.97	0.898	1.066	0.67	21.8
B1 (b)	1	0.000	90	60	0.506	1.26	-2.8		1.415		0.33	
	2	0.80	90	60	0.434	1.22	-3.05	-2.97	0.912	1.079	0.67	19.2
B1 (c)	1	0	90	30	0.376	1.2	-2.8		0.968		0.33	
	2	0.69	90	30	0.615	1.23	-2.86	-2.84	1.295	1.186	0.67	19.8
B1 (d)	1	0.000	90	0	0.369	1.208	-2.800		0.946		0.33	
	2	0.370	90	0	0.613	1.234	-2.800	-2.8	1.318	1.194	0.67	19
B2 (a)	1	0	90	90	0.573	1.26	-3.05		1.377		0.33	
	2	0.02	90	90	0.528	1.27	-2.8	-2.88	1.001	1.129	0.67	21.2
B2 (b)	1	0.61	90	60	0.426	1.20	-2.8		1.320		0.33	
	2	1.000	60	90	0.579	1.27	-2.99	-2.92	0.842	1.002	0.67	20.0
B2 (c)	1	0.33	90	30	0.614	1.25	-2.95		1.195		0.33	
	2	1.000	30	90	0.916	1.200	-2.95	-2.95	1.031	1.086	0.67	52
B2 (d)	1	0.000	90	0	0.256	1.27	-3.04		0.971		0.33	
	2	0.000	0	90	0.747	1.35	-2.80	-2.88	1.294	1.186	0.67	79.0
B3 (a)	1	0.000	90	90	0.262	1.25	-2.95		1.133		0.33	
	2	0.000	90	90	0.750	1.25	2.95	1.00	1.187	1.169	0.67	54.0
B3 (b)	1	0.000	90	60	0.268	1.25	-2.95		1.132		0.33	
	2	0.000	60	90	0.75	1.25	2.95	0.983	1.775	1.561	0.67	51.2
B3 (c)	1	0.000	90	30	0.441	1.25	-2.8		0.667		0.33	
	2	0.000	30	90	0.579	1.25	2.84	0.96	1.434	1.178	0.67	20.7
B3 (d)	1	0.198	90	0	0.427	1.25	-2.8		0.73		0.33	
	2	0.000	0	90	0.618	1.25	2.95	1.03	1.441	1.204	0.67	27.1
B4 (a)	1	0.000	90	90	0.369	1.21	-2.8		0.946		0.67	
	2	0.372	90	0	0.369	1.24	-2.8	-2.8	1.319	1.194	0.33	18.9
B4 (b)	1	0.000	90	60	0.334	1.25	-2.800		1.095		0.33	
	2	0.000	60	0	0.847	1.25	-2.95	-2.9	1.135	1.122	0.67	26.2
B4 (c)	1	0.08	90	30	0.352	1.25	-2.95		1.100		0.33	
	2	0.76	30	0	0.312	1.200	-2.95	-2.95	0.002	0.368	0.67	39.6
B4 (d)	1	0.651	90	0	0.256	1.27	-3.04		0.971		0.33	
	2	0.531	0	0	0.747	1.35	-2.80	-2.88	1.294	1.186	0.67	79.0
B5 (a)	1	0.020	90	90	0.354	1.25	-2.95		1.029		0.33	
	2	1.000	90	0	0.886	1.25	2.95	0.983	1.240	1.186	0.67	29.0
B5 (b)	1	0.000	90	60	0.329	1.35	-2.80		1.193		0.33	
	2	0.000	60	0	0.619	1.20	2.85	2.83	1.039	1.090	0.67	25.0
B5 (c)	1	0.000	90	30	0.472	1.25	-2.95		1.208		0.33	
	2	0.000	30	0	0.603	1.25	2.95	0.983	0.83	0.97	0.67	22.4
B5 (d)	1	0.000	90	0	0.427	1.25	-2.8		0.73		0.33	
	2	0.000	0	0	0.618	1.25	2.95	1.03	1.441	1.204	0.67	27.1

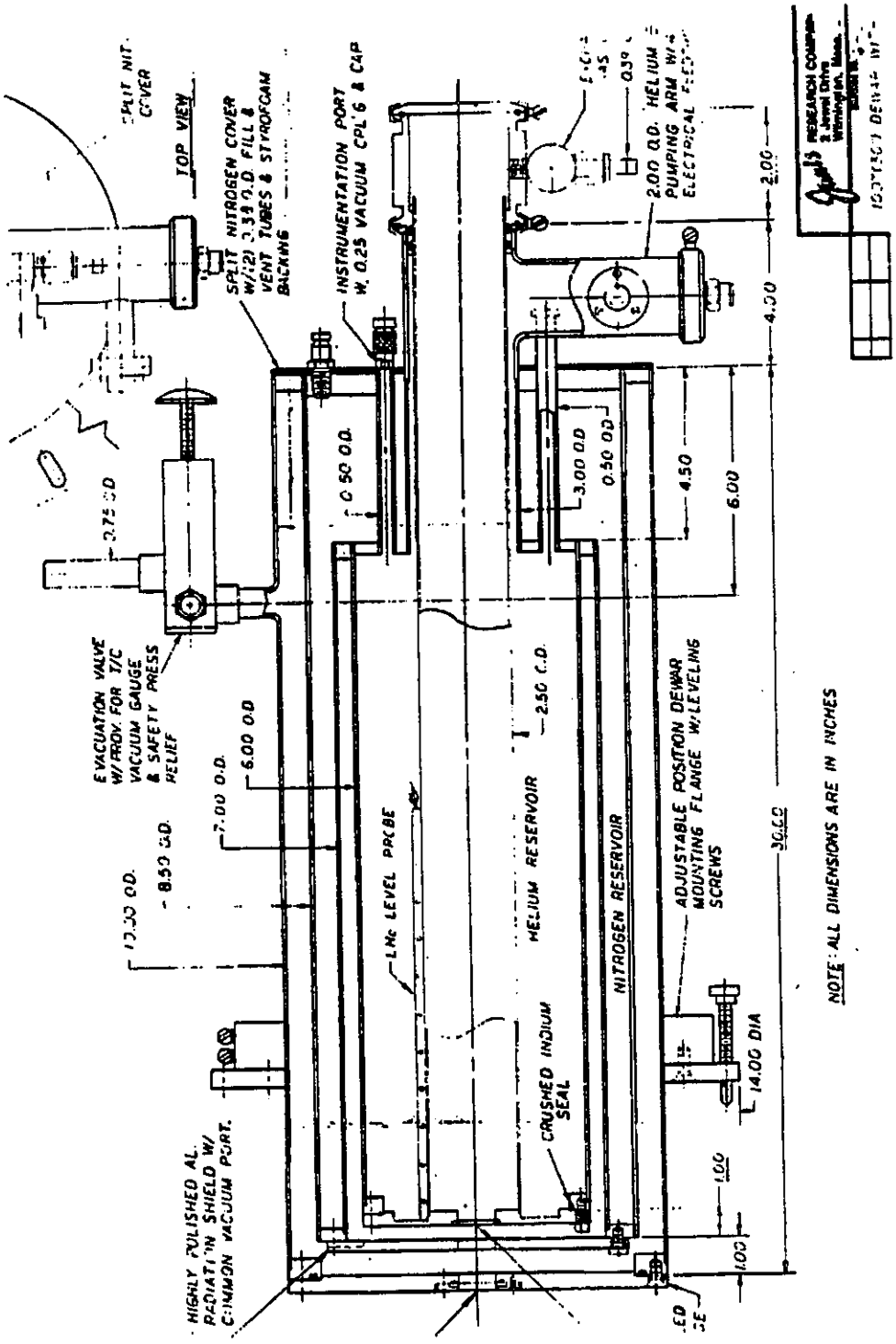

Figure 7.1a Blueprint of the Mössbauer cryostat.

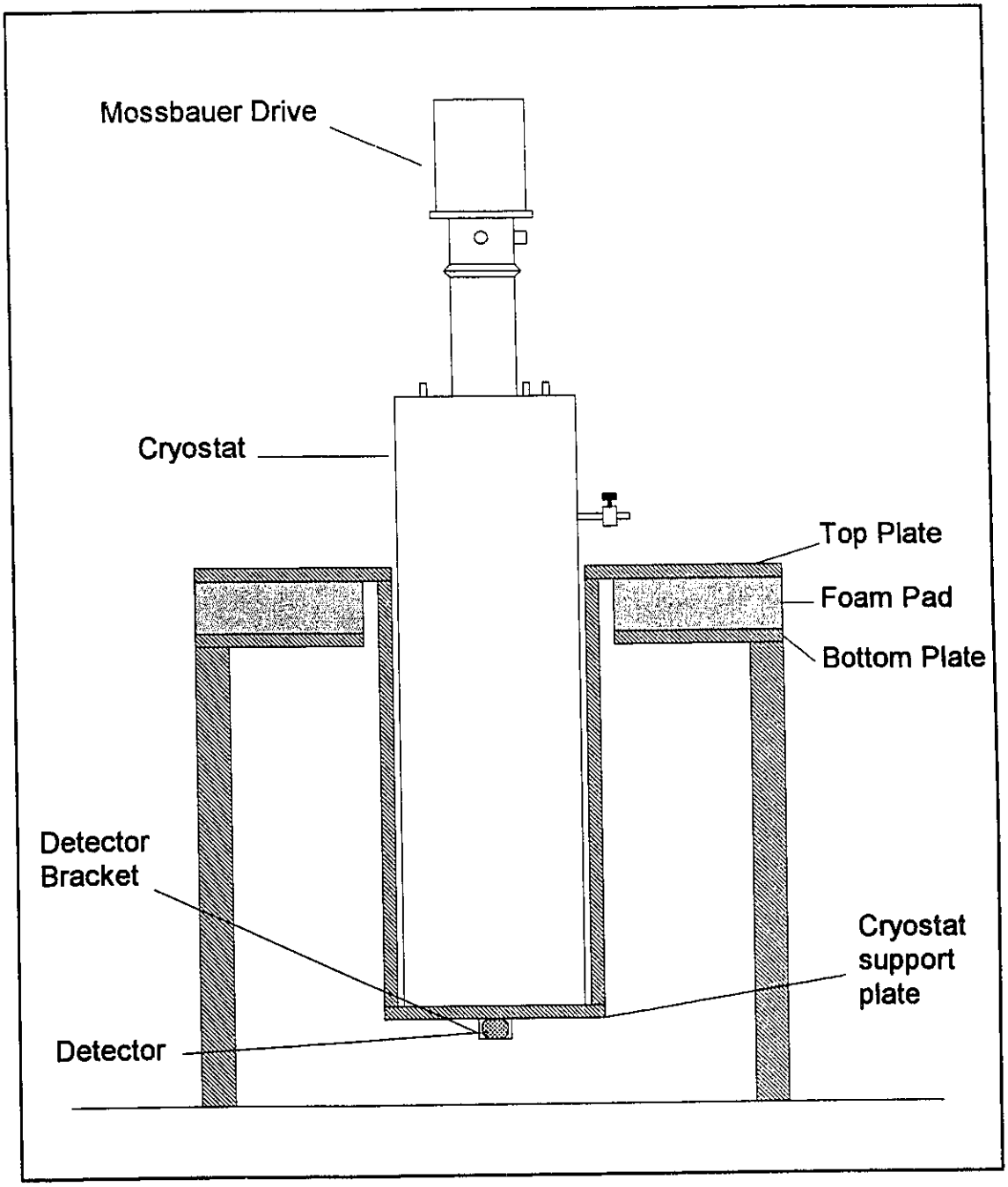

Figure 7.1b *Mössbauer Cryostat and Stand. The Janis 10Dt-Vt cryostat was supported by a custom designed stand which used an 4" foam pad for vibration isolation and incorporated a detector bracket to ensure alignment of the cryostat and detector windows. See Figure 7.2 for details of the spectrometer insert.*

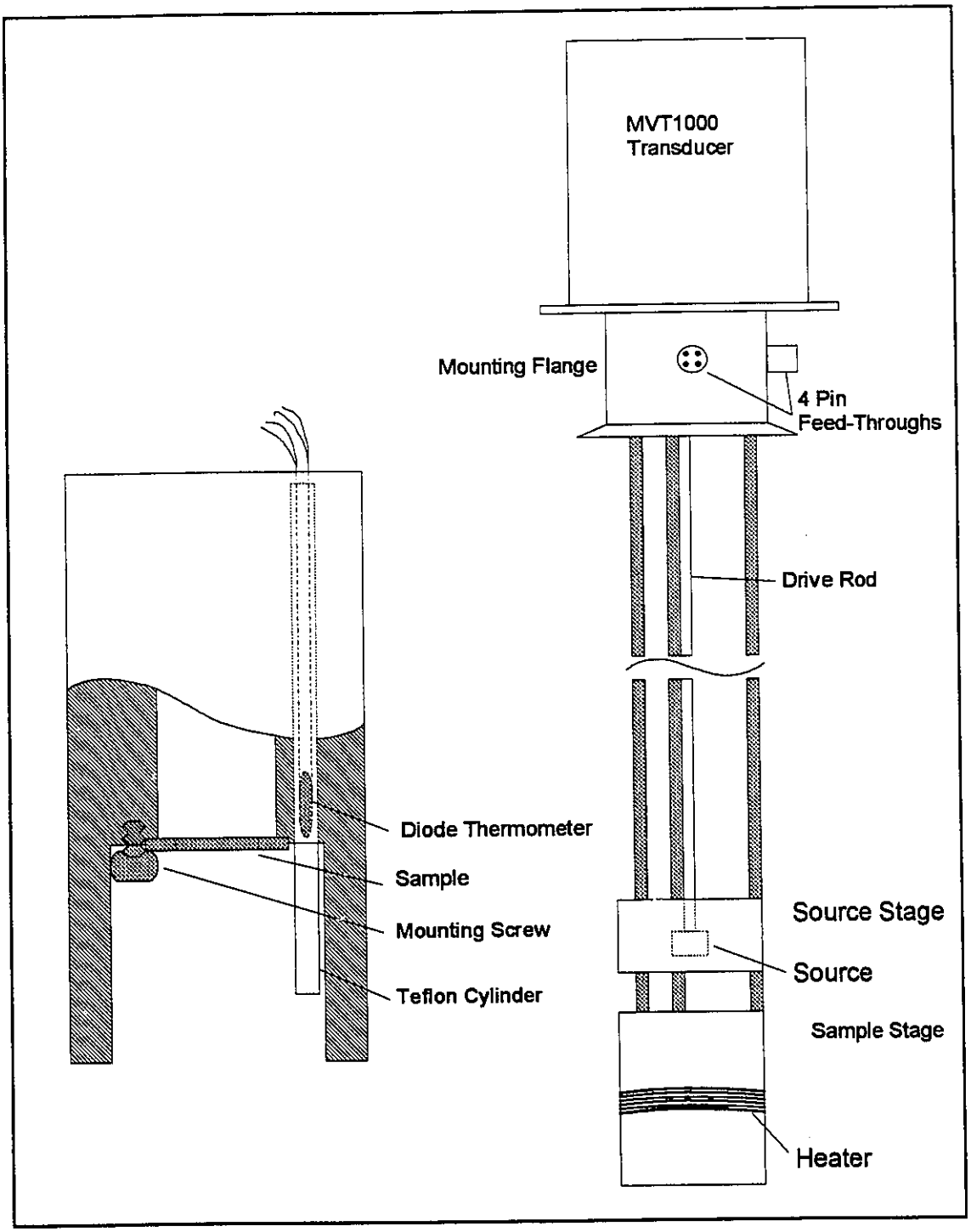

***Figure 7.2** Mössbauer Probe and Sample Stage. The Mössbauer probe consisted of three assemblies, the transducer, the source stage, and the sample stage. The assemblies were connected by three thin-walled stainless steel tubing legs. An expanded view of the sample stage is shown at left.*

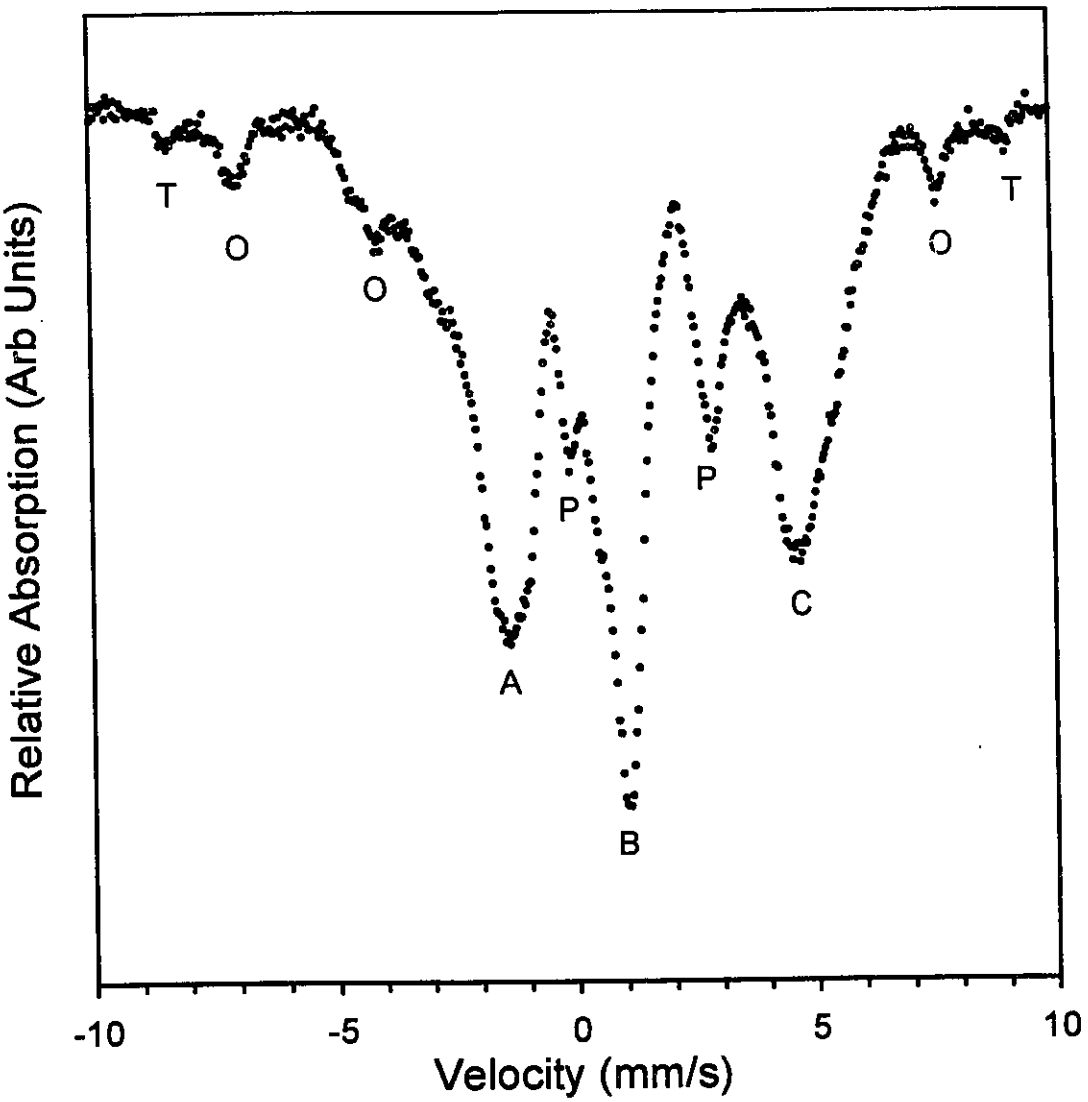

***Figure 7.3a** Mössbauer spectrum of synthetic annite at 7K. The T and O mark contributions attributed to ordered(Fe^{3+}) and [Fe^{3+}] respectively; P marks peaks from the paramagnetic [Fe^{2+}]; and A, B, and C mark contributions from ordered [Fe^{2+}].*

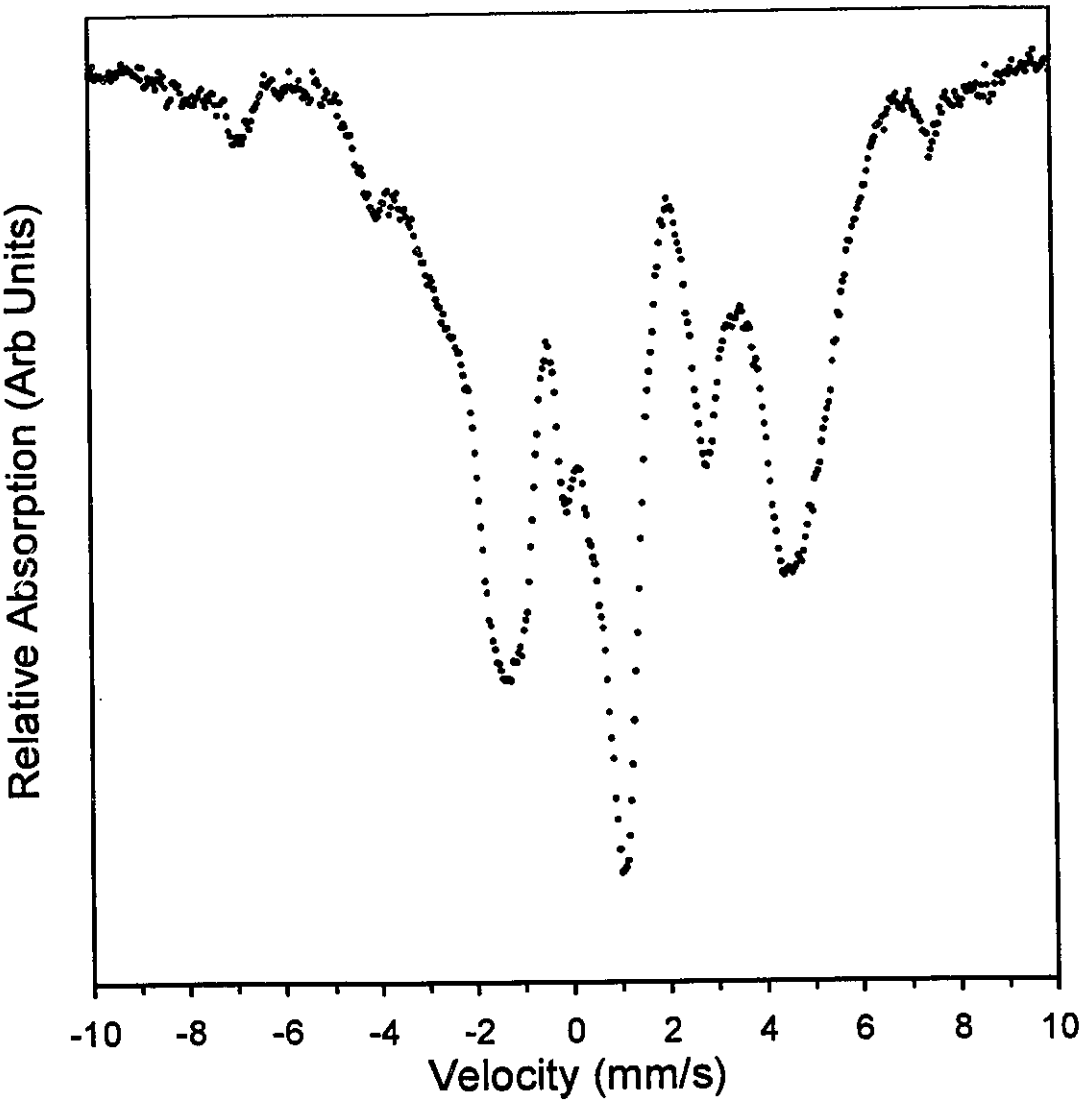

Figure 7.3b Mössbauer spectrum of synthetic annite at 15K.

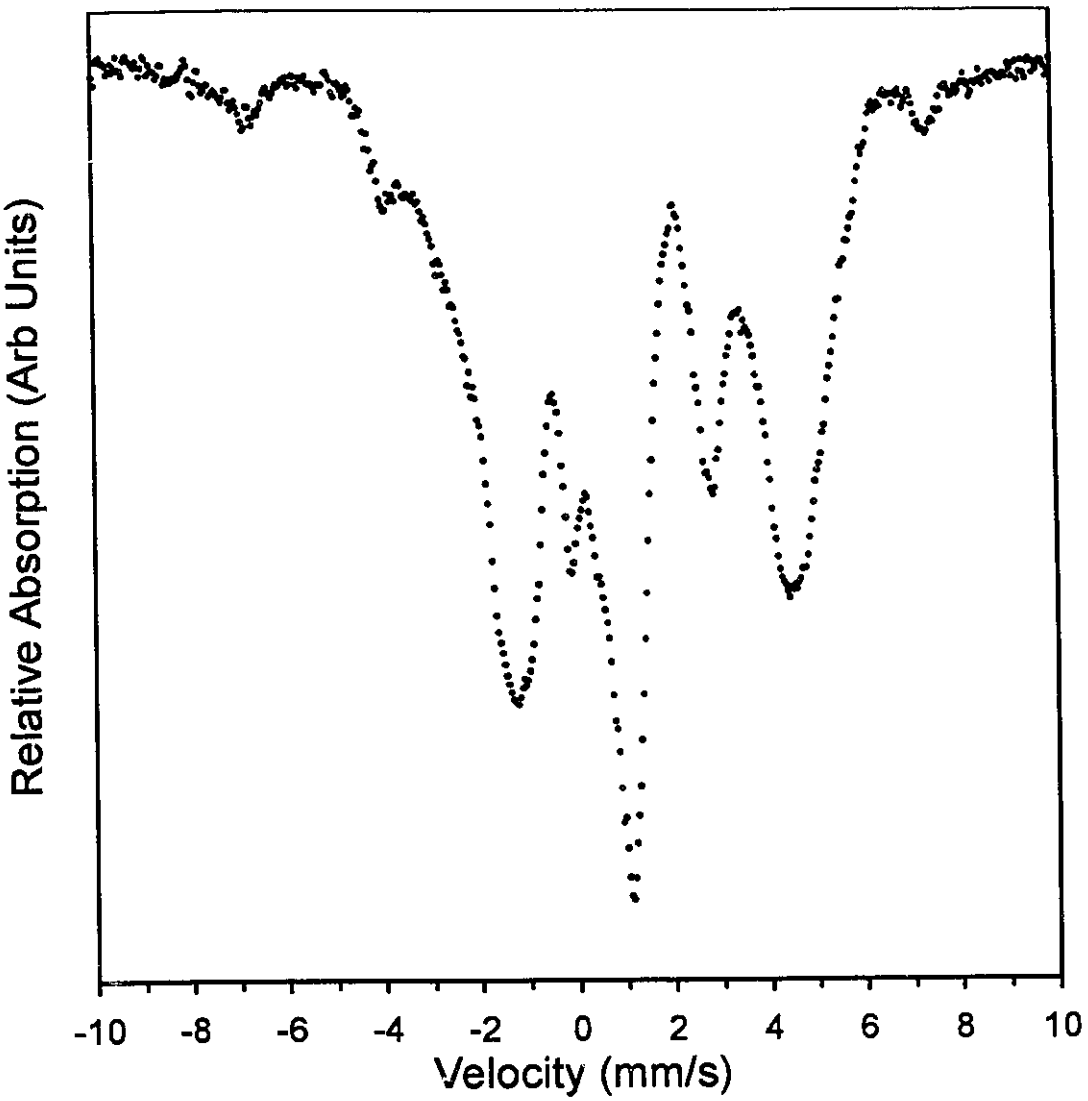

Figure 7.3c Mössbauer spectrum of synthetic annite at 25K.

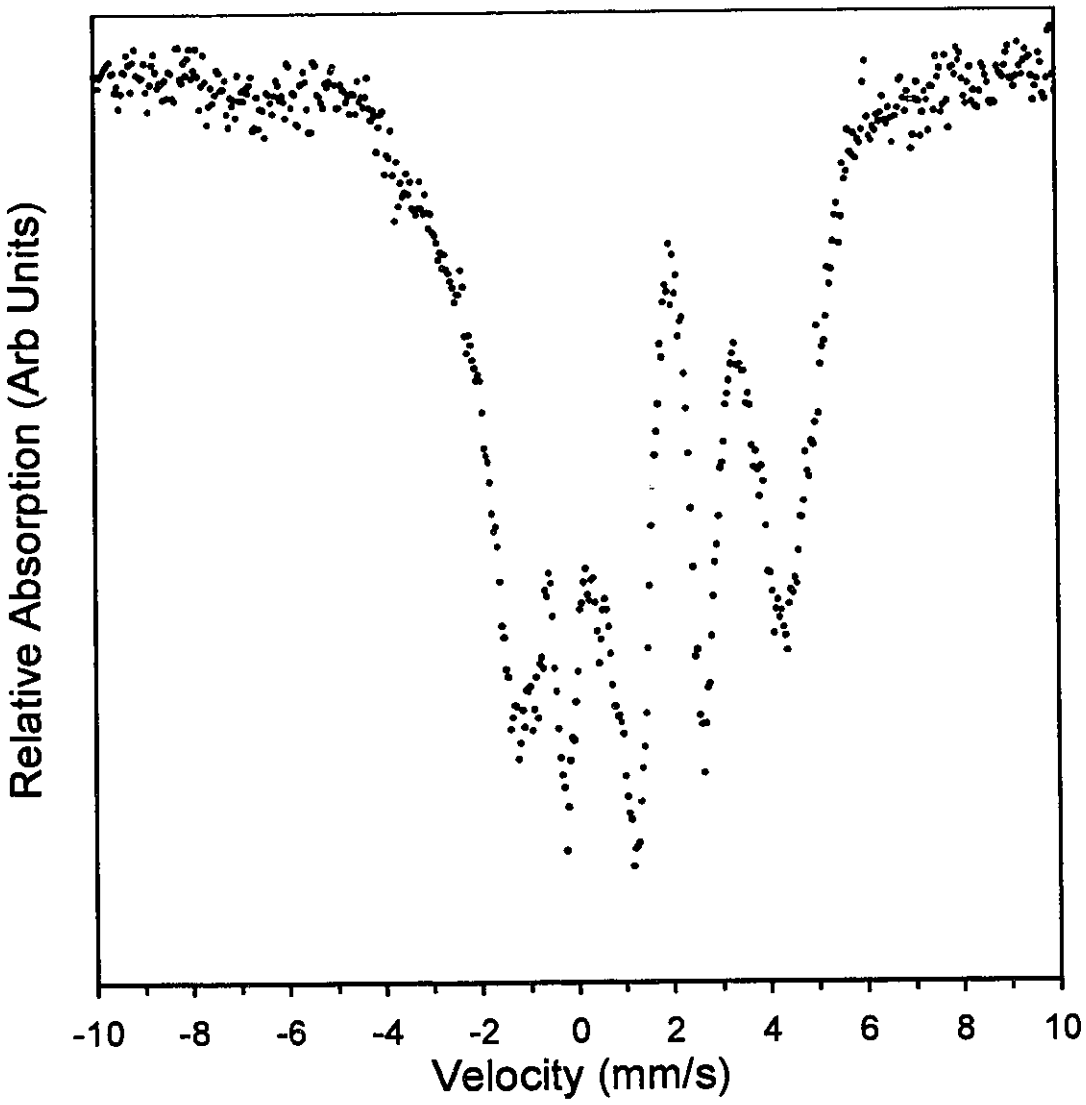

Figure 7.3d *Mössbauer spectrum of synthetic annite at 35K.*

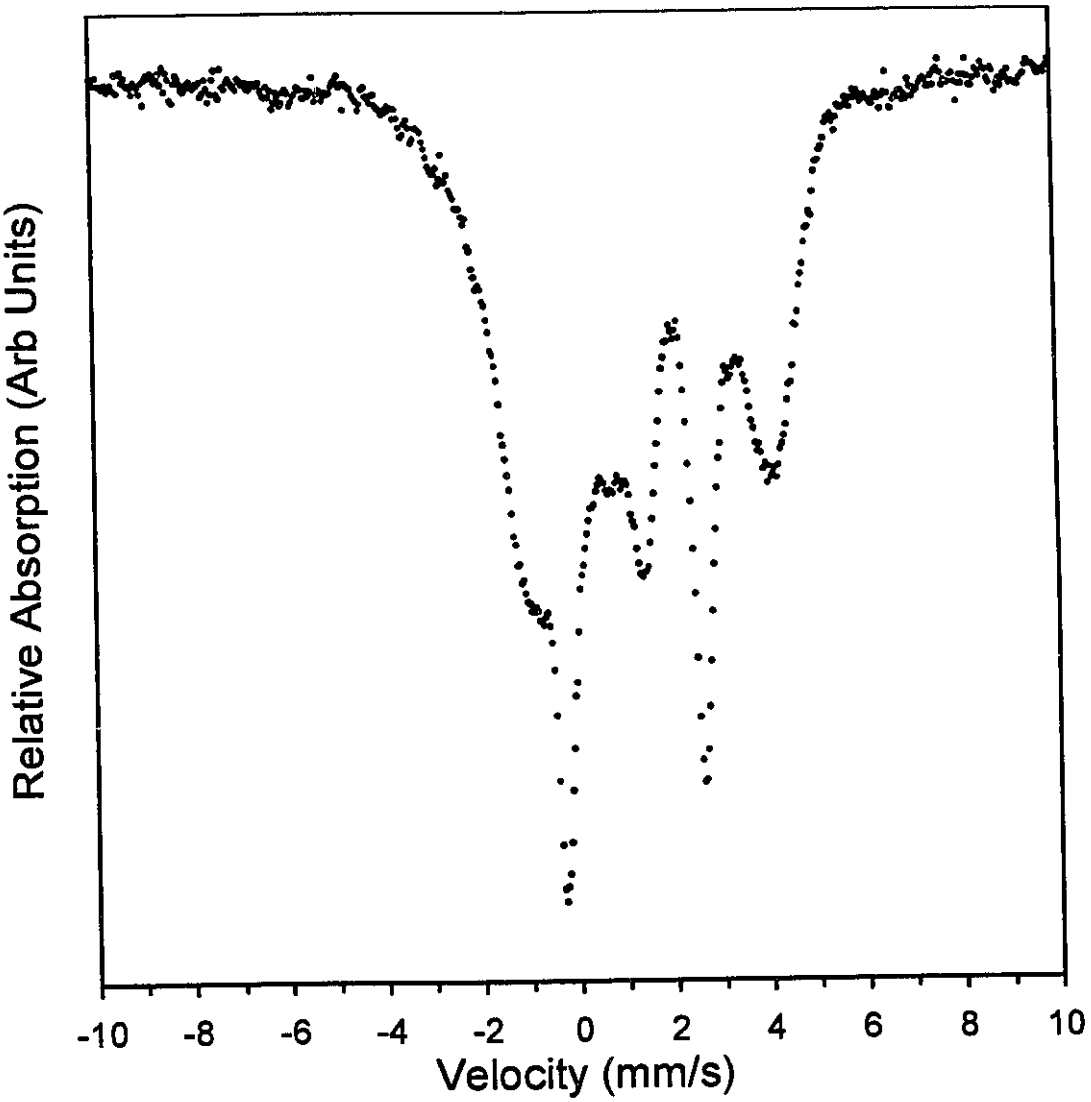

Figure 7.3e Mössbauer spectrum of synthetic annite at 45K

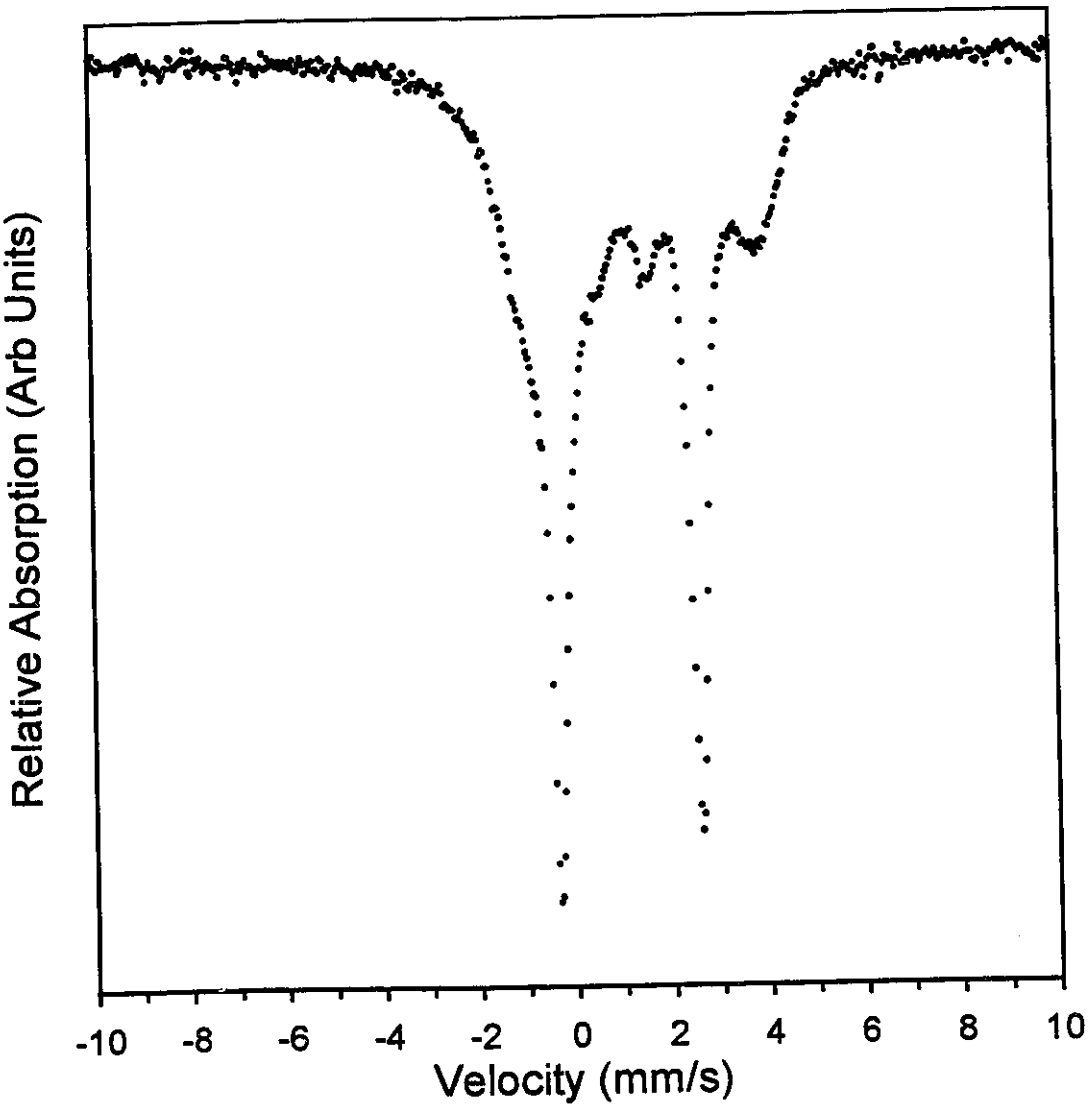

Figure 7.3f Mössbauer spectrum of synthetic annite at 50K.

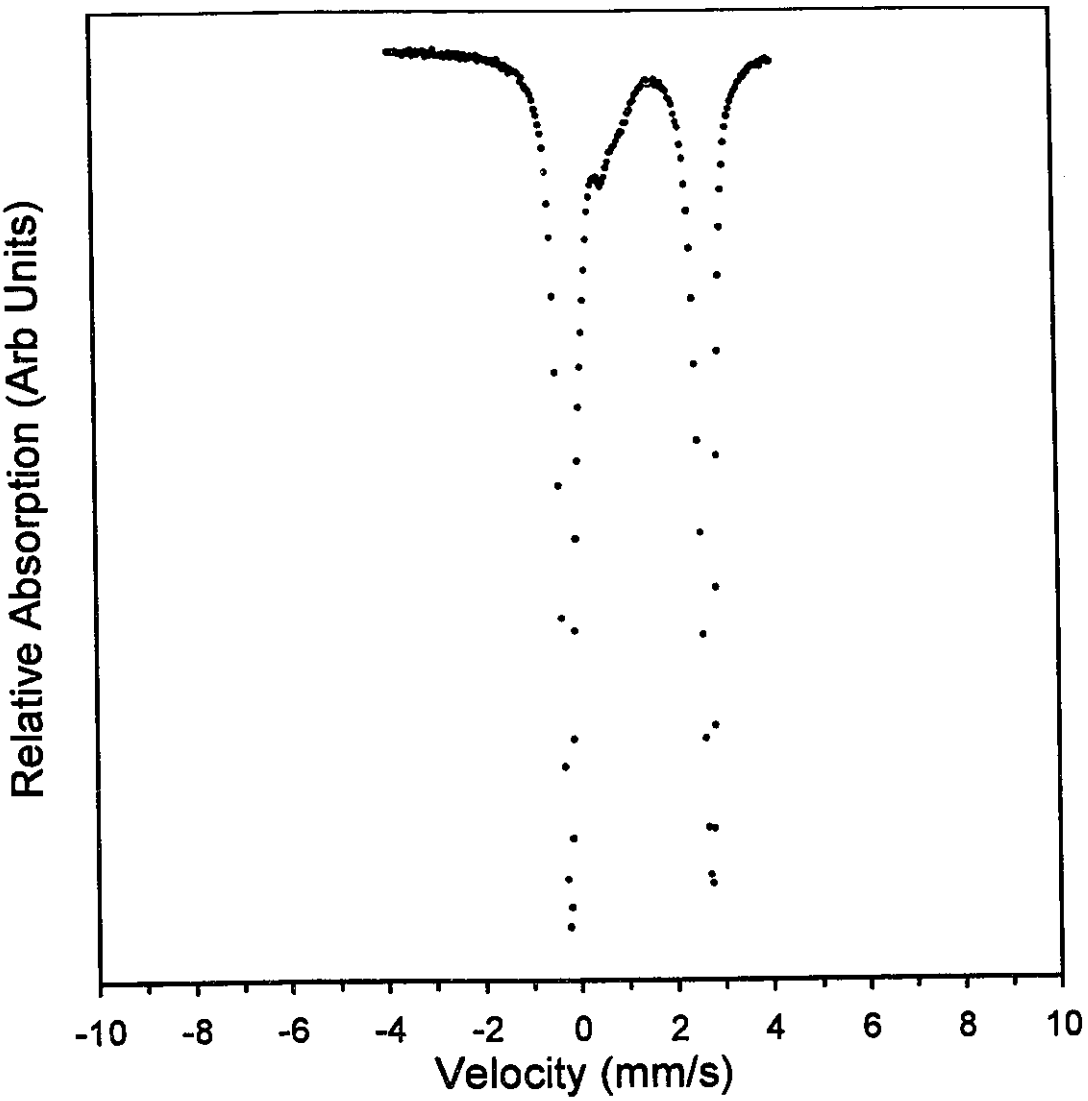

Figure 7.3g Mössbauer spectrum of synthetic annite at 83K.

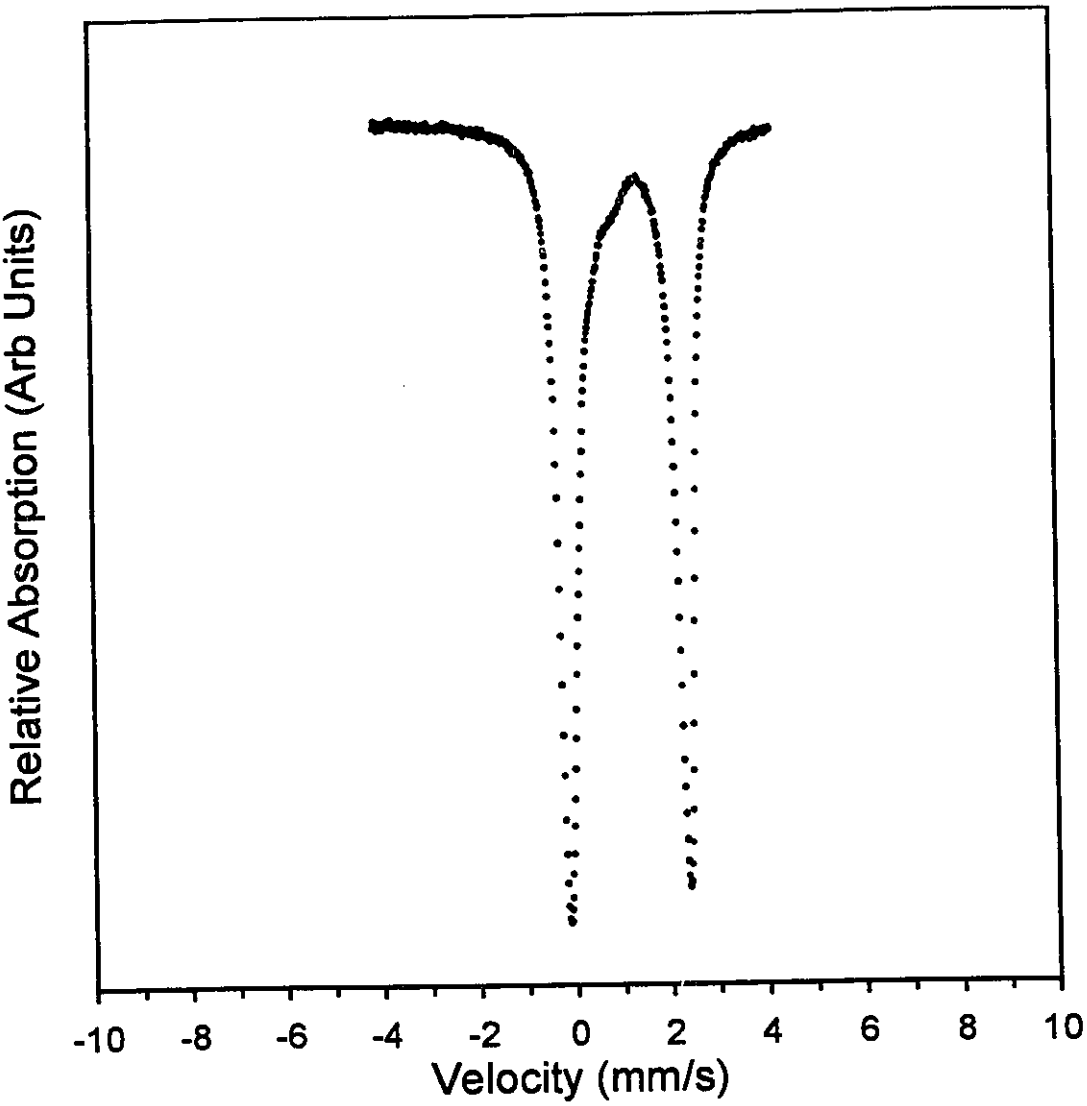

Figure 7.3h *Mössbauer spectrum of synthetic annite at 295K.*

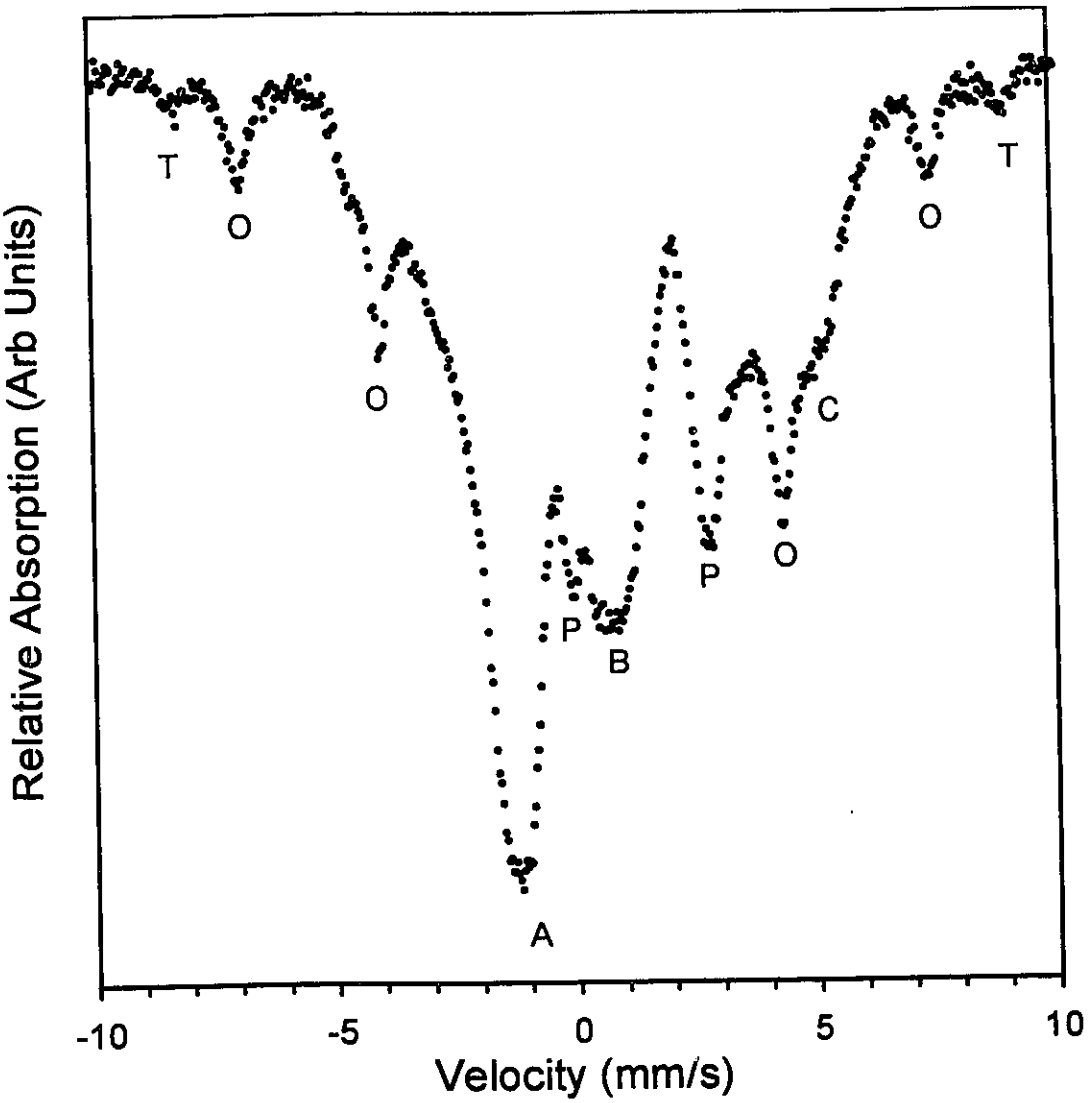

***Figure 7.4a** Mössbauer spectrum of natural annite at 4.2 K. The T and O mark contributions attributed to ordered $\langle Fe^{3+} \rangle$ and $[Fe^{3+}]$ respectively; P marks peaks from the paramagnetic $[Fe^{2+}]$; and A, B, and C mark contributions from ordered $[Fe^{2+}]$*

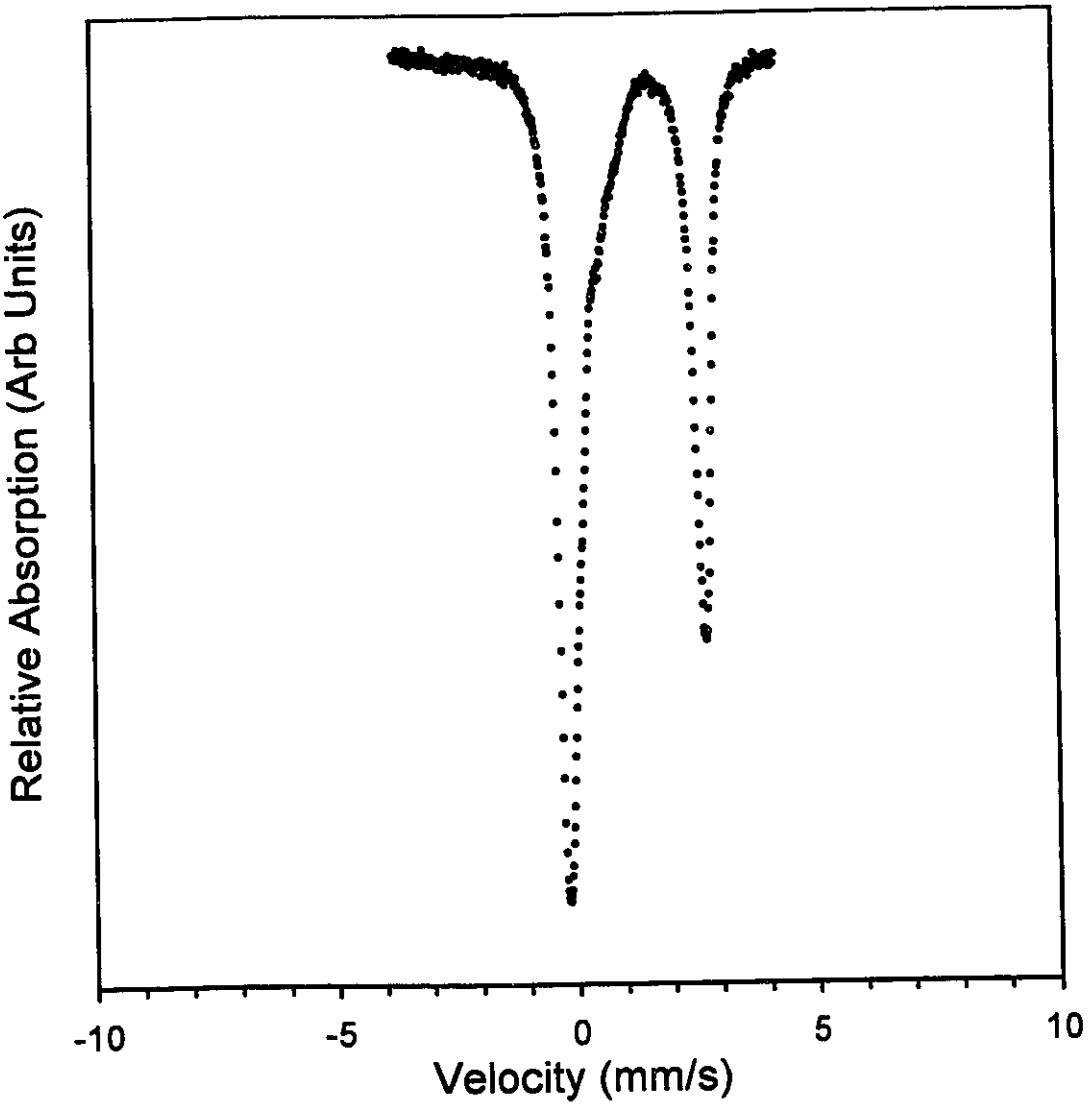

***Figure 7.4b** Mössbauer spectrum of natural annite at 83K.*

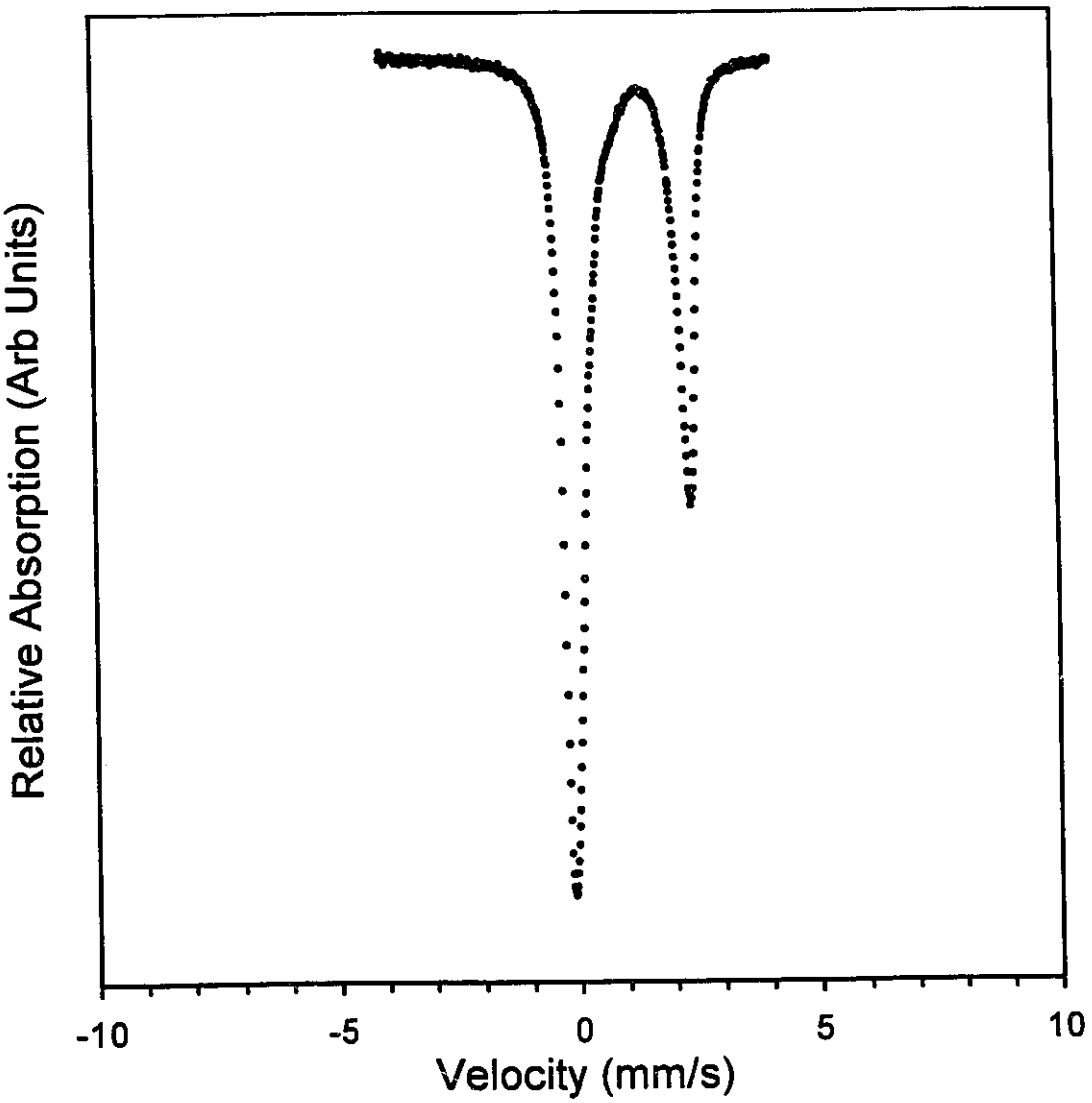

***Figure 7.4c** Mössbauer spectrum of natural annite at 295K.*

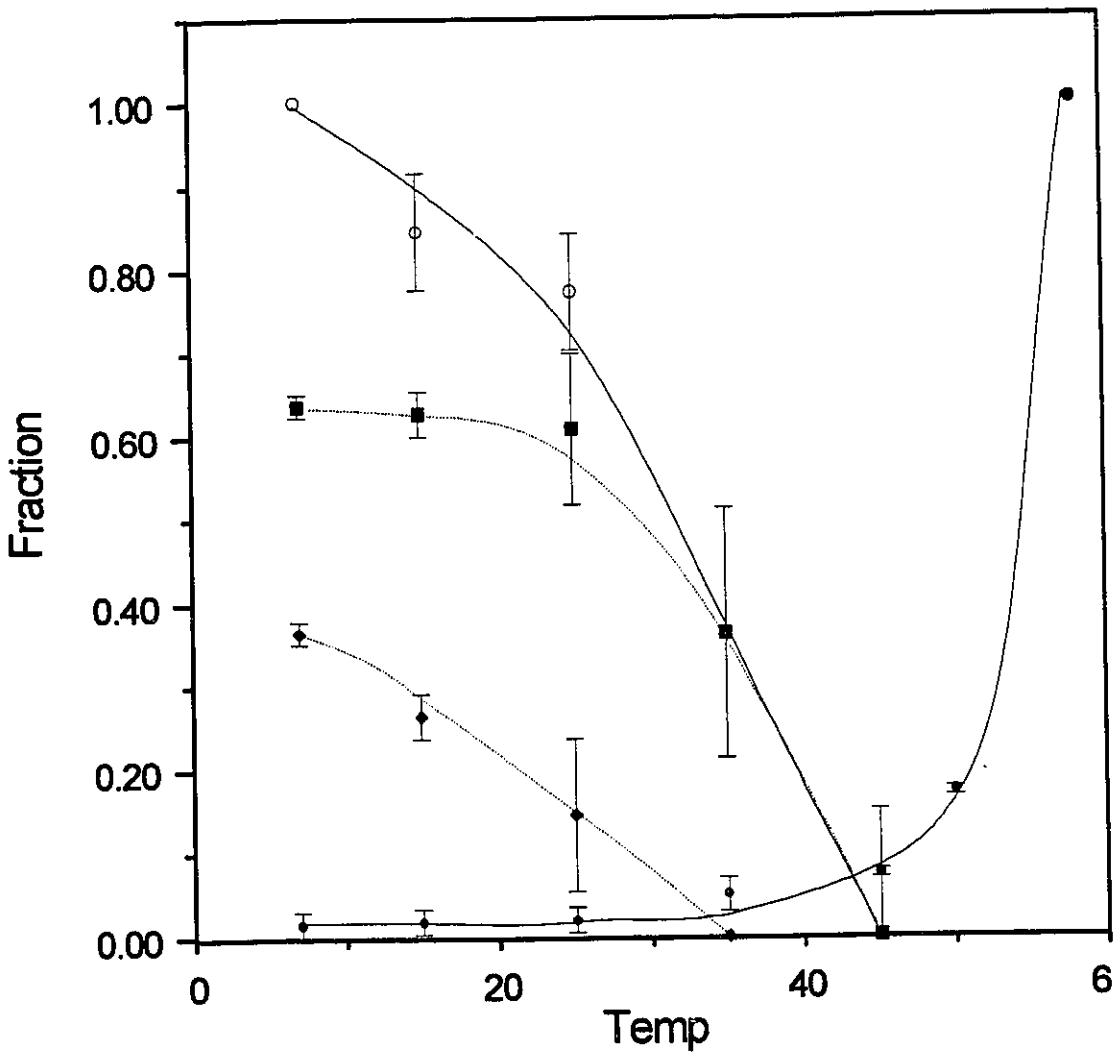

***Figure 7.5** The ratios of paramagnetic [Fe^{2+}] to total [Fe^{2+}](●), HFS ⟨Fe^{3+}⟩ to total Fe^{3+}(◆), HFS [Fe^{3+}]to total Fe^{3+} (■) and total HFS Fe^{3+} to total Fe^{3+} (○) as a function of temperature for synthetic annite. The lines in the figure are not fits, they are guides to the eye.*

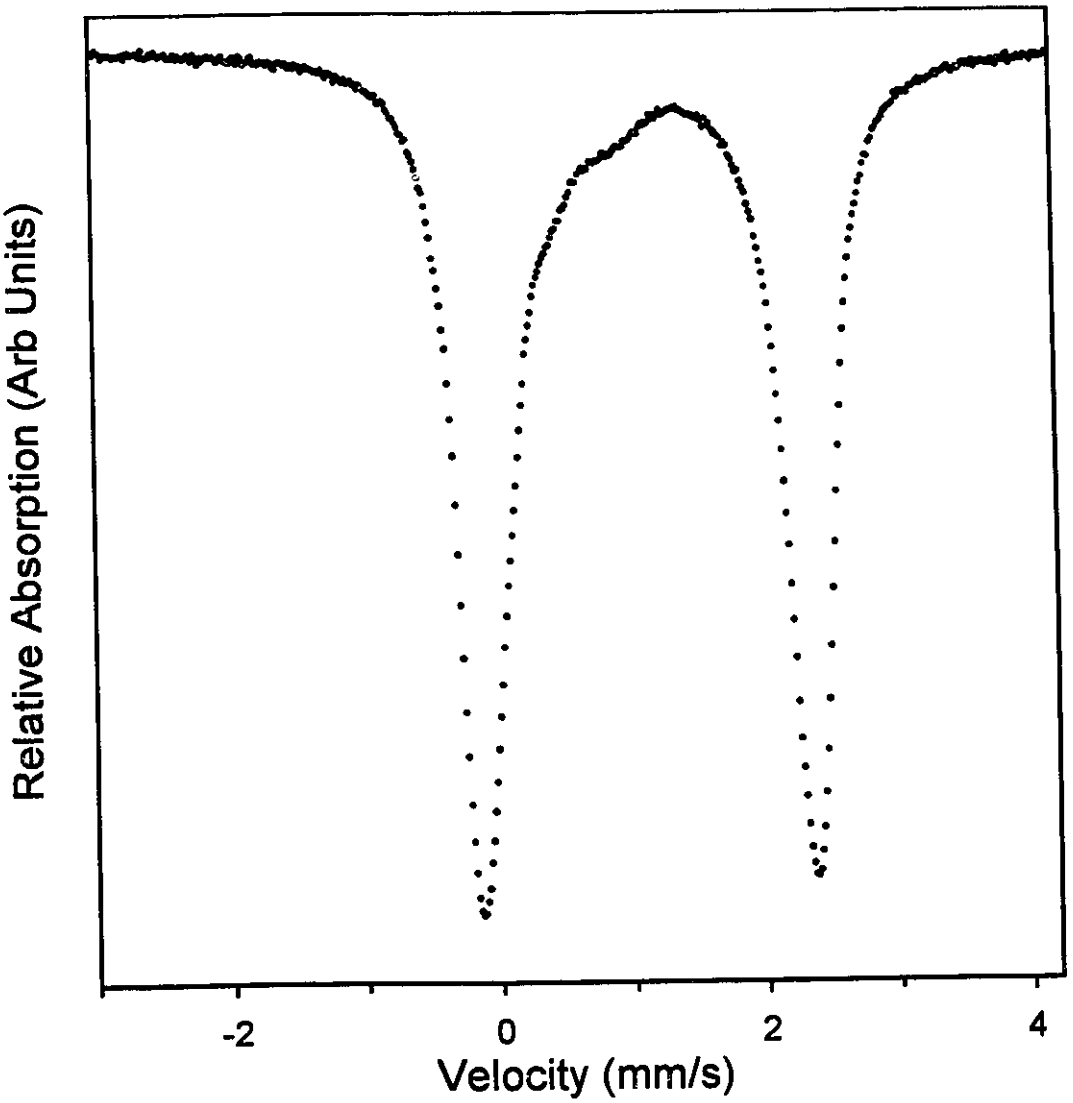

Figure 7.6a. *Mössbauer spectrum of synthetic annite at 295K, on expanded scale.*

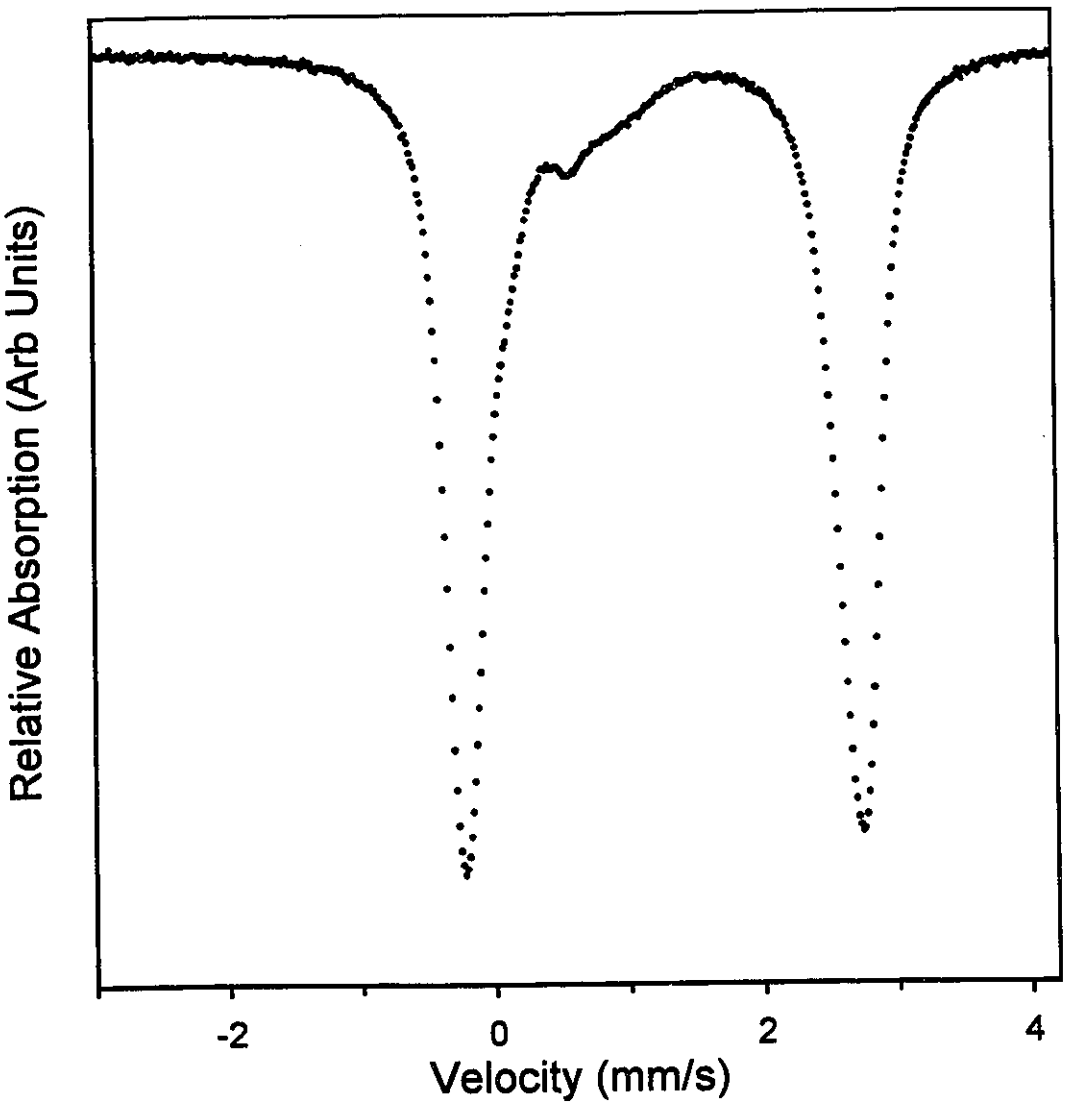

***Figure 7.6b** Mössbauer spectrum of synthetic annite at 83K, on expanded scale*

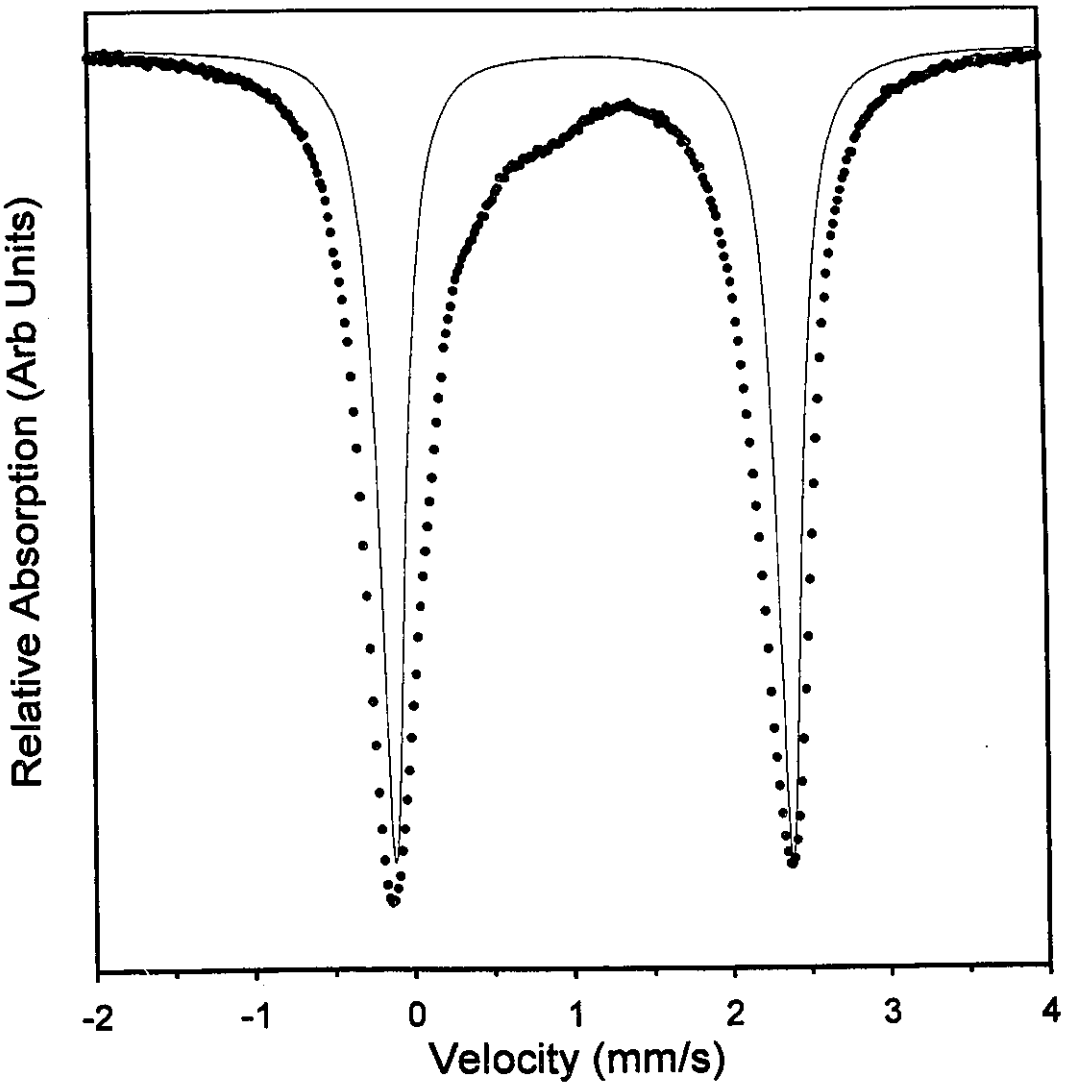

***Figure 7.7** Comparison of RT Mössbauer spectrum of synthetic annite to elemental Lorentzian doublet.*

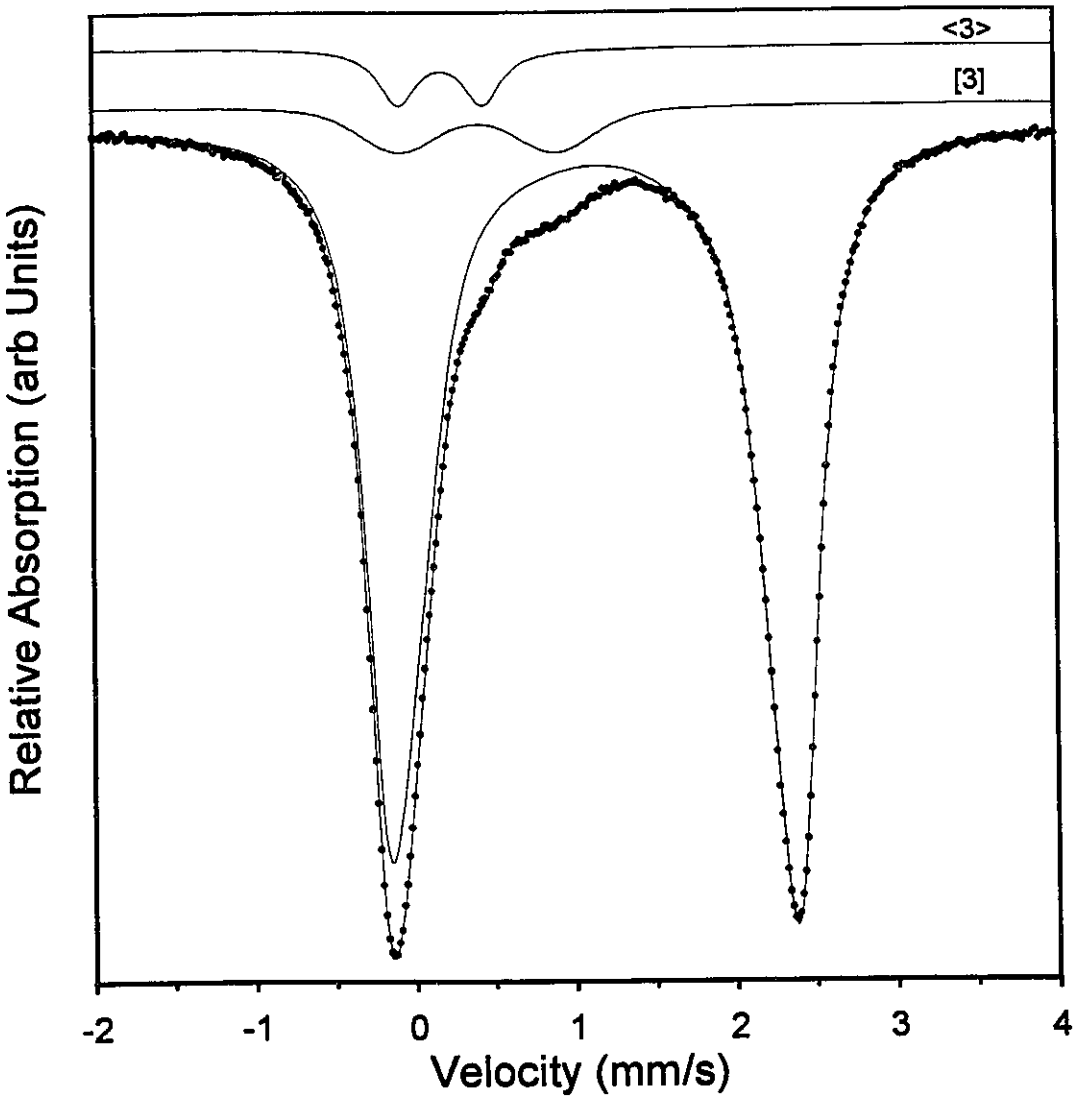

Figure 7.8a *Site specific contributions to the Mössbauer spectrum of synthetic annite at 295K. The unlabeled line is the contribution from [Fe^{2+}], the line labeled(3^{+}) is the contribution from Fe^{3+} in tetrahedral sites and the [3^{+}] line is the contribution from Fe^{3+} in octahedral sites. The fitting parameters for these contributions are found in table 7.1a.*

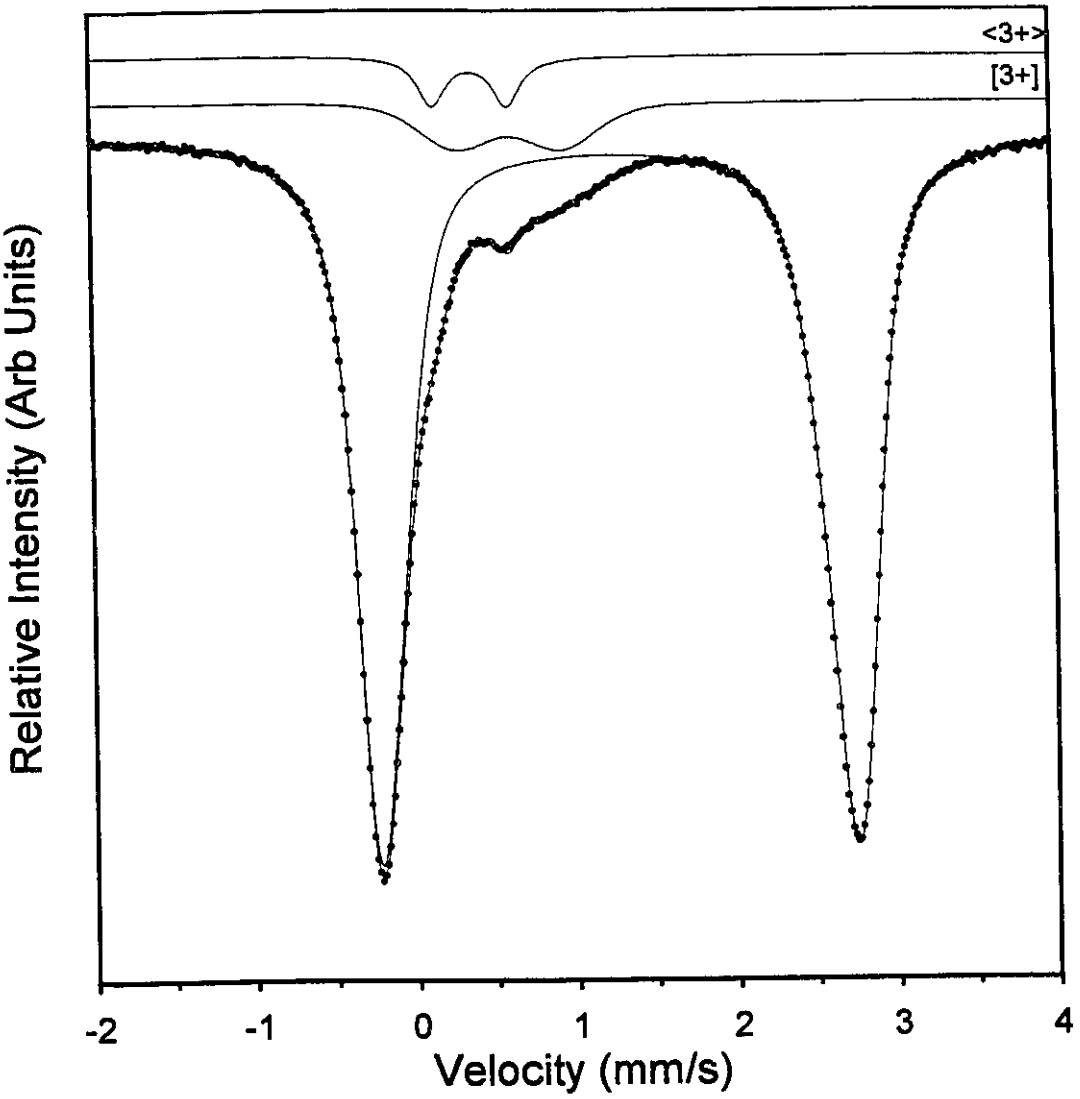

Figure 7.8b *Site specific contributions to the Mössbauer spectrum of synthetic annite at 83K. The unlabeled line is the contribution from* $[Fe^{2+}]$*, the line labeled* $\langle 3+ \rangle$ *is the contribution from* Fe^{3+} *in tetrahedral sites and the [3+] line is the contribution from* Fe^{3+} *in octahedral sites. The fitting parameters for these contributions are found in table 7.1b.*

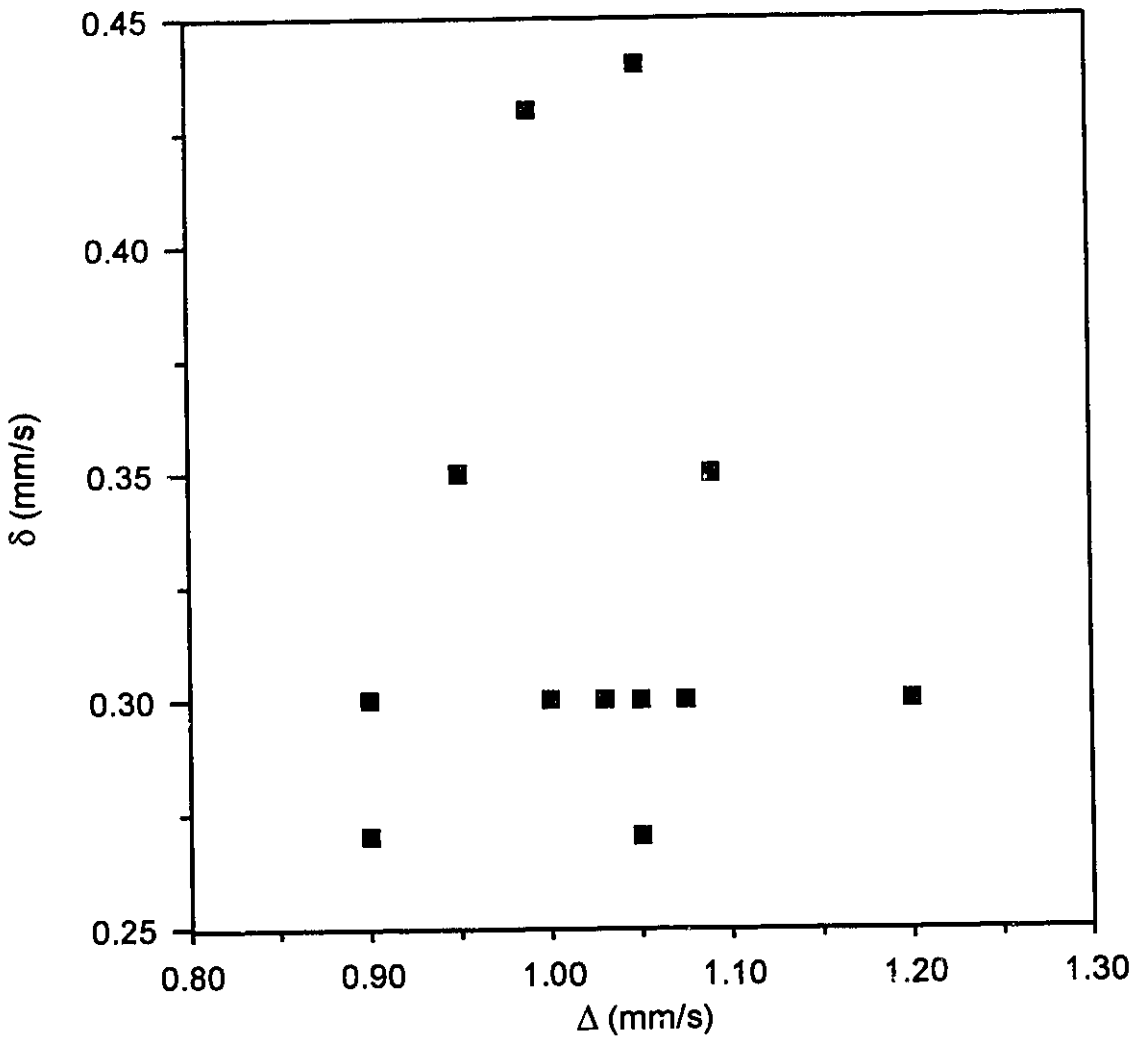

***Figure 7.9** Values of δ and Δ determined from various fits to room temperature Mössbauer spectra of synthetic annite.*

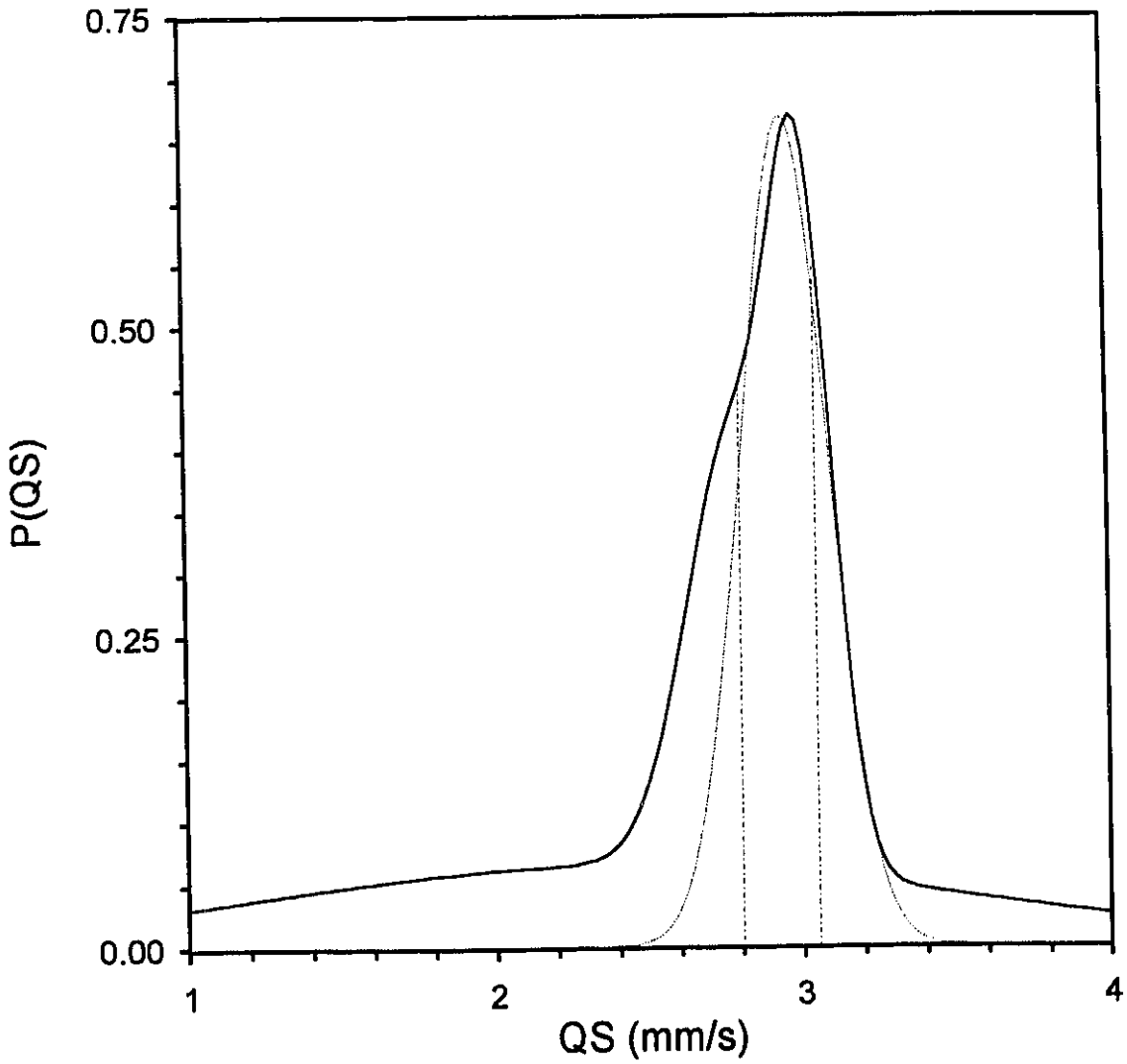

Figure 7.10 *Cumulative distribution of [Fe^{2+}] quadrupole splittings (QS) The solid line represents the distribution extracted from a fit to the synthetic annite Mössbauer spectrum at 83K. The dashed curve is a Gaussian distribution with σ_Δ = 0.2 mm/s. The dashed lines represent the upper and lower clamping limits used in fitting with the LW model.*

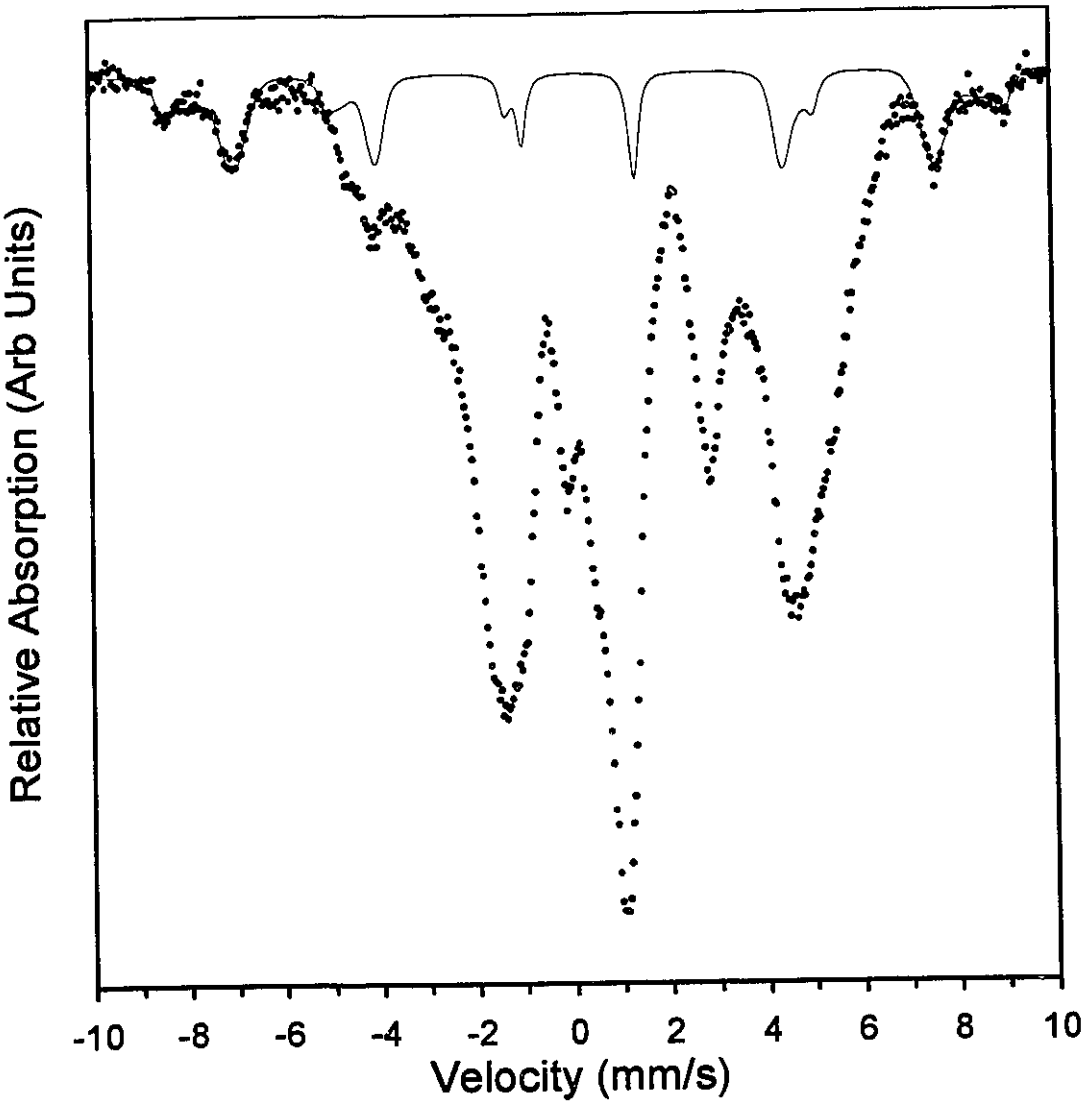

***Figure 7.11a** Fit to Fe^{3+} contribution to 7K Mössbauer spectrum of synthetic annite using 1-2 model. Fitting parameters are found in table 7.4.*

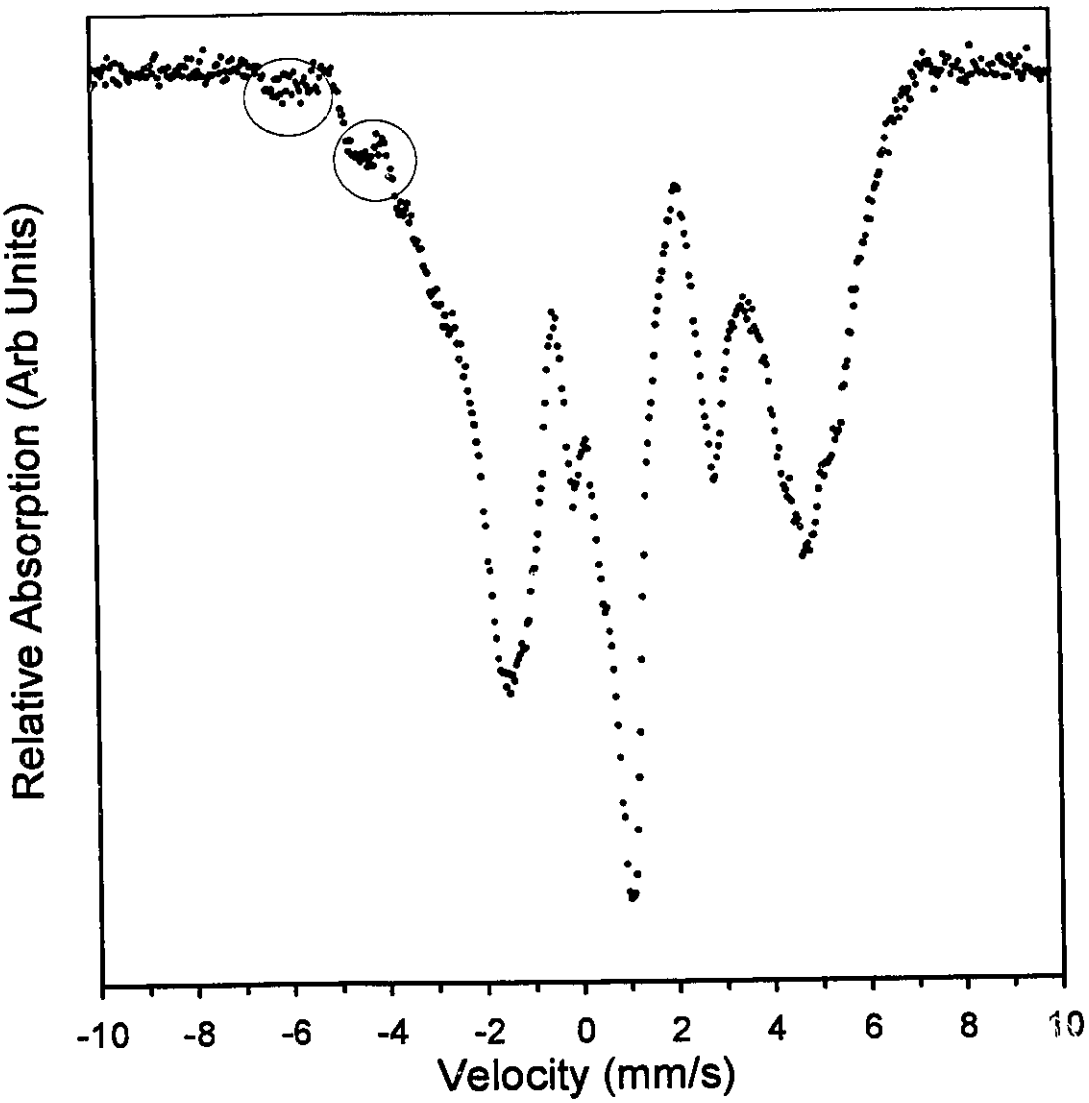

Figure 7.11b *7K Mössbauer spectrum of synthetic annite after stripping the Fe^{3+} contribution shown in figure 7.11a. The circled areas are anomalous intensity which indicate that this model of Fe^{3+} is not correct.*

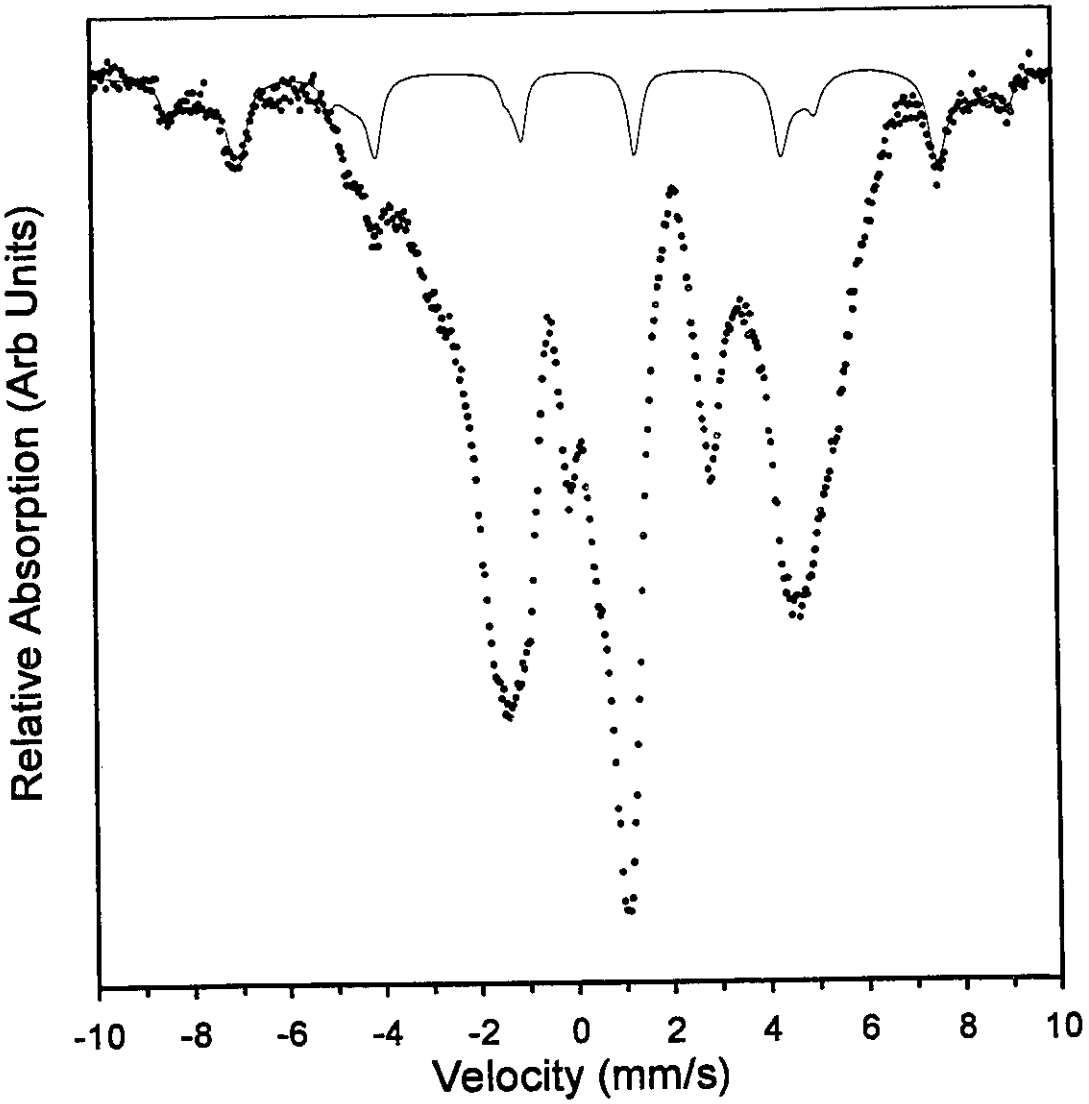

***Figure 7.12a** Fit to Fe^{3+} contribution to 7K Mössbauer spectrum of synthetic annite using 2-2 model. Fitting parameters are found in table 7.4.*

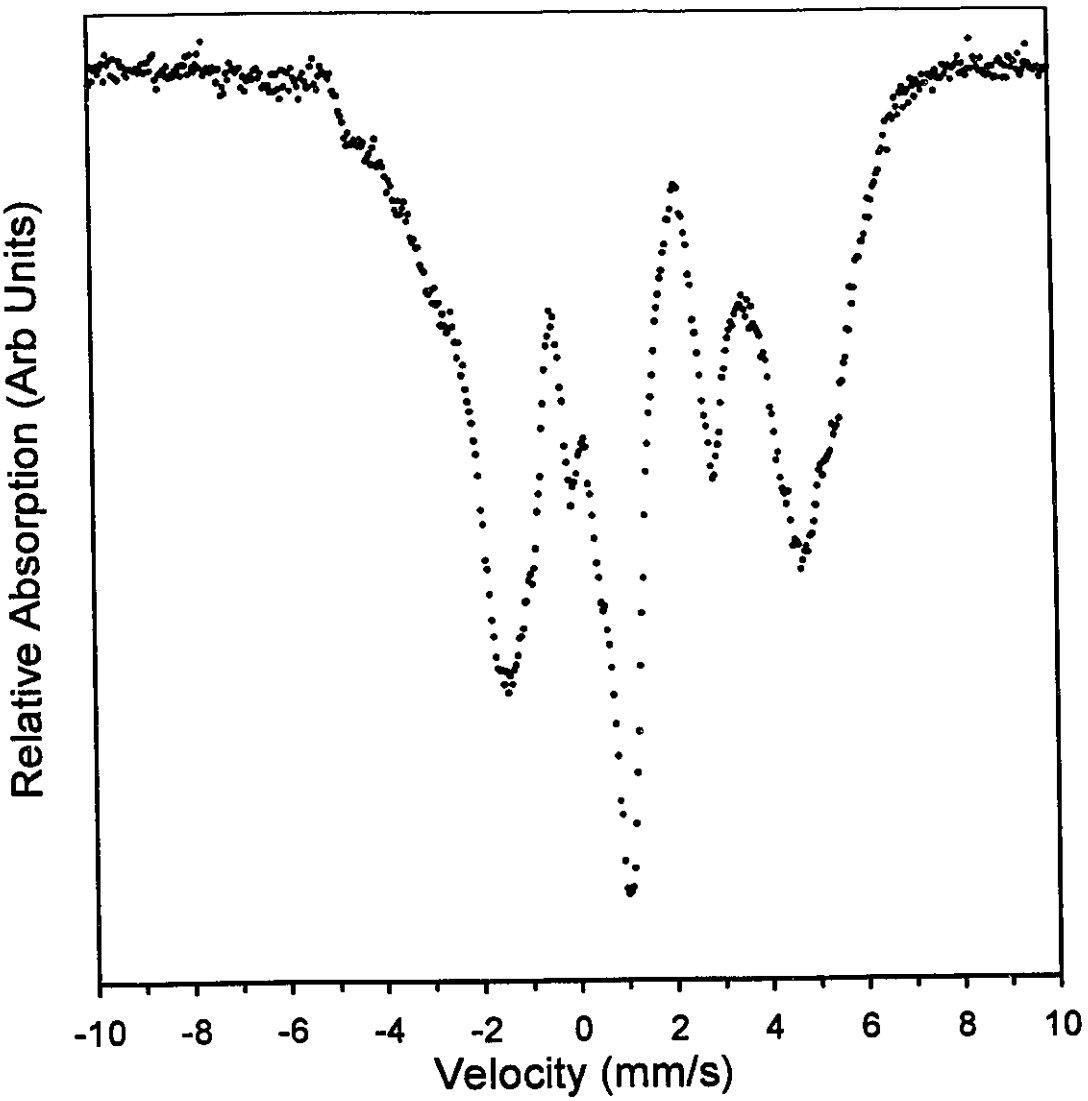

Figure 7.12b *7K Mössbauer spectrum of synthetic annite after stripping the* Fe^{3+} *contribution shown in figure 7.12a. The anomalous intensity evident in figure 7.11b are absent.*

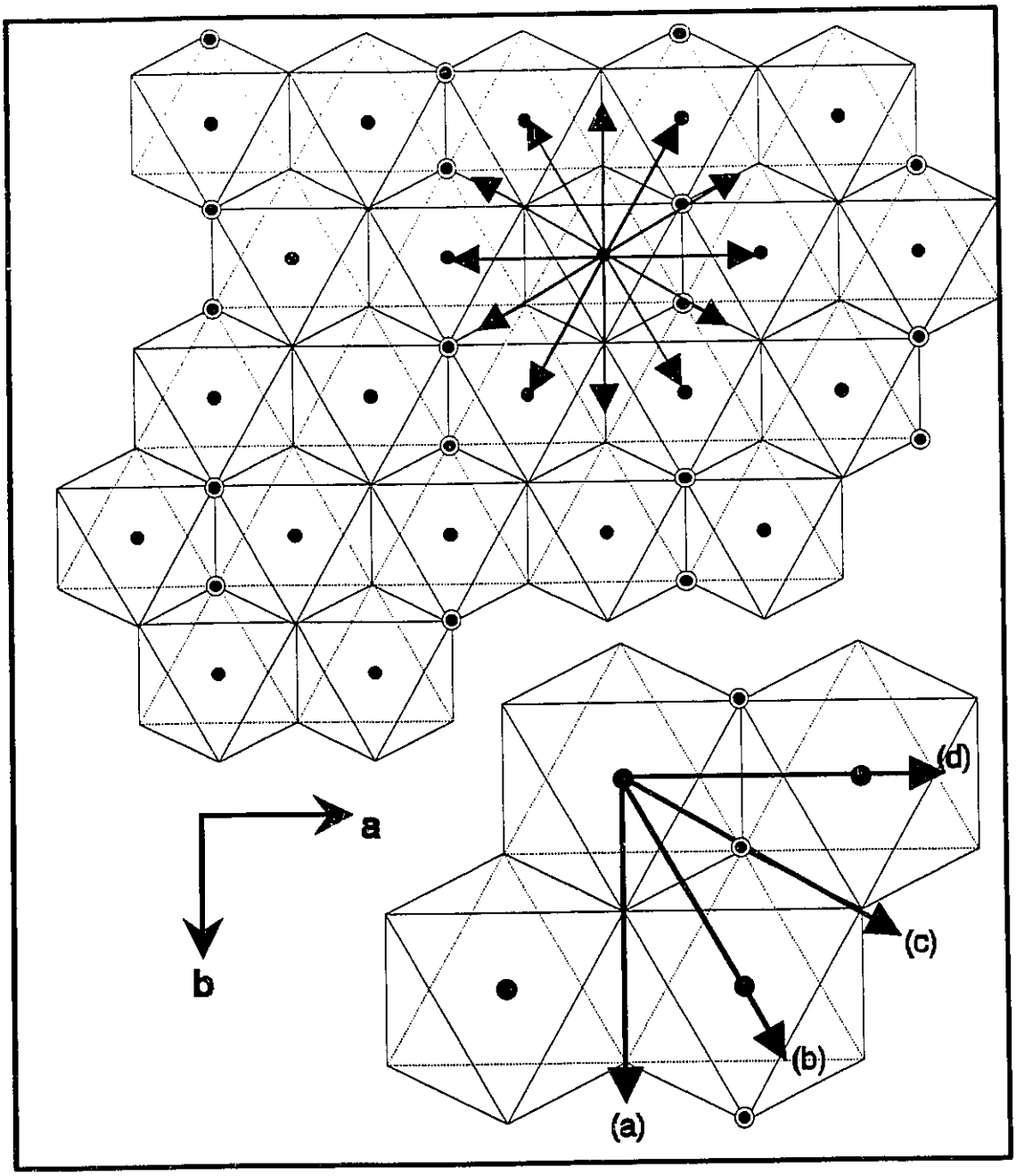

***Figure 7.13** Possible hyperfine field directions in the **ab** plane of the annite octahedral sheet. The twelve directions defined by the six nn cations and the six axes between the cations are reduced to four by the symmetry of the sheet (inset).*

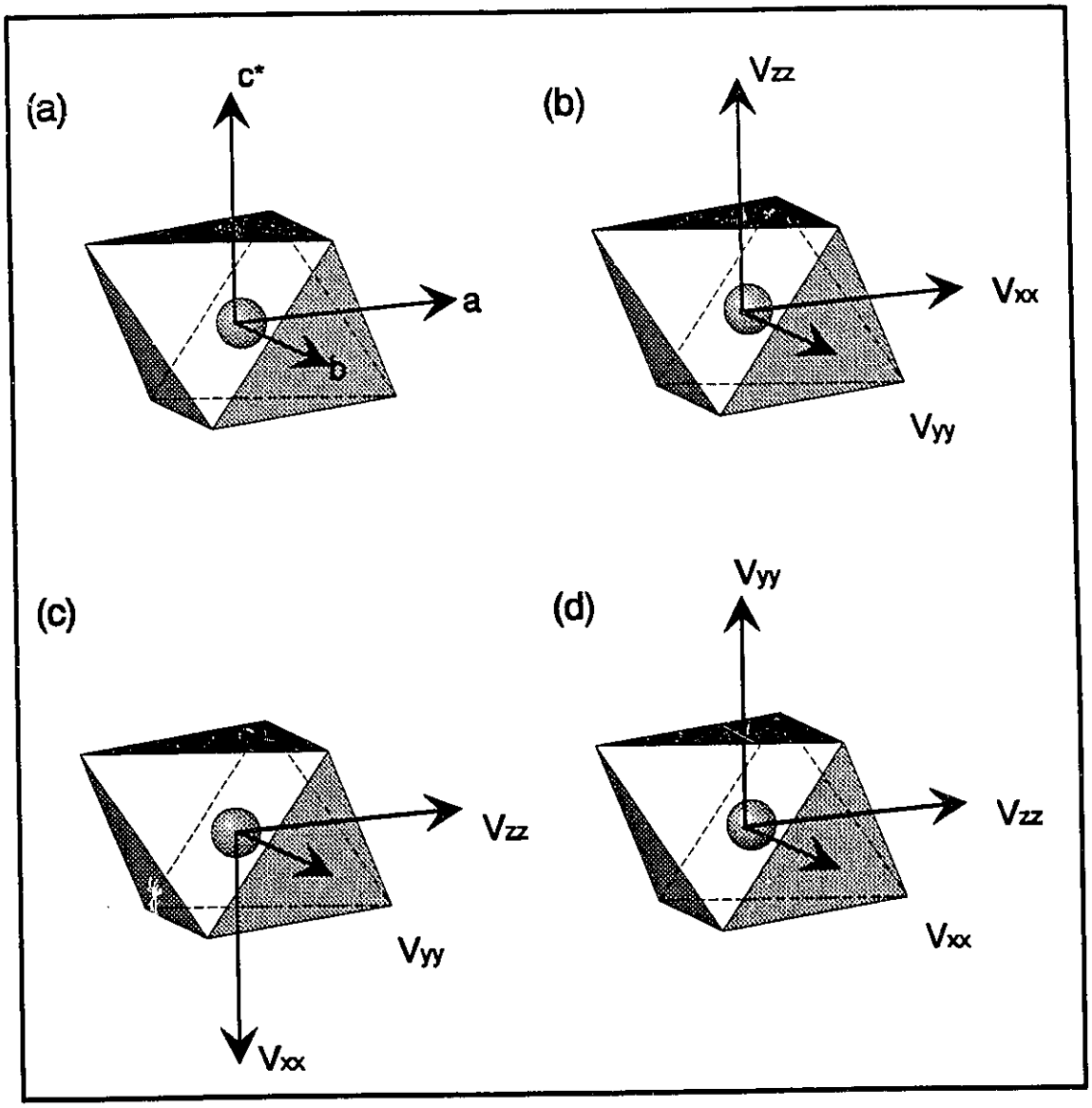

***Figure 7.14** Models of the EFG tensor principle axes at the octahedral cation site in annite. (a) crystalline axis, (b) EFG axes in the TRANS and CIS[1] models (c) EFG axes in the CIS[2] and CIS[3] models and (d) EFG axes in the CIS[4] and CIS[5] models.*

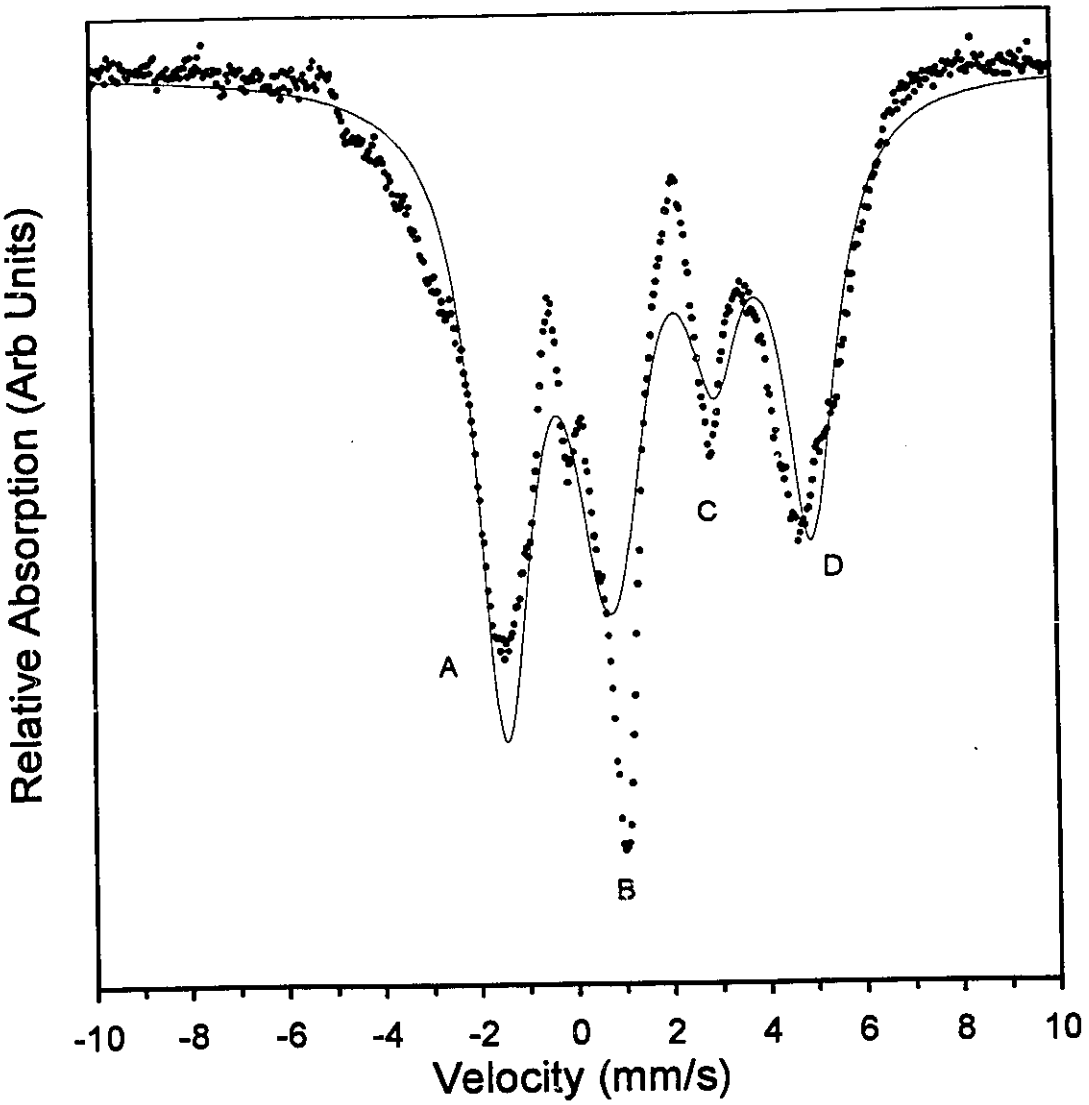

***Figure 7.15** Fit to stripped Mössbauer spectrum of synthetic annite at 7K using symmetric single site model with $e^2qQ < 0$. A, B,C, and D label spectral features which are discussed in the text.*

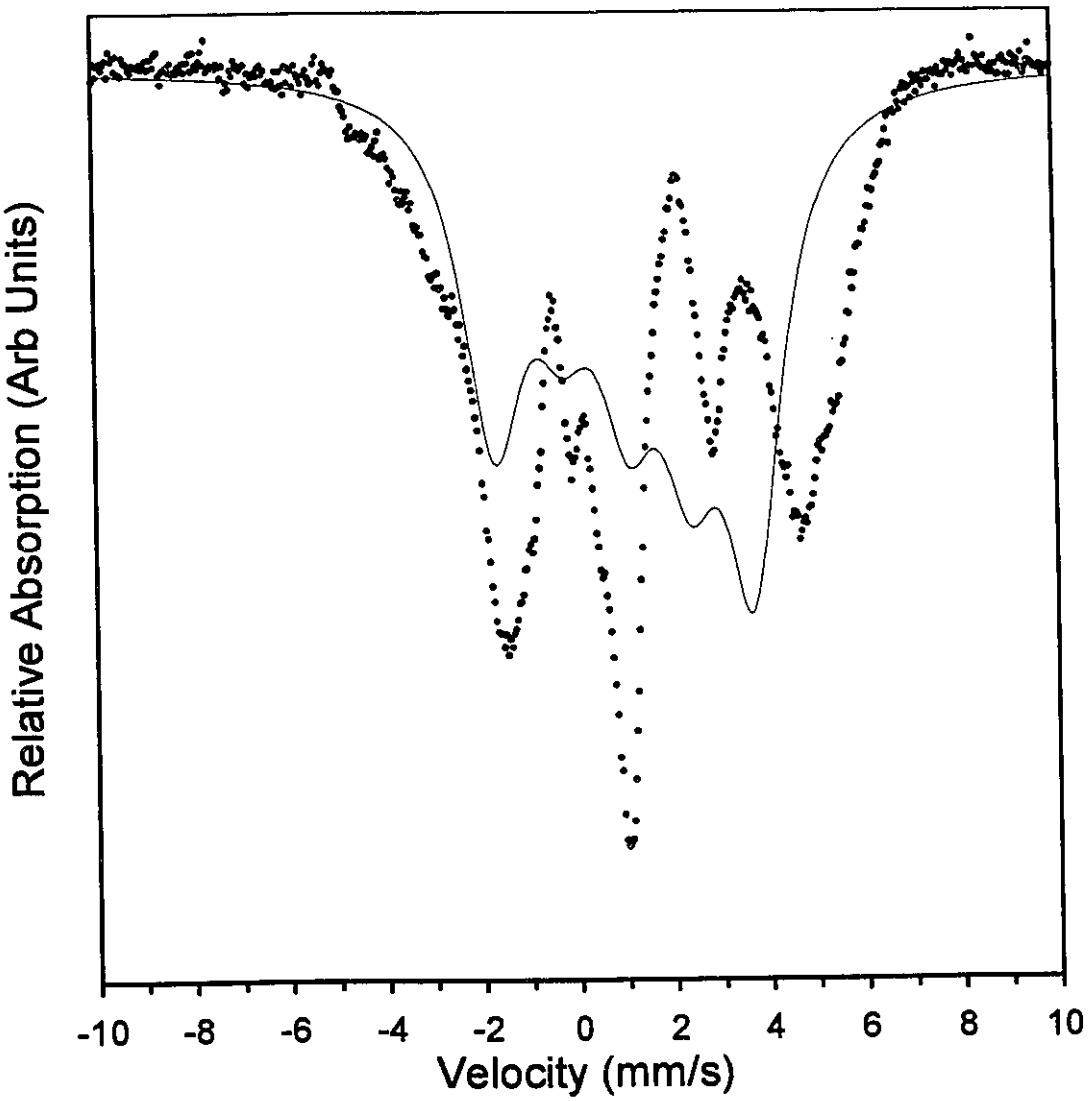

***Figure 7.16** Fit to stripped Mössbauer spectrum of synthetic annite at 7K using symmetric single site model with $e^2qQ > 0$.*

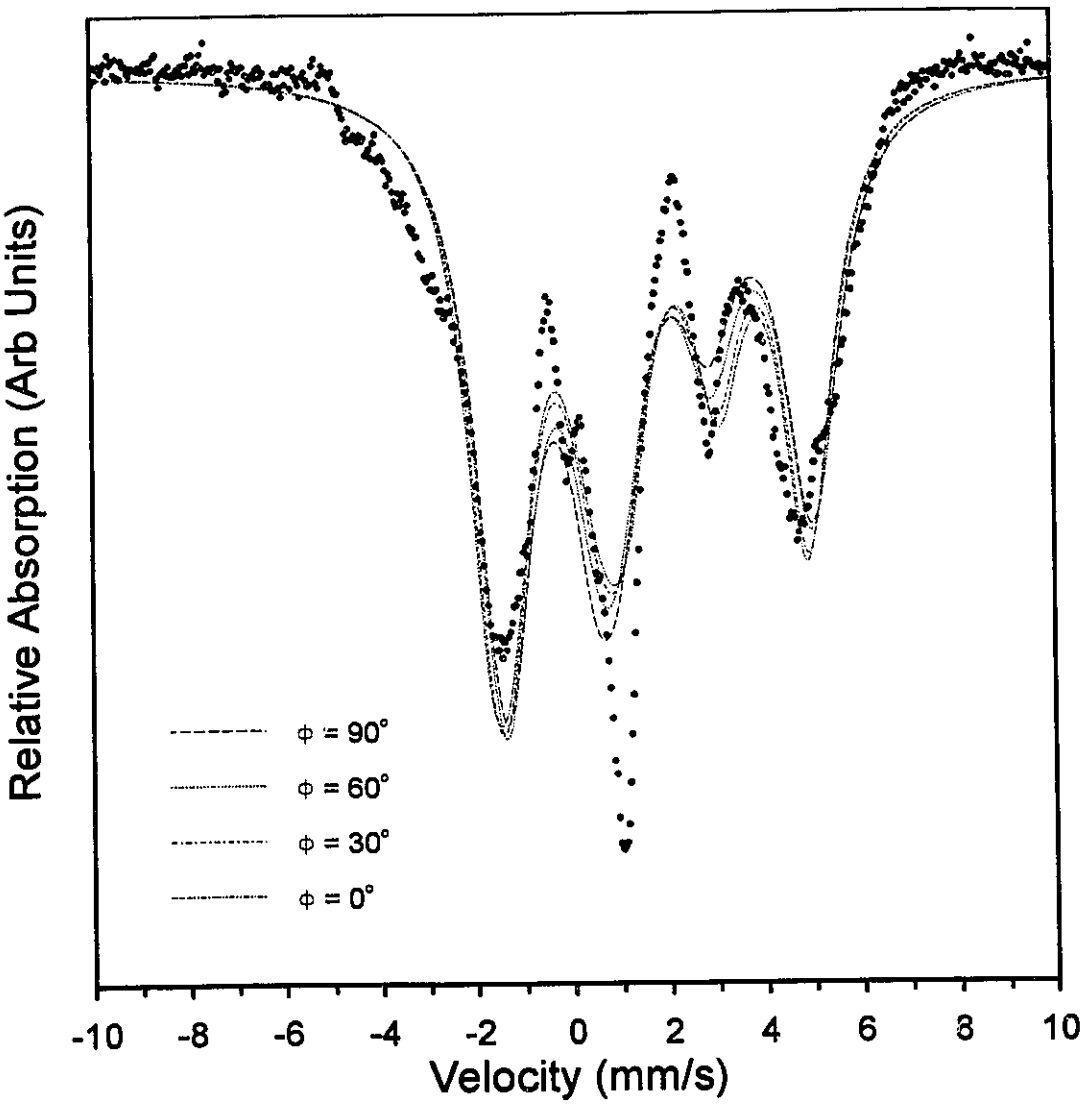

***Figure 7.17** Fit to stripped Mössbauer spectrum of synthetic annite at 7K using asymmetric single site model with $\eta = 0.2$ and line-width broadening. The four lines correspond to the four possible orientations of H in the octahedral sheet.*

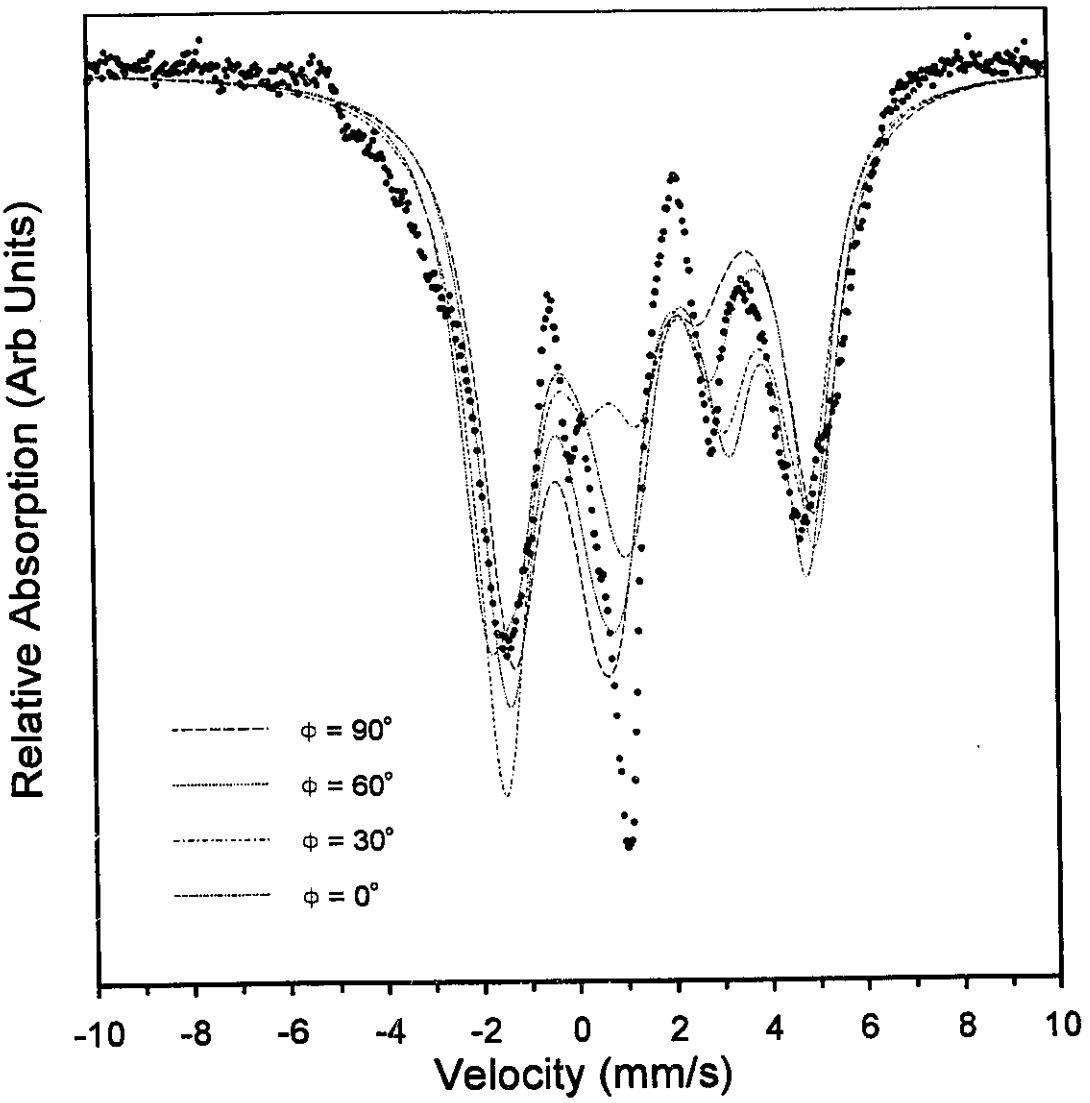

Figure 7.18 *Fit to stripped Mössbauer spectrum of synthetic annite at 7K using asymmetric single site model with $\eta = 0.5$ and line-width broadening. The four lines correspond to the four possible orientations of H in the octahedral sheet.*

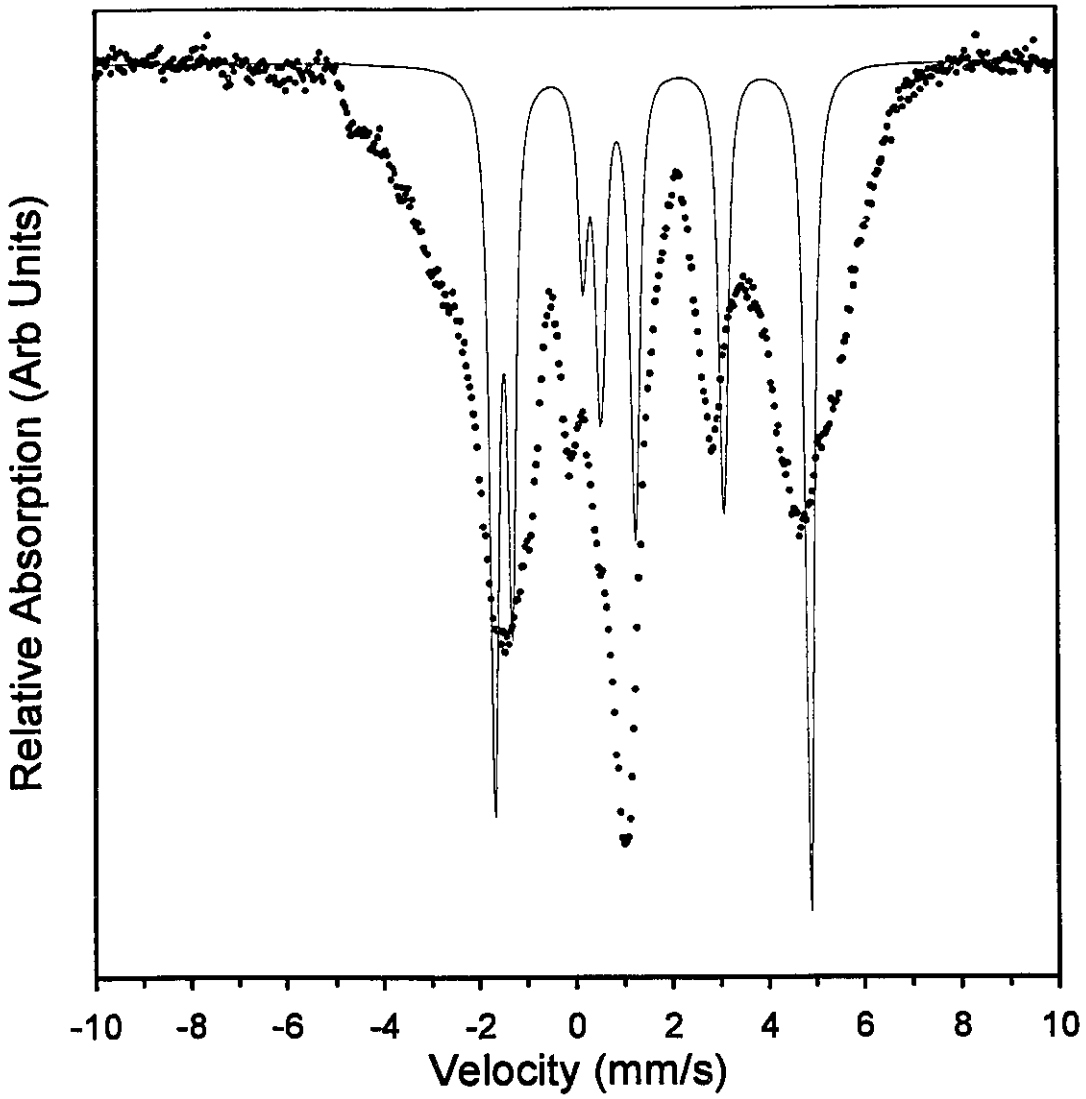

***Figure 7.19** Simulation demonstrating the effect of using dependent distribution line broadening model with a single asymmetric site model.*

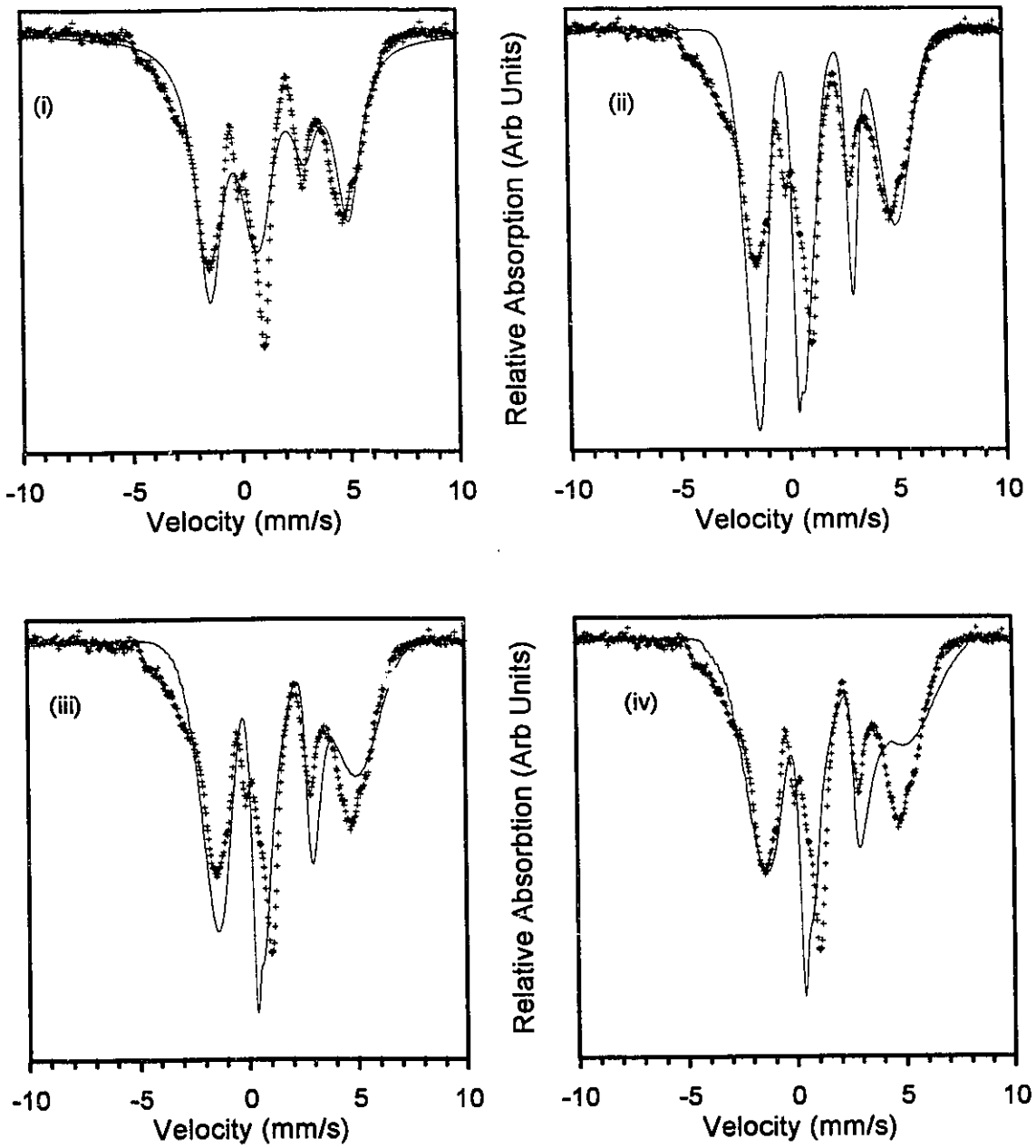

Figure 7.20 *Simulations demonstrating the effect of using independent distribution model with a single symmetric site model.(i) Line-width broadening model (single symmetric site fit from figure 7.15); (ii) Independent distribution model with* $\sigma_\Delta = 0.2$ *and* $\sigma_H = 0.3$ *and all other parameters equal to (i); (iii)* $\sigma_H = 0.45$*; (iv)* $\sigma_H = 0.60$.

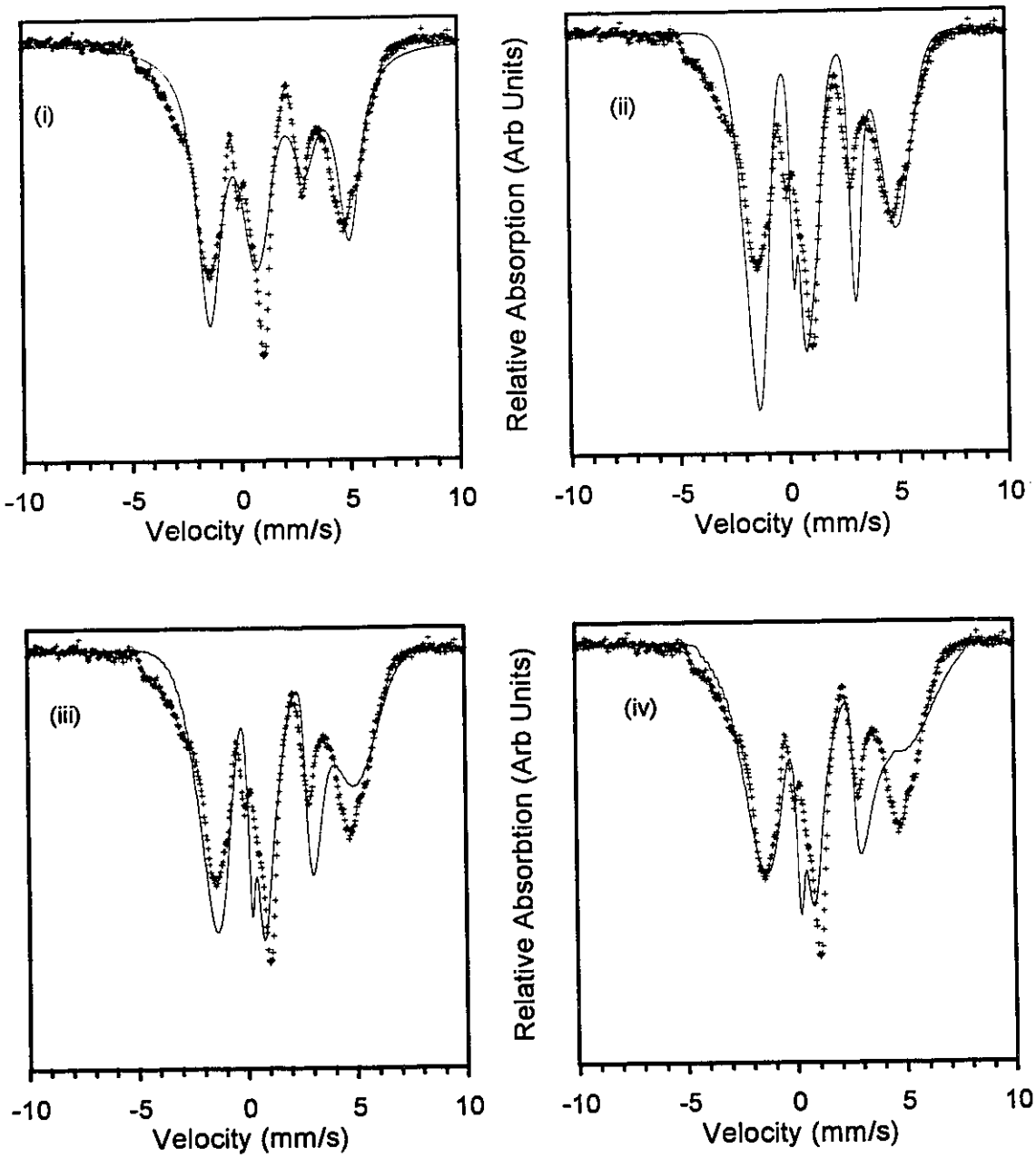

Figure 7.21 *Simulations demonstrating the effect of using independent distribution model with a single asymmetric site. The simulations use a single asymmetric site with* $\eta = 0.2$, *and* H *directed parallel to* V_{xx} *(case (a)). (i) Line-width broadening model; (ii) Independent distribution model with* $\sigma_\Delta = 0.2$ *and* $\sigma_H = 0.3$ *and all other parameters equal to (i); (iii)* $\sigma_H = 0.45$; *(iv)* $\sigma_H = 0.60$.

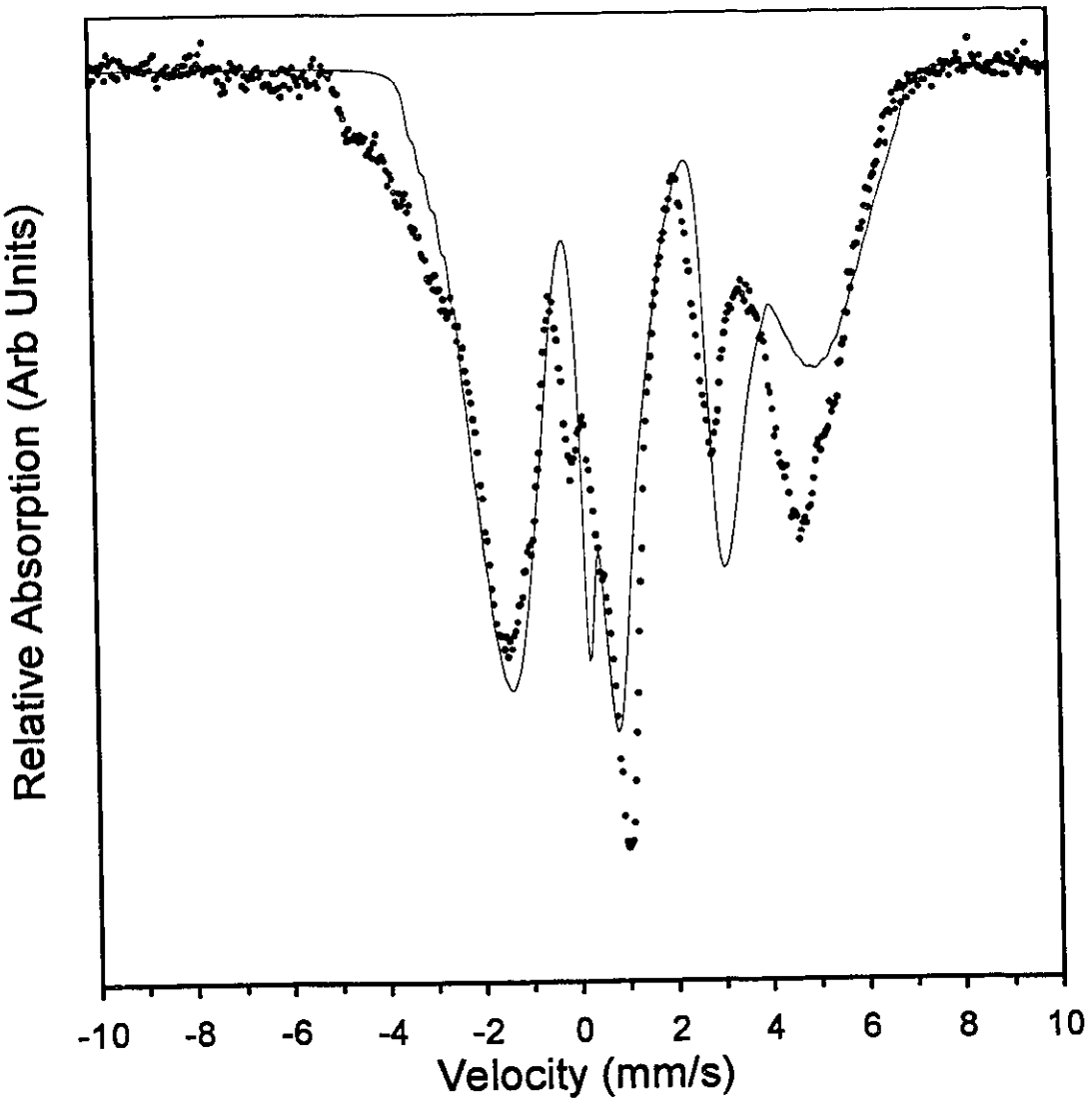

***Figure 7.22** Fit to stripped Mössbauer spectrum of synthetic annite at 7K using single asymmetric site and distribution broadening.*

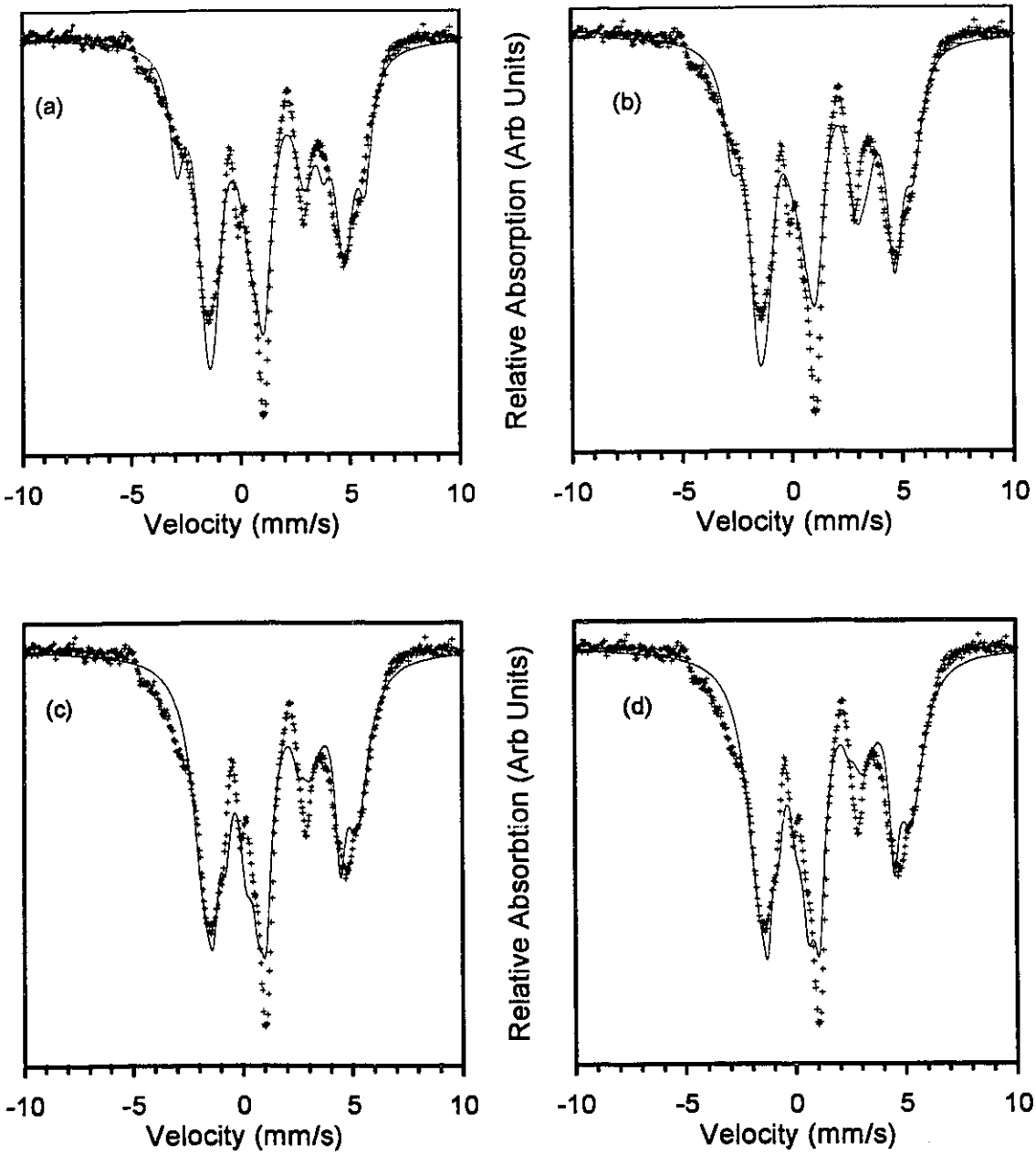

Figure 7.23 *Fit to stripped Mössbauer spectrum of synthetic annite at 7K using two-site model (TRANS and CIS[1] sites) and line-width broadening. The four figures correspond to the best fits for each of the four possible directions of H in the octahedral sheet.*

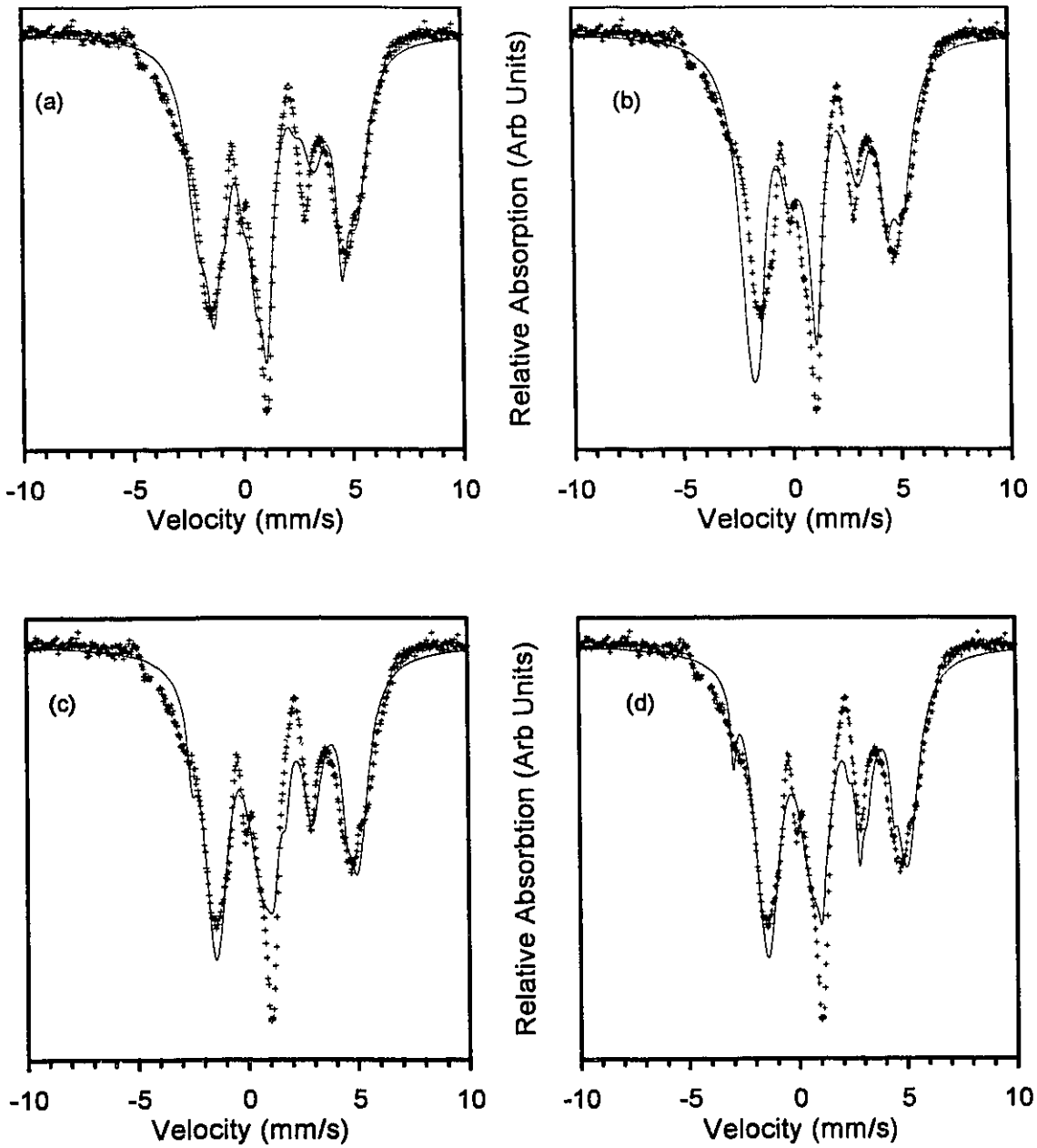

***Figure 7.24** Fit to stripped Mössbauer spectrum of synthetic annite at 7K using two-site model (TRANS and CIS[2] sites) and line-width broadening. The four figures correspond to the best fits for each of the four possible directions of H in the octahedral sheet.*

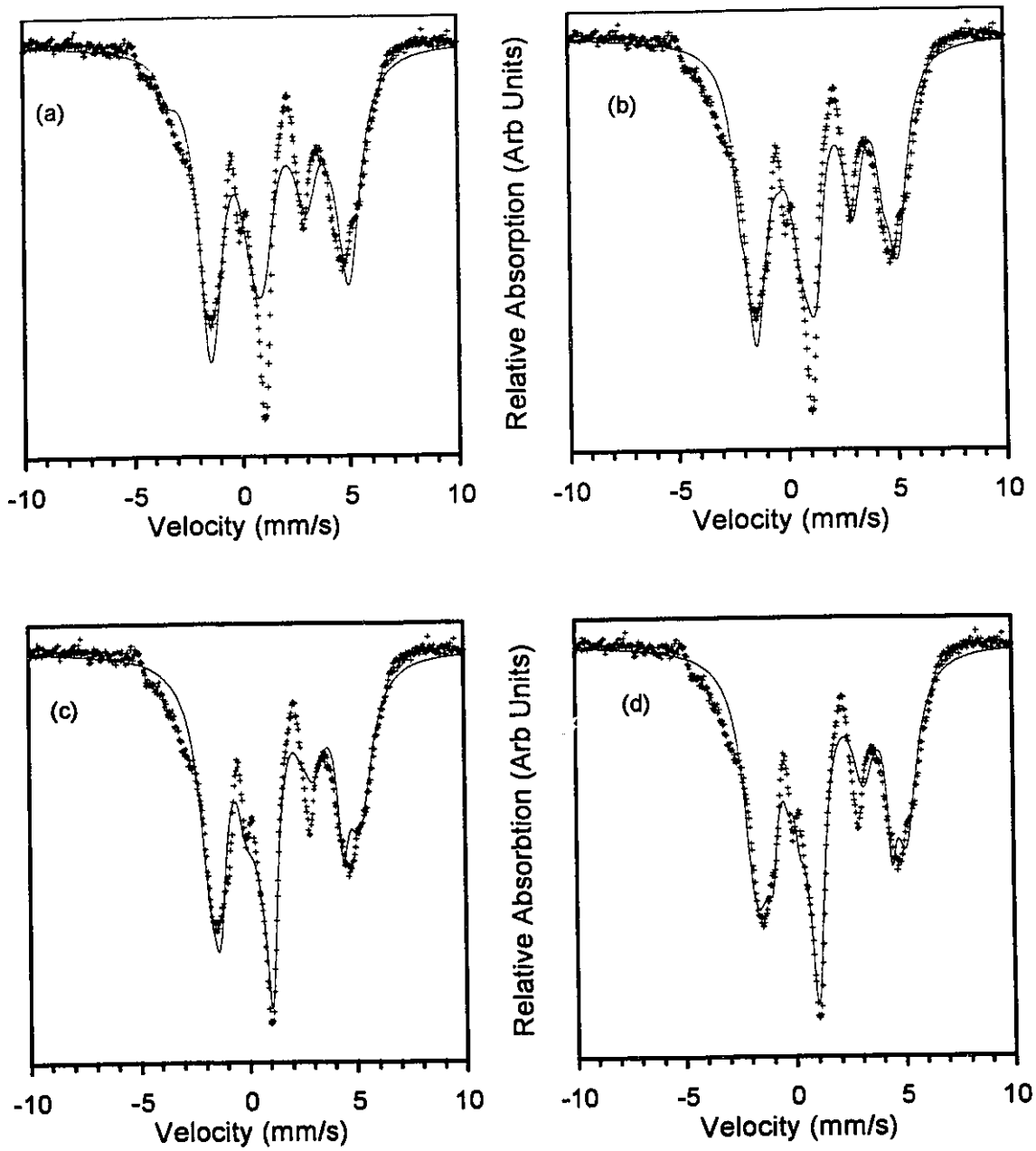

Figure 7.25 *Fit to stripped Mössbauer spectrum of synthetic annite at 7K using two-site model (TRANS and CIS[3] sites) and line-width broadening. The four figures correspond to the best fits for each of the four possible directions of H in the octahedral sheet.*

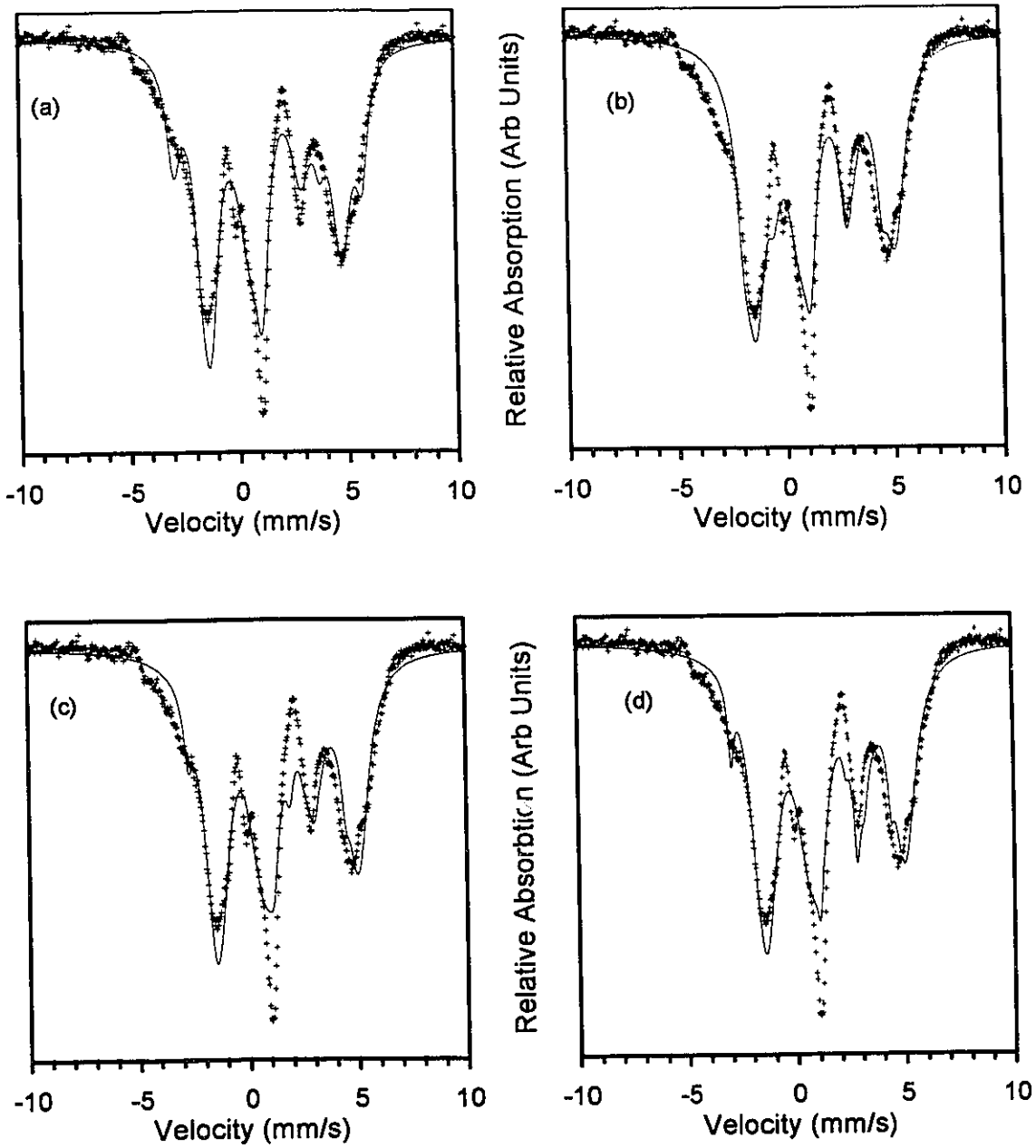

***Figure 7.26** Fit to stripped Mössbauer spectrum of synthetic annite at 7K using two-site model (TRANS and CIS[4] sites) and line-width broadening. The four figures correspond to the best fits for each of the four possible directions of H in the octahedral sheet.*

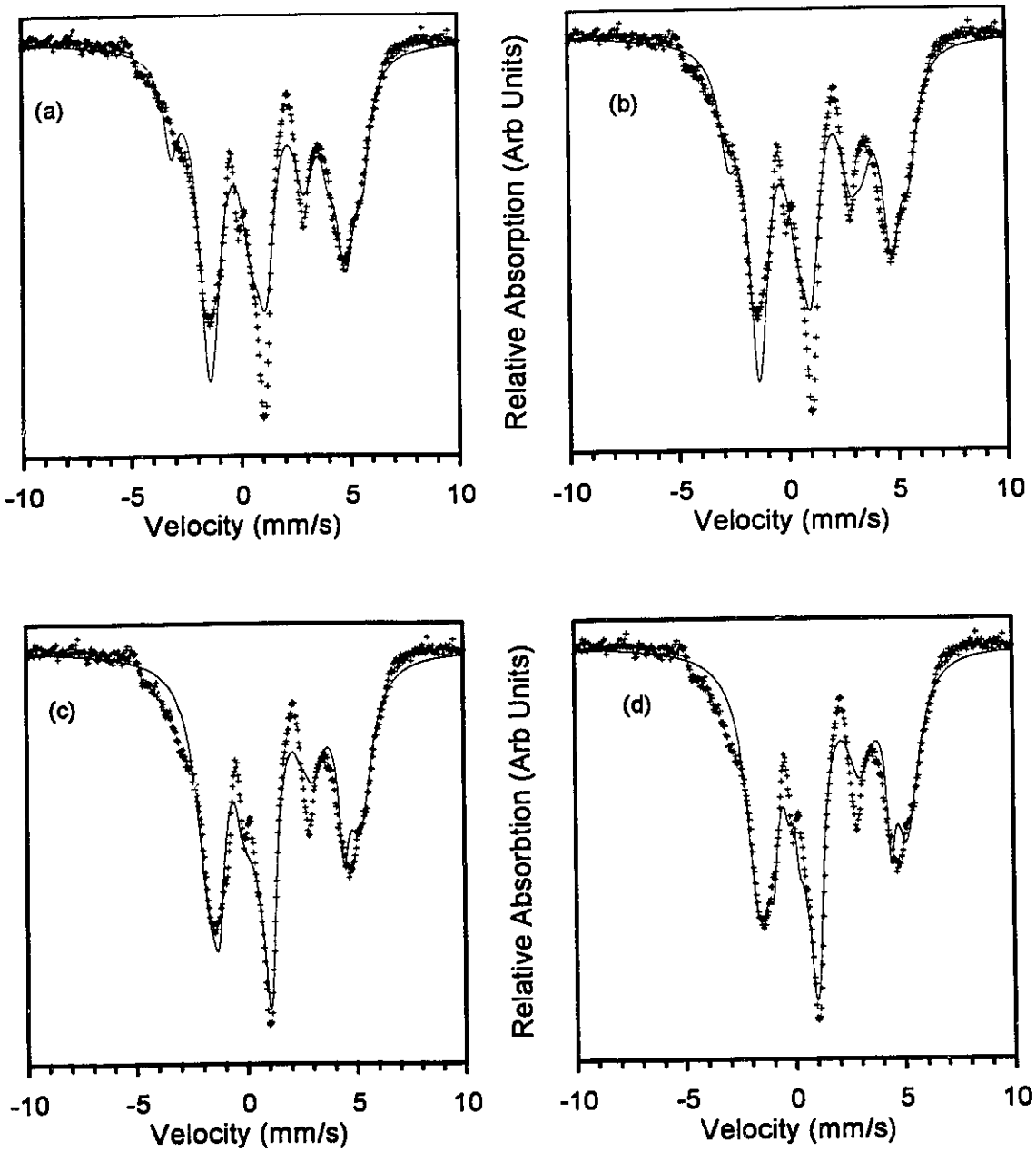

***Figure 7.27** Fit to stripped Mössbauer spectrum of synthetic annite at 7K using two-site model (TRANS and CIS[5] sites) and line-width broadening. The four figures correspond to the best fits for each of the four possible directions of H in the octahedral sheet.*

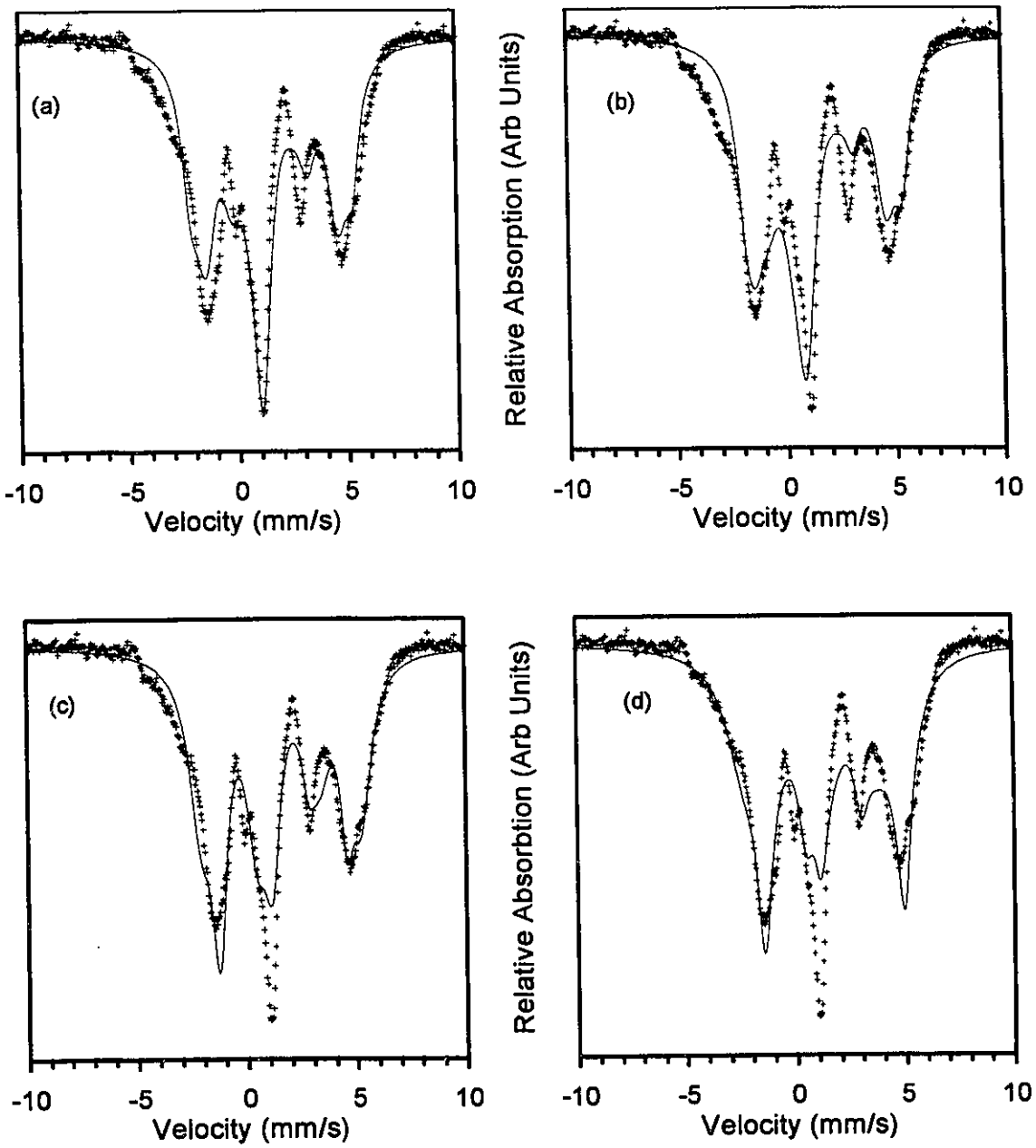

***Figure 7.28** Selected fits to 7K Mössbauer spectrum of synthetic annite using various a two-site models with a fixed 2:1 CIS to TRANS site ratio and line-width broadening model. (i) B2(b) model, (ii) B3(c) model, (iii) B4(a) model, and (iv) B5(a) model.*

Chapter 8

Conclusion

8.1 The Annite Magnetic Ground State

From the SQUID and Mössbauer measurements presented in this study a picture of the ground state of annite emerges. The [Fe^{2+}] moments lie in the **ab** plane and are aligned ferromagnetically in each sheet . These predominantly ferromagnetic sheets are stacked antiferromagnetically along the c* axis. Within the sheet the Fe^{3+} moments also lie in the plane with some fraction being parallel to the [Fe^{2+}] moments and the rest aligned antiparallel. The tetrahedral Fe^{3+} are also coupled to the octahedral moments and lie in the plane of the sheet as well.

Since the crystal structure of annite precludes any known mechanism of inter-layer exchange, the spin structure cannot be stabilized by such exchange forces. It appears that the antiferromagnetic stacking of planes is part of the intrinsic zero-field domain structure and that the structure is stabilized by inter-layer dipole dipole forces. Shape dependent SQUID results indicate that while these dipole-dipole forces are responsible for stabilizing the ordered state, the ordering temperature is determined by intra-layer forces alone and is intrinsic to each material.

8.2 T_N and Temperature Development of the Magnetic State

It has been determined that the ordering temperatures for the synthetic and natural samples of annite are: $T_N = 58$ K and $T_N = 42$ K respectively. These values are in direct contradiciton of the prediction that $T_N < 10$ K for all biotites (Coey and Ghose, 1988, Mitra, 1992).

The most striking features of the annite magnetic state concern the development of the state with temperature between 4.2 K and the ordering temperature. Mössbauer spectroscopy results indicate that the temperature dependence of the Fe^{3+} moments is very different than the predominant [Fe^{2+}] moments. Both species of Fe^{3+} have HFSs

which disappear at temperatures well below T_N. It appears that the disappearance of the Fe^{3+} HFS is related to the strength of the coupling of the Fe^{3+} moments to the [Fe^{2+}] backbone, with the weakest coupled moments (i.e. the $\langle Fe^{3+} \rangle$) disappearing first. This anomalous Fe^{3+} HFS temperature dependence is apparently linked to the persistence of a paramagnetic [Fe^{2+}] fraction at temperatures as low as 4.2K (or $< 0.1\ T_N$). Two plausible qualitative mechanisms for these results have been proposed which link these temperature dependecies to a mechanism which also generates the large distributions of Fe^{2+} HFS at $T<T_N$. The exact form of the HFS distribution has not been extracted but it has been determined that the central value is ~1.15 mm/s and that the width of the distribution is on the order of 0.4 mm/s.

8.3 Suggestions for Future Work

In addition to determining the magnetic state of annite this study has presented the first comprehensive attempt to fit a low temperature spectrum of annite. The study indicates that none of the proposed simple models are adequate. There are indications that a successful model must: (a) avoid the usual CIS/TRANS division of sites because such a division is clearly inappropriate for samples with significant cation substitutions and (b) use distributions of hyperfine parameters to achieve a good physical fit. The development of a more complete model should be a priority for future work.

With such a model it will be possible to obtain better quantitative estimates of the paramagnetic [Fe^{2+}] and HFS Fe^{3+} fractions in the spectrum as a function of temperature. As well, the model will also allow extraction of P(H), and because the dipolar and supertransferred terms in the hyprfine Hamiltonian are relatively small it can be expected that the extracted P(H) will allow calculation of the distribution of Fe^{2+} moments directly, without a detailed model of the spin structure. It is hoped that such calculations will inspire the theoretical work which is required to understand this 2D magnetic system.

As discussed in the introduction to this thesis, the description of the magnetic state of annite is a starting point for the description of the effects of bond, site and combined bond and site disorder on the annite magnetic state. The study of the three solid solutions mentioned in chapter 1 should also be explored, including a more detailed quantitative analysis of the samples in appendix D.

References

L P Aldridge, J Finch, G J Gainsford, K H Patterson, and W C Tennant; Single crystal Mössbauer studies of 1M biotite. *Physics and Chemistry Minerals.* **17** p.583, (1991).

N W Ashcroft and N D Mermin;Solid state Physics. Suanders College, Philadelphia, Pennsylvania, (1976).

S W Bailey, ed., Reviews in Mineralogy Vol. **13** (1984).

O Ballet; Comment on Magnetism in Biotites. *Physics and Chemistry Minerals.* **13** p.281, (1986).

O Ballet, and J M D Coey; Magnetic Properties of Sheet Silicates; 2:1 Layer Minerals. *Physics and Chemistry Minerals.* **8** p.218-29, (1982).

O Ballet, J M D Coey , P Mangin, and M G Townsend; Ferrous Talc - A Planar Antiferrromagnetic. *Solid State Communications.* **55**(9) p.787, (1985).

O Ballet, J M D Coey, and K J Burke; Magnetic Properties of Sheet Silicates; 2:1:1 Layer Minerals. *Physics and Chemistry Minerals.* **12** p.370, (1985).

N Beausoleil, P Lavallee, A Yelon, O Ballet, and J M D Coey; Magnetic properties of Biotite Micas. *Journal of Applied Physics.* **54**(2) p.906, (1983).

V L Beresinskii, and A Ya Blank; Thermodynamics of layered isotropic magnets at low temperatures. *Zh. eksp. teor. Fiz.* **64** p.725, (1973).

J Bonner, and M E Fisher; Linear Magnetic Chains with Anisotropic Coupling. *Physical Review A.* **135**(3A) p.640, (1964).

R A Brand; Improving the validity of Hyperfine field distributions from magnetic alloys. *Nuclear Instruments and Methods in Physics Research.* **B28** p.398, (1987).

I A D Christie, D G Rancourt, H Kodama, H Murad, and J L Robert; Oxidation of synthetic annite mica characterized by 57Fe Mössbauer spectroscopy: Hydrogen de-intercalation and host layer valence state populations, in Chemical Physics of Intercalation II, J E Fisher, P Bernier, S Roth, and S A Solin, eds., 1992. Plenum, New York, Nato ASI Series B: Physics p.387, (1993).

J M D Coey; Magnetic Order in Trioctahedral sheet silicates: A Review, in Proceedings of the International Clay Conference, L G Shultz, H van Olphen, and F A Mumpton, eds., 1985. The Clay Minerals Society, Bloomington, Indiana, p.261, (1987).

J M D Coey, O Ballet, A Moukarika, and J L Soubeyroux; Magnetic Properties of Sheet Silicates; 1:1 Layer Minerals. *Physics and Chemistry of Minerals.* **7** p.141, (1981).

J M D Coey, and S Ghose; Magnetic Phase Transitions in Silicate Minerals, in Advances in Physical Geochemistry, p.162, (1988).

J M D Coey, O Ballet, T Bakas, and P Mangin; Spin-Glass properties of a planar antiferromagnet. *Journal of Applied Physics.* **67**(9) p.5258, (1990).

L J De Jongh, and A R Meidema; Experiments on simple magnetic model systems. *Advances in Physics.* **23**(1) p.259, (1974).

W A Deer, R A Howie and J Zussman;An Introduction to the rock forming minerals. Longman, London, (1966).

C Dekker, and A F M / W H W Arts; $Rb_2Cu_{1-x}Co_xF_4$ A Two Dimensional Ising Spin Glass. *Journal of Applied Physics.* **63**(8) p.4334, (1968).

M D Dyar, and R G Burns; Mössbauer spectral study of ferruginous one-layer trioctahedral micas. *American Mineralogist.* **71** p.955, (1986).

H Ebert, H Winter, B L Gyorffy, D D Johnson, and F J Pinski; Theoretical study of the hyperfine fields of Ni and Fe in FCC NixFe1-x alloys. *Journal of Physics F: Metal Physics*. **18** p.719, (1988).

H Ebert, H Winter, D D Johnson, and F J Pinski; A Theoretical study of the hyperfine fields in BCC FexCr1-x and FexCo1-x alloys. *Journal of Physics: Condensed Matter*. **2** p.443, (1990).

B J Evans, and L J Swartzendruber; Supertransferred Hyperfine Fields and Covalency at Diamagnetic Cations in Magnetic Insulators. *Physical Review B*. **6**(1) p.223, (1972).

E Ferrow; Mössbauer and X-ray Studies on the oxidation and reduction of annite and ferrannite. *Physics and Chemistry of Minerals*. **14**(270)(1987).

F Grandjean; Chemical Influences on the Supertransferred Hyperfine Field, in Mossbauer Spectroscopy Applied to Inorganic Chemistry, Gary J. Long, ed., Plenum Press, New York and London, p.241, (1987).

N N Greenwood and T C Gibb;Mossbauer Spectroscopy. Chapman and Hall Ltd., London, England, (1971).

P Hargraves, D G Rancourt, and A E Lalonde; Single Crystal mossbauer study of phlogopite mica. *Canadian Journal of Physics*. **68** p.128, (1990).

F C Hawthorne; Mössbauer spectroscopy. in *Mineralogical Society of America Reviews in Mineralogy*. **18** p.255, (1989).

R M Hazen, and C W Burnham; The crystal structures of one-layer phlogopite and annite. *American Mineralogist*. **58** p.889, (1973).

R M Hazen, and D R Wones; The Effect of substitutions on the physical properties of trioctahedral micas. *American Mineralogist*. **57** p.103, (1972).

L Häggstrom, R Wäppling, and H Annersten; Mössbauer study of iron-rich biotites. *Chemical Physics Letters*. **4** p.107, (1969).

C S Hogg, and R E Meads; A Mössbauer study of thermal decompostion of biotites. *Mineralogy Magazine*. **40** p.79, (1975).

N L Huang, R Orbach, E Simanek, J Owen, and D R Taylor; Cation- Cation Interaction Contributions to the Hypefine Interaction. The Supertransferred Hyperfine Interaction. *Physical Review*. **156**(2) p.383, (1967).

R Ingalls; Electric-Field Gradient Tensor in Ferrous Compounds. *Physical Review*. **133**(3A) p.787, (1964).

F James, and M Ross; A system for function minimization and analysis of the parameter errors and correlations. *Computer Physics Communications*. **10** p.343, (1975)

B D Josephson; Temperature dependent shift of γ-rays emitted by a solid. *Physical Review Letters*. **4** p.341, (1960).

J M Kosterlitz, and D J Thouless; Ordering, metastability and phase transitions in two-dimensional solids. *Journal of Physics C: Solid State Physics*. **6** p.1181, (1973).

J M Kosterlitz; The Critical Properties of the two-dimensional xy model. *Journal of Physics C: Solid State Physics*. **7** p.1046, (1974).

H A Kramers, and G H Wannier; Statistics of the Two-Dimensional Ferromagnet. Part I. *Physical Review*. **60** p.252, (1941).

G Lamarche; Simple top-loading cryostat insert for a SQUID magnetometer. *Review of Scientific Intstruments*. **60**(5) p.943, (1989).

G Longworth, M G Townsend, R Provencher, and H Kodama; Magnetic Interactions in Biotites and Oxidised Biotites. *Phys Chem Minerals*. **15** p.71, (1987).

A Manceau, D Bonin, W E E Stone, and J Sanz; Distribution of Fe in the octahedral sheet of trioctahedral micas by polarized EXAFS. *Physics and Chemistry of Minerals*. **17** p.363, (1990).

E Matthias, W Schneider, and R M Steffen; Nuclear Level Splitting Caused by a combined quadropole and magnetic dipole interaction. *Physical Review*. **125** p.261, (1962).

N D Mermin, and H Wagner; Absence of Ferromagnetism or antiferromagnetism in one- of two-dimensional isotropic heisenberg models. *Physical Review Letters*. **17**(22) p.1134, (1966).

A A Migdal; Phase transition in guage and spin-lattice systems. *Zh. eksp. teor. Fiz.* **69** p.1457, (1975).

S Mitra, Applied Mössbauer Spectroscopy: Theory and Practice for Geochemists and Archaeologists. Pergammon Press, 1992

K Ohhashi, and I Tsujikawa; Magnetic Properties of $FeCl_2$-Graphite Compounds. Mossbauer Effect and Magnetic Susceptibility Studies. *Journal Of The Physical Society of Japan*. **37**(1) p.63, (1974).

L Onsager; Crystal Statistics. I. A Two-Dimensional Model with an Order-Disorder Transition. *Physical Review*. **65**(3) p.117, (1944).

V L Pokrovsky; Properties of ordered, continuously degenerate systems. *Advances in Physics*. **28**(5) p.595, (1979).

R V Pound, and G A Rebka; Variation with temperature of the energy of recoil-free gamma-rays from solids. *Physical Review Letters*. **4**(274)(1960).

D G Rancourt, J M Daniels, and H Y Lam; A ^{57}Fe Mossbauer study of Fe_2As: a magnetically induced electric-field-gradient asymmetry. *Canadian Journal of Physics*. **12** p.1540, (1985).

D G Rancourt; Accurate Site Populations from Mossbauer Spectroscopy. *Nuclear Instruments and Methods in Physics Research.* **B44** p.199, (1989).

D G Rancourt, and J Y Ping; Voigt based methods for arbitrary shape static hyperfine parameter distributions in Mössbauer spectroscopy. *Nuclear Instruments and Methods in Physics Research* **B58** p.85 (1991).

D G Rancourt, P Tume, G Lamarche, A E Lalonde, P Biensan, and S Flandrois; Dipole-Dipole Interlayer Interactions As Source of Spin Glass Behaviour in Random Ferromagnetic-Layer Compounds. *Canadian Journal of Physics.* **68** p.1134 (1990).

D G Rancourt; Magnetic Phenomena In layered and Intercalated Compounds, in Chemical Physics of Intercalation, A P Legrand, and S Flandrois, eds., 1989. Plenum Press, New York and London, NATO ASI Series B: Physics Vol. **172** p.79, (1990).

D G Rancourt, M.Z. Dang, and A.E. Lalonde; Mössbauer spectroscopy of tetrahedral Fe^{3+} in trioctahedral micas. *American Mineralogist.* 77 p.34 (1992).

D G Rancourt, P Tume, and A E Lalonde; Kinetics of the $(Fe^{2+} + OH^{-})_{mica} \rightarrow (Fe^{3+} + O^{2-})_{mica} + H$ oxidation reaction in bulk single crystal biotite studied by Mössbauer spectroscopy. *Physics and Chemistry of Minerals.* **20** p.276, (1993a).

D G Rancourt, M Dubé, and P Heron; General method for applying mean field theory to disordered magnetic alloys. *Journal of Magnetism and Magnetic Materials.* **125** p.39 (1993b).

D G Rancourt, A.M. MacDonald, A.E. Lalonde, and J.Y. Ping; Mössbauer absorber Thicknesses for accurate site populations in iron-bearing minerals. *American Mineralogist.* **78** p.1, (1993).

D G Rancourt, I.A.D. Christie, M. Royer, H. Kodama, J.-L. Robert, A.E. Lalonde, and E. Murad; Accurate $[4]Fe^{3+}$, $[6]Fe^{3+}$, $[6]Fe^{2+}$ site populations in synthetic annite. *American Mineralogist.* **79** p.51 (1994).

G J Redhammer, A Beran, E Dachs, and G Anthauer; A Mössbauer and X-Ray Diffraction Study of Annites Synthesized ar Different Oxygen Fugacities and Crystal Chemical Implications. *Physics and Chemistry of Minerals*. **20** p.382, (1993).

M Royer;Site-specific ^{57}Fe Mössbauer recoilless fractions in true trioctahedral micas. M.Sc. Thesis, University of Ottawa, Ottawa, Canada, (1991).

H E Stanley, and T A Kaplan; Possibility of a Phase Transition for the Two-Dimensional Heisenberg Model. *Physical Review Letters*. p.913, (1966).

M G Townsend, G Longworth, C A M Ross, and R Provencher; Ferromagnetic of Antiferromagnetic Fe III Spin Configurations in Sheet Silicates. *Physics and Chemistry of Minerals*. **15** p.64, (1987).

M G Townsend, G Longworth, and H Kodama; Magnetic interactions at low temperatures in chlorite and its products of oxidation: a mossbauer investigation. *Canadian Mineralogist*. **24** p.105, (1986).

M G Townsend, and G Longworth; Sign of the Magnetic Coupling of Fe^{2+} and Fe^{3+} in Biotite. *Physics and Chemistry of Minerals*. **12** p.141, (1985).

R P Tripathi, U Chandra, R Chandra, and S Lokanathan; A Mössbauer study of the effects of heating biotite, phlogopite and vermiculite. *Journal of Inorganic Nuclear Chemistry*. **40** p.1293, (1978).

J Villain; Quantum Theory of one- and two-dimensional ferro and antiferromagnets with and easy magnetization plane. I. Ideal 1-D or 2-D lattices without in-plane anisotropy. *Le Journal de Physique*. **35** p.27, (1974).

D R Wones, and H P Eugster; Stability of biotites, experiment theory and application. *American Mineralogist*. **50** p.1228, (1965).

T Zoltai and J H Stout; Mineralogy: concepts and principles. Burgess Publishing Company, Minneapolis, (1984).

Appendix A
Program Listings

A number of programs were created to support the fitting and simulation of the low temperature annite spectra. The fitting programs are summarized in chapter 7. The fitting and simulation programs were assembled from the modules listed below, and from existing FORTRAN routines and libraries.

The modules written specifically for this project are summarized below, the FORTRAN code listings follow.

MOSSDIST.FOR	Parameter file decoding and calculation for BRFIT
BRSHELL.FOR	Parent shell program for fitting and simulations using the Brand method of generating spectra
BRFIT.FOR	Routines to handle interface with MINUIT for fitting using the BRAND method of generating spectra
BRCALC.FOR	Routine to handle formulation and diagonalization of Hamiltonian according to the method of BRAND
LTSHELL.FOR	Parent shell program for fitting and simulations using the lookup table method of generating spectra. This module has many subroutines in common with BRSHELL.
LTFIT.FOR	Routines to handle interface with MINUIT for fitting using the lookup table method of generating spectra
LTCALC.FOR	Routines to calculate spectrum based on look-up table method.
LTGEN.FOR	Routine to generate look-up table from parameter file
SHOWFIT.FOR	Routines to display fitted spectra

A.1 Listing of MOSSDIST.FOR

```
      SUBROUTINE MossDist(Vel,Cts,FC,chisq,B,cflg)
      IMPLICIT DOUBLE PRECISION(A-H, O-Z)
c This subroutine decodes data in a MES DISTRIBUTIONS type parameter
c file. And calls one of three calculation programs to generate a
spectrum
c using the decoded parameters.
C Cflg has the following meanings
C     1. Crystalline Brand Method
C     2. Powder Brand Method
C     3. Crystalline Blaes Method
C     4. Look-Up Table Method
C     5. Generate Look-Up Table
C

      PARAMETER (NLMAX = 10)
      PARAMETER (NMAX = 512)
      PARAMETER (MMM = 50)
      PARAMETER (PI = 3.141592654)
      Real*8 LookTB(10,10,2,8)
      REAL HF,QS,HFW,HFC,HFH

      REAL MINQS,MAXQS,MINHF,MAXHF
      REAL VEL,CTS,SIG

      INTEGER STPQS,STPHF
      INTEGER STCHN,ENDCHN,NDATA
      INTEGER CFlg
      INTEGER NP, NPATT,I,J,K,HD,QD,QB

      DOUBLE PRECISION B,CHISQ,HTHF,HTQS
      DOUBLE PRECISION HT,Q,Q1,G,CS,DW,FC,ETA,TH,PHI,PHI0,TH0
      DOUBLE PRECISION AL,AL0,BT,BT0,GM,GM0

      DIMENSION HF(4,4),QS(4,4)
      DIMENSION VEL(512),CTS(512),SIG(512)
      DIMENSION B(*),FC(512)

      COMMON/CHANS/NDATA,STCHN,ENDCHN,INCH1,INCH2
C  PARAMETERS PASSED TO Calc Routines
      COMMON /MAFUN/ Q,G,TH,PHI,AL,BT,GM,ETA,DW,CS,HTQS
      COMMON/LTB/LookTB
      COMMON/QSHF/MINQS,MAXQS,STPQS,MINHF,MAXHF,STPHF



C
C     IT CALCS LINES FOR A SITE IN WHICH THE HAMILTONIAN IS DIAGONALISED
```

```
C     ASSUME BASIS WHERE Z AXIS ALONG (SMALL) Q, MAX E.F.G.
C
C     B(1) = NUMBER OF PATTERNS        = NPATT
C     B(2) = NUMBER OF HF DISTRIBUTIONS IN PATT #1
C     B(3) =    "   "  QS        "         "   "   "
C     :
C     B(2*NPATT + 2) = CS1
C     B(           3) = TH1
C     B(           4) = PHI1
C     B(           5) = ETA1
C     B(           6) = AL1
C     B(           7) = BT1
C     B(           8) = GM1
C     B(           9) = DW1
C     B(          10) = HFC11
C     B(          11) = HFW11
C     B(          12) = HFH11
C     B(          13) = HFB11
C     :
C     B(           N) = QSC11, VALUE OF QS NOT EQQ/2
C     B(        N+1) = QSW11
C     B(        N+2) = QSH11
C     B(        N+3) = QSB11
C     :
C
C     NOW CAN CALC ALL MES PARAMS FROM THESE
C     HF ANSD QS ARE CALCULATED FROM INDEPENDENT DISTRIBUTION
C     FUNCTIONS SO THAT FOR EACH HF CONTIBUTIONS ARE CALCULATED
C     FOR EACH VALUE OF QS BEFORE MOVEING TO A NEW HF.
C     THE OTHER PARAMETERS ARE GIVEN IN THE PARAMETER SET, HT
C     IS CALCULATED FROM THE HEIGHT OF BOTH THE QS AND HF DIST
C-----------------------------------------------------------------------
      OPEN(7,FILE = 'BRSIM.TXT')
      CHISQ = 0.
      DO 30 I = 1,NDATA
        IF (CTS(I).NE.0) THEN
           SIG(I) = 1./CTS(i)
        END IF
30    CONTINUE
         OPEN(7,FILE='BRSIM.TXT')
      NPATT = INT(B(1))
      NP  = 0
      DO 40 I = 2,2*NPATT + 1
40       NP = NP + 4*INT(B(I))
      NP = NP + 10*NPATT + 2
      IF (CFlg.NE.5) THEN
        DO 60 I = STCHN,ENDCHN
          FC(I) = B(NP)                !Set FC to BG
60      CONTINUE
      END IF
```

```
      J = 2*NPATT + 1
      DO 300 I = 1,NPATT
         CS = B(J+1)
         TH0 = B(J+2)
         ETA = B(J+4)
         PHI0 = B(J+3)
         AL0 = B(J+5)
         BT0 = B(J+6)
         GM0 = B(J+7)
C         IF (I.EQ.1) THEN
           DW = B(J+8)
C         ELSE
C           DW = DW
C         ENDIF
C ----------------------------------
         J = J + 8
         DO 80 HD = 1,B(2*I)
            DO 70 K = 1,4
               HF(HD,K) = B(J+K)
70          CONTINUE
            J = J + 4
         IF (I.EQ.1) THEN
          HFH =HF(1,3)
          HF(1,3) = 1.00
         ENDIF
80       CONTINUE
         DO 100 QD = 1,B(2*I+1)
            DO 90 K = 1,4
               QS(QD,K) = B(J+K)
90          CONTINUE
            J = J + 4
100      CONTINUE
           IF (cflg.NE.4) THEN
               DO 190 QD = 1,B(2*I+1)
                  DO 185 QB = 1,QS(QD,4)
                    HFW = HF(1,2)*QS(QD,2)
                    HFC = HF(QD,1)-HF(1,2)*QS(QD,1)
                    CALL GAUSSD(HFC,HFW,QS(QD,4),QB,G,HT)
                    HTHF= HF(QD,3)*HFH*HT
                    CALL GAUSSD(QS(QD,1),QS(QD,2),QS(QD,4),QB,Q1,HT)
                    HTQS = HTHF*QS(QD,3)*HT
                    A = (1 + (ETA**2D0)/3D0)**0.5D0
                    Q = Q1/A
                    Q1 =Q
                    IF (AL0.GT.0.AND.AL0.LT.1.5707) HTQS=HTQS/2D0
                    AL = AL0
                    BT = BT0
                    phi = phi0
                    th = th0
                    IA = -1
```

```
170                  IA = IA+1
                     AL= (1-IA)*AL + IA*(PI- AL)
                      IF (CFlg .EQ. 3) THEN
                        CALL BLCALC(VEL,FC)
                      ELSE IF (CFlg.LT.3) THEN
                        CALL BRCALC(Vel,FC,CFlg)
                      END IF
                     IF (AL.LT.1.5707.AND.AL.GT.0) THEN
                       GOTO 170
                     END IF
185                CONTINUE
190              CONTINUE
           ELSE
             Call LTCalc(Vel,FC)
           END IF
300    CONTINUE
       IF (CFlg.NE.5) THEN
         DO 310 K = STCHN, ENDCHN
c          IF (K .LT. INCH1 .OR. K .GT. INCH2) THEN
             CHISQ = CHISQ + (CTS(K)-FC(K))*(CTS(K)-FC(K))*SIG(K)
c          ENDIF
310      CONTINUE
       END IF
       CLOSE(7)
       RETURN

       END

C*********************************************************************
       SUBROUTINE GAUSSD(C,W,TB,NB,Z,HT)
C
       DOUBLE PRECISION A,B,Z,HT
       REAL NRM(29)
C       DATA PI/3.14159265/
       DATA(NRM(I),I=1,29)/1,0.0222,1.0222,1.2353,1.6715,2.0886,
      1  2.5059,2.9232,3.3403,3.7574,4.1743,4.5912,5.0081,5.4250,
      2  5.8418,6.2586,6.6754,7.0921,7.5089,7.9256,8.34233,8.75905,
      3  9.17576,9.59247,10.00917,10.42587,10.84256,11.25925,11.67594/

C      WRITE(*,900)'C,W,TB,NB',C,W,TB,NB
       Z = C
C      WRITE(*,*)'Z =',Z
       IF (TB .GT. 1) THEN
          A = C - 3*W
          B = 6*W/(TB-1)
          Z = A + (NB-1)*B
C      WRITE(*,*)'Z,C',Z,C
       ENDIF
       ITB = INT(TB)
       A = (TB-1)/(6*W*TB*NRM(ITB))
```

```
      IF (TB.EQ.1) A = 1.000
      B = ((Z-C)/W)**2
      HT = DEXP(-0.5D0*B)*A
c      WRITE(7,900)'Z,HT ',Z,HT
900      FORMAT(A10,5F10.4)
      RETURN
      END
C*************************************************************************
      Subroutine LTCALC(vel,Fc)
      real Vel(512)
      Double Precision FC(512)
      FC = DFLOAT(Vel)
      Return
      END

      Subroutine BLCALC(vel,Fc)
       real Vel(512)
       Double Precision FC(512)
       FC = DFLOAT(vel)
       Return
       END
```

A.2 Listing of BRSHELL.FOR

```
C PROGRAM BRSHELL, SHELL TO SIMULATE AND DISPLAY LOW-T SPECTRA OF
ANNITES
C Using Powder Spectrum method of BRAND.
C WRITTEN BY IAIN CHRISTIE March 1992, U OF O.

      INTEGER NDATA,STCHN,ENDCHN,INCH1,INCH2

      CHARACTER SPECFIL*14,PARFIL*14,FN*10
      CHARACTER  ParNam*10(120)

      REAL VEL(512),CTS(512)

      Double Precision B(120)

      COMMON/CHANS/NDATA,STCHN,ENDCHN,INCH1,INCH2

      FN = 'NONAME'

      DO WHILE(.TRUE.)
10    WRITE(6,20)
20    FORMAT(//10X,
C    $'* * * * * * * * * * * * * * * * * * * * * *'/10X,
C    $'*                                           *'/10X,
C    $'*         A N N I T E   P O W D E R         *'/10X,
C    $'*                                           *'/10X,
C    $'*           S I M U L A T I O N S           *'/10X
C    $'*                                           *'/10X,
C    $'*   U N I V E R S I T Y   O F   O T T A W A *'/10X,
C    $'*                                           *'/10X,
C    $'* * * * * * * * * * * * * * * * * * * * * *'//10X,
     $'Select From The Following:'/10X,
     $'1 - Change Spectrum file'/10X,
     $'2 - Change or Edit Parameter file'/10X,
     $'3 - Simulations'/10X,
     $'0 - Exit'/10X,'Your selection ? ')
      READ(5,'(I2)')K
      SELECT CASE(K)
      CASE (1)
        CALL GSF(FN,SPECFIL,Vel,Cts)
      CASE (2)
        CALL GPF(FN,PARFIL,B,ParNam)
      CASE (3)
        CALL BRSIM(SPECFIL,PARFIL,FN,Vel,Cts,B)
      CASE (0)
        Stop
      END Select
      END DO
```

```
      END

C=======================================================================
      SUBROUTINE FILNAM(FNext,FN,FNID)
C Reads filename entered by user, adds correct extension, if the user
presses
C <CR> only the default filename is used.

      IMPLICIT DOUBLE PRECISION (A-H,O-Z)
      CHARACTER FNID*14,FN*10,FNREAD*10,FNext*4

      READ(5,'(A10)')FNREAD
      IF(FNREAD.EQ.'          ')FNREAD=FN   !if no Name entered Use
default
      DO 10 L=1,10
10      IF(FNREAD(L:L).EQ.'.')FNREAD(L:10)='          '
      IF(FNREAD(2:2).NE.':')FNREAD(9:10)='  '
      DO 20 L=1,10
        IF(FNREAD(L:L).EQ.' ')GOTO 30
20    CONTINUE
      L=11
30    FN=FNREAD
      FNID=FNREAD
40    FNID(L:14)=FNEXT       ! add appropriate extension
      RETURN
      END
C=======================================================================
        SUBROUTINE GSF(FN,SPECFIL,Vel,Cts)
C Routine to get the name of the Spectrum File and read the spectrum
data

        INTEGER NDATA,STCHN,ENDCHN,INCH1,INCH2
        Real VEL(512),CTS(512)
        CHARACTER BUF*80
        LOGICAL EX
        INTEGER i

        CHARACTER SPECFIL*14,FN *10

        COMMON/CHANS/NDATA,STCHN,ENDCHN,INCH1,INCH2
25     WRITE(6,30) FN
30     FORMAT (//10X,'What is the name of the Spectrum File ?<',A10'>: ')
       CALL FILNAM('.FLD',FN,SPECFIL)
       INQUIRE(FILE=SPECFIL,EXIST=EX)
       IF(.NOT.EX)THEN
         WRITE(6,41)SPECFIL
41       FORMAT(/1X,A14,' does not exists, try again!')
         GOTO 25
       ENDIF
```

```
      OPEN(10, FILE = SPECFIL)
      READ(10,'(A80)') BUF
      NDATA = 512
      IF (STCHN .EQ. 0) THEN
        STCHN = 1
      ENDIF
      IF (ENDCHN .EQ. 0) THEN
        ENDCHN = NDATA
      ENDIF
      DO 17 I = 1,NDATA
         READ (10,*) VEL(I),CTS(I)
17    CONTINUE
      CLOSE(10)
      RETURN
      END
C=======================================================================
        SUBROUTINE GPF(FN,PARFIL,B,ParNam)
C Routine to get the Name of the Parameter File, and to Read the
Parameters

        LOGICAL EX
        CHARACTER PARFIL*14,FN *10, ParNam*10(120),dummy*25,PARBUF*80
        CHARACTER NUMBUF*15
        INTEGER PARNUM,I,CPOS,FPOS
        DOUBLE PRECISION B(120)

25    WRITE(6,30) FN
30    FORMAT(///1X,'Enter the parameter file name <',A10,'>: ')
      CALL FILNAM('.PAR',FN,PARFIL)
      INQUIRE(FILE=PARFIL,EXIST=EX)
      IF(.NOT.EX)THEN
        WRITE(6,41)PARFIL
41      FORMAT(/1X,A14,' does not exists, try again!')
        GOTO 25
      ENDIF
C  Read the Parameters
      OPEN(12, FILE = PARFIL)
      READ(12,'(A25)') dummy
      DO While (dummy(1:10).NE.'PARAMETERS')
        READ(12,'(A25)') dummy
      END DO
      READ(12,'(A80)') PARBUF
      CPOS = INDEX(PARBUF,'''')
      IF (CPOS .EQ. 0 ) THEN       ! OLD FORMAT
        BACKSPACE 12              ! BACKUP AND READ RECORD AGAIN
        i = 1
        READ(12,10) parnum,ParNam(i),B(I)
        DO While (parnum .ne. 0)     ! Until a blank Line Found
           i = i + 1
           READ(12,10) parnum,ParNam(i),B(I)
```

```
10          FORMAT (I10, A10,F10.5)
          END DO
        ELSE
          I = 1
          DO WHILE (CPOS.NE.0)
            FPOS = CPOS + INDEX(PARBUF(CPOS+1:),'''')
            PARNAM(I) = PARBUF(CPOS+1:FPOS-1)
            IPOS = FPOS+1
            DO WHILE (PARBUF(IPOS:IPOS).EQ.' ')
              IPOS = IPOS + 1
            END DO
            NUMBUF = PARBUF(IPOS:IPOS+13)
            READ(NUMBUF,'(BN,F13.6)',ERR = 200)B(I)
200         I = I + 1
            READ(12,'(A80)')PARBUF
            CPOS = INDEX(PARBUF,'''')
          END DO
        END IF


        CLOSE(12)
        RETURN
        END

C=======================================================================
=====
        SUBROUTINE BRSIM(SPECFIL,PARFIL,FN,Vel,Cts,B)
C Runs Simulation Calculation program

        CHARACTER SPECFIL*14,PARFIL*14,FN*10,ParNam*10(120)
        INTEGER  K, Ndata,STCHN,ENDCHN,INCH1,INCH2

        Real VEL(512),CTS(512)
        DOUBLE PRECISION FC(512),Chisq,B(120)
        COMMON/CHANS/NDATA,STCHN,ENDCHN,INCH1,INCH2

        IF (Cts(1).eq.0) THEN       ! If a valid Spectrum Exists
            CALL GSF(FN,SPECFIL,Vel,Cts)
        END IF
        IF (B(1) .EQ. 0) THEN     ! If a valid Parameter set exists
           CALL GPF(FN,PARFIL,B,ParNam)
        END IF
        CALL MossDist(Vel,Cts,FC,chisq,B,2)
        OPEN(11, FILE = 'SIM.FIT')
        WRITE (11,880) NDATA
        DO 310 K = 1,512
           WRITE(11,890) VEL(K), FC(K), CTS(K)
880        FORMAT (I5)
890        FORMAT (F10.5,1X,F12.3,1X,F12.3)
310     CONTINUE
```

```
      WRITE (11,*) '  CHI SQUARED IS'
      WRITE (11,*) CHISQ
C      CALL PKCHK(VEL,FC,PEAK)
C      DO 312 I = 1,8
C      WRITE(11,311) I,PEAK(I,1),PEAK(I,2)
C311     FORMAT(I2,F8.3,F10.0)
C312   CONTINUE
      CLOSE(11)
      Call ShowFit(Vel,Cts,FC,'  Powder Sim  ')
300   RETURN
      END
```

A.3 Listing of BRFIT.FOR

```
      INCLUDE 'C:\FORTRAN\INCLUDE\FLIB.FI'

C Program BRFIT, parent calling program to invoke MINUIT for use with
BRCALC
C and MOSSDIST.  Parent program gets Data File, Output file, and Save
File
C and opens them.
C NOTE, the user can leave input and output defined as the console.
C Once done the program calls MINUIT to do the fitting.
C The routine BRMIN is defined EXTERNAL and passed to MINUIT as its FCN

      IMPLICIT DOUBLE PRECISION (A-H, O-Z)
      INCLUDE 'C:\FORTRAN\INCLUDE\FLIB.FD'
      CHARACTER OutFil*14, InFil*14, SvFil*14, DatFil*14, FitFil*14
      CHARACTER FN*10
      INTEGER oUnit, iUnit, sUnit,DUNIT,FUNIT
      EXTERNAL FCN
      DIMENSION GRAD(1)

      COMMON/units/iunit,ounit,sUnit,funit,dunit

C Get Input File name
      grad = 0.0
      FN ='D:POWSIM'
      OutFil(1:10) = FN
      InFil(1:10) = FN
      DatFil(1:10) = FN
      FitFil(1:10) = FN
      SvFil(1:10) = FN
      DUNIT = 7
      IUNIT = 8
      OUNIT = 6
      FUNIT = 10
      SUNIT = 11
      DO WHILE(.TRUE.)
10    WRITE(6,20)
20    FORMAT(//10X,
C    $'* * * * * * * * * * * * * * * * * * * * * * *'/10X,
C    $'*                                             *'/10X,
C    $'*         A N N I T E   P O W D E R           *'/10X,
C    $'*                                             *'/10X,
C    $'*           S I M U L A T I O N S             *'/10X
C    $'*                                             *'/10X,
C    $'*   U N I V E R S I T Y   O F   O T T A W A   *'/10X,
C    $'*                                             *'/10X,
C    $'* * * * * * * * * * * * * * * * * * * * * * *'//10X,
```

```
     $'Select From The Following:'/10X,
     $'1 - Run New MINUIT Commands'/10X,
     $'0 - Exit'/10X,'Your selection ? ')
      READ(5,'(I2)')K
      SELECT CASE(K)
      CASE (1)
        CALL BRFIT(InFIL,DatFIL)
      CASE (0)
        Stop
      END Select
      END DO
      END
C=====================================================================
      SUBROUTINE BRFIT(InFIL, DatFil)
      IMPLICIT DOUBLE PRECISION (A-H, O-Z)

      CHARACTER OutFil*14, InFil*14, SvFil*14, DatFil*14, FitFil*14
      CHARACTER FN*10,NULSTR*14
      INTEGER oUnit, iUnit, sUnit,DUNIT,FUNIT
      LOGICAL EX
      EXTERNAL FCN
      DIMENSION GRAD(1)

      COMMON/units/iunit,ounit,sunit,funit,dunit
      NULSTR = '              '
      FN = 'IKOAS5J'
C Get Minuit Parameter, Command File
25      WRITE(*,30) FN
30      FORMAT(//1X,'Enter the Parameter/Command file name <',A10,'>')
        CALL FILNAM('.MIN',FN,InFIL)
        INQUIRE(FILE=InFIL,EXIST=EX)
        IF(.NOT.EX)THEN
           WRITE(*,31)InFIL
31         FORMAT(/1X,A14,' does not exists, try again!')
           GOTO 25
        END IF
        OPEN(iUnit,FILE = InFIL)
C Get Spectrum File
      INQUIRE(FILE=DatFIL,EXIST=EX)
      IF(.NOT.EX)THEN
45      WRITE(*,50) FN
50      FORMAT(//1X,'Enter the DATA file name <',A10,'>')
        CALL FILNAM('.FLD',FN,DatFIL)
        INQUIRE(FILE=DatFIL,EXIST=EX)
        IF(.NOT.EX)THEN
           WRITE(*,51)DatFIL
51         FORMAT(/1X,A14,' does not exists, try again!')
           GOTO 45
        END IF
      END IF
```

```
      OPEN(dunit,File=DatFil)
      Call FCN(NPAR,GRAD,CHISQ,B,1,FUTIL)
      CLOSE (DUNIT)
C Get Save File Name
      INQUIRE(FILE=SvFIL,EXIST=EX)
      IF(.NOT.EX)THEN
        WRITE(*,60) FN
60      FORMAT(//1X,'Enter the MINUIT Output file name <',A10,'> :  ')
        CALL FILNAM('.PAR',FN,SvFIL)
      END IF
      OPEN(SUNIT, FILE = SvFIL)
C Get FIT file Name
      INQUIRE(FILE=FitFIL,EXIST=EX)
      IF(.NOT.EX)THEN
        WRITE(*,70) FN
70      FORMAT(//1X,'Enter the FIT Output file name <',A10,'> :  ')
        CALL FILNAM('.FIT',FN,FitFIL)
      END IF
      OPEN(funit, FILE = FitFIL)
C Get Output (CONSOLE) file name
      INQUIRE(FILE=OutFIL,EXIST=EX)
      IF(.NOT.EX)THEN
        WRITE(*,84)
84      FORMAT(/1X,'Do you Wish to Save the results to a CON file <N>')
        READ(*,'(A1)')YN
        IF(YN.EQ.'Y'.OR.YN.EQ.'y')THEN
          WRITE(*,90) FN
90        FORMAT(//1X,'Enter the CON file name <',A10,'>')
          CALL FILNAM('.CON',FN,OutFIL)
          OUNIT = 9
        END IF
      END IF
      IF (OUNIT.NE.6)THEN
         OPEN(OUnit, FILE = OutFIL)
      ELSE
          OPEN(6,FILE='USER',IOFOCUS=.TRUE., TITLE = 'CON')
      END IF

C
C Call MINUIT to Do the Fitting
      WRITE(*,*) 'CALLING MINUIT'
      Call MNINIT(iunit,ounit,sunit)
      Call MNINTR(FCN,0)
      Close(iunit)
      IF (OUNIT.EQ.6) THEN
        CLOSE(OUNIT,STATUS = 'KEEP')
      ELSE
        CLOSE (OUNIT)
      END IF
      CLOSE(FUNIT)
```

```
      CLOSE(SUNIT)
      END

C=======================================================================
C This routine acts as FCN for Minuit

      SUBROUTINE FCN(NPAR,GRAD,CHISQ,B,IFLAG,FUTIL)
      IMPLICIT DOUBLE PRECISION (A-H,O-Z)
      REAL Vel(512), Cts(512)
      DIMENSION GRAD(*), B(*),  FC(512)
      INTEGER iUnit,oUnit,sUnit,dunit,funit
      INTEGER CFlg,i,idummy
      INTEGER*2, IHR,IMIN,ISEC,IHSEC
      REAL ETIME,TTIME,NTIME,OTIME


      INTEGER Ndata, StChn, EndChn, Inch1, Inch2
      CHARACTER Coment*80(20)

      COMMON/CHANS/NDATA,STCHN,ENDCHN,INCH1,INCH2
      COMMON/units/iUnit,oUnit,sUnit,funit,dunit
      idummy = Npar
      grad = 0
      futil = 0
      IF (IFlag.EQ.1) THEN     ! initialization, Minuit has already read
B
        IT = 1
        TTIME = 0.0
        CALL GETTIM(IHR,IMIN,ISEC,IHSEC)
        OTIME = FLOAT(3600*IHR+60*IMIN+ISEC+0.01*IHSEC)
        READ (dUNIT,'(5I12)') NDATA,STCHN,ENDCHN,INCH1,INCH2
        IF (STCHN .EQ. 0) THEN
          STCHN = 1
        ENDIF
        IF (ENDCHN .EQ. 0) THEN
          ENDCHN = NDATA
        ENDIF
        DO 17 I = 1,NDATA
          READ (dUnit,*) VEL(I),CTS(I)
17      CONTINUE
        DO i = 1,20
          Read(dUnit,'(A80)') Coment(i)
        END DO
        CLOSE(DUNIT)
      END IF

      IF (iFlag .ne. 1) THEN
        Cflg = 2                                          ! Powder Case
        CALL MossDist(Vel,Cts,FC,chisq,B,cflg)
        CALL GETTIM(IHR,IMIN,ISEC,IHSEC)
```

```
        NTIME = FLOAT(3600*IHR + 60*IMIN + ISEC + 0.01*IHSEC)
        ETIME = NTIME - OTIME
        OTIME = NTIME
        TTIME = TTIME+ETIME
        it = it + 1
        write(*,'(I4,F10.1,2F10.2)') it,chisq,ETIME,TTIME
      END IF




      IF (IFlag.eq.3)THEN                                    ! Output to Fitted
File
         write(fUnit,'(3I10)') Ndata,StChn,EndChn
         DO i = 1,ndata
           write(fUnit,'(F9.5,2F10.2)') Vel(i),FC(i),Cts(i)
         END DO
         Write(fUnit,*) '   Chi Squared is:', CHISQ
         DO i = 1,20
           Write(fUnit,*)Coment(i)
         END DO
         CLOSE(FUNIT)
      END IF
      RETURN
      END
C=======================================================================
      SUBROUTINE FILNAM(FNext,FN,FNID)
C Reads filename entered by user, adds correct extension, if the user
presses
INCLUDE 'MOSSDIST.FOR'
C <CR> only the default filename is used.
INCLUDE 'BRCALC.FOR'

INCLUDE 'JACOBI.FOR'
      IMPLICIT DOUBLE PRECISION (A-H,O-Z)
      CHARACTER FNID*14,FN*10,FNREAD*10,FNext*4

      READ(5,'(A10)')FNREAD
      IF(FNREAD.EQ.'          ')FNREAD=FN   !if no Name entered Use
default
      DO 10 L=1,10
10      IF(FNREAD(L:L).EQ.'.')FNREAD(L:10)='          '
      IF(FNREAD(2:2).NE.':')FNREAD(9:10)='  '
      DO 20 L=1,10
        IF(FNREAD(L:L).EQ.' ')GOTO 30
20    CONTINUE
      L=11
30    FN=FNREAD
      FNID=FNREAD
```

```
40      FNID(L:14)=FNEXT        ! add appropriate extension
        RETURN
        END
C=======================================================================

        INCLUDE 'MOSSDIST.FOR'
        INCLUDE 'BRCALC.FOR'
        INCLUDE 'JACOBI.FOR'
```

A.4 Listing of BRCALC.FOR

```
C*********************************************************************
      SUBROUTINE BRCALC(Vel,FC,LIFLG)
C  LiFlg = 1: Crystalline Intensities
C        = 2: Powder Intensities
C        = 3: Calc LP, LI only
C
C     SUBROUTINE WHICH GENERATES LINE POSITIONS AND INTENSITIES BY
C     DIAGONALIZING THE EXCITED STATE HAMILTONIAN AS GIVEN BY BRAND
C---------------------------------------------------------------------
C---------------------------------------------------------------------
      PARAMETER(GMU = .0006757)
      PARAMETER (G1G3 = 1.71)

      REAL Vel(512)
      REAL*4 LP(1:8),LI(1:8)

      DOUBLE PRECISION FC(512)
      DOUBLE PRECISION V
      DOUBLE PRECISION AL, BT, GM
      DOUBLE PRECISION QS,Q,ETA,G,TH,PHI,H,ZC,CS,DW,HTQS
      DOUBLE PRECISION HE(1:8,1:8),EU(1:8),EVR(1:8,1:8),GU(1:2)
      DOUBLE PRECISION U,ER,EI,FR,FI,DFE,XX,YY
      DOUBLE PRECISION GVR(1:4,1:4)
      DOUBLE PRECISION RT2,RT3,RT38
      DOUBLE PRECISION CA,SA,CB,SB,CG,SG,C2A,S2A,C2B,S2B,C2G,S2G
      DOUBLE PRECISION CTH,STH,C2TH,S2TH,CPH,SPH,C2PH,S2PH

      INTEGER LIFLG,i,j,ij,l ,k
      INTEGER NDATA,STCHN,ENDCHN,INCH1,INCH2

C  MOSSBAUER FITTING PARAMETERS PASSED TO BRCALC
      COMMON /MAFUN/ QS,G,TH,PHI,AL,BT,GM,ETA,DW,CS,HTQS
      COMMON/CHANS/NDATA,STCHN,ENDCHN,INCH1,INCH2
      COMMON/LILP/LI,LP

C---------------------------------------------------------------------
      Q = QS/6.D0
      RT2 = DSQRT(2.D0)
      RT3 = DSQRT(3.D0)
      RT38 = DSQRT(3.D0/8.D0)
      CB = DCOS(BT)
      SB = DSIN(BT)
      SA = DSIN(AL)
      CA = DCOS(AL)
      CG = DCOS(GM)
      SG = DSIN(GM)
      C2B = DCOS(2*BT)
      S2B = DSIN(2*BT)
```

```
      C2A = DCOS(2*AL)
      S2A = DSIN(2*AL)
      C2G = DCOS(2*GM)
      S2G = DSIN(2*GM)
      STH = DSIN(TH)
      CTH = DCOS(TH)
      SPH = DSIN(PHI)
      CPH = DCOS(PHI)
      S2TH = DSIN(2*TH)
      C2TH = DCOS(2*TH)
      S2PH = DSIN(2*PHI)
      C2PH = DCOS(2*PHI)
C----------------- SEE PAGE 203 IN BLAES FOR THE FOLLOWING-------------
      XX=FLOAT(3)
      YY = 3./4.
      U = (3*Q * (3*(CB**2) - 1 + ETA*(SB**2)*C2A))/2
      ER = SQRT(XX)*Q * (SB*CB*(ETA*C2A - 3)*CG - ETA*SB*S2A*SG)
      EI = SQRT(XX)*Q * (SB*CB*(ETA*C2A - 3)*SG + ETA*SB*S2A*CG)
      FR = SQRT(YY)*Q * ((3*SB**2 + ETA*(1 + CB**2)*C2A) * C2G -
     1          2*ETA*CB*S2A*S2G)
      FI = SQRT(YY)*Q * ((3*SB**2 + ETA*(1 + CB**2)*C2A) * S2G +
     1          2*ETA*CB*S2A*C2G)
      DFE = (FR**2 + FI**2) - (ER**2 + EI**2)
      HE = 0.0
c      Write(7,'(A10,4F10.5)')'Sin/Cos',sb,cb,s2a,c2a
C-----------------------------------------------------------------------
C  FILL THE EXCITED STATE MATRIX, IN THE MAG FIELD FRAME.  THE BASIS USE
C  IS |3/2>, |1/2>, |-1/2>, |-3/2>
C  PUT REAL PARTS IN U.L. QUADRANT (1,1)-(4,4)
C  PUT IMAGINARY PARTS IN L.L QUADRANT (5,1)-(8,4)
C-----------------------------------------------------------------------
      HE(1,1) = 1.5D0*G + U
      HE(2,2) = 0.5D0*G - U
      HE(4,4) = -1.5D0*G + U
      HE(3,3) = -0.5D0*G - U
      HE(1,2) = ER
      HE(5,2) = -1*EI
      HE(1,3) = FR
      HE(5,3) = -1*FI
      HE(2,1) = ER
      HE(6,1) = EI
      HE(2,4) = FR
      HE(6,4) = -1*FI
      HE(3,1) = FR
      HE(7,1) = FI
      HE(3,4) = -1*ER
      HE(7,4) = EI
      HE(4,2) = FR
      HE(8,2) = FI
      HE(4,3) = -1*ER
```

```
      HE(8,3) = -1*EI
C  COPY REAL PART TO L.R. QUADRANT (5,5)-(8,8)
C  COPY NGATIVE OF THE IMAGINARY PART TO U.R. (1,5)-(4,8)
      DO 200 I = 1,4
         DO 210 J = 1,4
            HE(I+4,J+4) = HE(I,J)
            HE(I,J+4) = -HE(I+4,J)
210      CONTINUE
200   CONTINUE

C-----------------------------------------------------------------------
C  DIAGONALIZE THE MATRIX WITH JACOBI
C-----------------------------------------------------------------------
      CALL JACOBI(HE,8,8,EU,EVR)
C-----------------------------------------------------------------------
C  CALCULATE THE GROUND STATE ENERGY LEVELS, THE GROUND STATE HAMILTONIA
C  IS DIAGONAL.  USE RATIO OF G FACTORS TO CALC ENERGY LEVELS
C-----------------------------------------------------------------------
      HB = -1*G1G3*G
      GU(1) = 0.5D0*HB
      GU(2) = -0.5D0*HB
      GVR = 0.0
      GVR(1,1) = 1
      GVR(2,2) = 1
C-----------------------------------------------------------------------
C  NOW USE E-VALS AND E-VECS CALC BY JACOBI.
C NEED ONLY EU(1:4) SINCE EU(5)= EU(1) ETC.
C  E-VEC FOR EU(I) IS EVR(X,I) + IEVR(X+4,I), X= 1,2,3,4
C-----------------------------------------------------------------------
C LINE POSISITIONS AND INTENSITIES
      DO 300 I = 1,4
         DO 310 J = 1,2
            ij = 2*(i-1) + j
            LP(IJ) = EU(I) - GU(J)
            AR = -1*RT3*(GVR(J,1)*EVR(I,1) + GVR(J,3)*EVR(I,5))-
     1           (GVR(J,2)*EVR(I,2) + GVR(J,4)*EVR(I,6))
            AI = -1*RT3*(GVR(J,1)*EVR(I,5) - GVR(J,3)*EVR(I,1))-
     1           (GVR(J,4)*EVR(I,2) - GVR(J,2)*EVR(I,6))
            BR = RT2*(GVR(J,1)*EVR(I,2) + GVR(J,3)*EVR(I,6))+
     1            RT2*(GVR(J,2)*EVR(I,3) + GVR(J,4)*EVR(I,7))
            BI = RT2*(GVR(J,1)*EVR(I,6) - GVR(J,3)*EVR(I,2))+
     1            RT2*(GVR(J,4)*EVR(I,3) - GVR(J,2)*EVR(I,7))
            CR = -1*(GVR(J,1)*EVR(I,3) + GVR(J,3)*EVR(I,7))-
     1             RT3*(GVR(J,2)*EVR(I,4) + GVR(J,4)*EVR(I,8))
            CI = -1*(GVR(J,1)*EVR(I,7) - GVR(J,3)*EVR(I,3))-
     1             RT3*(GVR(J,4)*EVR(I,4) - GVR(J,2)*EVR(I,8))
       IF (LIFLG .EQ. 1) THEN
            LI(IJ) = (AR**2 + AI**2 + CR**2 + CI**2)*(1 + CTH**2)
     1      + (BR**2 + BI**2)*2*STH**2
     2      - RT2*S2TH*(CPH*(AR*BR + AI*BI - BR*CR - BI*CI)
```

```
     3       + SPH*(AI*BR - AR*BI - BI*CR + BR*CI))
     4       + STH**2*(C2PH*(AR*CR + AI*CI) + S2PH*(AI*CR - AR*CI))
      ELSE IF (LiFlg .EQ. 2 .OR. LiFlg.EQ.3) THEN
            LI(IJ) = AR**2 + AI**2 + BR**2 + BI**2 + CR**2 + CI**2
      END IF
C      write(7,'(I4,F10.5,F10.2)')IJ,LP(IJ),LI(IJ)
310      CONTINUE
300   CONTINUE
      IF (LIFlg.LE.2) THEN
C Now Calculate Spectral contributions
        DO 180 L = 1,8
          DO 170 K = STCHN,ENDCHN
            H = HTQS/3D0 * LI(L)*0.2/DW
            ZC = CS + LP(L)
            IF (ABS(VEL(K)-ZC).LT.(30*DW)) THEN
                CALL LINE(VEL(K),ZC,H,DW,V)
                FC(K) = FC(K) + V
            END IF
170       CONTINUE
180     CONTINUE
      END IF
      RETURN
      END
C*********************************************************************


C*********************************************************************
C     SUBROUTINE TO GENERATE THE VALUE OF A LORENTZIAN LINE AT A
C      PARTICULAR CHANNEL, GIVEN THE LINE POSITION AND INTENSITY
C---------------------------------------------------------------------
      SUBROUTINE LINE(Z,ZC,H,G,V)
      DOUBLE PRECISION H,ZC,G,V
      DOUBLE PRECISION ZB,ZB2,C2,DEN

      ZB = Z - ZC
      ZB2 = ZB**2
      C2 = G**2
      DEN = ZB2+C2
      V = H*C2/DEN
      RETURN
      END
```

A.5 Listing of LTSHELL.FOR

```
C PROGRAM LTSHELL, SHELL TO SIMULATE AND DISPLAY LOW-T SPECTRA OF
ANNITES
C Using Look-Up Table Method.
C WRITTEN BY IAIN CHRISTIE March 1992, U OF O.

      INTEGER NDATA,STCHN,ENDCHN,INCH1,INCH2
      INTEGER STPQS,STPHF
      CHARACTER SPECFIL*14,PARFIL*14,LTFIL*14,FN*10
      CHARACTER  ParNam*10(120)

      REAL VEL(512),CTS(512)
      REAL MINQS,MAXQS,MINHF,MAXHF
      Real*4 LookTB(4,25,25,2,8)

      Double Precision B(120)

      COMMON/QSHF/MINQS,MAXQS,STPQS,MINHF,MAXHF,STPHF
      COMMON/LTB/LookTB
      COMMON/CHANS/NDATA,STCHN,ENDCHN,INCH1,INCH2

      FN = 'NONAME'

      DO WHILE(.TRUE.)
10    WRITE(6,20)
20    FORMAT(//10X,
C    $'* * * * * * * * * * * * * * * * * * * * * *'/10X,
C    $'*                                           *'/10X,
C    $'*   A N N I T E   L O O K  U P  T A B L E   *'/10X,
C    $'*                                           *'/10X,
C    $'*          S I M U L A T I O N S            *'/10X
C    $'*                                           *'/10X,
C    $'*   U N I V E R S I T Y   O F   O T T A W A *'/10X,
C    $'*                                           *'/10X,
C    $'* * * * * * * * * * * * * * * * * * * * * *'//10X,
     $'Select From The Following:'/10X,
     $'1 - Change Spectrum file'/10X,
     $'2 - Change Parameter file'/10X,
     $'3 - Change Look-Up Table'/10X,
     $'4 - Simulations'/10X,
     $'0 - Exit'/10X,'Your selection ? ')
      READ(*,'(I2)')K
      SELECT CASE(K)
      CASE (1)
        CALL GSF(FN,SPECFIL,Vel,Cts)
      CASE (2)
        CALL GPF(FN,PARFIL,B,ParNam)
      CASE (3)
```

```
        CALL GLT(FN,LTFIL)
      CASE (4)
        CALL LTSIM(SPECFIL,PARFIL,LTFIL,FN,Vel,Cts,B)
      CASE (0)
        Stop
      END Select
      END DO
      END


C=====================================================================
      SUBROUTINE FILNAM(FNext,FN,FNID)
C Reads filename entered by user, adds correct extension, if the user
presses
C <CR> only the default filename is used.

      IMPLICIT DOUBLE PRECISION (A-H,O-Z)
      CHARACTER FNID*14,FN*10,FNREAD*10,FNext*4

      READ(5,'(A10)')FNREAD
      IF(FNREAD.EQ.'          ')FNREAD=FN    !if no Name entered Use
default
      DO 10 L=1,10
10      IF(FNREAD(L:L).EQ.'.')FNREAD(L:10)='          '
      IF(FNREAD(2:2).NE.':')FNREAD(9:10)='  '
      DO 20 L=1,10
        IF(FNREAD(L:L).EQ.' ')GOTO 30
20    CONTINUE
      L=11
30    FN=FNREAD
      FNID=FNREAD
40    FNID(L:14)=FNEXT        ! add appropriate extension
      RETURN
      END
C=====================================================================
        SUBROUTINE GSF(FN,SPECFIL,Vel,Cts)
C Routine to get the name of the Spectrum File and read the spectrum
data

        INTEGER NDATA,STCHN,ENDCHN,INCH1,INCH2
        Real VEL(512),CTS(512)
        LOGICAL EX
        INTEGER i

        CHARACTER SPECFIL*14,FN *10

        COMMON/CHANS/NDATA,STCHN,ENDCHN,INCH1,INCH2
25     WRITE(6,30) FN
30     FORMAT (//10X,'What is the name of the Spectrum File ?<',A10'>: ')
       CALL FILNAM('.FLD',FN,SPECFIL)
```

```
      INQUIRE(FILE=SPECFIL,EXIST=EX)
      IF(.NOT.EX)THEN
        WRITE(6,41)SPECFIL
41      FORMAT(/1X,A14,' does not exists, try again!')
        GOTO 25
      ENDIF
      OPEN(10, FILE = SPECFIL)
      READ (10,'(5I12)') NDATA,STCHN,ENDCHN,INCH1,INCH2
      IF (STCHN .EQ. 0) THEN
        STCHN = 1
      ENDIF
      IF (ENDCHN .EQ. 0) THEN
        ENDCHN = NDATA
      ENDIF
      DO 17 I = 1,NDATA
         READ (10,*) VEL(I),CTS(I)
17    CONTINUE
      CLOSE(10)
      RETURN
      END
C=======================================================================
        SUBROUTINE GPF(FN,PARFIL,B,ParNam)
C Routine to get the Name of the Parameter File, and to Read the
Parameters

      LOGICAL EX
      CHARACTER PARFIL*14,FN *10, ParNam*10(120),dummy*25,PARBUF*80
      CHARACTER NUMBUF*15
      INTEGER PARNUM,I,CPOS,FPOS
      DOUBLE PRECISION B(120)

25    WRITE(6,30) FN
30    FORMAT(///1X,'Enter the parameter file name <',A10,'>: ')
      CALL FILNAM('.PAR',FN,PARFIL)
      INQUIRE(FILE=PARFIL,EXIST=EX)
      IF(.NOT.EX)THEN
        WRITE(6,41)PARFIL
41      FORMAT(/1X,A14,' does not exists, try again!')
        GOTO 25
      ENDIF
C  Read the Parameters
      OPEN(12, FILE = PARFIL)
      READ(12,'(A25)') dummy
      DO While (dummy(1:10).NE.'PARAMETERS')
        READ(12,'(A25)') dummy
      END DO
      READ(12,'(A80)') PARBUF
      CPOS = INDEX(PARBUF,'''')
      IF (CPOS .EQ. 0 ) THEN       ! OLD FORMAT
        BACKSPACE 12              ! BACKUP AND READ RECORD AGAIN
```

```
        i = 1
        READ(12,10) parnum,ParNam(i),B(I)
        DO While (parnum .ne. 0)     ! Until a blank Line Found
           i = i + 1
           READ(12,10) parnum,ParNam(i),B(I)
10         FORMAT (I10, A10,F10.5)
        END DO
      ELSE
        I = 1
        DO WHILE (CPOS.NE.0)
          FPOS = CPOS + INDEX(PARBUF(CPOS+1:),'''')
          PARNAM(I) = PARBUF(CPOS+1:FPOS-1)
          IPOS = FPOS+1
          DO WHILE (PARBUF(IPOS:IPOS).EQ.' ')
            IPOS = IPOS + 1
          END DO
          NUMBUF = PARBUF(IPOS:IPOS+13)
          READ(NUMBUF,'(BN,F13.6)',ERR = 200)B(I)
200       I = I + 1
          READ(12,'(A80)')PARBUF
          CPOS = INDEX(PARBUF,'''')
        END DO
      END IF
      CLOSE(12)
      RETURN
      END
C=======================================================================
      SUBROUTINE GLT(FN,LTFIL)

      Real*4 LookTB(4,25,25,2,8)

      LOGICAL EX
      CHARACTER LTFIL*14,FN *10
c      DIMENSION VEL(512),CTS(512), SIG(512), BG(512)

      REAL MINQS,MAXQS,MINHF,MAXHF
      INTEGER STPQS,STPHF, Npatt,p
      LOGICAL NOTEND

      COMMON/QSHF/MINQS,MAXQS,STPQS,MINHF,MAXHF,STPHF
      COMMON/LTB/LookTB

25    WRITE(6,30) FN
30    FORMAT (//10X,'What is the name of the Look Up Table ?<',A10'>: ')
      CALL FILNAM('.LTB',FN,LTFIL)
      INQUIRE(FILE=LTFIL,EXIST=EX)
      IF(.NOT.EX)THEN
        WRITE(6,41)LTFIL
41      FORMAT(/1X,A14,' does not exists, try again!')
        GOTO 25
```

```
      ENDIF
      OPEN(10, FILE = LTFIL)
      Read(10,100)MinHF,MaxHF,StpHF
      Read(10,100)MinQS,MAxQS,StpQS
      Read(10,'(I4)') Npatt
100   FORMAT(2F10.3,I4)
      IF(StpHF.GT.25.OR.StpQS.GT.25) THEN
        write(6,110)
110     FORMAT('This File Is TOO LARGE, Sorry')
      ELSE
        P = 1
        NOTEND = .TRUE.
        DO WHILE (NOTEND)
          DO i = 1,StpHF
            DO j = 1,StpQS
                Read(10,120,END=130) LookTB(p,i,j,1,1),lookTB(p,i,j,1,2)
     $           ,lookTB(p,i,j,1,3)
     $           ,LookTB(p,i,j,1,4),lookTB(p,i,j,1,5),lookTB(p,i,j,1,6)
     $           ,LookTB(p,i,j,1,7),lookTB(p,i,j,1,8)
                Read(10,120,END=130) LookTB(p,i,j,2,1),lookTB(p,i,j,2,2)
     $           ,lookTB(p,i,j,2,3)
     $           ,LookTB(p,i,j,2,4),lookTB(p,i,j,2,5),lookTB(p,i,j,2,6)
     $           ,LookTB(p,i,j,2,7),lookTB(p,i,j,2,8)
120           FORMAT(8F9.5)
            END DO
          END DO
          P = P+1
        END DO
130   CONTINUE
      END IF
      CLOSE(10)
      RETURN
      END
C=======================================================================
=====
      SUBROUTINE LTSIM(SPECFIL,PARFIL,LTFIL,FN,Vel,Cts,B)
C Runs Simulation Calculation program

      CHARACTER LTFIL*14,SPECFIL*14,PARFIL*14,FN*10,ParNam*10(120)
      INTEGER  K, Ndata,STCHN,ENDCHN,INCH1,INCH2
      INTEGER STPQS,STPHF
      Real*4 LookTB(4,25,25,2,8)
      Real VEL(512),CTS(512)
      REAL MINQS,MAXQS,MINHF,MAXHF

      DOUBLE PRECISION FC(512),Chisq,B(120)

      COMMON/CHANS/NDATA,STCHN,ENDCHN,INCH1,INCH2
      COMMON/QSHF/MINQS,MAXQS,STPQS,MINHF,MAXHF,STPHF
      COMMON/LTB/LookTB
```

```
      IF (Cts(1).eq.0) THEN        ! If a valid Spectrum doesn't Exist
          CALL GSF(FN,SPECFIL,Vel,Cts)
      END IF
      IF (B(1) .EQ. 0) THEN     ! If a valid Parameter Set doesn't exist
         CALL GPF(FN,PARFIL,B,ParNam)
      END IF
      IF (LookTB(1,1,1,1,1) .EQ.0) THEN  ! If a Look-Up Table doesn't
Exist
         Call GLT(FN,LTFIL)
      END IF
      CALL LTCALC(Vel,Cts,FC,chisq,B)
      OPEN(11, FILE = 'LTSIM.FIT')
      WRITE (11,880) NDATA
      DO 310 K = 1,512
         WRITE(11,890) VEL(K), FC(K), CTS(K)
880      FORMAT (I5)
890      FORMAT (F10.5,1X,F10.2,1X,F10.2)
310   CONTINUE
      WRITE (11,*) '  CHI SQUARED IS'
      WRITE (11,*) CHISQ
      CLOSE(11)
      Call ShowFit(Vel,Cts,FC,'  Powder Sim  ')
300   RETURN
      CLOSE(7)
      END
```

A.6 Listing of File LTFIT.FOR

```
      INCLUDE 'C:\FORTRAN\INCLUDE\FLIB.FI'

C Parent program gets Data File, Output file, and Save File
C and opens them.
C NOTE, the user can leave input and output defined as the console.
C Once done the program calls MINUIT to do the fitting.
      INCLUDE 'C:\FORTRAN\INCLUDE\FLIB.FD'

      CHARACTER OutFil*14, InFil*14, SvFil*14, DatFil*14, FitFil*14
      CHARACTER FN*10
      INTEGER oUnit, iUnit, sUnit,DUNIT,FUNIT
      INTEGER STPQS, STPHF
      EXTERNAL FCN
      DIMENSION GRAD(1)
      Real*4 LookTB(4,25,25,2,8)
      REAL MINQS,MAXQS,MINHF,MAXHF

      COMMON/units/iunit,ounit,sUnit,funit,dunit
      COMMON/QSHF/MINQS,MAXQS,STPQS,MINHF,MAXHF,STPHF
      COMMON/LTB/LookTB

      grad = 0.0
      FN ='D:POWSIM'
      OutFil(1:10) = FN
      InFil(1:10) = FN
      DatFil(1:10) = FN
      FitFil(1:10) = FN
      SvFil(1:10) = FN
      DUNIT = 7
      IUNIT = 8
      OUNIT = 6
      FUNIT = 10
      SUNIT = 11
      DO WHILE(.TRUE.)
10    WRITE(6,20)
20    FORMAT(//10X,
C    $'* * * * * * * * * * * * * * * * * * * * * *'/10X,
C    $'*                                           *'/10X,
C    $'*        A N N I T E   P O W D E R          *'/10X,
C    $'*                                           *'/10X,
C    $'*          S I M U L A T I O N S            *'/10X
C    $'*                                           *'/10X,
C    $'*   U N I V E R S I T Y   O F   O T T A W A *'/10X,
C    $'*                                           *'/10X,
C    $'* * * * * * * * * * * * * * * * * * * * * * *'//10X,
     $'Select From The Following:'/10X,
     $'1 - Run New MINUIT Commands'/10X,
```

```
     $'0 - Exit'/10X,'Your selection ? ')
      READ(5,'(I2)')K
      SELECT CASE(K)
      CASE (1)
        CALL LTFIT(InFIL,DatFIL)
      CASE (0)
        Stop
      END Select
      END DO
      END

C=====================================================================
      SUBROUTINE LTFIT(InFIL, DatFil)
      IMPLICIT DOUBLE PRECISION (A-H, O-Z)

      CHARACTER OutFil*14, InFil*14, SvFil*14, DatFil*14, FitFil*14
      CHARACTER FN*10,NULSTR*14,LTFIL*14
      INTEGER oUnit, iUnit, sUnit,DUNIT,FUNIT
      INTEGER STPQS, STPHF

      LOGICAL EX
      EXTERNAL FCN
      Real*4 LookTB(4,25,25,2,8)
      REAL MINQS,MAXQS,MINHF,MAXHF

      DIMENSION GRAD(1)

      COMMON/units/iunit,ounit,sUnit,funit,dunit
      COMMON/QSHF/MINQS,MAXQS,STPQS,MINHF,MAXHF,STPHF
      COMMON/LTB/LookTB

      NULSTR = '              '
      FN = 'IKOAS5j'
C Get Minuit Parameter, Command File
25      WRITE(*,30) FN
30      FORMAT(//1X,'Enter the Parameter/Command file name <',A10,'>')
        CALL FILNAM('.MIN',FN,InFIL)
        INQUIRE(FILE=InFIL,EXIST=EX)
        IF(.NOT.EX)THEN
           WRITE(*,31)InFIL
31         FORMAT(/1X,A14,' does not exists, try again!')
           GOTO 25
        END IF
        OPEN(iUnit,FILE = InFIL)
C Get Spectrum File
      INQUIRE(FILE=DatFIL,EXIST=EX)
      IF(.NOT.EX)THEN
45      WRITE(*,50) FN
50      FORMAT(//1X,'Enter the DATA file name <',A10,'>')
        CALL FILNAM('.FLD',FN,DatFIL)
```

```
        INQUIRE(FILE=DatFIL,EXIST=EX)
        IF(.NOT.EX)THEN
           WRITE(*,51)DatFIL
51         FORMAT(/1X,A14,' does not exists, try again!')
           GOTO 45
        END IF
      END IF
      OPEN(dunit,File=DatFil)
      Call FCN(NPAR,GRAD,CHISQ,B,1,FUTIL)
      CLOSE (DUNIT)
C Get Look-Up Table
      Call GLT(FN,LTFIL)

C Get Save File Name
      INQUIRE(FILE=SvFIL,EXIST=EX)
      IF(.NOT.EX)THEN
        WRITE(*,60) FN
60      FORMAT(//1X,'Enter the MINUIT Output file name <',A10,'> :  ')
        CALL FILNAM('.PAR',FN,SvFIL)
      END IF
      OPEN(SUNIT, FILE = SvFIL)
C Get FIT file Name
      INQUIRE(FILE=FitFIL,EXIST=EX)
      IF(.NOT.EX)THEN
        WRITE(*,70) FN
70      FORMAT(//1X,'Enter the FIT Output file name <',A10,'> :  ')
        CALL FILNAM('.FIT',FN,FitFIL)
      END IF
      OPEN(funit, FILE = FitFIL)
C Get Output (CONSOLE) file name
      INQUIRE(FILE=OutFIL,EXIST=EX)
      IF(.NOT.EX)THEN
        WRITE(*,84)
84      FORMAT(/1X,'Do you Wish to Save the results to a CON file <N>')
        READ(*,'(A1)')YN
        IF(YN.EQ.'Y'.OR.YN.EQ.'y')THEN
          WRITE(*,90) FN
90        FORMAT(//1X,'Enter the CON file name <',A10,'>')
          CALL FILNAM('.CON',FN,OutFIL)
          OUNIT = 9
        END IF
      END IF
      IF (OUNIT.NE.6)THEN
         OPEN(OUnit, FILE = OutFIL)
      ELSE
          OPEN(6,FILE='USER',IOFOCUS=.TRUE., TITLE = 'CON')
      END IF

C
C Call MINUIT to Do the Fitting
```

```
      WRITE(*,*) 'CALLING MINUIT'
      Call MNINIT(iunit,ounit,sunit)
      Call MNINTR(FCN,0)
      Close(iunit)
      IF (OUNIT.EQ.6) THEN
        CLOSE(OUNIT,STATUS = 'KEEP')
      ELSE
        CLOSE (OUNIT)
      END IF
      CLOSE(FUNIT)
      CLOSE(SUNIT)
      END



C=====================================================================
C This routine acts as FCN for Minuit

      SUBROUTINE FCN(NPAR,GRAD,CHISQ,B,IFLAG,FUTIL)
      IMPLICIT DOUBLE PRECISION (A-H,O-Z)
      REAL Vel(512), Cts(512)
      DIMENSION GRAD(*), B(*),  FC(512)
      INTEGER iUnit,oUnit,sUnit,DUNIT,FUNIT
      INTEGER i,idummy
      INTEGER Ndata, StChn, EndChn, Inch1, Inch2
      CHARACTER Coment*80(20)
      Real*4 LookTB(4,25,25,2,8)
      INTEGER STPQS,STPHF
      INTEGER*2, IHR,IMIN,ISEC,IHSEC
      REAL ETIME,TTIME,NTIME,OTIME
      REAL MINQS,MAXQS,MINHF,MAXHF

      COMMON/QSHF/MINQS,MAXQS,STPQS,MINHF,MAXHF,STPHF
      COMMON/LTB/LookTB
      COMMON/CHANS/NDATA,STCHN,ENDCHN,INCH1,INCH2
      COMMON/units/iUnit,oUnit,sUnit,FUNIT,DUNIT

      idummy = Npar
      grad = 0
      futil = 0
      IF (IFlag.EQ.1) THEN    ! initialization, Minuit has already read
B
        it = 1
        TTIME = 0.0
        CALL GETTIM(IHR,IMIN,ISEC,IHSEC)
        OTIME = FLOAT(3600*IHR+60*IMIN+ISEC+0.01*IHSEC)
        READ (DUNIT,'(5I12)') NDATA,STCHN,ENDCHN,INCH1,INCH2
        IF (STCHN .EQ. 0) THEN
          STCHN = 1
```

```
        ENDIF
        IF (ENDCHN .EQ. 0) THEN
          ENDCHN = NDATA
        ENDIF
        DO 17 I = 1,NDATA
          READ (DUnit,*) VEL(I),CTS(I)
17      CONTINUE
        DO i = 1,20
          Read(DUnit,'(A80)') Coment(i)
        END DO
      END IF

      IF (IFLAG .NE. 1) THEN
        CALL LTCALC(Vel, Cts, FC, Chisq, B)
        CALL GETTIM(IHR,IMIN,ISEC,IHSEC)
        NTIME = FLOAT(3600*IHR + 60*IMIN + ISEC + 0.01*IHSEC)
        ETIME = NTIME - OTIME
        OTIME = NTIME
        TTIME = TTIME+ETIME
        it = it + 1
        write(*,'(I4,F10.1,2F10.2)') it,chisq,ETIME,TTIME
      ENDIF

      IF (IFlag.eq.3) THEN                              ! Output to
Fitted File
         write(FUnit,'(3I10)') Ndata,StChn,EndChn
         DO i = 1,ndata
           write(FUnit,'(F9.5,2F10.2)') Vel(i),FC(i),Cts(i)
         END DO
         Write(FUnit,*) '   Chi Squared is:', CHISQ
         DO i = 1,20
           Write(FUnit,*)Coment(i)
         END DO
      END IF

      RETURN
      END
C=======================================================================
      SUBROUTINE GLT(FN,LTFIL)

      Real*4 LookTB(4,25,25,2,8)

      LOGICAL EX
      CHARACTER LTFIL*14,FN *10
      REAL MINQS,MAXQS,MINHF,MAXHF
      INTEGER STPQS,STPHF, Npatt,p
      logical notend

      COMMON/QSHF/MINQS,MAXQS,STPQS,MINHF,MAXHF,STPHF
      COMMON/LTB/LookTB
```

```
25    WRITE(6,30) FN
30    FORMAT (//10X,'What is the name of the Look Up Table ?<',A10'>: ')
      CALL FILNAM('.LTB',FN,LTFIL)
      INQUIRE(FILE=LTFIL,EXIST=EX)
      IF(.NOT.EX)THEN
        WRITE(6,41)LTFIL
41      FORMAT(/1X,A14,' does not exists, try again!')
        GOTO 25
      ENDIF
      OPEN(10, FILE = LTFIL)
      Read(10,100)MinHF,MaxHF,StpHF
      Read(10,100)MinQS,MAxQS,StpQS
      Read(10,'(I4)') Npatt
100   FORMAT(2F10.3,I4)
      IF(StpHF.GT.25.OR.StpQS.GT.25) THEN
        write(6,110)
110     FORMAT('This File Is TOO LARGE, Sorry')
      ELSE
        P = 1
        NOTEND = .TRUE.
        DO WHILE (NOTEND)
          DO i = 1,StpHF
            DO j = 1,StpQS
                Read(10,120,END=130) LookTB(p,i,j,1,1),lookTB(p,i,j,1,2)
     $          ,lookTB(p,i,j,1,3)
     $          ,LookTB(p,i,j,1,4),lookTB(p,i,j,1,5),lookTB(p,i,j,1,6)
     $          ,LookTB(p,i,j,1,7),lookTB(p,i,j,1,8)
                Read(10,120,END=130) LookTB(p,i,j,2,1),lookTB(p,i,j,2,2)
     $          ,lookTB(p,i,j,2,3)
     $          ,LookTB(p,i,j,2,4),lookTB(p,i,j,2,5),lookTB(p,i,j,2,6)
     $          ,LookTB(p,i,j,2,7),lookTB(p,i,j,2,8)
120           FORMAT(8F9.5)
            END DO
          END DO
          P = P+1
        END DO
130   CONTINUE
      END IF
      CLOSE(10)
      RETURN
      END
C=======================================================================
=====
      SUBROUTINE FILNAM(FNext,FN,FNID)
; Reads filename entered by user, adds correct extension, if the user
presses
C <CR> only the default filename is used.

      IMPLICIT DOUBLE PRECISION (A-H,O-Z)
```

```
      CHARACTER FNID*14,FN*10,FNREAD*10,FNext*4

      READ(5,'(A10)')FNREAD
      IF(FNREAD.EQ.'          ')FNREAD=FN   !if no Name entered Use
default
      DO 10 L=1,10
10      IF(FNREAD(L:L).EQ.'.')FNREAD(L:10)='          '
      IF(FNREAD(2:2).NE.':')FNREAD(9:10)='  '
      DO 20 L=1,10
        IF(FNREAD(L:L).EQ.' ')GOTO 30
20    CONTINUE
      L=11
30    FN=FNREAD
      FNID=FNREAD
40    FNID(L:14)=FNEXT       ! add appropriate extension
      RETURN
      END

C=============================================================================
==
      INCLUDE 'LTCALC.FOR'
```

A.7 Listing of File LTCALC.FOR

```
      SUBROUTINE LTCALC(Vel, Cts, FC, Chisq, B)
      IMPLICIT DOUBLE PRECISION (A-H, O-Z)

      INTEGER STPQS,STPHF,HD,QD
      INTEGER NDATA,STCHN,ENDCHN,INCH1,INCH2

      REAL HC,HW,QC,QW,Q,G
      REAL HF(4,4), QS(4,4)
      REAL VEL(512),CTS(512),SIG(512)
      REAL MINQS,MAXQS,MINHF,MAXHF
      Real*4 PHF(100),PQS(100)
      Real*4 LookTB(4,25,25,2,8)
      Real*4 LI(1:8), LP(1:8)

      Double Precision B(120)
      Dimension FC(512)

      COMMON/QSHF/MINQS,MAXQS,STPQS,MINHF,MAXHF,STPHF
      COMMON/LTB/LookTB
      COMMON/CHANS/NDATA,STCHN,ENDCHN,INCH1,INCH2
      PARAMETER(MAXDW = 15)
      OPEN(7,FILE = 'D:\LTSIM.TXT')
      QSINC = (MAXQS - MINQS)/(STPHF - 1)
      HFINC = (MAXHF - MINHF)/(STPHF - 1)
      CHISQ = 0.
      DO 30 I = 1,NDATA
        IF (CTS(I).NE.0) THEN
           SIG(I) = 1./CTS(i)
        END IF
30    CONTINUE
      NPATT = INT(B(1))
      NP  = 0
      DO 40 I = 2,2*NPATT + 1
40       NP = NP + 4*INT(B(I))
      NP = NP + 10*NPATT + 2
      DO 60 I = STCHN,ENDCHN
        FC(I) = B(NP)                    !Set FC to BG
60    CONTINUE
      J = 2*NPATT + 1
      IP = 0
      DO 300 I = 1,NPATT
         IP = IP + 1
         CS = B(J+1)
         DW = B(J+8)
         AL = B(J+5)
```

```
          IF (AL.LT.1.5707.AND.AL.GT.0) THEN
           HTAL = 0.5
          ELSE
           HTAL = 1.0
          END IF
C ---------------------------------
          J = J + 8
          DO 80 HD = 1,B(2*I)
             DO 70 K = 1,4
                HF(HD,K) = B(J+K)  !Center, Width, Height, Bins
70           CONTINUE
             J = J + 4
80        CONTINUE
          DO 100 QD = 1,B(2*I+1)
             DO 90 K = 1,4
                QS(QD,K) = B(J+K)
90           CONTINUE
             J = J + 4
100       CONTINUE
          DO HD = 1,B(2*I+1)
             IF (HD.EQ.1.and.i.eq.1)THEN
               HTHF= HF(HD,3)
               HT0=HF(1,3)
             ELSE
               HTHF = HF(HD,3)*HT0
             END IF
             Hc = HF(HD,1)
             Hw = HF(HD,2)
             DO QD = 1,B(2*I+1)
               Qc = QS(QD,1)
               Qw = QS(QD,2)
               CALL LTGAUSS(PHF,Hc,Hw,PQS,Qc,Qw)
               IHF = 0
               II = 1
               htqst=0.0
               DO ii = 1,StpHF
                 IF (PHF(II).GT.0.001) THEN
                   IHF = IHF + 1
                   JJ = 1
                   IQS = 0
                   DO jj = 1,StpQS
                     IF (PQS(JJ)*PHF(II).GT.0.001) THEN
                       Q = MINQS + QSINC*(JJ-1)
                       G = MINHF + HFINC*(II-1)
                       IQS = IQS + 1
                       HTQS = HTHF*QS(QD,3)*PHF(II)*PQS(JJ)*HTAL
                       htqst = htqst+htqs/htal
                       DO L = 1,8
                         LP(L) = LOOKTB(ip,II,JJ,1,L)
                         LI(L) = LOOKTB(ip,II,JJ,2,L)
```

```
                        ZC = CS + LP(L)
                        K = STCHN
                        DO WHILE (K.LE.ENDCHN)
                          IF (ABS(VEL(K)-ZC).LT.(MAXDW*DW)) THEN
                            H = HTQS/3D0 * LI(L)*0.2/DW
                            CALL LINE(VEL(K),ZC,H,DW,V)
                            FC(K) = FC(K) + V
                          ELSE IF(VEL(K).GT.ZC) THEN
                            K = ENDCHN
                          END IF
                          K = K + 1
                        END DO    ! K < EndChn
                      END DO     ! L = 8
                      IF (AL.LT.1.5707.AND.AL.GT.0) THEN
                        DO L = 1,8
                          LP(L) = LOOKTB(iP+1,II,JJ,1,L)
                          LI(L) = LOOKTB(ip+1,II,JJ,2,L)
                          ZC = CS + LP(L)
                          K = STCHN
                          DO WHILE (K.LE.ENDCHN)
                            IF (ABS(VEL(K)-ZC).LT.(MAXDW*DW)) THEN
                              H = HTQS/3D0 * LI(L)*0.2/DW
                              CALL LINE(VEL(K),ZC,H,DW,V)
                              FC(K) = FC(K) + V
                            ELSE IF(VEL(K).GT.ZC) THEN
                              K = ENDCHN
                            END IF
                            K = K + 1
                          END DO    ! K<ENDCHN
                        END DO  ! L
                      END IF
C                      WRITE(7,800)G,Q,LP
                    END IF     ! PQS > 0.001
                  END DO     ! jj < StpQS
                END IF     ! PHF > 0.001
              END DO     ! ii < StpHF
            END DO     !QD
          END DO !HD
C         WRITE(6,910)IHF,IQS
C         READ(*,*)
800   FORMAT('HF',F8.3,'QS ',F8.3,' : ',8F8.3)
900     FORMAT(A10,5F15.4)
910     FORMAT('THIS DIST USED',I3,' HF BINS AND',I3,' QS BINS')
      IF (AL.LT.1.5707.AND.AL.GT.0) IP = IP+1
300   END DO            !NPATT
        DO 310 K = STCHN, ENDCHN
c         IF (K .LT. INCH1 .OR. K .GT. INCH2) THEN
            CHISQ = CHISQ + (CTS(K)-FC(K))*(CTS(K)-FC(K))*SIG(K)
c         ENDIF
310     CONTINUE
```

```
      RETURN
      END
C*********************************************************************
CRY02210
      SUBROUTINE LTGAUSS(PHF,HC,HW,PQS,QC,QW)
      DOUBLE PRECISION B
      REAL MINQS,MAXQS,MINHF,MAXHF,QSINC,HFINC
      INTEGER STPQS,STPHF
      COMMON/QSHF/MINQS,MAXQS,STPQS,MINHF,MAXHF,STPHF
      REAL*8 PQST,PHFT
      Real*4 PHF(100),PQS(100)

      PHFT = 0.0
      PQST = 0.0
      HFINC = (MAXHF - MINHF)/(STPHF - 1)
C Calculate un-normalized intensities, sum intensities to derive
C normalization constant
      DO 3100 I = 1,STPHF
        PHF(I) = 0.0
        Z = MINHF + HFINC*(I-1)
        B = ((Z-HC)/HW)**2
        PHF(I) = EXP(-0.5*B)
        PHFT = PHFT + PHF(I)*ABS(HFINC)
3100  CONTINUE
C Repeat process for QS
      QSINC = (MAXQS - MINQS)/(STPQS - 1)
      DO 3200 I = 1,STPQS
        PQS(I)= 0.0
        Z = MINQS + QSINC*(I-1)
        B = ((Z-QC)/QW)**2
        PQS(I) = EXP(-0.5*B)
        PQST = PQST + PQS(I)*ABS(QSINC)
3200  CONTINUE
C Now renormalize all values, Z is calculated only for debugging
C purposes.
      thf = 0.0
      DO 3300 I = 1,STPHF
        PHF(I) = PHF(I)/PHFT
        thf = thf+phf(i)
        Z = MINHF + HFINC*(I-1)
C        write(7,900)'hf,phf',z,phf(i)
3300  CONTINUE
      tqs = 0
      DO 3400 I = 1,STPQS
        PQS(I) = PQS(I)/PQST
        tqs =tqs+pqs(i)
        Z = MINQS + QSINC*(I-1)
C        write(7,900)'qs,pQS',z,pQS(i)
3400  CONTINUE
      IF (PHF(1).GT.0.1.OR.PHF(STPHF).GT.0.1)THEN
```

```
c         WRITE(*,910)
C         READ(*,*)
       END IF
       IF (PQS(1).GT.0.1.OR.PQS(STPQS).GT.0.1)THEN
c         WRITE(*,920)
       END IF
c       PAUSE

900    FORMAT(A10,5F10.3)
910    FORMAT('THE VALUE OF HF IS TOO CLOSE TO THE EDGE '/,
      $'OF THE LOOK-UP TABLE, THIS WILL DISTORT THE RESULTS')
920    FORMAT('THE VALUE OF QS IS TOO CLOSE TO THE EDGE '/,
      $'OF THE LOOK-UP TABLE, THIS WILL DISTORT THE RESULTS')
       RETURN
       END
C*************************************************************************
C      SUBROUTINE TO GENERATE THE VALUE OF A LORENTZIAN LINE AT A
C       PARTICULAR CHANNEL, GIVEN THE LINE POSITION AND INTENSITY
C-------------------------------------------------------------------------
       SUBROUTINE LINE(Z,ZC,H,G,V)
RY04720
       DOUBLE PRECISION H,ZC,G,V
       DOUBLE PRECISION ZB,ZB2,C2,DEN

       ZB = Z - ZC
       ZB2 = ZB**2
       C2 = G**2
       DEN = ZB2+C2
       V = H*C2/DEN
       RETURN
       END
```

A.8 Listing of File LTGEN.FOR

```
C=================================================================================
=====
C       SUBROUTINE LTGen(PARFIL,FN)

C       INTEGER SS
       INTEGER StpQS, StpHF, Npatt,p

       CHARACTER OutFil*14,PARFIL*14,ParNam*10(120)
       CHARACTER FN*10

       Real*4 LI(1:8),LP(1:8)

       Real Vel(512)
       REAL MinQS,MaxQS,MinHF,MaxHF

       DOUBLE PRECISION Q,G,TH,PHI,AL,BT,GM,ETA,DW,CS,HTQS
       DOUBLE PRECISION FC(512),CHISQ, B(120)
       COMMON/LILP/LI,LP
       COMMON /MAFUN/ Q,G,TH,PHI,AL,BT,GM,ETA,DW,CS,HTQS

       CALL GPF(FN,PARFIL,B,ParNam)
       FC = 0.0
       Vel = 0.0
       WRITE(6,15) FN
15     FORMAT (/5X,'What is the name of the Look-Up Table  ?<',A10,'>: ')
         CALL FILNAM('.LTB',FN,OUTFIL)
C20     WRITE(6,30)
C30     FORMAT(/10X,
C      $'Select one of the following programs:'/10X,
C      $'1 - Blaes method for crystalline spectra'/10X,
C      $'2 - Brand method for  crystalline spectra'/10X,
C      $'3 - Powder spectra method'/10X,
C      $'Your selection ? '/)
C       READ(5,'(I2)')ss
         chisq = 0
       OPEN(11, FILE = OUTFIL)
       Write(6,130)
       Read(5,*) minHF
       Write(6,140)
       Read(5,*) maxHF
       Write(6,150)
       Read(5,*) stpHF
       Write(6,100)
       Read(5,*) minQS
       Write(6,110)
       Read(5,*) maxQS
       Write(6,120)
```

```
      Read(5,*) stpQS
130   Format(/5X,'Min Value Of HF:'\)
140   Format(5X,'Max Value Of HF:'\)
150   Format(5X,'Number of HF Steps:'\)
100   Format(/5X,'Min Value Of QS:'\)
110   Format(5X,'Max Value Of QS:'\)
120   Format(5X'Number of QS Steps:'\)
      QSinc = (maxQS - MinQS)/(StpQS-1)
      HFinc = (maxHF - MinHF)/(StpHF-1)
      Write(11,200)MinHF,MaxHF,StpHF
      Write(11,200)MinQS,MaxQS,StpQS
200   Format(2F10.3,I4)
      Npatt = B(1)
      Write(11,'(I4)')Npatt
      DO p = 1,Npatt
        J = 2*B(1) + 1 + (p-1)*16
        CS = 0.0
        TH = B(J+2)
        ETA = B(J+4)
        PHI = B(J+3)
        AL = B(J+5)
        BT = B(J+6)
        GM = B(J+7)
        DW = B(J+8)
        DO  i = 0,(StpHF-1)
          G = MinHF + i*HFinc
          DO  j = 0, (StpQS-1)
            Q = MinQS + J*Qsinc
            CALL BRCALC(Vel,FC,3)
            Write(11,210)LP
            Write(11,210)LI
210         FORMAT(8F9.5)
          END DO
        END DO
        IF (AL.LT.1.5707.AND.AL.GT.0) THEN
          AL = 3.14159 - AL
          DO  i = 0,(StpHF-1)
            G = MinHF + i*HFinc
            DO  j = 0, (StpQS-1)
              Q = MinQS + J*Qsinc
              CALL BRCALC(Vel,FC,3)
              Write(11,210)LP
              Write(11,210)LI
            END DO
          END DO
        END IF
      END DO
      CLOSE(11)
      RETURN
      END
```

```
C=======================================================================
      SUBROUTINE FILNAM(FNext,FN,FNID)
C Reads filename entered by user, adds correct extension, if the user
presses
C <CR> only the default filename is used.

C      IMPLICIT DOUBLE PRECISION (A-H,O-Z)
      CHARACTER FNID*14,FN*10,FNREAD*10,FNext*4

      READ(5,'(A10)')FNREAD
      IF(FNREAD.EQ.'          ')FNREAD=FN    !if no Name entered Use
default
      DO 10 L=1,10
10      IF(FNREAD(L:L).EQ.'.')FNREAD(L:10)='          '
      IF(FNREAD(2:2).NE.':')FNREAD(9:10)='  '
      DO 20 L=1,10
        IF(FNREAD(L:L).EQ.' ')GOTO 30
20    CONTINUE
      L=11
30    FN=FNREAD
      FNID=FNREAD
40    FNID(L:14)=FNEXT        ! add appropriate extension
      RETURN
      END


C=======================================================================
        SUBROUTINE GPF(FN,PARFIL,B,ParNam)
C Routine to get the Name of the Parameter File, and to Read the
Parameters

        LOGICAL EX
        CHARACTER PARFIL*14,FN *10, ParNam*10(120),dummy*25,PARBUF*80
        CHARACTER NUMBUF*15
        INTEGER PARNUM,I,CPOS,FPOS
        DOUBLE PRECISION B(120)

25    WRITE(6,30) FN
30    FORMAT(///1X,'Enter the parameter file name <',A10,'>: ')
      CALL FILNAM('.PAR',FN,PARFIL)
      INQUIRE(FILE=PARFIL,EXIST=EX)
      IF(.NOT.EX)THEN
        WRITE(6,41)PARFIL
41      FORMAT(/1X,A14,' does not exists, try again!')
        GOTO 25
      ENDIF
C  Read the Parameters
      OPEN(12, FILE = PARFIL)
      READ(12,'(A25)') dummy
      DO While (dummy(1:10).NE.'PARAMETERS')
```

```
        READ(12,'(A25)') dummy
      END DO
      READ(12,'(A80)') PARBUF
      CPOS = INDEX(PARBUF,'''')
      IF (CPOS .EQ. 0 ) THEN       ! OLD FORMAT
        BACKSPACE 12              ! BACKUP AND READ RECORD AGAIN
        i = 1
        READ(12,10) parnum,ParNam(i),B(I)
        DO While (parnum .ne. 0)     ! Until a blank Line Found
           i = i + 1
           READ(12,10) parnum,ParNam(i),B(I)
10         FORMAT (I10, A10,F10.5)
        END DO
      ELSE
        I = 1
        DO WHILE (CPOS.NE.0)
          FPOS = CPOS + INDEX(PARBUF(CPOS+1:),'''')
          PARNAM(I) = PARBUF(CPOS+1:FPOS-1)
          IPOS = FPOS+1
          DO WHILE (PARBUF(IPOS:IPOS).EQ.' ')
            IPOS = IPOS + 1
          END DO
          NUMBUF = PARBUF(IPOS:IPOS+13)
          READ(NUMBUF,'(BN,F13.6)',ERR = 200)B(I)
200       I = I + 1
          READ(12,'(A80)')PARBUF
          CPOS = INDEX(PARBUF,'''')
        END DO
      END IF
      CLOSE(12)
      RETURN
      END
```

A.9 Listing of SHOWFIT.FOR

```
C Show Fit, a program to Display graphs of Fitted Files.
      INCLUDE 'C:\FORTRAN\INCLUDE\FGRAPH.FI'
      SubRoutine ShowFit(Vel,Cts,FC,Title)

      INCLUDE 'C:\FORTRAN\INCLUDE\FGRAPH.FD'

      Double Precision Xmax,Xmin,Ymax,Ymin,Ymid,Yrang,Wmax,Wmin
      Real Vel(512), Cts(512), rcol,cinc
      Double Precision FC(512),Y(2,512),X(512),Diff(512)
      Integer*2 status2,nrows,col
      Integer*4 nint,v
      CHARACTER Dstr*10,nstr*3, Title*14
      RECORD /videoconfig/vc
      RECORD /rccoord/s
      RECORD /WXYcoord/r

      X = Vel
       status2 = setvideomode($maxresmode)
c      call ClearScreen($GCLEARSCREEN)
      CALL GetVideoConfig(vc)


      DO i = 1,512
         Y(1,i) = Cts(i)
         Y(2,i) = FC(i)
         Diff(i) = FC(i) - Cts(i)
      END DO
C Get min and max of all arrays
       Xmax = X(1)
       Xmin = X(512)
       Ymax = 0.
       Dmax = 0.
       Dmin = 10000000000.
       Ymin = 10000000000.
       Do j = 1 ,512
         Do i = 1 ,2
            Ymax = max(ymax,Y(i,j))
            Ymin = Min(ymin,Y(i,j))
         END DO
         Dmax = Max(dmax,diff(j))
         Dmin = Min(dmin,diff(j))
      END DO
C Draw the Fitted Spectrum Graph, using the min and max info
      Ymid = (Ymax+Ymin)/2
      Yrang = 1.5*(Ymax - Ymin)
      Wmax = Ymid + 0.5*Yrang
      Wmin = Ymid - 0.5*Yrang
      nrows = vc.numtextrows
```

```
      ncols = vc.numtextcols
      xpix = vc.numxpixels
      ypix = vc.numypixels
      Charw = INT(xpix/ncols)
      Charh = INT(ypix/nrows)
      Status2 = SetBkColor($White)
      Status2 = SetColor(1)
C Write Title
      status2 = SetTextColor(1)
      Call SetTextPosition(2,int(ncols/2 - 7),s)
      Call outtext(Title)
C Write Y Titles
      Call SetTextWindow(3,1,nrows-1,10)
      write(dstr,'(F10.0)')wmax
      Call SetTextPosition(3,1,s)
      Call OutText(dstr)
      write(dstr,'(F10.0)')wmin
      Call SetTextPosition(nrows-1,1,s)
      Call OutText(dstr)
      write(dstr,'(F10.0)')Ymid
      Call SetTextPosition(int2((nrows-4)/2),1,s)
      Call OutText(dstr)
C Write X Titles
      Call SetTextWindow(nrows,1,nrows,ncols)
      nint = int4 (vel(512) - vel(1) + 0.5)
      V = int(vel(1))
      col = 10
      rcol = 10.0
      cinc = Float(ncols-10)/Float(nint)
      DO i = 1,nint,2
        write(nstr,'(i3)')v
        IF (col.lt.(Ncols-2)) THEN
           Call SetTextPosition(nrows,col,s)
           Call OutText(nstr)
        END IF
        col = 10 + int(i*cinc + 0.5)
        v = v + 2
      END DO
C Set the Viewport and Window for the graph
      xminpx = 10*charw
      xmaxpx = xpix-5
      yminpx = 3*Charh
      ymaxpx = ypix - int(3*charH/2)
      Status2 = Rectangle($GBORDER,xminpx,yminpx,xmaxpx,ymaxpx)
      Call SetViewPort(xminpx,yminpx,xmaxpx,ymaxpx)
      status2 = SetWindow(.TRUE.,Xmin,wmin,Xmax,wmax)
C Plot Tick Marks on X axis
      v = int(vel(1))
      DO i = 1,nint,2
         call MoveTo_w(v,wmin,r)
```

```
         Status2 = LineTo_w(v,wmin+(0.02*Yrang))
         v = v + 2
      END DO
C Plot the counts as points  Plot the Fitted points as a Line
      Status2 = Setpixel_w(vel(1),Cts(1))
      Call moveTo_w(vel(1),FC(1),r)
      DO i = 2,512
          Status2 = setcolor(1)
          Status2 = SetPixel_w(vel(i),Cts(i))
          Status2 = setcolor(4)
          Status2 = LineTo_w(vel(i),Fc(i))
      END DO
      Read(*,*)              ! wait for User to hit enter
      Call ClearScreen ($GCLEARSCREEN)
C Rescale the graph for the Diff spectrum
      Ymid = (Dmax+Dmin)/2
      Yrang = 1.5*(Dmax - Dmin)
      Wmax = Ymid + 0.5*Yrang
      Wmin = Ymid - 0.5*Yrang
C Write Title
      Call SetTextWindow(0,0,nrows,ncols)
      status2 = SetTextColor(1)
      Call SetTextPosition(2,int(ncols/2 - 7),s)
      Call outtext(Title)

C Write Y Titles for Diff Spectrum
      status2 = SetTextColor(1)
      Call SetTextWindow(3,1,nrows-1,10)
      write(dstr,'(F10.0)')wmax
      Call SetTextPosition(3,1,s)
      Call OutText(dstr)
      write(dstr,'(F10.0)')wmin
      Call SetTextPosition(nrows-1,1,s)
      Call OutText(dstr)
      write(dstr,'(F10.0)')Ymid
      Call SetTextPosition(int2((nrows-4)/2),1,s)
      Call OutText(dstr)

C Write X Titles
      Call SetTextWindow(nrows,1,nrows,ncols)
      nint = int4 (vel(512) - vel(1) + 0.5)
      V = int(vel(1))
      col = 10
      rcol = 10.0
      cinc = Float(ncols-10)/Float(nint)
      DO i = 1,nint,2
        write(nstr,'(i3)')v
        IF (col.lt.(Ncols-2)) THEN
           Call SetTextPosition(nrows,col,s)
           Call OutText(nstr)
```

```
        END IF
        col = 10 + int(i*cinc + 0.5)
        v = v + 2
      END DO
      status2 = setcolor(1)
C Set ViewPort and Window for Diff Spectrum
      Status2 = Rectangle($GBORDER,0,0,xmaxpx-xminpx,ymaxpx-yminpx)
      status2 = SetWindow(.TRUE.,Xmin,wmin,Xmax,wmax)
C Plot Tick Marks on X axis
      v = int(vel(1))
      DO i = 1,nint,2
         call MoveTo_w(v,wmin,r)
         Status2 = LineTo_w(v,wmin+(0.02*Yrang))
         v = v + 2
      END DO
C
      Call MoveTo_w(vel(1),0,r)
      Status2 = setcolor(1)
      Status2 = LineTo_w(vel(512),0)
      Status2 = SetColor(4)
      Call MoveTo_w(vel(1),Diff(1),r)
      DO i = 2,512
          Status2 = LineTo_w(vel(i),Diff(i))
      END DO
      Read(*,*)              ! wait for User to hit enter
      Status2 = SetVideoMode($defaultmode)
      RETURN
      END
```

Appendix B
Calculation of Dipolar Hyperfine Field

The dipolar contribution to the hyperfine field is given by (see equation 6.16)

$$H_D = \mu_B q \ . \tag{B.1}$$

In order to apply this factor to fitting it is necessary to establish the ratio $k_{H\Delta}$:

$$k_{H\Delta} = \frac{g^* \mu_N H_D}{\Delta} = \frac{g^* \mu_N H_D}{\frac{1}{2} e^2 qQ}. \tag{B.2}$$

We begin by calculating the value of q_1, which is the value of q when $\frac{1}{2}e^2qQ = 1$ mm/s. Using cgs units, in which:

$$mm/s = 7.7028 \times 10^{-20} erg, \tag{B.3}$$

$$e = 4.803 \times 10^{-10} esu, \tag{B.4}$$

$$\mu_B = 9.27 \times 10^{-21} \ {}^{erg}/_{G} \tag{B.5}$$

and for $[Fe^{2+}]$,

$$Q = 0.21 \times 10^{-21} cm^2, \tag{B.6}$$

the value of q_1 is:

$$q_1 = 3.18 \times 10^{-24} \ {}^{G^2}/_{erg}. \tag{B.7}$$

So that

$$H_{D1} = \mu_B q_1 = 29.4 kG \tag{B.8}$$

and therefore:

$$g^* \mu_N H_{D1} = 6.757 \times 10^{-3} H_D = 0.1986 \ {}^{mm}/_{s}. \tag{B.9}$$

Finally, then,

$$k_{H\Delta} = 0.2, \tag{B.10}$$

Which is the value which is used in equation 7.3.

Appendix C
Channel-Wise Spectral Area Calculations

In the absence of an acceptable physical fit to Mössbauer spectrum site populations may be obtained using channel-wise spectral area calculations. The calculation is carried out by first identifying channels which contain a contribution from only one population. Now, the spectral area, A, in any n channels (between channels n_i and n_f) is obtained simply as the sum of the differences between the counts in each channel, C(i), and the spectral background, BG:

$$A = \sum_{i=n_i}^{n_f} \left(BG - C(i)\right) \qquad \text{(C.1)}$$

As an example, the site populations of the Fe^{3+} lines were determined using this by first calculating the spectral area of the well resolved outside lines of each pattern (to which only Fe^{3+} contributes) and then extrapolating to obtain the area of the entire six line patterns. Since the six lines in the Fe^{3+} patterns have the standard powder intensity ratios (3:2:1:1:2:3)[1]; the total intensity contained in a pattern was taken to be twice the area of the outer lines. These areas were then compared to the total spectral area (obtained by summing over all channels) to give relative subspectral areas (see table C.1). The error bounds on these spectral areas result principally from uncertainty in which channels to include in each of the patterns, as each line is not perfectly resolved but overlaps with lines on either side. There is also some uncertainty in determining the BG level. There is good agreement between the site populations determined by this method and those determined by analysis of the high temperature spectra.

[1] The $[Fe^{3+}]$ pattern has the standard sextet intensity ratios because, unlike $[Fe^{2+}]$, $\frac{1}{2}e^2qQ \ll g^*\mu_N H$.

Table C.1 Site populations of Fe^{3+} contributions as determined from RT, LNT, and LHT spectra.

Spectrum	A_{3+}	$A_{[]}$	$A_{<>}$
RT	11.2± 0.3	7.7 ± 0.5	3.6 ± 0.4
LNT	11.1 ± 0.3	7.5 ± 0.4	3.5 ± 0.4
7K	11.0± 0.3	7.4 ± 0.4	3.6 ± 0.4

The RT and LNT populations are determined from the results of Rancourt *et al.* (1994). The LHT populations are determined by channel-wise spectral area calculation.

Appendix D
Mössbauer Spectra of Oxidized Synthetic Annite

D.1 Introduction

Two portions of the synthetic sample were oxidized to modify the relative populations of [Fe^{2+}] and [Fe^{3+}]. The samples were heated in 1 atm for 5 hrs at 300° C and 370° C respectively. As in the case of the virgin samples, the site populations of the three Fe species were determined from RT and LNT Mössbauer spectroscopy (table D.1).

Originally, it was hoped that the temperature series of the three synthetic samples would allow for the description of the combined effects of temperature and composition on the magnetic state of annite. It was also hoped that the highly oxidized sample would provide a clear picture of the Fe^{3+} sites which could then be used as an aid in stripping the Fe^{3+} contributions from the virgin sample. This hope was based on the erroneous assumption that the [Fe^{3+}] sites produced by oxidation would be equivalent to the [Fe^{3+}] sites resulting from synthesis. However, upon further investigation it was found that this was not, in fact, the case. In particular, it was found that the oxidation process did not produce [Fe^{3+}] homogeneously throughout the sample (Rancourt, unpublished).

Furthermore, the low temperature spectrum of the virgin synthetic annite proved to be sufficiently complex that time did not permit expanding the analysis to the oxidized samples. However, even without detailed analysis the Mössbauer spectra of the oxidized samples support many of the findings from the discussion of virgins samples.

D.2 Results

For each oxidized sample Mössbauer spectra were recorded at 4.2K, 15K, 25K, 40K (for the partially oxidized sample only), 77K, and 295K. The two temperature sequences are shown in figures D.1 and D.2.

Figure D.1 shows the results for the partially oxidized sample. The 4.2K spectrum is similar to the 7K spectrum of the virgin sample (compare to figure 7.3a),. Note that the increased Fe^{3+} population in this sample is obvious in the growth of the outer peaks in figure D.1a compared to figure 7.3a. The increased Fe^{3+} population also allows the distinction between the temperature dependences of the [Fe^{2+}] and Fe^{3+} be seen even more clearly than in the virgin sample (contrast the relative intensities of the [Fe^{2+}] and

Fe^{3+} lines in the figures D.1a and b) However, it also appears that the proportion of HFS [Fe^{2+}] decreases more rapidly in the partially oxidized sample than in the virgin sample (compare figure C.1c and d to Figure 7.3c, d, and e). At high temperatures the partially oxidized sample spectra are similar to those of the virgin sample except that a prominent Fe^{3+} peak is visible between the peaks of the [Fe^{2+}] doublet.

The low temperature spectra of the oxidized sample (figure D.2) show the presence of a predominantly HFS Fe^{3+} contribution. Note, however, that the lines in the spectrum a so broad as to prevent the discrimination of the [Fe^{3+}] and $\langle Fe^{3+} \rangle$ contributions. The rapid decrease in HFS Fe^{3+} intensity at temperatures above 4.2K is also evident in this temperature series. For instance, notice that at 15 K there is already evidence of a significant paramagnetic Fe^{3+} fraction in the centre of the spectrum. At 25 K the HFS Fe^{3+} has all but disappeared, and the 40K spectrum looks similar to the high temperature spectrum except for a vestigial HFS [Fe^{2+}] contribution at 5.5 mm/s and in the low velocity shoulder of the dominant paramagnetic Fe^{3+} peak.

Table D.1 Site populations of Fe^{3+} contributions as determined from RT spectra of samples of annite oxidized for five hours at 300° C (partially oxidized) and 370° C (oxidized).

Sample	A_{3+} (%)	$A_{[]}$ (%)	$A_{\langle\rangle}$ (%)
Partially Oxidized	24± 2	20 ± 2	4.0 ± 0.5
Oxidized	65 ± 2	60 ± 2	4.0 ± 0.5

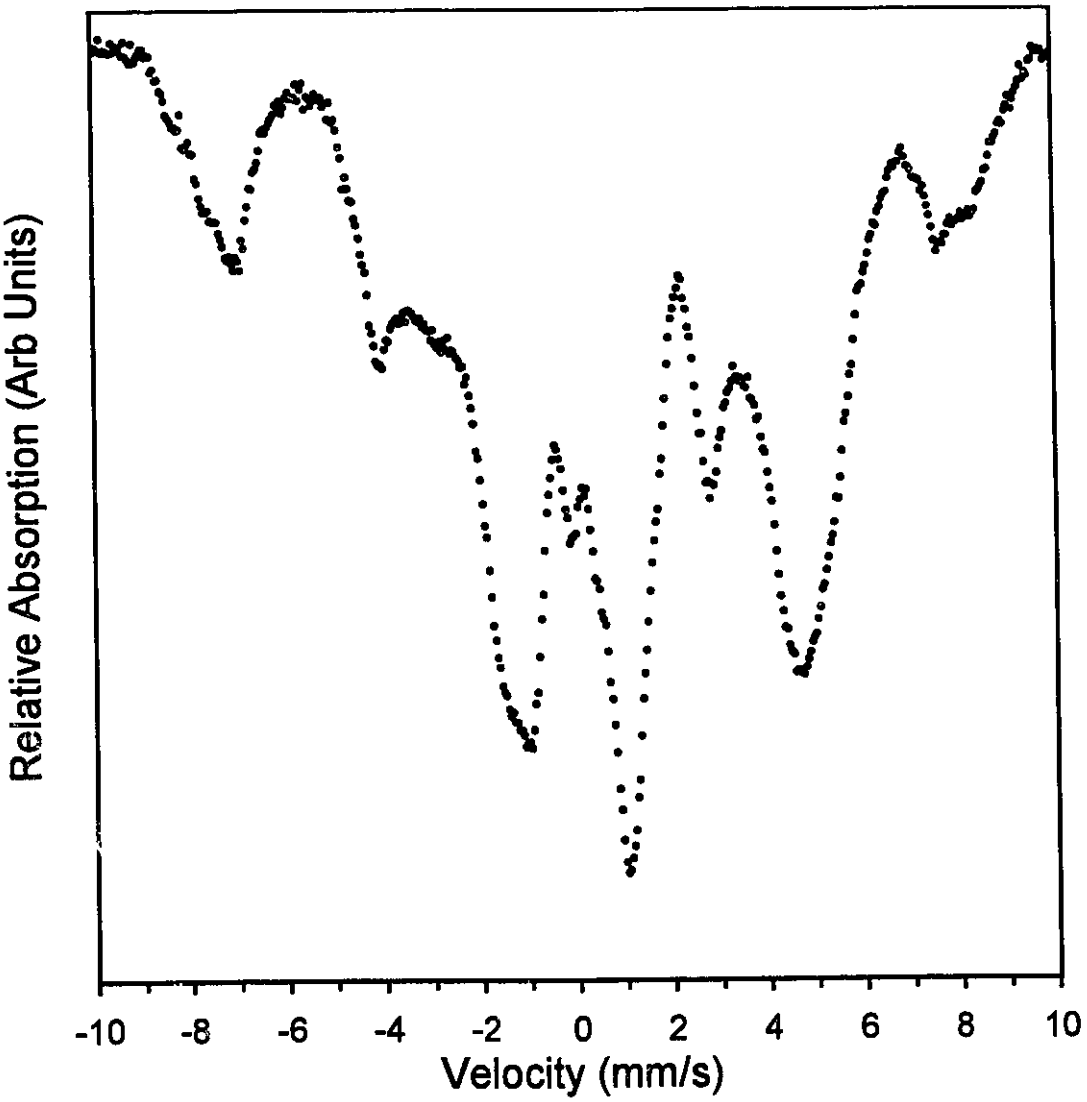

Figure D.1a *Mössbauer spectrum of partially oxidized synthetic annite at 4.2K.*

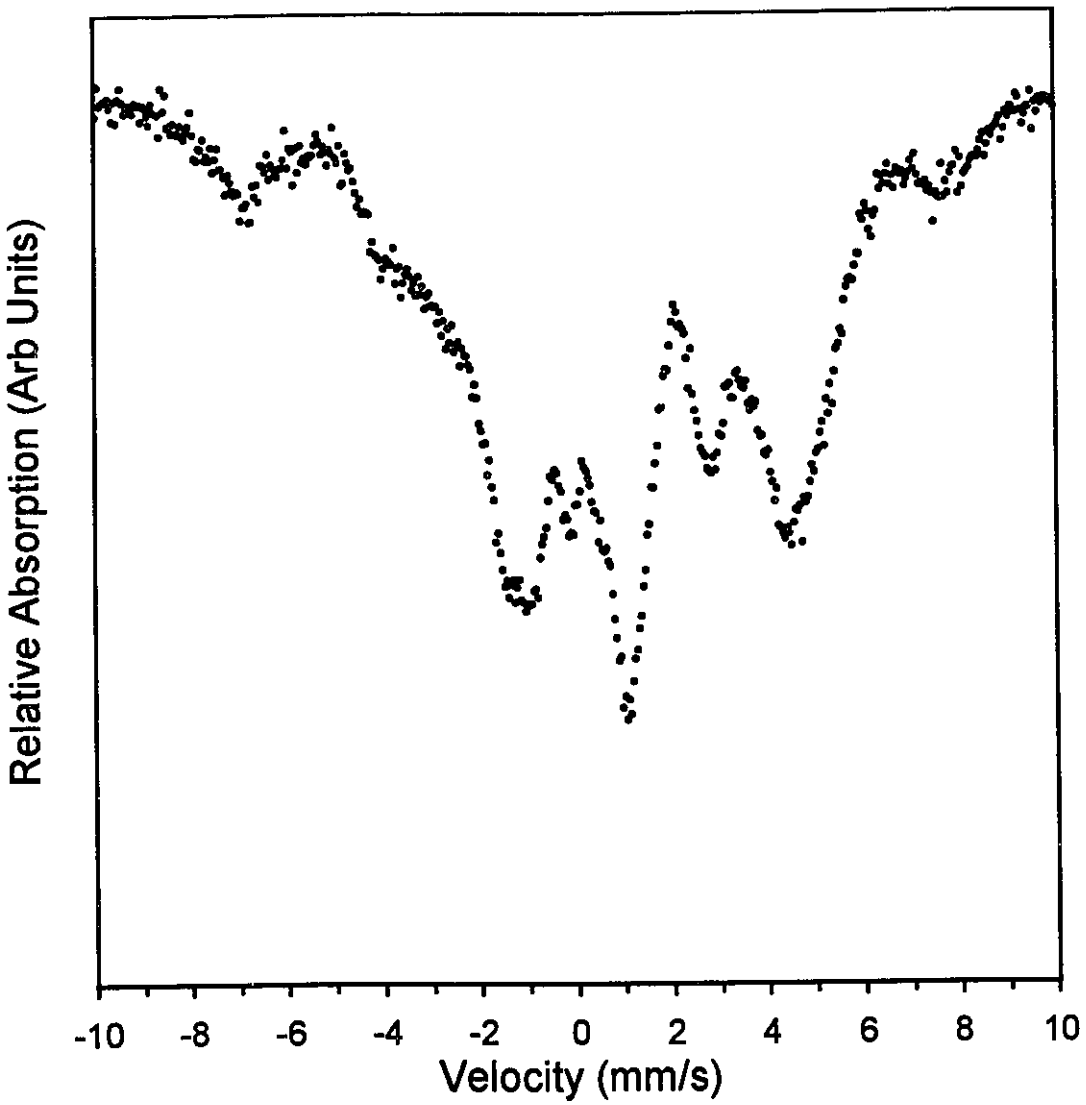

Figure D.1b *Mössbauer spectrum of partially oxidized synthetic annite at 15K.*

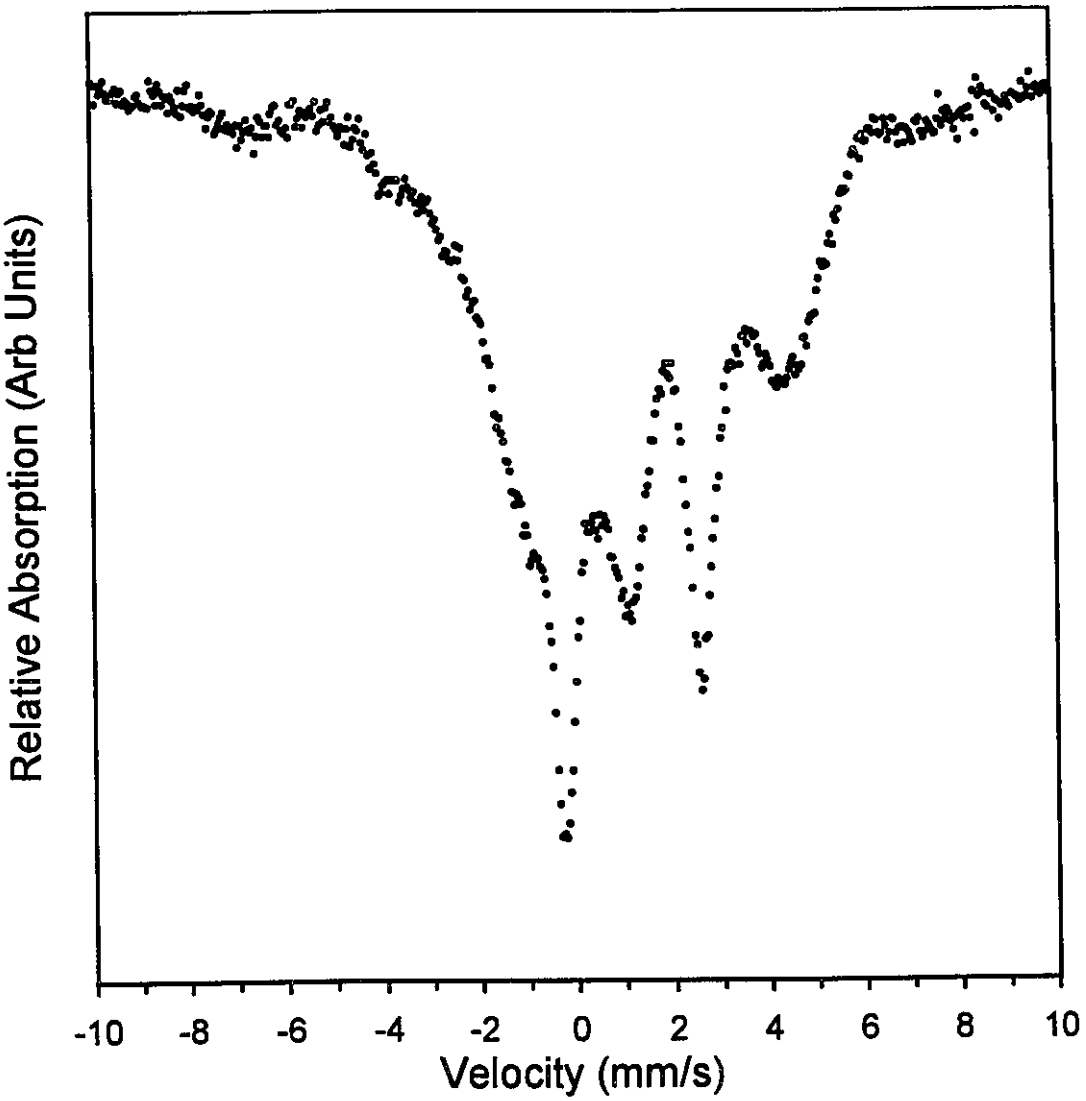

Figure D.1c *Mössbauer spectrum of partially oxidized synthetic annite at 25K.*

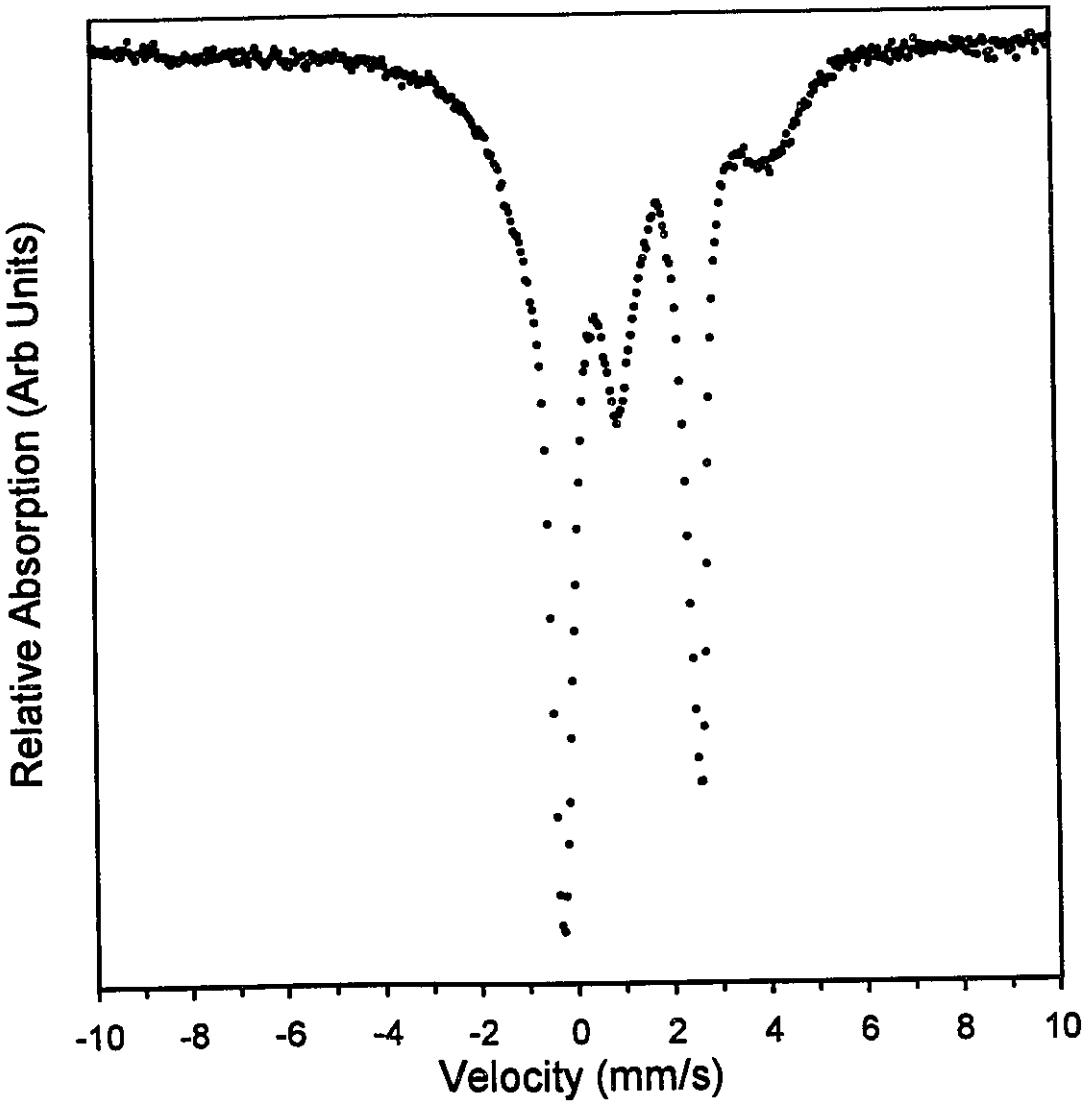

Figure D.1d *Mössbauer spectrum of partially oxidized synthetic annite at 40K.*

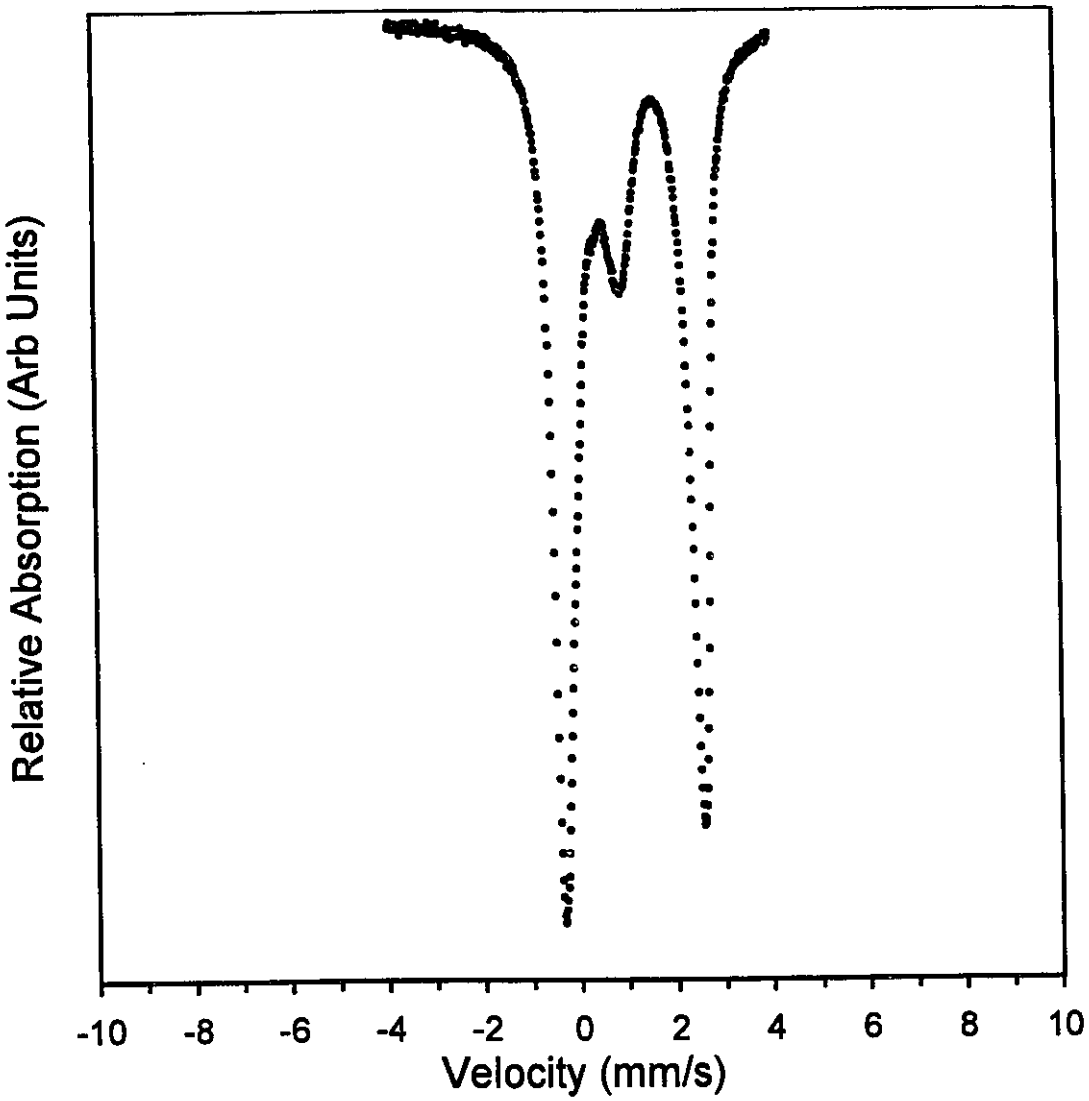

Figure D.1e *Mössbauer spectrum of partially oxidized synthetic annite at 77K*

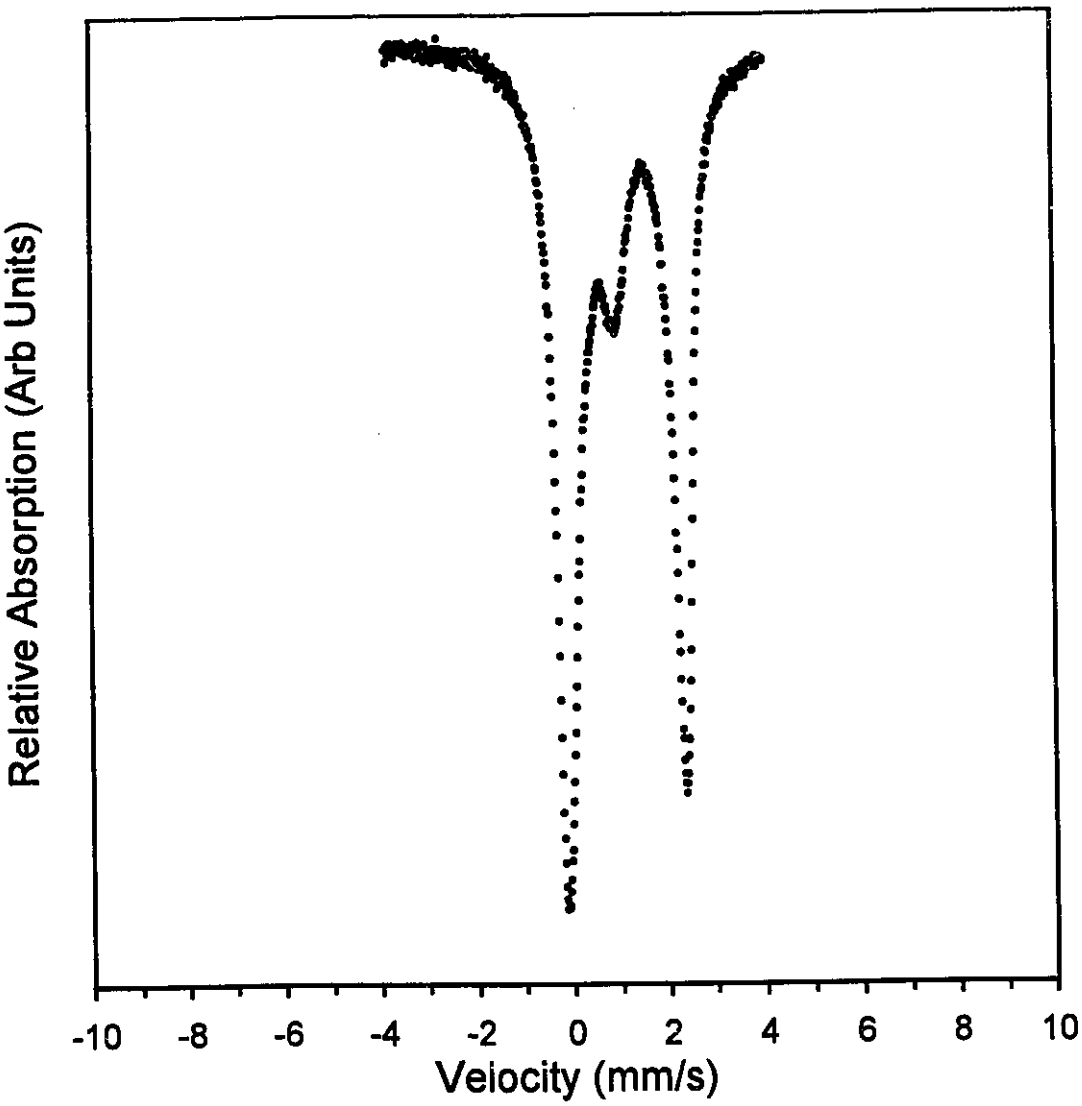

Figure D.1f *Mössbauer spectrum of partially oxidized synthetic annite at 295K.*

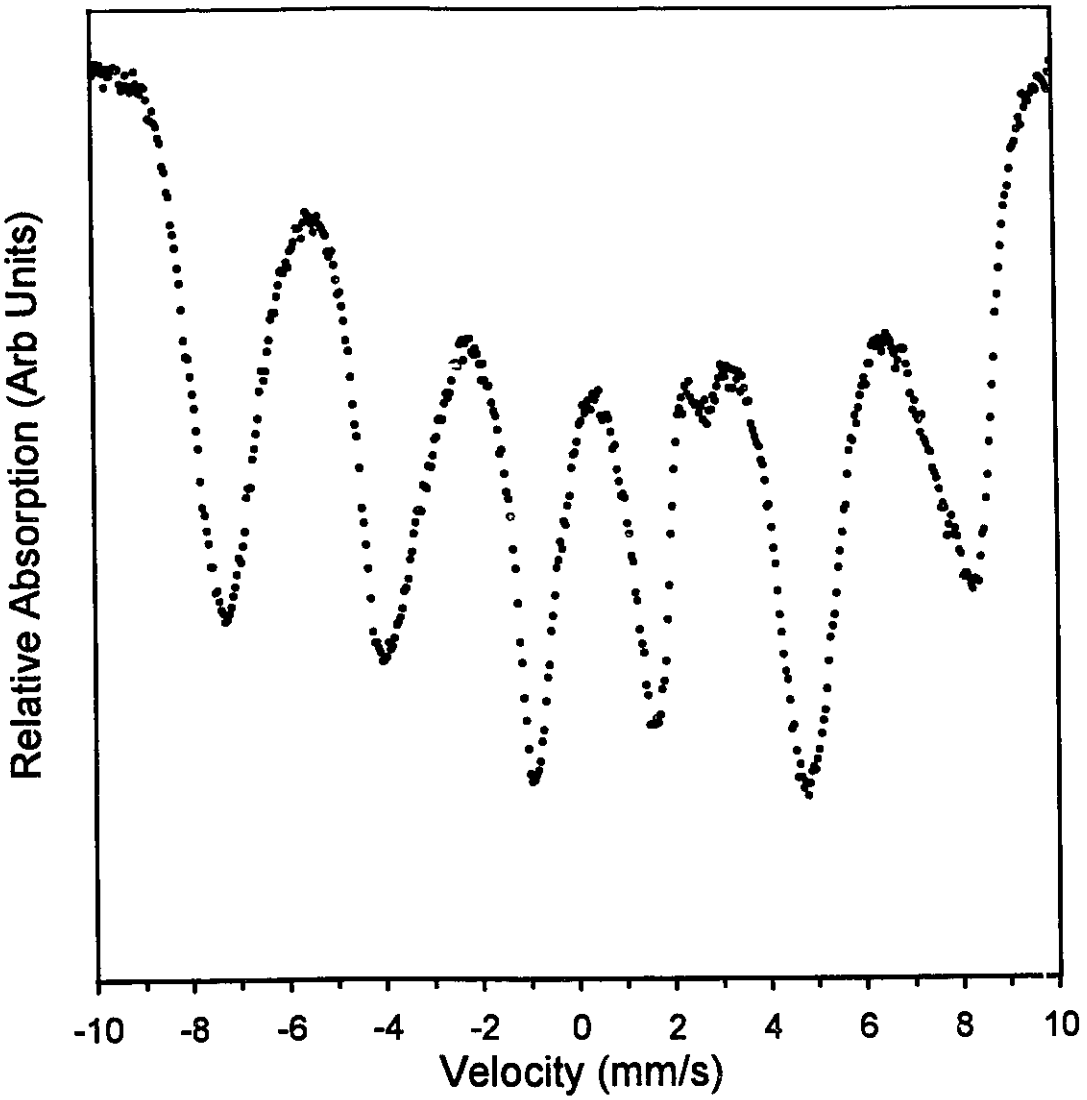

Figure D.2a *Mössbauer spectrum of oxidized synthetic annite at 4.2K.*

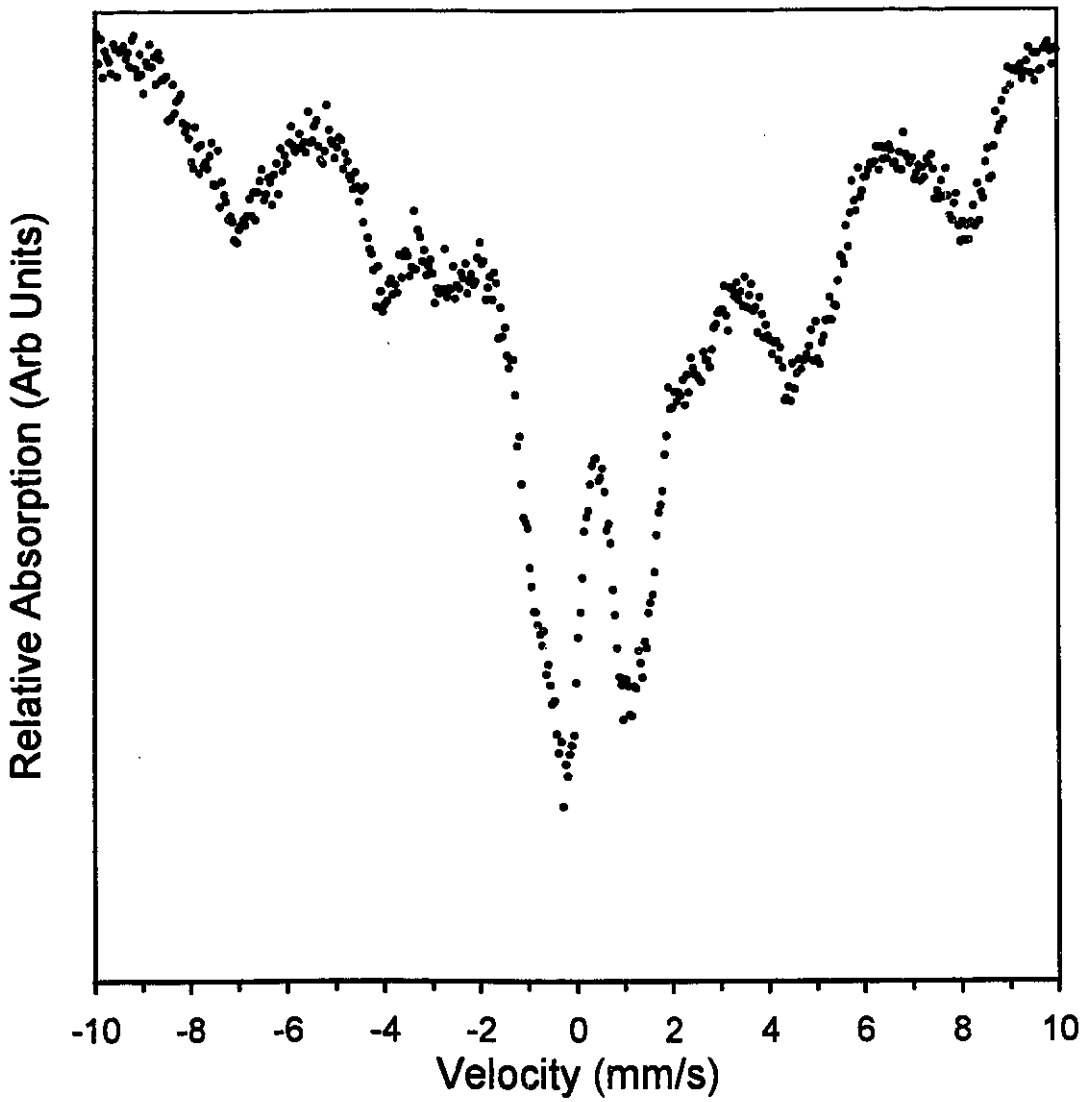

Figure D.2b *Mössbauer spectrum of oxidized synthetic annite at 15K.*

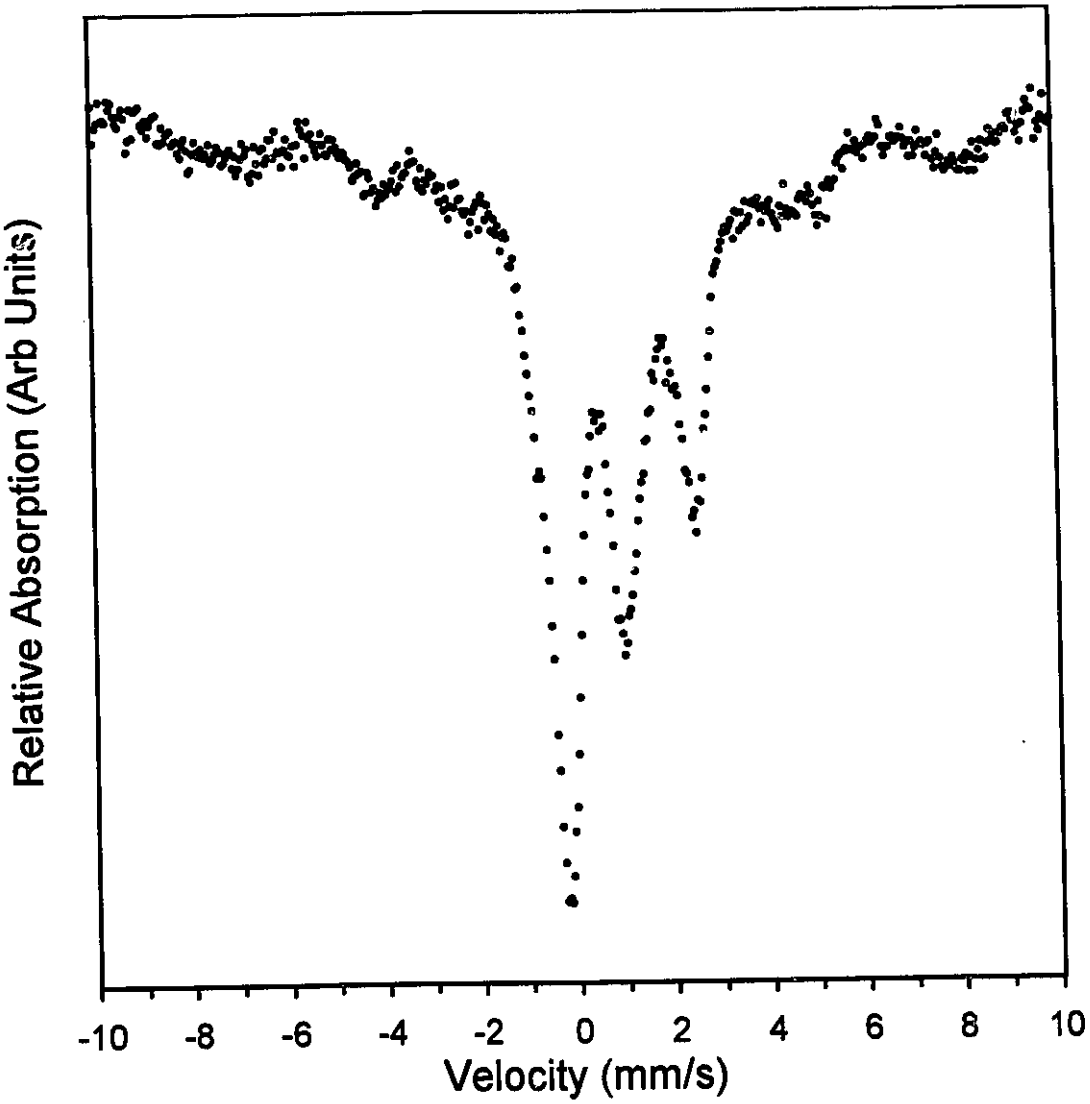

Figure D.2c *Mössbauer spectrum of oxidized synthetic annite at 25K.*

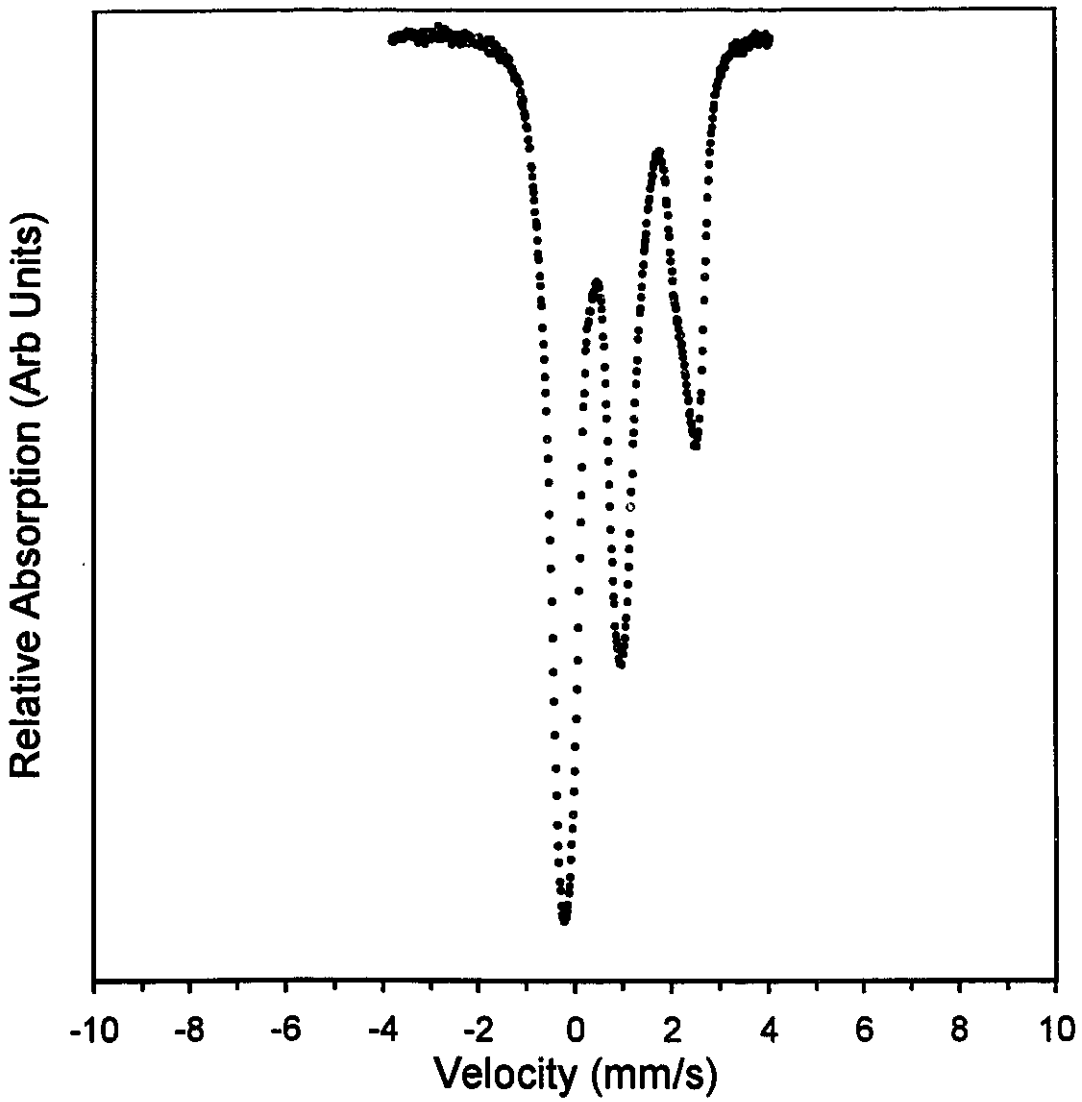

Figure D.2d *Mössbauer spectrum of oxidized synthetic annite at 83K.*

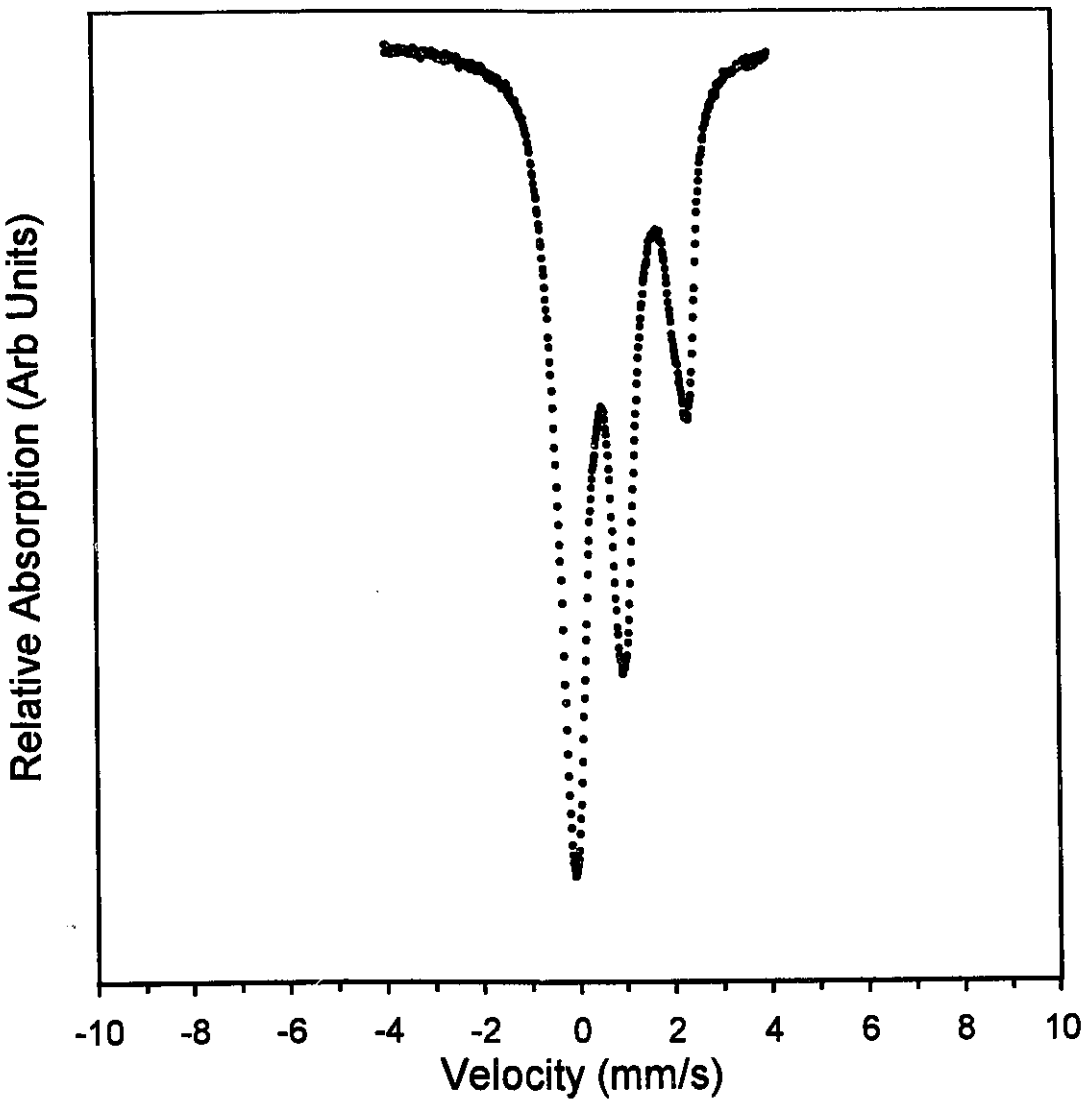

Figure D.2e *Mössbauer spectrum of oxidized synthetic annite at 295K.*

Appendix E
Annite Mössbauer Spectra Simulations

Because of the large number of fitting options available for fitting the low temperature Mössbauer spectrum of annite it was important to attempt to gain a qualitative understanding of the behaviour of the Mössbauer spectrum of annite via simulation as well as fitting. In particular, an appreciation of the development of the spectrum with changing $g^*\mu_N H$ is important in attempting to visualize the contributions to the differentially broadened spectrum.

While including all of the possible simulations would have added unnecessary length to the thesis, the following figures are included as examples of the development of elemental Mössbauer patterns with increasing $g^*\mu_N H$. Figures are shown for the symmetric TRANS-site and for all five CIS sites. All patterns begin from a quadrupole doublet (i.e. $g^*\mu_N H = 0$) with QS = 2.95 mm/s and with CS = 1.35 mm/s. This CIS site patterns use $\eta = 0.75$. The sign of e^2qQ and the values of θ and ϕ are varied to correspond to the sites described in table 7.7.

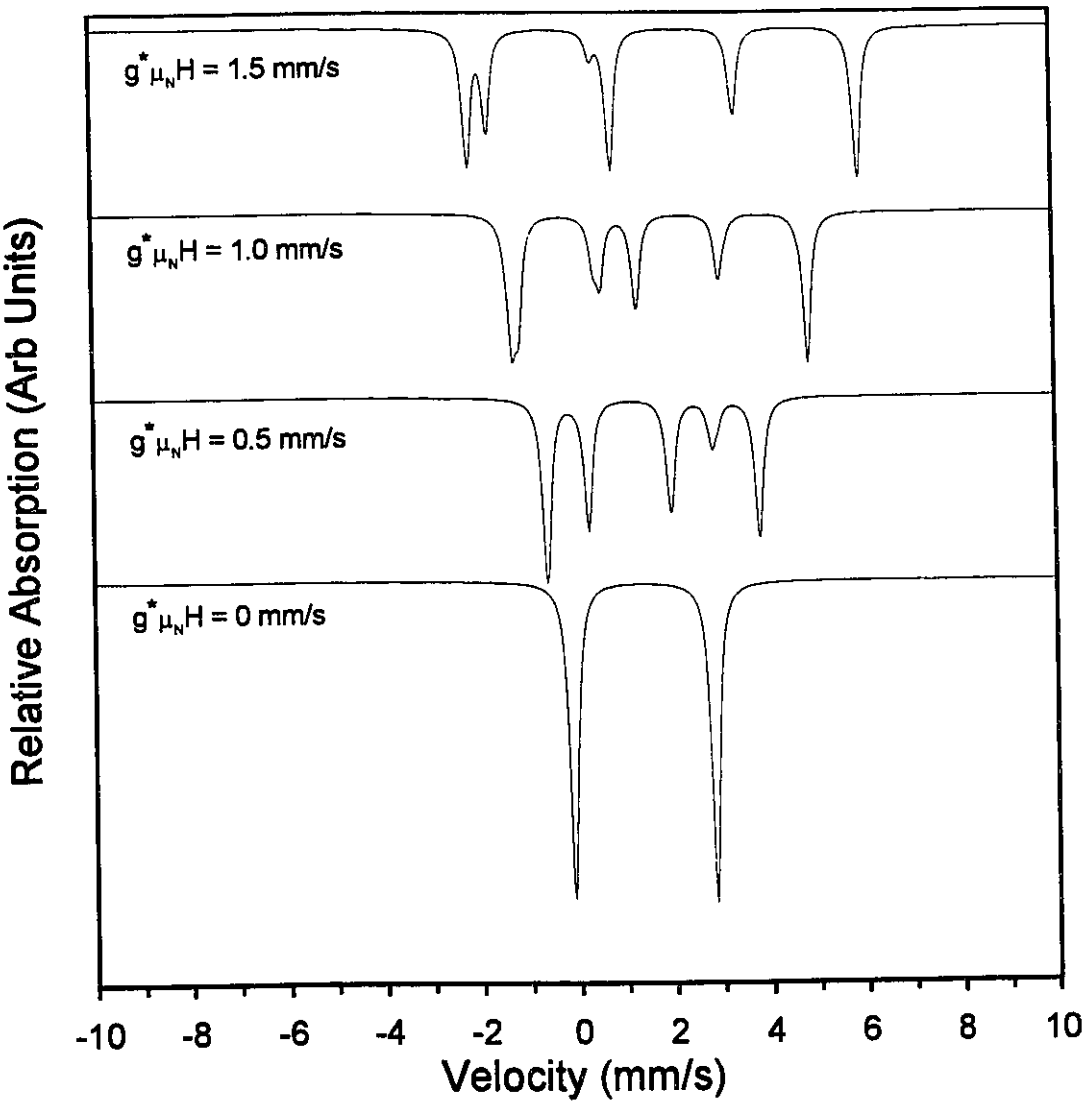

Figure E.1 *Development of elemental Mössbauer spectrum with increasing* $g^*\mu_N H$ *for a symmetric TRANS site with* $e^2qQ < 0$..

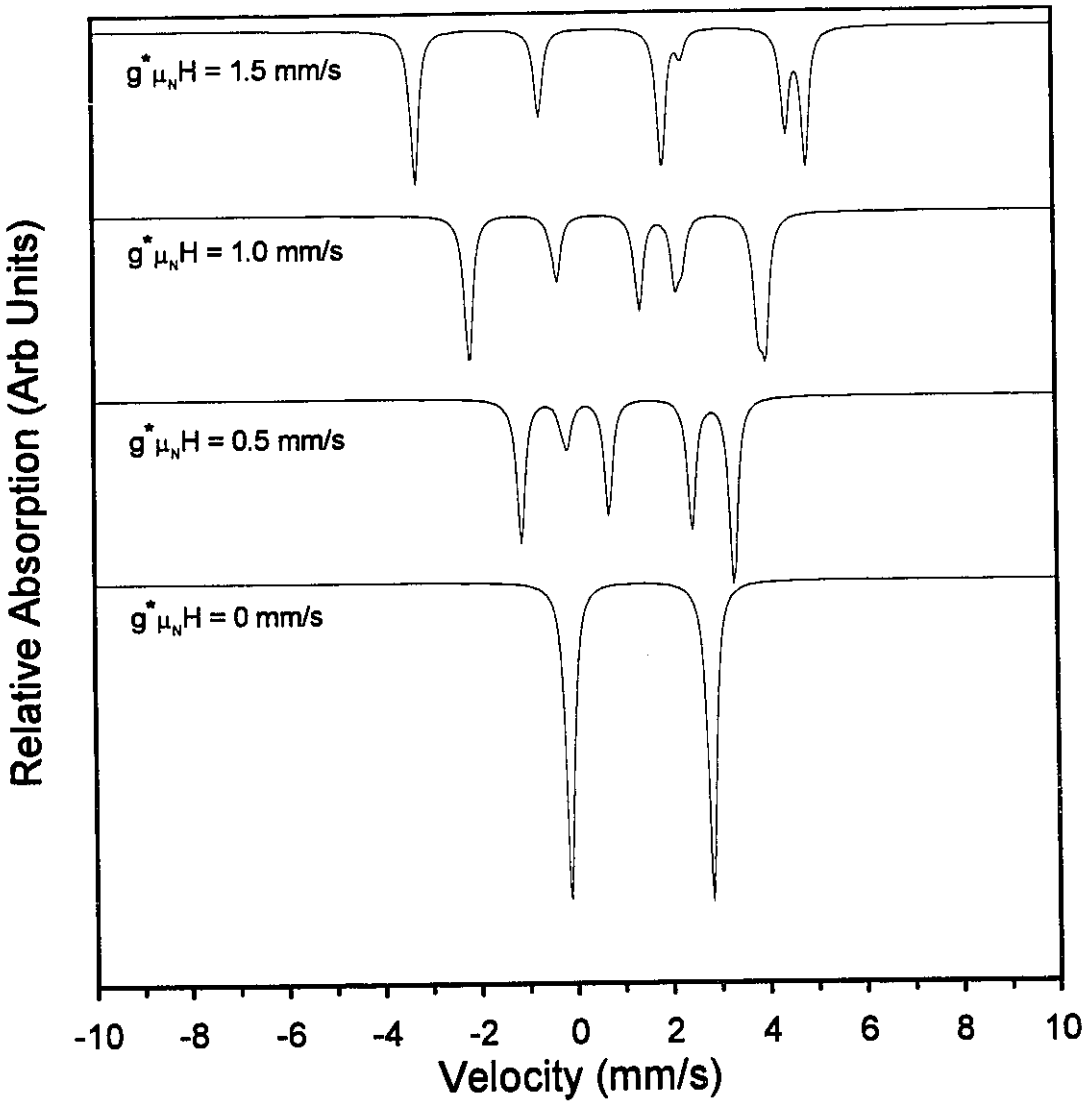

Figure E.2 *Development of elemental Mössbauer spectrum with increasing* $g^*\mu_N H$ *for a symmetric TRANS site with* $e^2qQ > 0$.

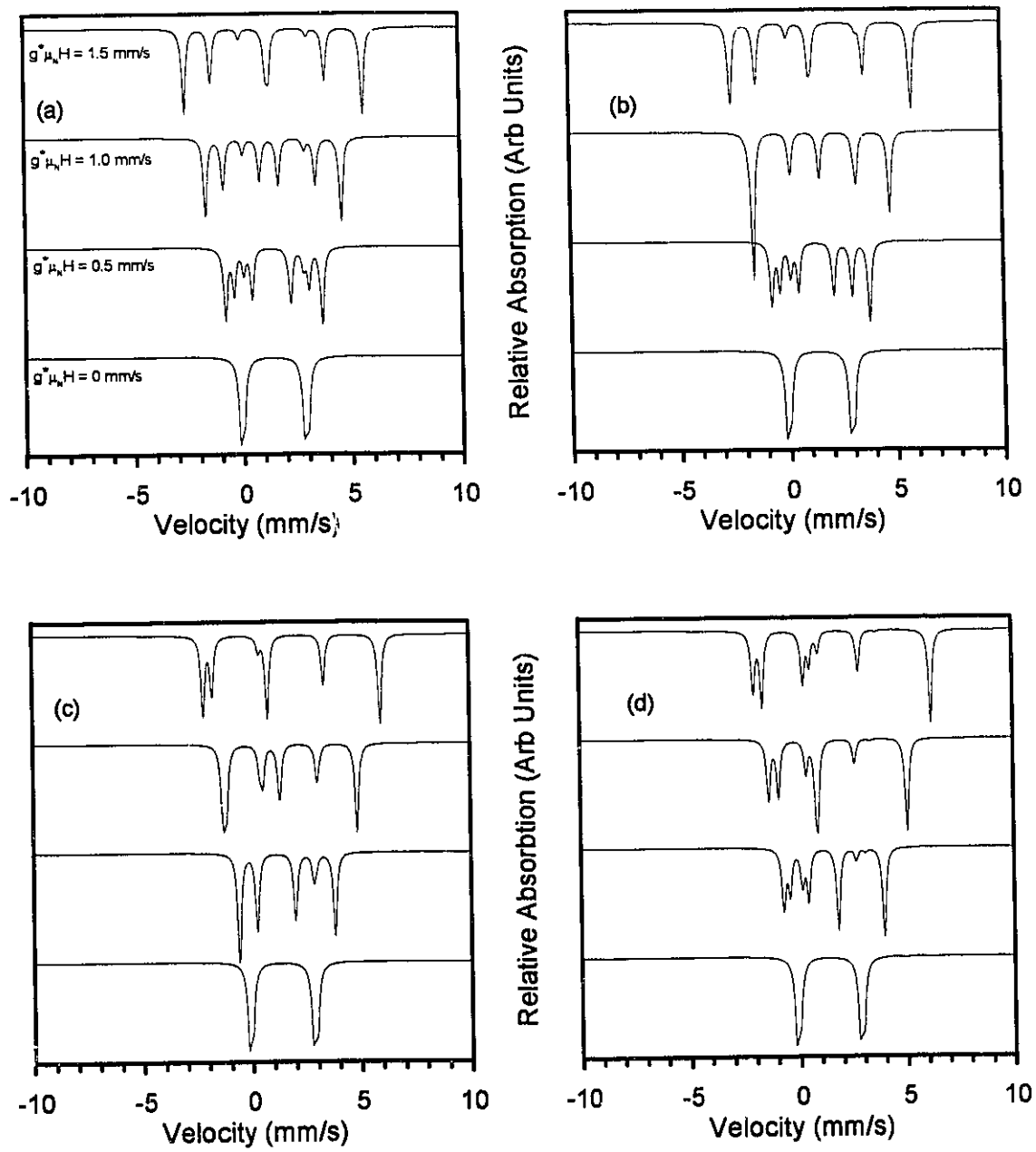

Figure E.3 *Development of elemental Mössbauer spectrum with increasing $g^*\mu_N H$ for a CIS[1] site with $\eta = 0.75$ for (a) $\phi=0^o$, (b) $\phi=30^o$, (c) $\phi=60^o$, and (d) $\phi=90^o$.*

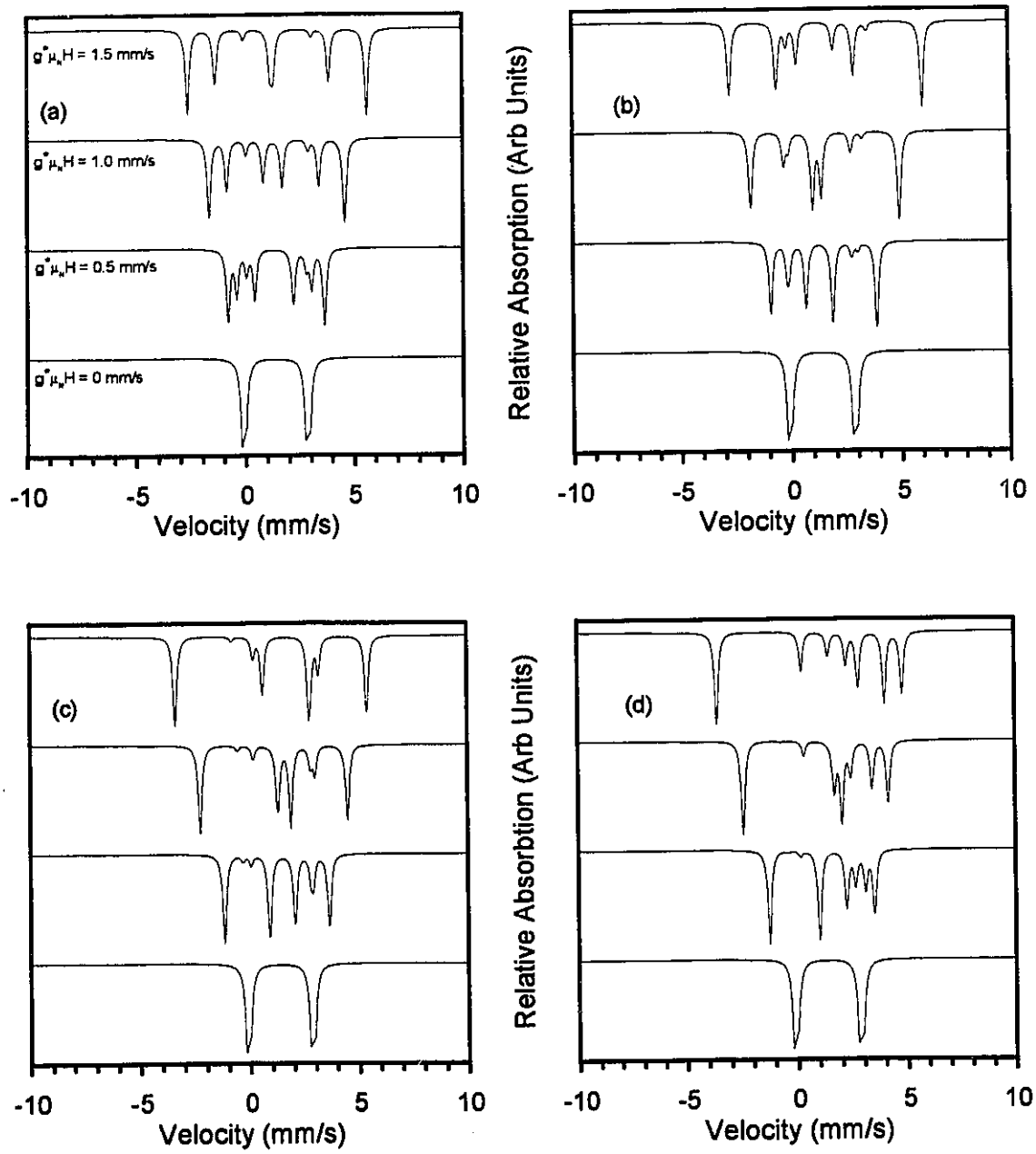

Figure E.4 *Development of elemental Mössbauer spectrum with increasing $g^*\mu_N H$ for a CIS^2 site with $\eta = 0.75$ for (a) $\theta=0^o$, (b) $\theta=30^o$, (c) $\theta=60^o$, and (d) $\theta=90^o$.*

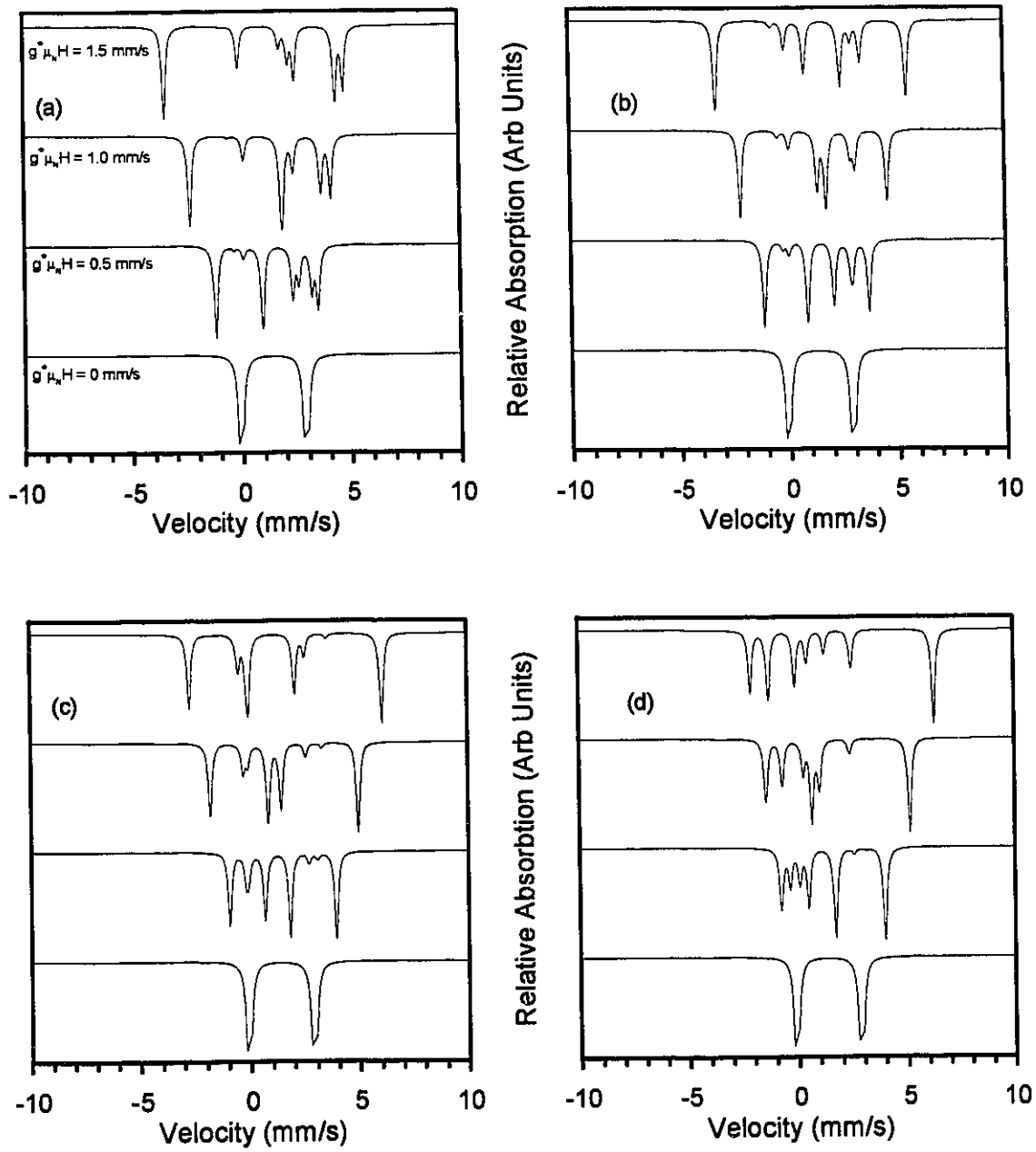

Figure E.5 *Development of elemental Mössbauer spectrum with increasing $g^*\mu_N H$ for a CIS^3 site with $\eta = 0.75$ for (a) $\theta=0^o$, (b) $\theta=30^o$, (c) $\theta=60^o$, and (d) $\theta=90^o$.*

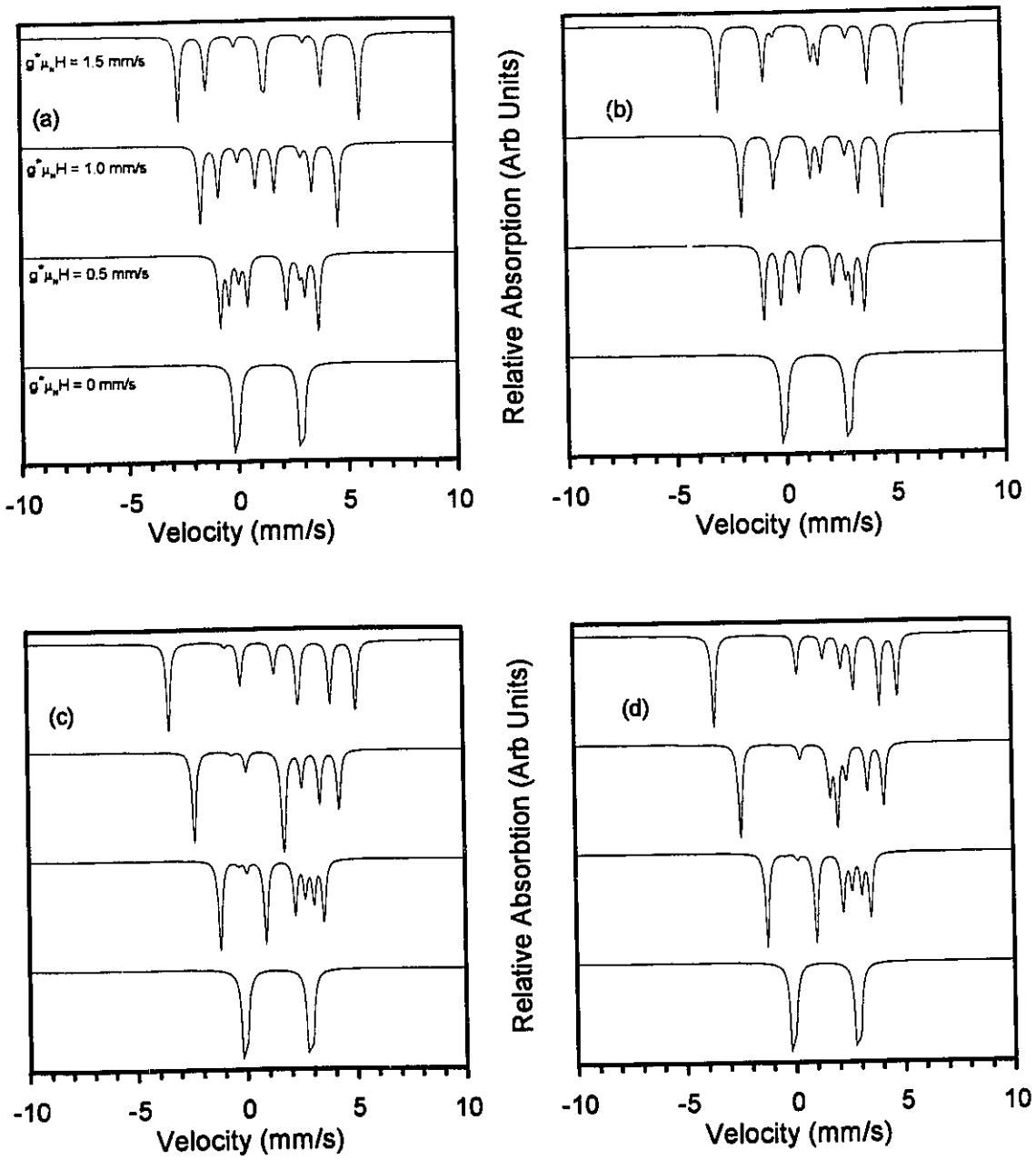

Figure E.6 *Development of elemental Mössbauer spectrum with increasing $g^*\mu_N H$ for a CIS^4 site with $\eta = 0.75$ for (a) $\theta=0^o$, (b) $\theta=30^o$, (c) $\theta=60^o$, and (d) $\theta=90^o$.*

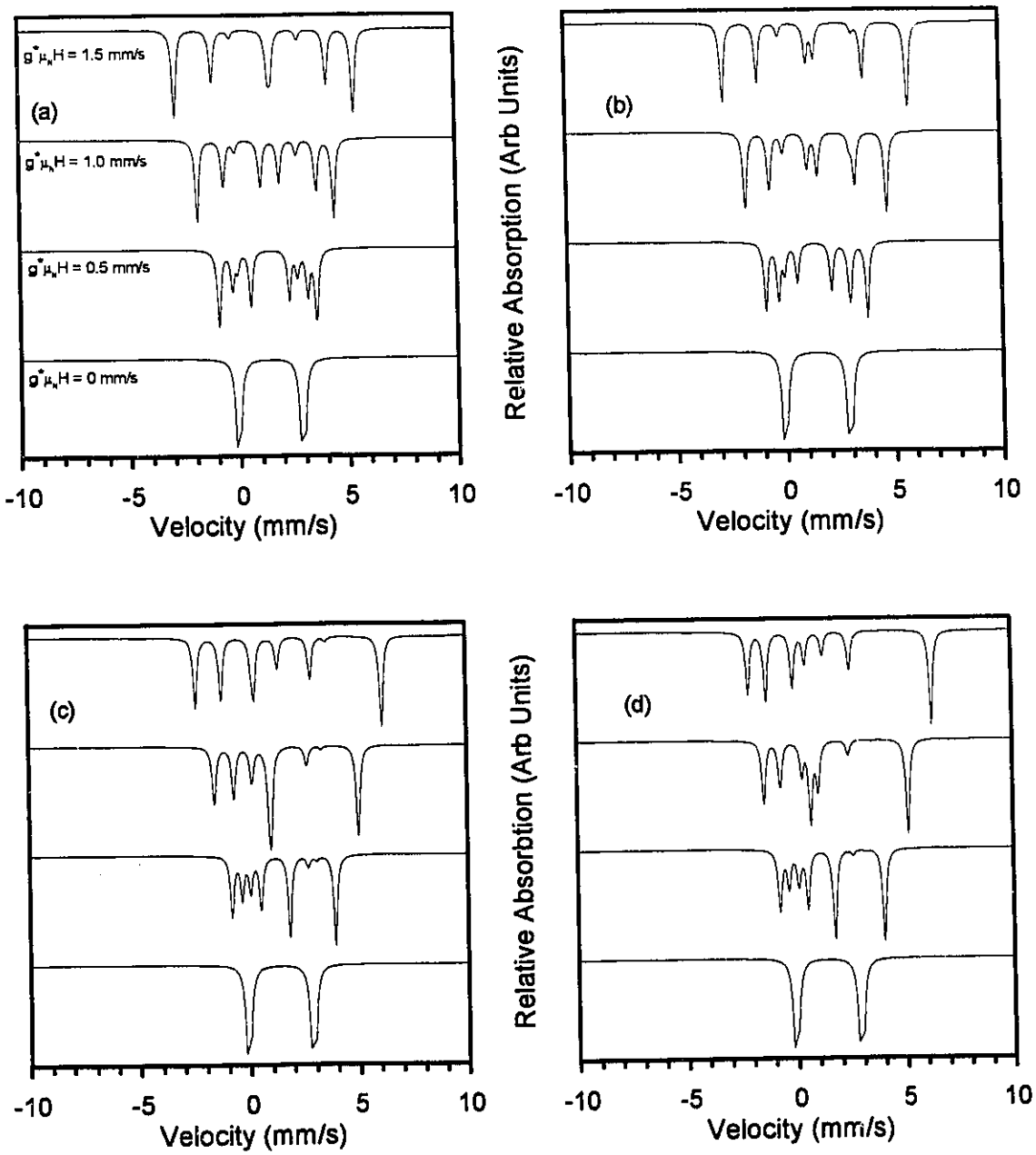

Figure E.7 *Development of elemental Mössbauer spectrum with increasing $g^*\mu_N H$ for a CIS[5] site with $\eta = 0.75$ for (a) $\theta=0^o$, (b) $\theta=30^o$, (c) $\theta=60^o$, and (d) $\theta=90^o$.*